
COMPUTATIONAL STUDY OF PROTON TRANSFER IN DIFORMYL DIPYRROMETHANES AND DENITROGENATION OF 1-PYRAZOLINES

By

RENUKA PRADHAN

CHEM11201104006

National Institute of Science Education and Research Bhubaneswar

*A thesis submitted to the
Board of Studies in Chemical Sciences
in partial fulfillment of requirements for the degree of
DOCTOR OF PHILOSOPHY
of*

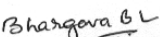
HOMI BHABHA NATIONAL INSTITUTE



APRIL 2018

Homi Bhabha National Institute¹
Recommendations of the Viva Voce Committee

As members of the Viva Voce Committee, we certify that we have read the dissertation prepared by **Renuka Pradhan** entitled "Computational Study of Proton Transfer in Diformyl Dipyrromethanes and Denitrogenation of 1-Pyrazolines" and recommend that it may be accepted as fulfilling the thesis requirement for the award of Degree of Doctor of Philosophy.

Chairman	 Prof. A. Srinivasan	9.4.18 Date
Guide	 Dr. U. Lourderaj	9.4.2018 Date
External Member	 Prof. K. Srihari	Apr 09, 2018 Date
Member 1	 Dr. B. L. Bhargava	09.04.2018 Date
Member 2	 Dr. S. Peruncheralathan	09.04.2018 Date
Member 3	 Dr. A. V. Anil Kumar	09/04/2018 Date

Final approval and acceptance of this thesis is contingent upon the candidate's submission of the final copies of the thesis to HBNI.

We hereby certify that we have read this thesis prepared under our direction and recommend that it may be accepted as fulfilling the thesis requirement.

Date: 9.4.2018
Place: Bhubaneswar



Dr. U. Lourderaj
Guide

¹This page is to be included only for final submission after successful completion of viva voce.

STATEMENT BY AUTHOR

This dissertation has been submitted in partial fulfillment of requirements for an advanced degree at Homi Bhabha National Institute (HBNI) and is deposited in the Library to be made available to borrowers under rules of the HBNI.

Brief quotations from this dissertation are allowable without special permission, provided that accurate acknowledgement of source is made. Requests for permission for extended quotation from or reproduction of this manuscript in whole or in part may be granted by the Competent Authority of HBNI when in his or her judgment the proposed use of the material is in the interests of scholarship. In all other instances, however, permission must be obtained from the author.

Renuka Pradhan

Signature of the Student

Renuka Pradhan

DECLARATION

I hereby declare that the investigation presented in the thesis has been carried out by me. The work is original and has not been submitted earlier as a whole or in part for a degree/diploma at this or any other Institution/University.

Renuka Pradhan

Signature of the Student
Renuka Pradhan

LIST OF PUBLICATIONS ARISING FROM THE THESIS

Journal

1. Sreedevi, K. G.; Thomas, A. P.; Aparna, K.; **Pradhan, R.**; Reddy, M.; Lourderaj, U.; Srinivasan, A. Photoenolization via Excited State Double Proton Transfer Induces “turn on” Fluorescence in Diformyl Diaryl Dipyrromethane. *Chem. Commun.* **2014**, *50*, 8667-8669.
2. **Pradhan, R.**; Harshan, A. K.; Krishnavilasam, Chandrika G. S.; Srinivasan, A.; Lourderaj, U. Time-Dependent Density Functional Theoretical Investigation of Photoinduced Excited-State Intramolecular Dual Proton Transfer in Diformyl Dipyrromethanes. *J. Phys. Chem A* **2016**, *120*, 9894-9906
3. **Pradhan, R.**; Lourderaj, U. Quantum Chemical Investigation of the Thermal Denitrogenation of 1-pyrazoline. *Phys. Chem. Chem. Phys* **2017**, *40*, 27468-27477

Manuscripts under preparation

1. **Pradhan, R.**; Lourderaj, U. Ab Initio Chemical Dynamics Simulations of Denitrogenation of 1-Pyrazoline
2. **Pradhan, R.**; Lourderaj, U. Ab Initio Chemical Dynamics Simulations of Denitrogenation of Substituted 1-Pyrazolines
3. **Pradhan, R.**; Lourderaj, U. Quantum Chemical Investigation of Denitrogenation of Dimethyl-1-pyrazolines in the Presence of External Force

Renuka Pradhan

Signature of the Student

Renuka Pradhan

CONFERENCES

1. Presented a Poster Entitled, "**Mechanism of Thermal Denitrogenation of 1-pyrazoline**"- Renuka Pradhan, Upakarasamy Lourderaj* at Spectroscopy and Dynamics of Molecules and Clusters (SDMC) - 2014 conference, organized by school of chemical sciences, NISER, BBSR.
2. Presented a Poster Entitled, "**Ab Initio Chemical Dynamics of Thermal Denitrogenation of 1-pyrazoline**"- Renuka Pradhan, Upakarasamy Lourderaj* at Theoretical Chemistry Symposium - 2014, organized by National Chemical Laboratory, pune.
3. Presented a Poster Entitled, "**Mechanism and Dynamics of Thermal Denitrogenation of 1-pyrazoline**"- Renuka Pradhan, Upakarasamy Lourderaj* at Spectroscopy and Dynamics of Molecules and Clusters (SDMC) - 2015 conference, organized by IIT Kanpur.

Renuka Pradhan

Signature of the Student
Renuka Pradhan

ACKNOWLEDGEMENTS

Firstly, I would like to express my sincere gratitude to my thesis advisor Dr. U. Lourderaj for his patience, motivation and continuous support during the course of my Ph.D work. I would also like to thank Prof. A. Srinivasan, Dr. Gowri Sridevi and Dr. Ajesh P Thomas for their collaboration in the project on ESIDPT. I also thank the thesis monitoring committee members Prof. A. Srinivasan, Dr. S. Peruncheralathan, Dr. B. L. Bhargava, and Dr. A. V. Anil Kumar for their support. I thank my labmates for all the stimulating discussions and for all the fun i have had in the last five years. Last but not the least, I would like to thank my family members for their unconditional love and support.

SYNOPSIS

Computational study of chemical reactions is of fundamental importance to understand the atomic-level mechanisms. It gives us information about the geometrical parameters, stability, and reactivity of molecules, which help in designing new molecules, maximize product yield and control chemical reactions to get desired products. Computing the potential energy surfaces (PESs) for various possible reaction pathways and their corresponding stationary points - reactants, products, intermediates, and transition-state structures, enable us to estimate rate constant that can be compared with experiments. To this end, transition state theory (TST) and Rice-Ramsperger-Kassel-Marcus (RRKM) theory have been used to model the rate constants. However, there are some reactions that do not follow minimum energy path (MEP) and deviations from statistical behaviour are observed. In such cases, dynamical calculations are essential to understand the atomic-level mechanisms and calculation of rate constants. Hence it is important that the popular statistical theories need to be tested to have a better understanding of chemical reactions in general.

The present thesis is focused to understand the atomic-level mechanism of photoinduced excited state intramolecular double proton transfer (ESIDPT) in diformyl dipyrromethanes, thermal denitrogenation of 1-pyrazolines, and denitrogentaion of 1-pyrazolines in the presence of an external force. The thesis is organized as follows: a general introduction to computational study of chemical reactions is discussed in Chapter 1, Chapters 2 to 6 discuss the various results obtained from different studies.

In Chapter 1, a general introduction of current status of computational studies of chemical reactions is discussed. Computationally, information about the structures, relative energies, electron density distribution, vibrational frequencies, reactivity of molecules and spectral information can be obtained by solving the time independent Schrödinger equation $\hat{H}\Psi = E\Psi$. Several ab initio methods such as HF, DFT, MP2, CASSCF, CI are available to solve this Schrödinger equation. The dynamic properties of molecules can be obtained either quantum mechanically by solving the time dependent Schrödinger equation $i\hbar\frac{\partial}{\partial t}\Psi(\mathbf{r}, t) = \hat{H}\Psi(\mathbf{r}, t)$ or classically by integrating the Newton's equation of motion $F = \frac{dp}{dt}$. In this chapter, a brief description of all these methods will be given.

Chapter 2 discusses the mechanism of photoinduced ESIDPT in diformyl dipyrromethanes. Experimentally, it was observed that photoinduced enolization occurred in 1,9-diformyl-5,5-diaryldipyrromethane (DA_{KK}) by excited state dual proton transfer resulting in a red shifted absorption, a phenomena not observed in 1,9-diformyl-5,5-dimethyldipyrromethane (DM_{KK}), and 1,9-diformyl-5-aryldipyrromethane (MA_{KK}). The observation was supported by preliminary Density Functional Theoretical (DFT) calculations. In the work reported here, a detailed and systematic study was undertaken considering four molecules, 1,9-diformyldipyrromethane (DH_{KK}), DM_{KK}, MA_{KK}, and DA_{KK} and their rotational isomers using DFT methods. Different processes, namely, cis-trans isomerization, single and double proton transfer processes and their mechanistic details were investigated in the ground and excited states. From the simulation studies, it was seen that the presence of different substituents at the meso carbon does not affect the λ_{abs} values during cis \rightarrow trans isomerization. However, enolization by proton transfer processes were found to be influenced by the substituents as seen in the experiments. Enolization was observed to follow a step-wise mechanism i.e. diketo \rightarrow monoenol \rightarrow dienol. While monoenols showed negligible substituent effects on the λ_{abs} values, a large red shift in λ_{abs} was seen only in DA_{KK} in agreement with the experimental findings. This observation can be attributed to the lowering of keto \rightarrow enol activation barrier, stabilization of DA_{EE} in the S₁ state, and the charge transfer nature of the transitions involved in DA_{EE}.

Quantum chemical investigation of thermal denitrogenation of 1-pyrazolines is discussed in Chapter 3. The mechanism of denitrogenation of azo compounds has been a subject of study for both experiment and theory due to its unusual stereochemical preference in product formation. Thermal denitrogenation of 3,5-dimethyl-1-pyrazoline, exo- and endo-2-methyl-3,4-diazabicyclo[3.3.0] oct-3-enes, and 4-methyl-2,3-diazabicyclo[3.2.0] hept-2-ene result in major single inverted cyclopropane. Several mechanisms have been proposed to account for the inversion of stereochemistry however the studies are still inconclusive. In the present work, a detailed investigation on mechanism of thermal denitrogenation of 1-pyrazoline was undertaken using CASSCF and CASPT2 methods and 6-31+G* basis set. CASSCF calculations were performed with a series of different active spaces and it was found that the energetics obtained from CASSCF(4,4), where both the C-N σ - σ^* orbitals were included in the active space is similar to that obtained from CASSCF energies with larger active spaces and CASPT2(4,4)//CASSCF(4,4) calculations. Three different denitrogenation paths were obtained: (1) a synchronous path where a simultaneous breaking of both the C-N σ bonds lead to a planar trimethylene diradical intermediate, (2) an asynchronous concerted path involving the unsymmetrical breaking of C-N σ bonds resulting in the single inverted cyclopropane formation, and (3) an asynchronous step-wise path which involves the unsymmetrical breaking

of the C–N σ bonds leading to diazenyl diradical intermediates. The barrier for synchronous denitrogenation path was found to be lower in energy than that of the asynchronous paths which is in contrast to the previous reports where asynchronous paths were more favourable. To check the validity of DFT and MP2 methods for this reaction, the potential energy profile for denitrogenation paths were mapped with different DFT functionals (B2LYP, B2PLYP, M06-2X) and MP2 method. However, DFT and MP2 methods failed to provide a correct description of PES in the diradical region. In addition, the energetics of denitrogenation paths were found to be remain unaffected with the increase in basis sets.

In Chapter 4, ab initio chemical dynamics of denitrogenation of 1-pyrazoline is discussed. The detailed mapping of potential energy profile for denitrogenation of 1-pyrazoline using CASSCF and CASPT2 methods does not explain the experimentally observed stereochemical preference in cyclopropane formation. So, to understand the atomic-level mechanism of thermal denitrogenation of 1-pyrazoline, ab initio classical trajectory simulations were performed at the CASSCF(4,4)/6-31+G* level of theory. Trajectories were integrated from transition states and reactant regions. A microcanonical sampling of initial state was constructed at the experimental temperature (510.45 K). The amount of energy available to system at this temperature was found to be 119.10 kcal/mol. 150 trajectories were integrated from the synchronous transition state and 100 trajectories were integrated from each asynchronous transition states by giving an excess energy corresponding to a total of 119.10 kcal/mol. It was observed that, most of the trajectories dissociates directly from transition states with out following the minimum energy path (MEP). Similarly, 3000 trajectories were integrated from reactant by giving a total energy of 119.10 kcal/mol. Out of 3000 trajectories, 262 trajectories were reactive with in the 1.5 ps time scale. Among 262 reactive trajectories, 117 trajectories lead to single inverted cyclopropane (SI), 88 trajectories lead to double inverted cyclopropane (DI), 57 trajectories lead to cyclopropane with retention of configuration (Ret) of configuration. So the product stereochemistry obtained from trajectory simulation are in reasonable agreement with the experimentally observed product stereochemistry. The simulations indicate that the denitrogenation follow both synchronous and asynchronous paths and most of the trajectories did not follow MEP. Interestingly, some of the synchronous trajectories dissociate through second-order saddle point region.

In Chapter 5, the effects of substitution on the energetics and dynamics of denitrogenation of 1-pyrazoline is discussed. The potential energy profiles for the denitrogenation of four different substituted pyrazolines, trans- and cis-3,5-dimethyl-1-pyrazoline and exo- and endo-2-methyl-3,4-diazabicyclo[3.3.0]oct-3-ene were mapped at the CASSCF(4,4)/6-31+G* level of theory. No significant effects of substitution on the energetics of denitrogenation paths were observed. To understand the effect of substitution on the dynamics of the denitrogenation of

1-pyrazoline, 500 trajectories were integrated from trans-3,5-dimethyl-1-pyrazoline. From the trajectory simulation results, a preference for formation of single inverted cyclopropane over double inverted cyclopropane and cyclopropane with retention of configuration was observed as seen in the experimental studies. The dissociation of trajectories happen via both synchronous and asynchronous paths. Most of the synchronous trajectories follow MEP whereas the majority of the asynchronous trajectories do not follow MEP.

In Chapter 6, quantum chemical investigation of effects of external force on 1-pyrazoline, cis- and trans-3,5-dimethyl-1-pyrazoline, and the denitrogenation of cis- and trans-3,5-dimethyl-1-pyrazoline are discussed. In mechanochemistry, an external force (mechanical) is exerted on the system and the response of the system to the force is investigated. Recently studies show that mechanochemistry can be used to promote forbidden chemical reactions [*Nature*, 2007, **446**, 424, *Nat. Chem.*, 2015, **7**, 323]. In the present study, constrained geometry simulate external force (COGEF) method was used to model the effect of external force. In COGEF method, two atoms of a molecule are considered as pulling points (PPs) and mechanical stress is simulated by increasing distance between the two PPs gradually in a step-by-step process. For 1-pyrazoline, two ring carbon atoms were considered as PPs whereas for trans- and cis-3,5-dimethyl-1-pyrazoline, the two methyl carbon atoms were considered as PPs. For 1-pyrazoline, a synchronous increase in C–N and C–C distances were observed with the increase in PPs distance up to 0.8 Å beyond which the molecule dissociates to form diazomethane and ethene. For cis- and trans-3,5-dimethyl-1-pyrazoline, two different approaches were used to calculate the effect of external force: (1) symmetrical stretching of both the C–CH₃ covalent bond and (2) asymmetrical stretching of the C–CH₃ bond. For symmetric stretching of both the C–CH₃ bonds, a significant changes in geometrical parameters of cis- and trans-3,5-dimethyl-1-pyrazolines were observed with the increase in PPs distance whereas for the asymmetrical stretching pathway, no significant changes in geometrical parameters were observed except the C–N and C–CH₃ distances associated with the stretching. The potential energy profiles for denitrogenation of cis- and trans-3,5-dimethyl-1-pyrazoline were also mapped in the presence of external force of magnitude 0.5, 1.8, 4.6, and 10.2 nN. It was observed that for cis-3,5-dimethyl-1-pyrazoline, the barrier for denitrogenation paths initially increase with the increase in external force upto 4.6 nN and then decreases. However, for trans-3,5-dimethyl-1-pyrazoline the barrier for denitrogenation paths decreases with the increase in external force. Thus, external force are expected to affect the mechanism and the dynamics of denitrogenation.

TABLE OF CONTENTS

	Page
Synopsis	xiii
List of Figures	xxi
List of Tables	xxvii
1 Introduction	1
2 TDDFT Investigation on Photoinduced Excited State Intramolecular Dual Proton Transfer in Diformyl Dipyrromethane	15
2.1 Introduction	15
2.2 Methodology	17
2.3 Results and Discussions	18
2.3.1 Ground state studies	19
2.3.2 Photophysics	30
2.4 Discussion	44
2.5 Conclusion	47
3 Thermal Denitrogenation of 1-pyrazoline: Energetics	49
3.1 Introduction	49
3.2 Methodology	52
3.3 Results and Discussions	54
3.3.1 Synchronous Cleavage of the Two C–N Bonds	54
3.3.2 Asynchronous Cleavage of the C–N bonds	58
3.3.3 Asynchronous concerted elimination of N ₂	67
3.3.4 Alkene formation	68
3.3.5 Effect of Basis sets	70
3.3.6 DFT and MP2 methods	70

3.4	Discussion and Conclusion	74
4	Thermal Denitrogenation of 1-Pyrazoline: Dynamics	77
4.1	Introduction	77
4.2	Computational Details	79
4.3	Results and Discussion	81
4.3.1	Trajectories Initiated from the Transition State Region	81
4.3.2	Trajectories Integrated from the Reactant Region	98
4.3.3	Significance of Second-Order Saddle Point on the Dynamics of Denitrogenation	104
4.3.4	Product Energies	111
4.4	Conclusion	114
5	Effect of Substitution on the Thermal Denitrogenation of 1-Pyrazoline	119
5.1	Introduction	119
5.2	Computational Details	121
5.3	Results and Discussion: Energetics	122
5.3.1	Synchronous Cleavage of the Two C–N Bonds	123
5.3.2	Asynchronous Cleavage of the two C–N Bonds	128
5.3.3	Alkene Formation	132
5.4	Results and Discussion: Dynamics	134
5.4.1	Trajectories Following Synchronous Denitrogenation Path	135
5.4.2	Trajectories Following Asynchronous Denitrogenation Path	136
5.5	Conclusion	138
6	Denitrogenation of Pyrazolines Under Mechanical Stress	139
6.1	Introduction	139
6.2	Methodology	141
6.3	Results and Discussion	144
6.3.1	Effect of External Force on the 1-Pyrazoline	144
6.3.2	Effect of External Force on trans-3,5-dimethyl-1-pyrazoline	146
6.3.3	Effect of External Force on Cis-3,5-dimethyl-1-pyrazoline	149
6.3.4	Effect of External Force on Energetics of Denitrogenation Paths Obtained for Trans- and Cis-3,5-dimethyl-1-pyrazoline	150
6.3.5	Comparison of the Energetics of Denitrogenation	158
6.4	Summary and Conclusion	159

LIST OF FIGURES

FIGURE	Page
1.1 Schematic diagram showing relations between different quantum chemical models used for understanding static properties ⁷	10
2.1 Molecules considered in the study: R ₁ and R ₂ are [−H, −H], [−CH ₃ , −CH ₃], [−H, −C ₆ H ₅ CH ₃] and [−C ₆ H ₅ CH ₃ , −C ₆ H ₅ CH ₃].	18
2.2 Potential energy contours showing the existence of different rotational isomers of DH _{KK} for different values of ϕ_1 and ϕ_2 . Labels KK1 to KK8 correspond to different rotational isomers in the respective regions.	19
2.3 Minimum energy structures representing different rotational isomers of DH _{KK}	20
2.4 (a) Illustration depicting operations used to relate and group the rotational isomers (b) Three stable rotational isomers of DH _{KK}	20
2.5 Potential energy contours of DH _{KK} for different values of ϕ_1 and ϕ_2 and a sample trajectory (white line) showing anti1 to syn isomerization.	23
2.6 Potential energy contours showing the existence of different rotational isomers of DH _{KE} for different values of ϕ_1 and ϕ_2 . KE1 to KE6 correspond to different rotational isomers in the respective regions.	27
2.7 Minimum energy structures of different rotational isomers of the monoenol DH _{KE}	27
2.8 Potential energy contours showing the existence of different rotational isomers of DH _{EE} for different values of (ϕ_1) and (ϕ_2). EE1 to EE10 correspond to different rotational isomers in the respective regions.	28
2.9 Minimum energy structures of different rotational isomers of the dienol DH _{EE}	28
2.10 Stepwise cis-trans isomerization paths for DH in ground and first excited-state.	32
2.11 Molecular orbital diagram of anti2 isomer of DH _{KK} , DH _{KE} , and DH _{EE} calculated at the B3LYP/6-31+G* level.	34
2.12 Molecular orbital diagram of anti2 isomer of DA _{KK} , DA _{KE} , and DA _{EE} calculated at the B3LYP/6-31+G* level.	35

2.13	Potential energy surface along the reaction paths for proton transfer processes using (r_1, θ_1) and (r_2, θ_2) as sets of coordinates. (a), (b), (c), and (d) represent $S_0, S_1, S_2,$ and S_3 states for DH and (e), (f), (g), and (h) represent $S_0, S_1, S_2,$ and S_3 states for DA. r_1 and r_2 are in Å and θ_1 and θ_2	41
2.14	Ground state minimum energy structures of KK···KK and EE···EE dimers of DA.	43
2.15	Potential energy profile depicting the absorption and keto-enol isomerization processes for anti2 isomers of (a) DA and (b) DH. The dots represent points for which DFT energies were calculated. Dots representing minima/maxima on the potential energy profile of S_0 and S_1 states are stationary points while all other dots represent single point vertical excitation energies from S_0 . The optimized diketo, monoenol, and dienol structures in S_1 states for DA and DH are shown for clarity.	46
3.1	Mechanism proposed for the thermal denitrogenation of 1-pyrazoline. ⁹⁷	50
3.2	Orbitals used in the active space for CASSCF calculations.	52
3.3	Structure of 1-pyrazoline with atom labels and atom numbers used to define geometrical parameters.	53
3.4	Synchronous denitrogenation paths at CASSCF(4,4)/6-31+G* level of theory.	54
3.5	Potential energy profile for conrotatory and disrotatory closure of Int1 to cyclopropane obtained at CASSCF(4,4)/6-31+G* level of theory.	57
3.6	Potential energy profile for cis-trans isomerization of cyclopropane via TS1g	58
3.7	(a) Potential energy profile for asynchronous stepwise elimination of N_2 through planar diazenyl intermediates at CASSCF(4,4)/6-31+G* level (b) stationary point structures obtained at CASSCF(4,4)/6-31+G* level.	59
3.8	(a) Potential energy profile for asynchronous step-wise elimination of N_2 through pyramidal diazenyl intermediates at CASSCF(4,4)/6-31+G* level (b) stationary point structures obtained at CASSCF(4,4)/6-31+G* level.	60
3.9	Relative energies along constrained geometry optimization path of Int4f with fixed C(2)–N(4) distance.	62
3.10	Relative energies of diazenyl diradical intermediate along the Int4b to Int3b path obtained at CASSCF(4,4) and CASPT2(4,4)//CASSCF(4,4) levels using 6-31+G* basis set.	67
3.11	Energy profile for the asynchronous concerted denitrogenation path at CASSCF(4,4)/6-31+G* level.	68
3.12	A schematic representation of the two different paths that lead to formation of propene.	69
3.13	Synchronous denitrogenation paths obtained using DFT and MP2 methods.	72

3.14	Asynchronous step-wise denitrogenation paths obtained using DFT and MP2 methods.	72
3.15	Asynchronous concerted denitrogenation paths obtained using DFT and MP2 methods.	73
4.1	Procedure used for calculation of total energy used in microcanonical sampling. ($E_{\text{thermal}} = E_{\text{vib}} + E_{\text{rot}} + RT$)	80
4.2	Energetics (kcal/mol) of the isomerization of TS1	82
4.3	Initial coordinate distribution for the trajectories initiated from TS1 . The solid lines correspond to the C-N bond distances at the TS1 stationary point.	82
4.4	Plot of C3–N4 distance (Å) vs time (fs) for trajectories that exhibit recrossing.	83
4.5	Plot of C3–N4 and C1–N5 distance (Å) for trajectories initiated from TS1	84
4.6	Polar plot of $\angle\text{C1-C2-C3-N4}$ vs C3–N4 distance for TS1 , TS1' , IRC, and all the trajectories.	85
4.7	Correlation diagram of orbitals along synchronous denitrogenation of 1-pyrazoline to Int1 and cyclopropane formation.	86
4.8	Plot of C1–C3 bond distance and electron densities ρ_5 and ρ_6 in σ_5 and σ_6 orbitals vs time for trajectories initiated from TS1 : (a) Type 1 trajectories having short Int1 lifetime and (b) Type 2 trajectories having longer Int1 lifetime.	87
4.9	Lifetime distribution of trimethylene diradical for Type 1 (light shade) and Type 2 (dark shade) trajectories.	88
4.10	Number of C–C bond rotations in the trimethylene diradical intermediate for Type 2 trajectories	88
4.11	Plot of $\angle\text{C2-C3-N4-N5}$ (degree) vs C3–N4 distance (Å) for (a) trajectories that do not follow MEP (b) trajectories following MEP. The location of the stationary points along the MEP is given in the box for clarity. The solid thick blue line indicates the MEP.	90
4.12	Plot of $\angle\text{C2-C3-N4-N5}$ (degree) vs C3–N4 distance (Å) for (a) trajectories that do not follow MEP (b) trajectories following MEP. The location of the stationary points along the MEP is given in the box for clarity. The solid thick blue line indicate MEP.	92
4.13	Plot of $\angle\text{C2-C3-N4-N5}$ (degree) vs C3–N4 distance (Å) for (a) trajectories that do not follow MEP (b) trajectories following MEP. The location of the stationary points along the MEP is given in the box for clarity. The solid thick blue line indicate MEP.	94

4.14	Plot of $\angle\text{C2-C3-N4-N5}$ (degree) vs C3-N4 distance (\AA) for (a) trajectories that do not follow MEP (b) trajectories following MEP. The location of the stationary points along the MEP is given in the box for clarity. The solid thick blue line indicate MEP.	96
4.15	Plot of $\angle\text{C2-C3-N4-N5}$ and C1-N5 distance for MEP and trajectories initiated from TS5 . Thick filled circle represents TS5	97
4.16	(a) Trajectories following synchronous denitrogenation path. (b) Trajectories following asynchronous denitrogenation path.	99
4.17	Plot of $\angle\text{C1-C2-C3-N4}$ and $\angle\text{C3-C2-C1-N5}$ (degree) vs C3-N4 distance (\AA) for trajectories that follow MEP.	100
4.18	Plot of $\angle\text{C1-C2-C3-N4}$ and $\angle\text{C3-C2-C1-N5}$ vs C3-N4 distance for trajectories that do not follow MEP.	101
4.19	Lifetime of trimethylene diradical obtained for the synchronous trajectories . . .	101
4.20	$\angle\text{C2-C3-N4-N5}$ vs C3-N4 distance for all the asynchronous trajectories.	102
4.21	$\angle\text{C2-C3-N4-N5}$ vs C3-N4 distance for all the asynchronous trajectories that follow MEP.	103
4.22	Plot of $\angle\text{C2-C3-N4-N5}$ vs C1-N5 distance for trajectories that dissociate via TS5	104
4.23	Synchronous denitrogenation path for 1-pyrazoline obtained at CASSCF(4,4)/6-31+G* level of theory.	106
4.24	Potential energy contours of 1-pyrazoline for different values of ϕ_S (degree) and d_S (\AA) and the MEPs connecting the stationary points projected PES for the synchronous path.	107
4.25	Plot of ϕ_S (degree) and d_S (\AA) for 15 trajectories projected on the relaxed PES for the synchronous denitrogenation path. The trajectories form cyclopropane from the reactants passing through the SO1 region.	108
4.26	Plot of ϕ_S (degree) and d_S (\AA) for 73 trajectories projected on relaxed PES for synchronous path. The trajectories directly form cyclopropane from SO1	109
4.27	Plot of ϕ_S (degree) and d_S (\AA) for 6 trajectories projected on relaxed PES for synchronous denitrogenation path. The trajectories labeled and form reactants first before forming cyclopropane.	110
4.28	Snapshots of a representative trajectory that lead to SI cyclopropane.	110
4.29	Plot of $\angle\text{C2C1N5N4}$ angle (degree) and C1-N5 distance (\AA) for a few representative trajectories.	111
4.30	Product energies distributions obtained for total reactive trajectories	113
4.31	Product energies distributions obtained for the synchronous trajectories	114

4.32	Product energies distributions obtained for the asynchronous trajectories	115
4.33	Product energies distributions obtained for the trajectories dissociated from second order saddle region	116
5.1	exo- and endo-2-methyl-3,4-diazabicyclo[3.3.0]oct-3-enes (1 and 2) and exo- and endo-4-methyl-2,3-diazabicyclo[3.2.0]hept-2-enes (3 and 4 , respectively.)	120
5.2	Molecules considered in the present study: (3R, 5R) trans-3,5-dimethyl-1-pyrazoline (1), (3R, 5S) cis-3,5-dimethyl-1-pyrazoline (2), (3S, 5R) cis-3,5-dimethyl-1-pyrazoline (3), (3R, 5R) exo-2-methyl-3,4-diazabicyclo[3.3.0]oct-3-enes (4), and (3S, 5R) endo-2-methyl-3,4-diazabicyclo[3.3.0]oct-3-enes (5).	121
5.3	A schematic representation of synchronous denitrogenation of the isomers trans-3,5-dimethyl-1-pyrazoline leading to cyclopropane.	123
5.4	Synchronous denitrogenation paths for (3R, 5R) trans-3,5-dimethyl-1-pyrazoline obtained at CASSCF(4,4)/6-31+G* level of theory.	124
5.5	Potential energy profile for conversion of Int1 to cyclopropane obtained for trans-3,5-dimethyl-1-pyrazoline at CASSCF(4,4)/6-31+G* level of theory.	126
5.6	A schematic representation of synchronous denitrogenation of the isomers of cis-3,5-dimethyl-1-pyrazoline leading to cyclopropane formation.	127
5.7	Potential energy profile for asynchronous step-wise denitrogenation path (planar intermediate) for trans-3,5-dimethyl-1-pyrazoline obtained at CASSCF(4,4)/6-31+G* level of theory.	129
5.8	Potential energy profile for asynchronous step-wise denitrogenation path (pyramidal intermediate) for trans-3,5-dimethyl-1-pyrazoline obtained at CASSCF(4,4)/6-31+G* level of theory.	130
5.9	Asynchronous concerted denitrogenation path obtained for cis and trans-3,5-dimethyl-1-pyrazoline at CASSCF(4,4)/6-31G* level of theory.	132
5.10	A schematic representation of pentane-2,4-diyl to pent-2-ene formation via H-transfer.	133
5.11	(a) Trajectories following synchronous denitrogenation path (b) Trajectories following asynchronous denitrogenation path.	135
5.12	Plot of $\angle C(3)-C(4)-C(5)-N(1)$ (degree) vs $C(5)-N(1)$ distance (Å) for IRC, and TS1a , and all the trajectories following synchronous path.	136
5.13	Snapshots of a representative trajectory that dissociates via synchronous denitrogenation path.	136
5.14	Plot of $\angle C(4)-C(5)-N(1)-N(2)$ (degree) vs $C(5)-N(1)$ distance (Å) for all the asynchronous trajectories, IRC for rotation of N_2 group about $C(5)-N(1)$ bond, and stationary points along the IRC.	137

5.15	Snapshots of a representative trajectory that dissociates via asynchronous path leading to single inverted cyclopropane. This trajectory does not follow the MEP.	138
6.1	Orbitals used in the active space for the CASSCF calculations of (a) 1-pyrazoline and (b) trans-3,5-dimethyl-1-pyrazoline.	142
6.2	Molecules considered in the study and their atom numbering schemes.	143
6.3	The two possible dissociation pathways of 1-pyrazoline in the presence of external force along C(1) and C(3) carbon atoms.	144
6.4	(a) Plot of relative energy of 1-pyrazoline vs Δr distance (b) force along terminal C(1)–C(3) carbon atoms in nano Newton (nN) vs Δr distance.	145
6.5	Schematic representation of the two approaches used to simulate the effect of external force on trans-3,5-dimethyl-1-pyrazoline.	147
6.6	(a) Plot of relative energies of trans-3,5-dimethyl-1-pyrazoline vs Δr and (b) F values vs Δr	147
6.7	Schematic representation of the two approaches used to simulate effect of external force on cis-3,5-dimethyl-1-pyrazoline.	149
6.8	(a) Plot of relative energies of cis-3,5-dimethyl-1-pyrazoline vs Δr and (b) F values vs Δr	150
6.9	Synchronous denitrogenation paths of trans-3,5-dimethyl-1-pyrazoline for different F values.	152
6.10	Synchronous denitrogenation path of cis-3,5-dimethyl-1-pyrazoline at different external forces.	154
6.11	Effect of force on the energetics of (a) trans-3,5-dimethyl-1-pyrazoline (b) cis-3,5-dimethyl-1-pyrazoline.	158

LIST OF TABLES

TABLE	Page
2.1 Relative energies (kcal/mol) for anti1 to syn and syn to anti2 isomerization in DH_{KK} , DM_{KK} , MA_{KK} , and DA_{KK} in the ground state. Values in parentheses indicate relative percentage population of each isomer assuming Boltzmann distribution at 300 K .	22
2.2 Relative energies (kcal/mol) for stepwise and concerted cis-trans isomerization paths	24
2.3 Relative energies (kcal/mol) for stepwise and concerted intramolecular keto-enol tautomerization in the ground state	26
2.4 Relative Energies (kcal/mol) of anti1 forms of DA_{KK} , DA_{KE} and DA_{EE} using B3LYP and M05-2X functionals	30
2.5 Vertical excitation wavelengths(nm) and transition type types for S_1 , S_2 , and S_3 states for CC, CT, and TT isomers of DH, DM, MA, and DA.	31
2.6 Relative energies (kcal/mol) of stationary points along the $CC \rightarrow TT$ isomerization paths in the first excited-state for the diketo forms of DH, DM, MA, and DA . . .	33
2.7 Calculated vertical excitation wavelengths (nm) and transition types of S_1 , S_2 , and S_3 states for different tautomeric forms of DH, DM, MA, and DA	36
2.8 Relative energies (kcal/mol) of stepwise intramolecular keto-enol tautomerization in S_1 state	38
2.9 Vertical excitation wavelengths (nm) for anti2 isomers of DH and DA in acetonitrile and cyclohexane solvents	42
2.10 Relative energies (kcal/mol) for diketo and dienol dimers of DH and DA and their respective enolization energies for diketo-dimer \rightarrow dienol-dimer processes in the ground state	43
2.11 Vertical excitation wavelengths (nm) for KK and EE dimers of DH and DA . . .	44
2.12 Emission wavelengths (nm) obtained from theory and experiments ⁷⁵	44
3.1 Orbitals used for the different CASSCF calculations	53
3.2 Relative energies (kcal/mol) for synchronous denitrogenation paths obtained from CASSCF and CASPT2 calculations ^a	55

3.3	Geometrical parameters for synchronous denitrogenation path obtained at different CASSCF active space and 6-31+G* basis set	56
3.4	Relative energies (kcal/mol) of stationary points along conrotatory and disrotatory closure of Int1 to cyclopropane obtained at CASSCF(4,4)/6-31+G* level of theory	57
3.5	Relative energies (kcal/mol) for asynchronous denitrogenation paths obtained from CASSCF and CASPT2 calculations using 6-31+G* basis set ^a	64
3.6	Geometrical parameters for asynchronous denitrogenation path (Planar intermediate) obtained at CASSCF(<i>n, m</i>) levels using 6-31+G* basis set	65
3.7	Geometrical parameters for asynchronous denitrogenation path (Pyramidal intermediate) obtained at CASSCF(<i>n, m</i>) levels using 6-31+G* basis set	66
3.8	Relative energies (kcal/mol) of stationary point structures obtained for the propene formation pathways at CASSCF(4,4)/6-31+G* and CASSCF(6,6)/6-31+G* levels of theory ^a	69
3.9	Energetics of denitrogenation of 1-pyrazoline at CASSCF(4,4) with different basis sets	71
3.10	Relative energies (kcal/mol) of stationary point structures obtained for the denitrogenation pathways obtained at the MP2, B2PLYP, and B3LYP levels of theory	74
4.1	Stereochemistry of cyclopropane obtained in the trajectory simulations initiated from different transition states	98
4.2	Distribution of cyclopropane products obtained from the trajectory simulations initiated from the reactant region	105
5.1	Relative energies (kcal/mol) of stationary points along synchronous denitrogenation path for substituted 1-pyrazolines (1 to 5) obtained at CASSCF(4,4)/6-31+G* level of theory	125
5.2	Relative energies (kcal/mol) of stationary point structures along asynchronous denitrogenation paths obtained for substituted pyrazolines at CASSCF(4,4)/6-31+G* level of theory ^a	131
5.3	Relative energies (kcal/mol) of stationary point structures along the alkene formation paths obtained for substituted 1-pyrazolines at CASSCF(4,4)/6-31+G* level of theory ^a	134
5.4	Stereochemistry of cyclopropane obtained for the trajectory simulations from trans-3,5-dimethyl-1-pyrazoline	134
6.1	Important geometrical parameters considered in the present study ^a	143

6.2	Geometrical parameters of 1-pyrazoline for different Δr values obtained at CASSCF(8,8)/6-31+G* level of theory ^a	145
6.3	Geometrical parameters of trans-3,5-dimethyl-1-pyrazoline at different Δr values obtained at CASSCF(8,8)/6-31+G* level of theory ^a	148
6.4	Geometrical parameters of cis-3,5-dimethyl-1-pyrazoline at different Δr distances obtained at CASSCF(8,8)/6-31+G* level of theory ^a	151
6.5	Relative energies (kcal/mol) of stationary points along synchronous denitrogenation path of trans-3,5-dimethyl-1-pyrazoline at different F values obtained at CASSCF(8,8)/6-31+G* level of theory	152
6.6	Geometrical parameters for stationary points along the synchronous denitrogenation path for different F values obtained at CASSCF(8,8)/6-31+G* level of theory ^a	153
6.7	Relative energies (kcal/mol) of stationary points along synchronous denitrogenation path of cis-3,5-dimethyl-1-pyrazoline for different F values obtained at CASSCF(8,8)/6-31+G* level of theory	153
6.8	Geometrical parameters for stationary points along synchronous denitrogenation path for different F values obtained at CASSCF(8,8)/6-31+G* level of theory . .	154
6.9	Geometrical parameters of TS3a , TS3c , TS4a , TS4c at different F values obtained at CASSCF(8,8)/6-31+G* level of theory ^a	155
6.10	Relative energies (kcal/mol) of TS3a , TS3c , TS4a and TS4c for different F values obtained at CASSCF(8,8)/6-31+G* level of theory ^a	156
6.11	Geometrical parameters of TS3a , TS3c , TS4a , TS4c at different F values obtained at CASSCF(8,8)/6-31+G* level of theory ^a	157
6.12	Relative energies (kcal/mol) of TS3a , TS3c , TS4a , and TS4c at different F values obtained at CASSCF(8,8)/6-31+G* level of theory	158

INTRODUCTION

Over the last few decades, computational chemistry has extended the range of phenomena that can be investigated within the framework of chemistry and physics. The ranges of systems that are studied vary from a single atom to as large as proteins. Much of this advance can be attributed to the development in the field of computers, both in terms of hardware and software. Computational chemistry has been successfully used to understand experimental results. Different methods namely classical, quantum, semiclassical, and statistical theories have been used to study the various systems depending on the nature of the system and the properties of interest and have been discussed in several reviews and books.^{1,2} Two different approaches have been used to understand chemical reactions: (1) static approach and (2) dynamic approach.

(1) Static approach - It involves understanding the static properties of chemical reactions such as stability, reactivity, and the nature of the potential energy surface (PES) by solving the time-independent Schrödinger equation (TISE):

$$\hat{H}\Psi = E\Psi \quad (1.1)$$

where \hat{H} is the Hamiltonian operator, Ψ is the wavefunction, and E is the energy of the system.

The wavefunction Ψ is a function of the positions of electrons and nuclei of the system :

$$\hat{H}\Psi(\vec{r}, \vec{R}) = E\Psi(\vec{r}, \vec{R}) \quad (1.2)$$

where \vec{r} and \vec{R} represent the coordinates of the electrons and nuclei respectively. The molecular Hamiltonian for a time-independent multielectron system can be written as:

$$\begin{aligned} \hat{H} = & -\frac{\hbar^2}{2m_e} \sum_i^{\text{electrons}} \nabla_i^2 - \frac{\hbar^2}{2} \sum_A^{\text{nuclei}} \frac{1}{M_A} \nabla_A^2 - \frac{e^2}{4\pi\epsilon_0} \sum_i^{\text{electrons}} \sum_A^{\text{nuclei}} \frac{Z_A}{r_{iA}} + \frac{e^2}{4\pi\epsilon_0} \sum_j^{\text{electrons}} \sum_{i>j}^{\text{electrons}} \frac{1}{r_{ij}} \\ & + \frac{e^2}{4\pi\epsilon_0} \sum_B^{\text{nuclei}} \sum_{A>B}^{\text{nuclei}} \frac{Z_A Z_B}{R_{AB}} \end{aligned} \quad (1.3)$$

where Z_A is the nuclear charge, M_A is the mass of nucleus A, m_e is the mass of the electron, R_{AB} is the distance between nuclei A and B, r_{ij} is the distance between electrons i and j , r_{iA} is the distance between electron i and nucleus A, ϵ_0 is the permittivity of free space, and \hbar is the Planck constant divided by 2π . The first two terms of the equation represent the kinetic energy of electrons and nuclei respectively, the third term represent the electrostatic interaction between the nuclei and the electrons, the fourth and fifth terms represent the electron-electron and nucleus-nucleus repulsive interactions. Since motion of the nucleus is much more slower than the electrons, we can assume the nuclei to be stationary from the perspective of the electrons which is known as the Born-Oppenheimer (BO) approximation. BO approximation allows the separation of electronic and nuclear coordinates. Within the BO approximation,

$$\psi(\vec{r}, \vec{R}) = \psi_N(\vec{R})\psi_{el}(\vec{r}; \vec{R}) \quad (1.4)$$

where $\psi_N(\vec{R})$ is the nuclear wavefunction and $\psi_{el}(\vec{r}; \vec{R})$ is the electronic wavefunction. The nuclear kinetic energy term in equation 1.3 can be set to zero and the nuclear-nuclear repulsive term is a constant. The Hamiltonian now becomes:

$$\hat{H} = -\frac{\hbar^2}{2m_e} \sum_i^{\text{electrons}} \nabla_i^2 - \sum_i^{\text{electrons}} \sum_A^{\text{nuclei}} \frac{Z_A}{r_{iA}} + \sum_j^{\text{electrons}} \sum_{i>j}^{\text{electrons}} \frac{1}{r_{ij}} + \sum_B^{\text{nuclei}} \sum_{A>B}^{\text{nuclei}} \frac{Z_A Z_B}{R_{AB}} = \hat{H}_{el} + \hat{V}_{NN} \quad (1.5)$$

where

$$\widehat{H}_{el} = -\frac{\hbar^2}{2m_e} \sum_i^{\text{electrons}} \nabla_i^2 - \sum_i^{\text{electrons}} \sum_A^{\text{nuclei}} \frac{Z_A}{r_{iA}} + \sum_j^{\text{electrons}} \sum_{i>j}^{\text{electrons}} \frac{1}{r_{ij}} \quad (1.6)$$

and

$$\widehat{V}_{NN} = \sum_B^{\text{nuclei}} \sum_{A>B}^{\text{nuclei}} \frac{Z_A Z_B}{R_{AB}} \quad (1.7)$$

The potential energy surface of the system is then separated as:

$$V(R) = E_{el}(r; R) + \widehat{V}_{NN}(R) \quad (1.8)$$

where E_{el} is the electronic energy obtained by solving the electronic Schrödinger equation and V_{NN} is the nuclear-nuclear repulsion energy. The electronic Schrödinger equation is

$$\widehat{H}_{el} \Psi_{el}(\vec{r}) = E_{el} \Psi_{el}(\vec{r}). \quad (1.9)$$

This equation cannot be solved exactly for multielectron systems and hence approximate methods are used. Some common approaches are the Hartree-Fock (HF) method, configuration interaction (CI) method, Møller-Plesset perturbation theory, and density functional theory (DFT). A brief description of the different approaches are discussed below.

(i) Hartree-Fock Theory (HF)

In the Hartree-Fock method, the Hamiltonian is divided into two parts: a core Hamiltonian H_i^c describing the kinetic energy and the electron-nuclei attraction potential and a part describing the electron-electron repulsion:

$$H = \sum_i [H^c(i) + \sum_{j>i} \frac{1}{r_{ij}}] \quad (1.10)$$

with

$$H^c(i) = -\frac{1}{2} \nabla_i^2 - \sum_A \frac{Z_A}{r_{iA}} \quad (1.11)$$

The core Hamiltonian can be solved exactly whereas the electron-electron repulsion part is treated in an average way, i.e. each electron is considered to be moving independently of the others in an average field created by the other electrons. The energy obtained from the HF

method is always higher than the actual energy because Hartree-Fock wave function takes the interactions between the electrons in an average way. The difference between Hartree-Fock energy E_{HF} and the exact non-relativistic energy $E_{\text{non-rel}}$ is called the correlation energy E_{corr} .

$$E_{\text{corr}} = E_{\text{non-rel}} - E_{\text{HF}} \quad (1.12)$$

The correlation energy can be separated into two parts: (1) Static correlation (2) Dynamic correlation. The correlation energy arising from long-range correlation effects observed on molecular dissociation is referred as static correlation. The correlation energy arising from overestimation of short-range electron repulsion in Hartree-Fock wavefunctions is referred as dynamic correlation. When static correlation is weak, Hartree-Fock method provides a reasonably correct description of the wave-function. However, when chemical reactions involve bond-breaking then Hartree-Fock is a poor approximation. The Hartree-Fock theory can be improved in two different ways (a) by adding the excited state wave function to the Hartree-Fock wave function associated with the ground state (the configuration interaction models) and (b) by introducing an explicit term in the Hamiltonian to account for the electron-electron repulsion (Density functional models).

(ii) Configuration Interaction Models

The wave function in a full configuration interaction model (full CI) is obtained by the linear combination of ground-state electronic wavefunction (ψ_0) obtained from HF theory and all possible excited-state electronic configuration state functions (CSFs, ψ_s) formed by the promotion of one or more electrons from occupied to unoccupied molecular orbitals.

$$\psi = a_0\psi_0 + \sum_s a_s\psi_s \quad (1.13)$$

In the limit of a complete basis set, the energy obtained from full CI will be same as that obtained by solving the full many electron Schrödinger equation. Since the number of excited-state electronic CSFs are infinite, it is practically impossible to solve the wave function for a full CI model. So, the number of excited state CSFs of full CI are restricted in such a way that

the approximate CI wavefunction and energy are as close as possible to the exact values. There are several different approaches to restrict the number of CSFs.

The CIS Method- It involves generation of CSFs by single electron promotion to unoccupied MOs and leads to no improvement of the HF energy or wave function.

The CID Method- It involves double-electron promotions and leads to improvement over Hartree-Fock method. The wave function for CID method can be written as:

$$\psi_{CID} = a_0\psi_0 + \sum_j^{\text{occ}} \sum_{i<j}^{\text{occ}} \sum_b^{\text{unocc}} \sum_{a<b}^{\text{unocc}} a_{ij}^{ab} \psi_{ij}^{ab} \quad (1.14)$$

The CISD Method- It considers both single and double electron excitations. The wave function for CISD method can be written as:

$$\psi_{CISD} = a_0\psi_0 + \sum_i^{\text{occ}} \sum_a^{\text{unocc}} a_i^a \psi_i^a + \sum_{i<j}^{\text{occ}} \sum_{a<b}^{\text{unocc}} a_{ij}^{ab} \psi_{ij}^{ab} \quad (1.15)$$

In both CID and CISD methods, the expansion coefficients are determined variationally. The energy obtained from both the methods are larger than the exact energy. CISD recovers around 80-90% of the correlation energy for molecules built from atoms of the first row. However, the correlation energy obtained by CISD decreases drastically as the size of the molecule increases. Two desirable properties of a method which is used to study bond dissociation are size consistency and size extensive. A method is size-consistent if the energy computed for two fragments of a molecule infinitely separated are same as the sum of energy of both the fragments calculated separately. A method is size-extensive if the computed energy of a system composed of n noninteracting identical systems equals n times the energy of one subsystem computed using the same methods. Both CIS and CISD methods are neither size-consistent nor size-extensive.

The MCSCF Method- In multiconfiguration self-consistent-field (MCSCF) methods,³ the molecular wave function is written as a linear combination of CSFs (ϕ_I) generated from using

a subset of the HF MOs.

$$\psi = \sum_i^M c_i \Phi_i = c_1 \Phi_1 + c_2 \Phi_2 + \cdots + c_M \Phi_M \quad (1.16)$$

where c_i is the coefficient associated with CSF Φ_i and the summation extends over all possible M CSFs. Thus, for MCSCF calculations the SCF calculation is performed in concert with the variational calculation of the linear combination of electronic states. This differs from CISD, where the HF MO's are used to form the excited states.

If all the important CSFs for the chemical reaction under study are included in the set of Φ_i , then this method gives a correct description of the electronic structure. The most commonly used MCSCF method is complete active space self consistent field (CASSCF) method.⁴ In the CASSCF method, the orbitals ϕ_i used in the CSFs is written as linear combinations of basis functions:

$$\phi_i = \sum_{r=1}^b C_{ri} \chi_r \quad (1.17)$$

The orbitals used to generate CSFs are divided into three groups: (i) the active orbitals (ii) the inactive occupied orbitals, and (iii) inactive unoccupied orbitals. The inactive occupied orbitals are doubly occupied throughout the calculation and the inactive unoccupied orbitals remain unoccupied. The occupation number for the active orbitals which consist of a combination of occupied and unoccupied orbitals is allowed to vary from 0 to 2. The wavefunction for CASSCF calculation is written as linear combination of all CSFs ϕ_i that can be formed by distributing the active electrons among the active orbitals in all possible ways:

$$\psi = \sum_i c_i \Phi_i \quad (1.18)$$

CASSCF calculations are then performed to get the optimum coefficients C_{ri} and c_i . The CASSCF method can take into account the static electron correlation by allowing for partially occupied orbitals and describes the chemical reaction which involves bond breaking but it cannot take into account the dynamic electron correlation. The dynamic electron correlation can be accounted for either perturbatively or variationally.

The CASPT2 Method - In the CASPT2 method, dynamical electron correlation is treated perturbatively using the CASSCF wavefunction as the reference wavefunction. The Hamiltonian for CASPT2 method can be written as:

$$\hat{H} = \hat{H}_0 + \lambda\hat{H}_1 \quad (1.19)$$

Here, \hat{H}_0 is the zeroth order Hamiltonian, λ is a small parameter which defines the perturbation \hat{H}_1 .

The MRCI Method - The MRCI method combines MCSCF and CI methods. MRCI calculation uses MCSCF wave function as the reference and a CISD calculation starting with the MCSCF wavefunction is performed. Because of the complexity and computational cost, MRCI uses only single and double excitations. The wave function for the MRCI method that includes only the single and double excitations (MRCISD) can be written as:

$$\psi = \sum_I c_I \Phi_I + \sum_S \sum_a c_a^S \Phi_S^a + \sum_P \sum_{ab} B_{ab}^P \Phi_P^{ab} \quad (1.20)$$

here, a and b refer to external orbitals those are not included in the reference configurations.

(iii) Møller-Plesset Perturbation Theory

The simplest alternative to configuration interaction models are the second-order Møller-plesset perturbation theory (MP2). Here, the correlation energy is calculated as a perturbation to the Hartree-Fock Hamiltonian and solving the Schrödinger equation using perturbation theory. The exact Hamiltonian \hat{H} for MP2 method can be written as:

$$\hat{H} = \hat{H}_0 + \lambda\hat{V} \quad (1.21)$$

Here, \hat{H}_0 is the Hartree-Fock Hamiltonian, \hat{V} is a small perturbation, and λ is a dimensionless parameter. Using perturbation theory, the exact wavefunction and energy are expanded in terms of the Hartree-Fock wave function and energy and can be written as:

$$\psi = \psi_0 + \lambda\psi^{(1)} + \lambda^2\psi^{(2)} + \lambda^3\psi^{(3)} + \dots \quad (1.22)$$

$$E = E^{(0)} + \lambda E^{(1)} + \lambda^2 E^{(2)} + \lambda^3 E^{(3)} + \dots \quad (1.23)$$

Here, ψ_1, ψ_2, ψ_3 are the first, second, and third order corrections to the wave function. Similarly, $E^{(1)}, E^{(2)},$ and $E^{(3)}$ are first, second, and third order corrections to the ground state energy. Substituting the equations 1.18, 1.19, and 1.20 into the Schrödinger equation and equating λ 's of the same order gives:

$$\hat{H}_0\psi_0 = E^{(0)}\psi_0 \quad (1.24)$$

$$\hat{H}_0\psi^{(1)} + \hat{V}\psi_0 = E^{(0)}\psi^{(1)} + E^{(1)}\psi_0 \quad (1.25)$$

$$\hat{H}_0\psi^{(2)} + \hat{V}\psi^{(1)} = E^{(0)}\psi^{(2)} + E^{(1)}\psi^{(1)} + E^{(2)}\psi_0 \quad (1.26)$$

Multiplying equation 1.21, 1.22, and 1.23 by ψ_0 and integrating over all space yields the expression for nth-order (MPn) energy:

$$E^{(0)} = \int \cdots \int \psi_0 \hat{H}_0 \psi_0 d\tau_1 d\tau_2 \cdots d\tau_n \quad (1.27)$$

$$E^{(1)} = \int \cdots \int \psi_0 \hat{V} \psi_0 d\tau_1 d\tau_2 \cdots d\tau_n \quad (1.28)$$

$$E^{(2)} = \int \cdots \int \psi_0 \hat{V} \psi^{(1)} d\tau_1 d\tau_2 \cdots d\tau_n \quad (1.29)$$

Here, the Hartree-Fock energy is the sum of zero and first order Møller-Plesset energies:

$$E^{(0)} + E^{(1)} = \int \cdots \int \psi_0 (\hat{H}_0 + \hat{V}) \psi_0 d\tau_1 d\tau_2 \cdots d\tau_n \quad (1.30)$$

and $E^{(2)}$ is the first perturbation to HF energy.

Unlike configuration interaction models, MP2 is size consistent in nature. The predicted energy for every order of perturbation in MP2 scales with the number of non-interacting particles in the system. However, MP2 method is not variational and therefore the calculated energy may be lower than the exact value.

(iv) Density Functional Theory

The second approach for moving beyond the HF model is Density Functional theory (DFT)^{5,6} which is based on electron density rather than on wavefunction.

The DFT energy can be written as:

$$E^{\text{DFT}} = E_T + E_V + E_J + E_{XC} \quad (1.31)$$

Where, E_T is the kinetic energy, E_V the potential energy, E_J the Coulomb energy, and E_{XC} the exchange-correlation energy. Except E_T , all components depend on the total electron density, $\rho(r)$:

$$\rho(r) = 2 \sum_i^{\text{orbitals}} |\psi_i(r)|^2 \quad (1.32)$$

Within a finite basis set, the components of density functional energy, E^{DFT} can be written as:

$$E_T = \sum_{\mu}^{n_b} \sum_{\nu}^{n_b} \int \phi_{\mu}(r) \left[-\frac{\hbar^2 e^2}{2m_e} \nabla^2 \right] \phi_{\nu}(r) dr \quad (1.33)$$

$$E_V = \sum_{\mu}^{n_b} \sum_{\nu}^{n_b} P_{\mu\nu} \sum_A^{\text{nuclei}} \int \phi_{\mu}(r) \left[-\frac{Z_A e^2}{4\pi\epsilon_0 |r - R_A|} \right] \phi_{\nu}(r) dr \quad (1.34)$$

$$E_J = \frac{1}{2} \sum_{\mu}^{n_b} \sum_{\nu}^{n_b} \sum_{\lambda}^{n_b} \sum_{\sigma}^{n_b} P_{\mu\nu} P_{\lambda\sigma} (\mu\nu|\lambda\sigma) \quad (1.35)$$

$$E_{XC} = \int f(\rho(r), \nabla_{\rho}(r) \dots) dr \quad (1.36)$$

where, Z is the nuclear charge, $|r - R_A|$ is the distance between the nucleus and the electron density, P is the density matrix, n_b is the number of basis functions and $(\mu\nu|\lambda\sigma)$ are the two electron integrals. Accuracy of the DFT method strongly depends on the quality of exchange-correlation functional E_{XC} used for the calculations. If exact exchange-correlation functional is known for a problem, then the density functional approach would be exact. So, the challenging task in DFT is the development of an accurate functional for expressing the exchange correlation energy E_{XC} in terms of density. Several functions have proposed for the same.

The different theoretical approaches used to get information about the static properties of chemical systems are summarized in Figure 1.1.

Potential Energy Surface (PES)

The potential energy surface of a chemical reaction is a function of $3N-6$ variables. The important features of PESs are stationary points such as reactants, products, transition states, and intermediates of the chemical reactions. For the stationary points, the first derivative of the

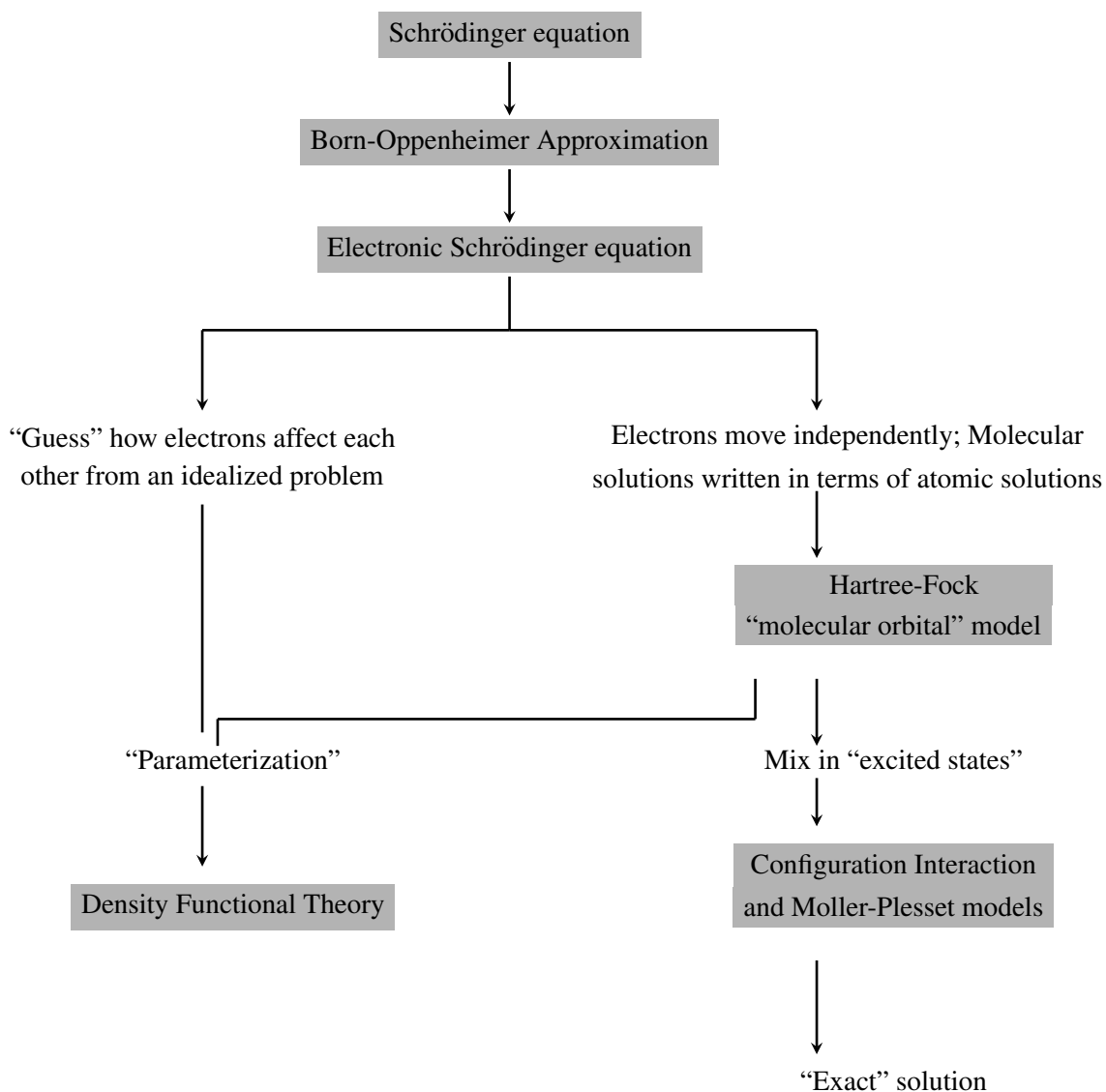


Figure 1.1: Schematic diagram showing relations between different quantum chemical models used for understanding static properties⁷

potential energy with respect to each geometric ($3N-6$) independent coordinates (R_i) are zero:

$$\frac{\partial V}{\partial R_i} = 0; \quad i = 1, 2, 3, \dots, 3N - 6 \quad (1.37)$$

The stationary points can be distinguished by looking at the second derivatives of the potential energy with respect to the coordinates. A stationary point can be characterized as a minima or a maxima by computing the eigenvalues of the Hessian matrix and the eigenvectors (\vec{Q}). In the

set of orthogonal normal coordinates (Q_i), for a minima,

$$\frac{\partial^2 V}{\partial Q_i^2} > 0; \quad i = 1, 2, 3, \dots, 3N - 6 \quad (1.38)$$

and for a transition state

$$\frac{\partial^2 V}{\partial Q_i^2} > 0; \quad i = 1, 2, 3, \dots, 3N - 7 \quad (1.39)$$

except along the reaction coordinate (Q_j), for which

$$\frac{\partial^2 V}{\partial Q_j^2} < 0 \quad (1.40)$$

Thus, the stationary points on the PES can be characterized by computing the classical vibrational frequencies. Similarly, if one assumes a statistical distribution be maintained during a reaction then the information about rate of the reaction can be obtained from the potential energy surface using statistical rate theories. For example, consider a chemical reaction



The rate of the reaction $r = k'[A]^a[B]^b$. The rate constant k' can be obtained from transition state theory (TST):^{8,9}

$$k'_{\text{TST}} = \frac{k_B T}{h} e^{\frac{\Delta S^\ddagger}{R}} e^{-\frac{\Delta H^\ddagger}{RT}} (c^\circ)^{1-n} \quad (1.42)$$

Here, ΔS^\ddagger is the entropy of activation, ΔH^\ddagger is the enthalpy of activation, k_B is the Boltzmann's constant, $c^\circ = 1 \text{ mol L}^{-1}$, n is the molecularity, and T is the temperature of the reaction.

(2) Dynamic Approach - In the static approach, the evolution of the system with time was not considered in the study. However, the real system is dynamic in nature and can adapt dynamical effects during the course of the reaction such as localization of energies in certain vibrational modes, redistribution of excitation energy to different vibrational or rotational modes. The dynamic properties of the system can be understood by solving equations of motion (EOM) by either using quantum mechanics or classical mechanics. In quantum mechanics, the change

in state $\psi(r, t)$ of the system with time is given by solving the time-dependent Schrödinger equation:

$$i\hbar \frac{\partial}{\partial t} \psi(r, t) = \hat{H} \psi(r, t) \quad (1.43)$$

where \hat{H} is Hamiltonian of the system. However, quantum dynamical simulations are computationally expensive due to large dimensional problem. Quantum dynamics can be used to study systems containing upto 4-5 atoms. In classical mechanics, the evolution of system as a function of time can be obtained by numerically integrating the Newton's classical equation of motion:

$$F_i = m_i a_i = m_i \frac{d^2 q_i}{dt^2} = - \frac{\partial V(q)}{\partial q_i} \quad (1.44)$$

where F_i is the force, m_i the mass, and a_i the acceleration associated with the coordinate q_i . Integration of the Newton's EOM results in $p_i(t)$ and $q_i(t)$ called the trajectory. In the studies reported here classical trajectory simulations are used to understand the dynamics of chemical reactions. In trajectory simulations, an ensemble of trajectories are integrated.¹⁰ Each trajectory in the ensemble is specified by the system's initial coordinates q_i and momenta p_i which are chosen randomly by using different sampling procedure such as microcanonical normal mode sampling or sampling a Boltzmann distribution. The Newton's equation of motion is then integrated by using different integration algorithm such as Verlet algorithm, leap-frog algorithm, or velocity-Verlet algorithm. The velocity-Verlet integrator is most commonly used to integrate Newton's equation of motion because it is time reversible and symplectic in nature. The trajectories are followed with time and once the reaction is complete the final coordinates and momenta thus obtained can be used to understand the product distributions and their energies. While it is desirable to have an analytical description for the PES for the system under study, it is not possible for systems of large number of atoms. In such cases, for systems with "reasonable" size ab initio classical trajectory method can be employed.¹¹ In ab initio classical trajectory method, the forces necessary for the integration of the EOM are obtained directly by solving the TISE for a given level of theory.

In the work reported in the thesis, DFT and ab initio methods such as HF, MP2, CASSCF, and CASPT2 were used to investigate the electronic structure properties and the nature of the potential energy surface of various chemical reactions. The dynamics of the reactions were studied using ab initio classical trajectory methods.

TDDFT INVESTIGATION ON PHOTOINDUCED EXCITED STATE INTRAMOLECULAR DUAL PROTON TRANSFER IN DIFORMYL DIPYRROMETHANE

2.1 Introduction

Understanding of the excited-state proton transfer (ESPT) process is of fundamental importance because of its relevance in various chemical and biological processes¹²⁻¹⁶ and has been a topic of research for several years.¹⁷⁻²² In ESPT process, a molecule initially gets excited to an energized state and the photoexcited molecule then transfers a proton from a proton donor, usually a $-OH$ or $-NH$ group, to the proton acceptor, generally $-C=O$ or $-N=N$ group. Several experimental and theoretical studies have been reported that address different aspects of this elementary process including the mechanisms, dynamics, and the role of solvent and electronic effects on the proton transfer (PT) processes.²³⁻²⁸ Proton transfer can happen within a molecule (intra) or between two molecules (inter) via a dimer or complex, with one monomer being the proton donor and the other proton acceptor.

Hydrogen bonding interactions, $\text{H} \cdots \text{O}$ or $\text{H} \cdots \text{N}$, between the proton donor and the acceptor are ubiquitous to PT processes and act as the driving force for them. Hence, the role of hydrogen bonds on PT processes has been studied extensively. It was found that strengthening of the hydrogen bond in the excited-state resulted in red shifts while weakening of the hydrogen bond strength resulted in a blue shift in the electronic spectra.^{29–33} Excited state intramolecular proton transfer (ESIPT) is observed in molecules with intramolecular hydrogen bond between the donor and the acceptor atoms. The processes are unimolecular in nature and are usually enol \rightarrow keto or imine \rightarrow enamine tautomerizations. Most reported cases of ESIPT^{34–49} involve six membered ring type structures with strong intramolecular hydrogen bonds, where the barrier for proton transfer is very less. However, there are a few reports on systems such as 3-hydroxychromones and their derivatives^{50–60} where ESIPT occurs involving weak $\text{O}-\text{H} \cdots \text{O}$ hydrogen bonded five membered ring type structures. The ESIPT dynamics in these systems were found to be highly sensitive to the solvent properties and substituents^{54,56,57}.

Since ESIPT commonly occurs in ultrafast time scale, experimental understanding of the correlation between hydrogen bond strength and ESIPT dynamics is not easy. So, to understand the potential energy surface (PES) and dynamics of ESIPT experimentally, Chou and coworkers^{61–63} synthesized weak $\text{N}-\text{H} \cdots \text{N}$ hydrogen bonded five membered 2-pyridyl pyrazole systems where excited-state proton transfer is associated with a barrier of ~ 2 kcal/mol. From the studies of a series of 2-pyridyl pyrazole derivatives⁶², they concluded that electron withdrawing groups at pyrazole C(3) increase the intramolecular hydrogen bond strength and facilitates the ESIPT process, while electron donating group on pyridine facilitates ESIPT process by strengthening the intramolecular hydrogen bond due to increased nitrogen basicity. In a series of experimental and theoretical studies on pyrrole derivatives Chowdhury and coworkers proposed the possibility of intra or intermolecular proton transfer in the excited-state in pyrrole-2-carboxaldehyde^{64,65} and 2-acetylpyrrole⁶⁶. An important photophysical property of molecules that undergo ESIPT is that their emission spectra exhibit large Stokes shifts due to

the formation of the new proton-transferred species. Exploiting this property, several molecules have been strategically synthesized to explore their use as luminescent materials,^{20,21,67,68} fluorescence probes^{16,20,69–71}, light emitting diodes^{20,72–74}. Spectroscopic evidence for a similar situation was found while carrying out absorption and emission studies for 1,9-diformyl-5,5-diaryldipyrromethane (DA_{KK}).⁷⁵ When DA_{KK} was irradiated with 310 nm light, a new peak at 390 nm was observed in the absorption spectrum after irradiation. In case of emission spectrum, the weak peak at 560 nm enhanced continuously with irradiation. However, the additional red shifted peak observed for DA_{KK} in the absorption spectrum was not observed for dimethyl and monoaryl substituted compounds.

In the study reported here, a detailed systematic DFT study on the ground and excited-state PES of dipyrromethanes: (i) 1,9-diformyldipyrromethane (DH_{KK}) (ii) 1,9-diformyl-5,5-dimethyldipyrromethane (DM_{KK}) (iii) 1,9-diformyl-5-aryldipyrromethane (MA_{KK}), and (iv) 1,9-diformyl-5,5-diaryldipyrromethane (DA_{KK}) is reported.⁷⁶ The complete potential energy profile, that covers all the stationary points considering the different rotamers, cis-trans isomers, and enol tautomers (mono and dienols) of DH_{KK}, DM_{KK}, MA_{KK}, and DA_{KK} and their interconversion mechanisms were mapped in both the ground and excited-states to understand the experimental observations. The results are compared with the experimental observations considering both the mono-enol and dienol tautomers.⁷⁶

2.2 Methodology

To understand the experimentally observed photophysics of dipyrromethanes, the potential energy profile was mapped using DFT methods. The stationary points on the ground state were calculated at B3LYP^{77–80}/6-31+G*^{81–84} level of theory while those on the excited-states were calculated using time-dependent density functional theoretical (TDDFT) method^{85,86} at the same level of theory. The stationary points were characterized by performing frequency calculations. All transition states (TS) and intermediates were connected by following the

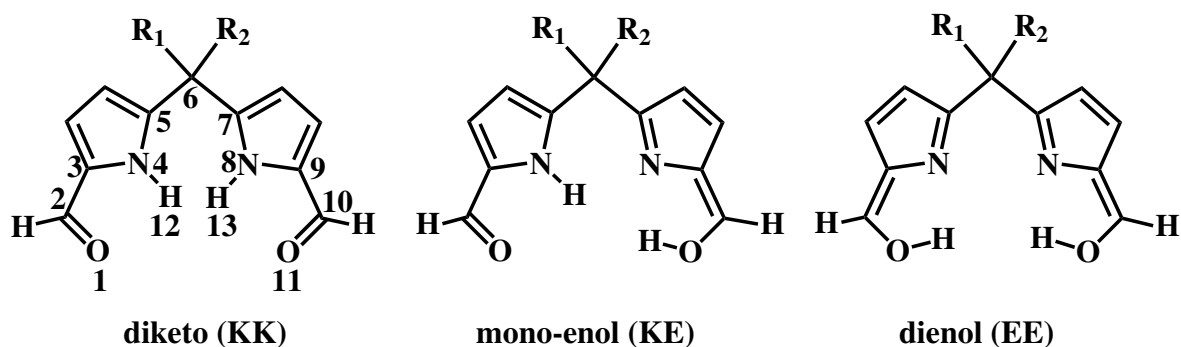


Figure 2.1: Molecules considered in the study: R_1 and R_2 are $[-H, -H]$, $[-CH_3, -CH_3]$, $[-H, -C_6H_5CH_3]$ and $[-C_6H_5CH_3, -C_6H_5CH_3]$.

intrinsic reaction coordinate (IRC) only in the ground state. For the excited-states, IRC could not be performed and the TS structures were confirmed by computing the frequencies and inspecting the TS eigen vectors. The effects of basis sets and DFT functionals were examined by computing the stationary points on the ground state potential energy surface with 6-311++G** basis set⁸¹⁻⁸⁴ and M05-2X functional.⁸⁷ Vertical excitation energies were computed by using ground state stationary point structures using TDDFT method. All calculations were performed using GAMESS software package.⁸⁸

2.3 Results and Discussions

The four analogues of dipyrromethane with different substituents that were considered in the study are given in Figure 2.1. In the rest of the chapter, KK, KE, and EE refer to keto-keto (diketo), keto-enol (mono-enol), and enol-enol (dienol) forms respectively. The labels for excited-state (S_1) stationary points are appended with ‘*’ symbol. The four molecules considered in the study differ in the substituents R_1 and R_2 attached to the methylenic carbon atom (C6). The numbering scheme shown in Figure 2.1 is used for defining geometrical parameters.

2.3.1 Ground state studies

2.3.1.1 Rotational and Conformational Isomers

Due to free rotation of groups attached to the methylenic carbon atom about the C–C bond, diformyl dipyrromethanes can exhibit rotational isomerism. A potential energy surface scan by varying the dihedral angles $\angle N4C5C6C7$ (ϕ_1) and $\angle C5C6C7N8$ (ϕ_2) was carried out to locate the stable rotational isomers of DH_{KK} . The potential energy contour plot with respect to the dihedral angles is shown in Figure 2.2. Eight isomers (**KK1** to **KK8**) with different orientations of the two –NH groups with respect to each other were identified from the PES scan and their minimum energy structures are given in Figure 2.3. Interestingly, the eight rotamers can be related to each other by operations: reflection plane (σ_1) containing the methylenic atoms (C, H, H), or a 180° rotation (C_2) about the methylene carbon atom (C6) or a reflection plane (σ_2)

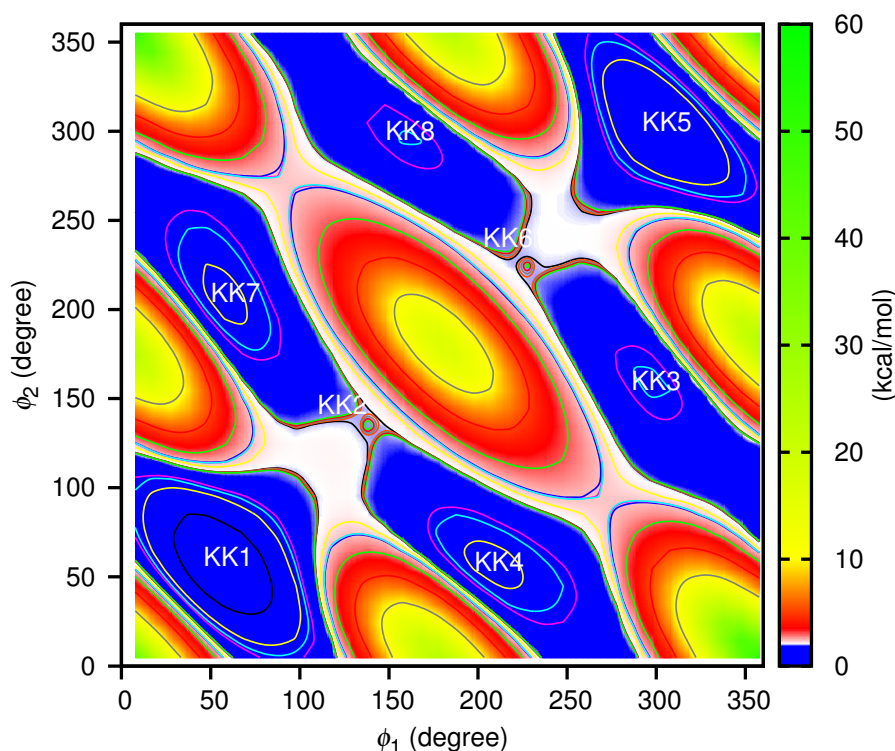


Figure 2.2: Potential energy contours showing the existence of different rotational isomers of DH_{KK} for different values of ϕ_1 and ϕ_2 . Labels **KK1** to **KK8** correspond to different rotational isomers in the respective regions.

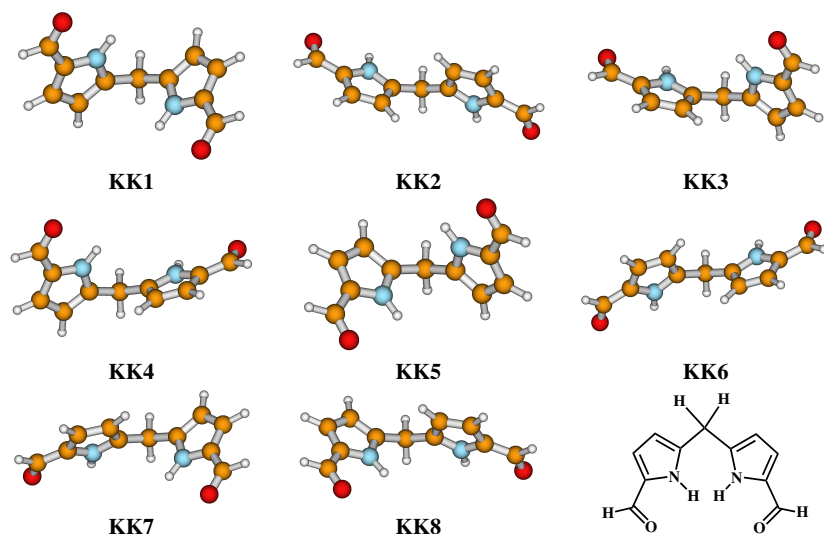
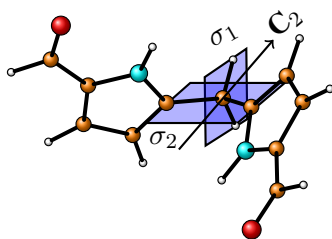


Figure 2.3: Minimum energy structures representing different rotational isomers of DH_{KK} .

(a)



(b)

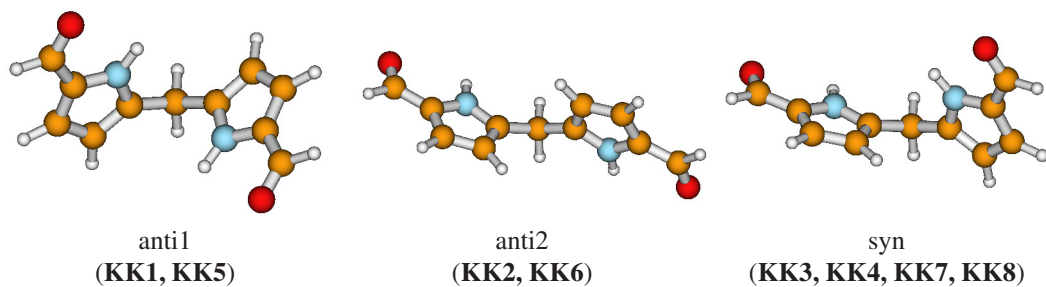


Figure 2.4: (a) Illustration depicting operations used to relate and group the rotational isomers (b) Three stable rotational isomers of DH_{KK} .

containing C5, C6, and C7 atoms as illustrated in Figure 2.4(a). It can be seen in Figure 2.2 that the PES is symmetrical about the diagonal through $\phi_1 = 0^\circ$, $\phi_2 = 360^\circ$. The pairs (**KK1**, **KK5**), (**KK2**, **KK6**), (**KK3**, **KK4**), and (**KK7**, **KK8**) are mirror images and are related by

the σ_1 operation. The cross pairs (**KK3**, **KK7**) and (**KK4**, **KK8**) are related by σ_2 operation. The PES is also symmetrical about the diagonal through $\phi_1 = \phi_2 = 0^\circ$ and the rotamers (**KK4**, **KK7**), and (**KK3**, **KK8**) are related by C_2 operation. Hence, the structures **KK3**, **KK4**, **KK7**, and **KK8** are isoenergetic and represent identical arrangement of atoms. DH_{KK} can then be thought of as existing in three stable (rotational) isomeric forms as illustrated in Figure 2.4(b). In isomers **KK1** and **KK5**, the $-NH$ groups of both pyrrole rings are anti and face towards each other. In isomers **KK2** and **KK6**, the $-NH$ groups are anti and face away from each other and in **KK3**, **KK4**, **KK7**, and **KK8**, the $-NH$ groups of both pyrrole rings face the same side. The three stable forms are hence labeled as *anti1*, *anti2*, and *syn* respectively (Figure 2.4(b)). The energetics and different photophysical processes involved in dipyrromethanes can be understood with respect to these three forms only. Isomers **KK1**, **KK2**, and **KK3** were considered as representative structures for *anti1*, *anti2*, and *syn* forms in further studies.

The relative energies for the three forms of DH_{KK} , DM_{KK} , MA_{KK} , and DA_{KK} are given in Table 2.1. The N–H bond distances (1.0 Å) and N–H–O bond angles ($\sim 92^\circ$) of the pyrrole rings are similar for all the isomers of the four molecules. In DH_{KK} , DM_{KK} , and MA_{KK} *anti1* is the most stable isomer, whereas in DA_{KK} , *anti2* is the most stable isomer. However, it is important to note that the PES is shallow for variations in ϕ_1 and ϕ_2 with the energy varying within 2 kcal/mol for the rotational isomers. The transition state structures (r-TS1) connecting *anti1* and *syn* and structures (r-TS2) connecting *syn* and *anti2* were calculated and the barriers for isomerization from *anti1* to *syn* and *syn* to *anti2* are also given in Table 2.1. The barriers are similar in DH_{KK} , DM_{KK} , and MA_{KK} , (~ 1.3 kcal/mol and ~ 2 kcal/mol) and DA_{KK} has the highest barrier of 3.72 kcal/mol for *anti1* to *syn* due to constraints induced by aryl rings. It is to be noted that *anti1* and *anti2* are not connected directly by a transition state. The relative population of the different diketo isomers computed using Boltzmann distribution at 300 K with degeneracies for *anti1*, *anti2*, and *syn* taken as 2, 2, and 4 respectively are also given in Table 2.1. It can be seen that *anti2* is more populated for DA_{KK} compared to that of DH_{KK} .

Table 2.1: Relative energies (kcal/mol) for anti1 to syn and syn to anti2 isomerization in DH_{KK} , DM_{KK} , MA_{KK} , and DA_{KK} in the ground state. Values in parentheses indicate relative percentage population of each isomer assuming Boltzmann distribution at 300 K

Molecule	Relative Energy ^a				
	anti1	r-TS1	syn	r-TS2	anti2
DH_{KK}	0 (62)	1.35	0.77 (34)	1.82	1.64 (04)
DM_{KK}	0 (64)	1.34	0.82 (33)	2.27	1.78 (03)
MA_{KK}	0 (28)	1.14	0.06 (51)	2.15	0.17 (21)
DA_{KK}	0 (18)	3.72	-0.15 (47)	3.32	-0.40 (35)

^a Relative energies are with respect to anti1 isomer for each molecule.

2.3.1.2 Ab initio Classical Trajectory Simulation

To get an insight into the possible isomerization processes that can happen at room temperature, ab initio molecular dynamics simulations were carried out at B3LYP/6-31+G* level of theory. The trajectories were initiated at anti1 form of DH_{KK} (**KK1**) using microcanonical sampling method with 7.4 kcal/mol excess energy above the zero-point-energy which is the average thermal energy (vibration and rotation) at 300 K. 10 trajectories were integrated for 1.5 ps and 5 of them exhibited isomerization reaction from **KK1** (anti1) to **KK8** (syn). The simulations indicate the possibility of rotational isomerization between the conformers at 300 K. Figure 2.5 shows a representative trajectory (white line) that exhibits anti1 to syn isomerization.

2.3.1.3 Cis-Trans Isomerization

In addition to the rotational isomers formed by the rotation of methylenic C–C bonds, dipyrromethanes can also exist in *cis* and *trans* forms defined by the orientation of –NH and –CHO groups with respect to each other. Here, *cis* refers to CO of formyl group syn to –NH group of pyrrole ring ($\angle\text{O1C2C3N4} = 0^\circ$) and *trans* refers to the CO of formyl group anti to –NH ($\angle\text{O1C2C3N4} = 180^\circ$). Three isomers are possible considering the positions of –NH and –CHO groups : (i) cis-cis (CC), (ii) cis-trans (CT), and (iii) trans-trans (TT). The three isomers can transform from one form to the other. Two possible cis-trans isomerization paths

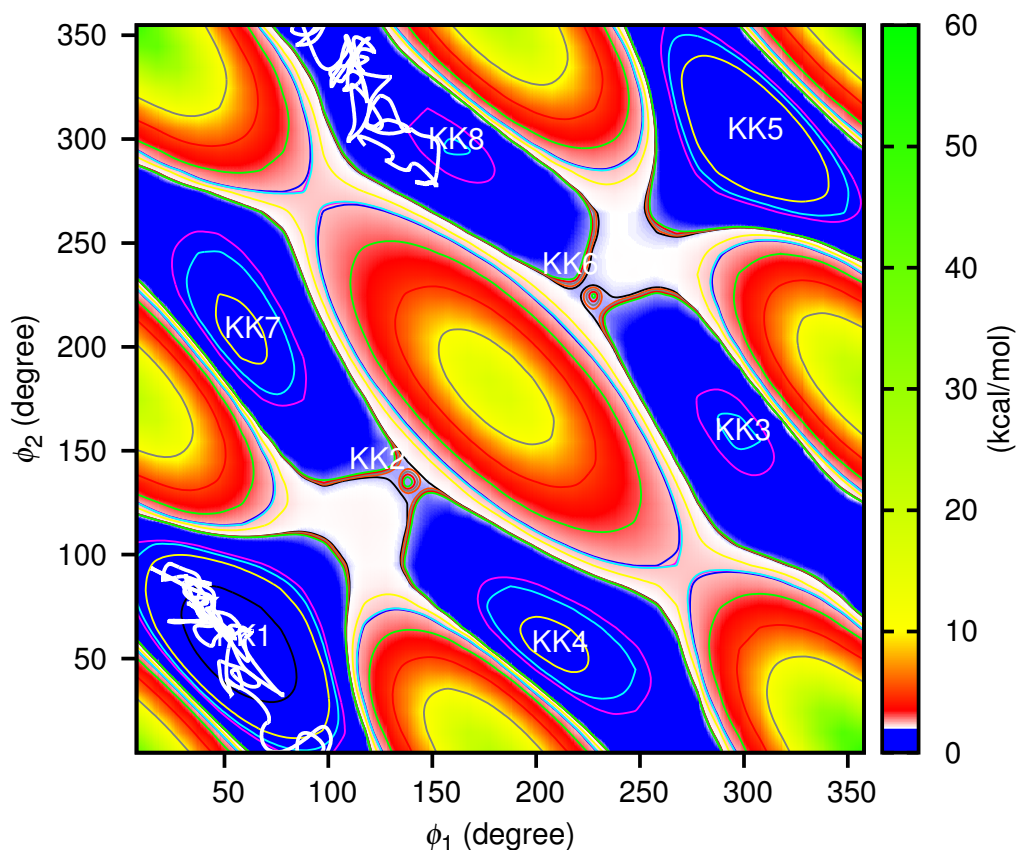


Figure 2.5: Potential energy contours of DH_{KK} for different values of ϕ_1 and ϕ_2 and a sample trajectory (white line) showing anti1 to syn isomerization.

were considered in this study (i) a stepwise path where one of the formyl groups isomerizes to trans via c-TS1 first and then the other formyl group isomerizes via c-TS2 (ii) a concerted path where both the formyl groups isomerize to trans simultaneously. The relative energies and isomerization barriers of stepwise and concerted isomerization paths for all the three isomers of DH_{KK}, DM_{KK}, MA_{KK}, and DA_{KK} are given in Table 2.2. The CC form is the most stable isomer for all the the four molecules considered in this study. The relative stabilities of isomers follow the order CC>CT>TT. However, the relative energies of CT and TT isomers for all the four molecules are similar. The isomerization of one formyl group results in a destabilization of ~ 3 -5 kcal/mol and isomerization of second formyl group results in a further destabilization of ~ 3 -5 kcal/mol. The higher stability of CC isomer compared to CT and TT isomers is possibly due to the presence of two weak hydrogen bonds (N–H \cdots O=C) between pyrrole

Table 2.2: Relative energies (kcal/mol) for stepwise and concerted cis-trans isomerization paths

Molecule	Isomer	Relative Energy ^a					
		CC	c-TS1	CT	c-TS2	TT	ΔE^\ddagger ^b
DH	anti1	0.00	16.15	3.81	19.82	7.50	34.55
	anti2	1.64	18.66	5.81	22.82	10.07	37.74
	syn	0.77	17.59	5.10	21.37	8.83	36.08
DM	anti1	0.00	16.13	3.79	19.77	7.45	34.50
	anti2	1.78	19.06	6.00	23.08	10.30	38.34
	syn	0.82	17.75	5.13	21.45	8.78	36.22
MA	anti1	0.00	16.19	4.02	19.92	7.35	34.58
	anti2	0.17	16.60	3.81	20.52	7.45	35.84
	syn	0.06	16.37	3.85	20.34	7.68	34.90
DA	anti1	0.00	16.20	3.61	19.56	6.66	33.57
	anti2	-0.40	15.86	2.98	19.23	6.44	32.90
	syn	-0.15	15.82	3.40	19.60	6.66	34.23

^a Relative energies are with respect to anti1 isomer for each molecule.

^b ΔE^\ddagger is the barrier for concerted CC→TT isomerization.

N-H and formyl C=O groups that are absent in trans isomers. The transition state structures (c-TS1 and c-TS2) connecting the cis and trans forms were also calculated. The barriers for CC to CT and CT to TT isomerization paths for the molecules with different substituents were found to be 16-20 kcal/mol and 19-22 kcal/mol respectively. The substitution at the methylenic carbon does not exhibit any significant effect on the relative stabilities and isomerization barriers for cis-trans isomerization. In transition states structures c-TS1 and c-TS2, the angles $\angle\text{O1C2C3N4}$ and $\angle\text{N8C9C10O11}$ were found to be 90° . For the concerted isomerization of both the formyl groups, a second order saddle point that is 34-36 kcal/mol higher than that of the CC isomer was obtained by constrained geometry optimization by fixing $\angle\text{O1C2C3N4} = 90^\circ$ and $\angle\text{N8C9C10O11} = 90^\circ$ for each. This barrier (ΔE^\ddagger) for the concerted isomerization path was found to be 14-16 kcal/mol higher in energy than the step-wise isomerization path for the compounds considered in this study.

2.3.1.4 Keto-Enol Tautomerization

The IR spectra of DA_{KK} after irradiation showed an intense broad band at 3436 cm⁻¹ in addition to a weak N–H band at 3227 cm⁻¹, which indicates possible formation of enolic species after irradiation.⁷⁵ Formation of enol is a tautomerization process involving proton transfer from –NH group to C=O group often called as ground state intramolecular proton transfer (GSIPT). So, to understand enol formation in DA_{KK} and the role of diaryl substitution at the meso carbon atom in the enolization process, potential energy profile and energy barriers for intramolecular keto-enol tautomerization paths were mapped for the three rotameric forms anti1, anti2, and syn of DH_{KK}, DM_{KK}, MA_{KK}, and DA_{KK}. Two possible keto-enol tautomerization paths were considered in this study : (i) a step-wise path where proton transfer from the pyrrole N–H group to C=O of formyl group in one ring happens first resulting in a mono-enol (KE) followed by another proton transfer in the other ring forming a di-enol (EE) (ii) a concerted path where proton transfer from pyrrole N–H group to formyl C=O group happens simultaneously in both the pyrrole rings. The relative energies of the enols and tautomerization barriers for stepwise and concerted proton transfer processes in the isomers of DH_{KK}, DM_{KK}, MA_{KK}, and DA_{KK} obtained from B3LYP/6-31+G* level of theory are given in Table 2.3.

In the step-wise proton transfer process, the stability of the tautomers follow the order KK>KE>EE. Enolization of one pyrrole ring results in a destabilization of 15-18 kcal/mol and in the formation of mono-enols. The KE form is very interesting in that it exhibits the existence of N–H···N intramolecular hydrogen bond between the pyrrole rings. The formation of KE is associated with significant changes in the nature of the PES compared to that for KK due to the formation of hydrogen bond. Figure 2.6 gives the potential energy surface for DH_{KE} as a function of ϕ_1 and ϕ_2 . In addition to the changes in the position of the rotamers, the number of rotamers is reduced from eight to six compared to that for DH_{KK}. The six stable rotamers are given in Figure 2.7. It can be seen that the PES is symmetrical about the diagonal passing through $\phi_1 = 40^\circ$ and $\phi_2 = 340^\circ$. Of the six isomers (**KE1** to **KE6**), the pairs (**KE1**, **KE4**),

Table 2.3: Relative energies (kcal/mol) for stepwise and concerted intramolecular keto-enol tautomerization in the ground state

Molecule	Isomer	Relative Energy ^a							
		KK	t-TS1	ΔE_1^b	KE	t-TS2	ΔE_2^c	EE	ΔE^\ddagger^d
DH	anti1	0.00	28.80	28.80	17.85	46.84	28.99	35.50	58.36
	anti2	1.64	29.16	27.52	17.45	45.40	27.95	34.00	57.13
	syn	0.77	28.28	27.51	15.89	46.10	30.21	35.58	58.36
DM	anti1	0.00	28.85	28.85	18.29	47.01	28.72	35.79	58.49
	anti2	1.78	29.10	27.32	17.51	45.30	27.80	34.01	56.96
	syn	0.82	28.23	27.41	16.41	46.15	29.73	35.83	58.08
MA	anti1	0.00	28.27	28.27	17.10	45.89	28.79	34.77	57.87
	anti2	0.17	28.32	28.15	16.75	46.41	29.66	35.65	58.16
	syn	0.06	28.49	28.42	17.16	46.66	29.50	36.14	58.36
DA	anti1	0.00	29.25	29.25	18.35	47.02	28.67	35.89	58.64
	anti2	-0.40	29.07	29.47	18.30	47.80	29.50	36.87	59.23
	syn	-0.15	29.25	29.40	18.04	48.17	30.13	37.71	59.55

^a Energies are relative to anti1 isomer for each molecule.

^b $\Delta E_1 = E_{t\text{-TS1}} - E_{\text{KK}}$.

^c $\Delta E_2 = E_{t\text{-TS2}} - E_{\text{KE}}$.

^d ΔE^\ddagger is the barrier for concerted $\text{KK} \rightarrow \text{EE}$ double proton transfer.

(**KE2**, **KE5**), and (**KE3**, **KE6**) are related by σ_2 . It is to be noted that rotamer pairs (**KK3**, **KK4**) and (**KK7**, **KK8**) are merged to form single minimum hydrogen bonded structures **KE3** and **KE6** respectively in KE. Similar to KK, in KE the rotamers can be identified as anti1 (**KE1**, **KE4**), anti2 (**KE2**, **KE5**), and syn (**KE3**, **KE6**) with the syn form being the most stable due to the presence of $\text{N}-\text{H} \cdots \text{N}$ intramolecular hydrogen bonds. The $\text{H} \cdots \text{N}$ distance is 2.26 Å. However, the three forms are within a maximum energy range of 2 kcal/mol. The relative energies for the three forms of DH_{KE} , DM_{KE} , MA_{KE} , and DA_{KE} in the ground state is given in Table 2.3. The $\text{O}-\text{H}$ bond distances (~ 0.98 Å) and $\text{N}-\text{H}-\text{O}$ angles ($\sim 114^\circ$) of the enol groups are similar for all the isomers of DH_{KE} , DM_{KE} , MA_{KE} , and DA_{KE} .

In addition to the mono-enols **KE1** to **KE6**, enolization of the second ring results in further destabilization of 16-19 kcal/mol and in the formation of dienols. The PES contours of **EE** with respect to ϕ_1 and ϕ_2 for DH_{EE} are given in Figure 2.8. The nature of the PES is very different

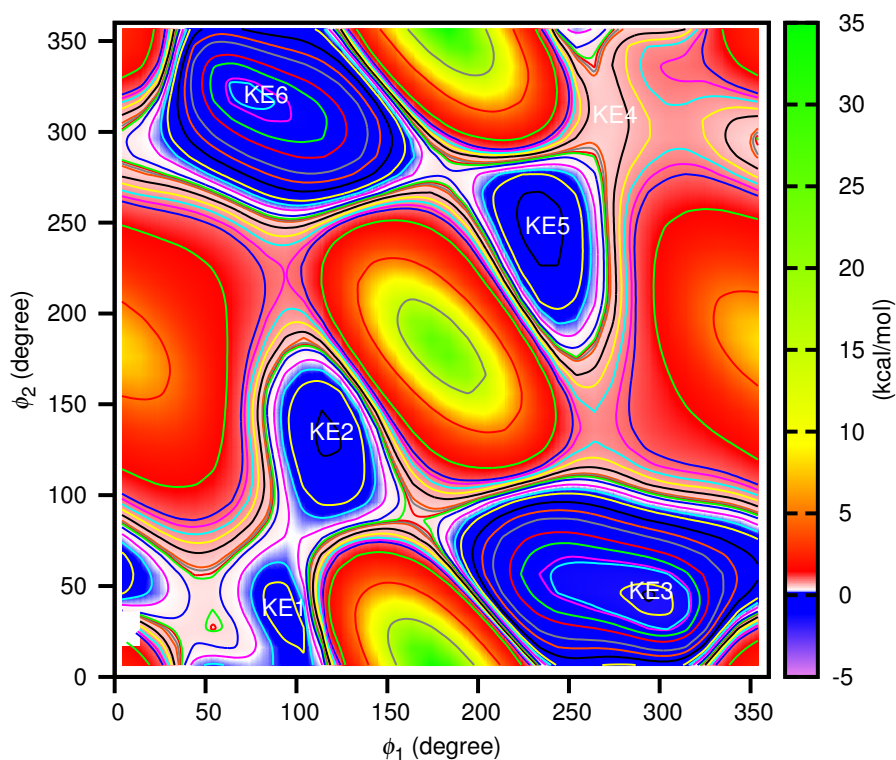


Figure 2.6: Potential energy contours showing the existence of different rotational isomers of DH_{KE} for different values of ϕ_1 and ϕ_2 . **KE1** to **KE6** correspond to different rotational isomers in the respective regions.

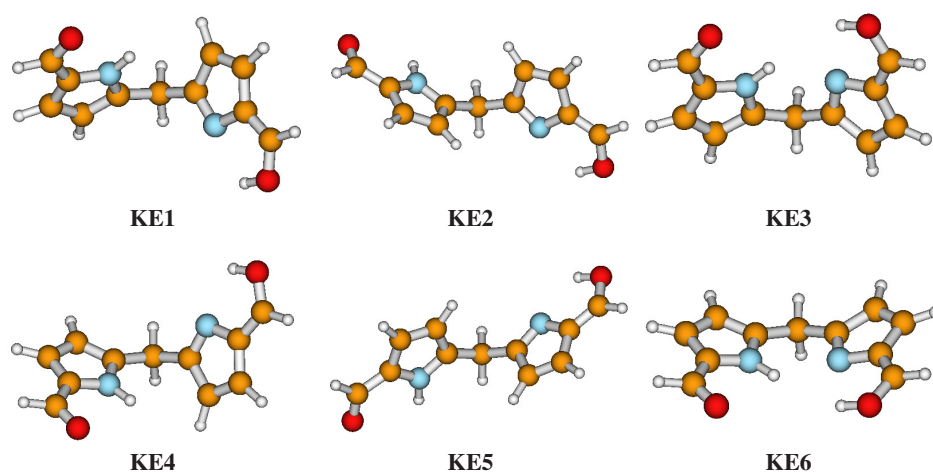


Figure 2.7: Minimum energy structures of different rotational isomers of the mono-enol DH_{KE} .

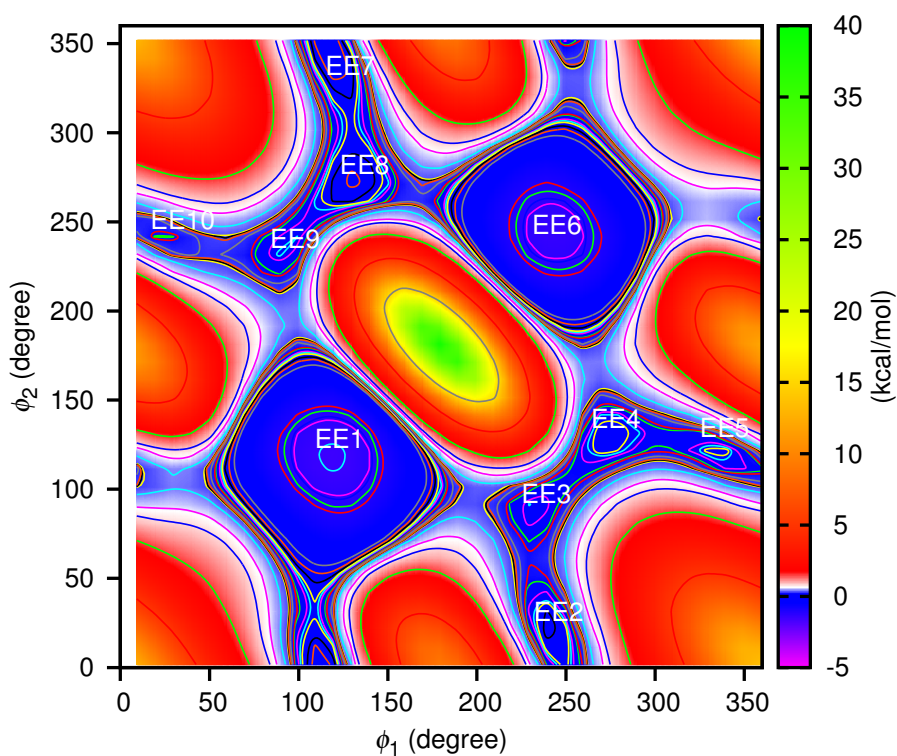


Figure 2.8: Potential energy contours showing the existence of different rotational isomers of DH_{EE} for different values of (ϕ_1) and (ϕ_2) . **EE1** to **EE10** correspond to different rotational isomers in the respective regions.

from that for **KK** and **KE** forms. The dienols exist in rotameric forms **EE1** to **EE10** (Figure

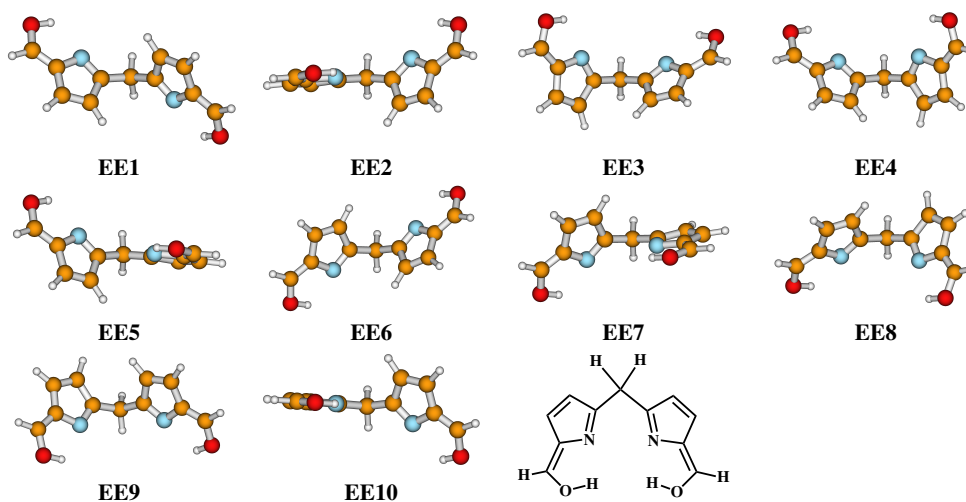


Figure 2.9: Minimum energy structures of different rotational isomers of the dienol DH_{EE} .

2.9). As can be seen in Figure 2.8, the PES is symmetric about the diagonal through $\phi_1 = 0^\circ$ and $\phi_2 = 360^\circ$. The pairs (**EE1**, **EE6**), (**EE2**, **EE5**), (**EE3**, **EE4**), (**EE7**, **EE10**), and (**EE8**, **EE9**) are related by σ_1 operation. Cross pairs (**EE2**, **EE7**), (**EE3**, **EE8**), (**EE4**, **EE9**), and (**EE5**, **EE10**) are related by a C_2 rotation about the methylenic C atom. The PES is also symmetric about the diagonal through $\phi_1 = \phi_2 = 0^\circ$. The symmetric pairs (**EE2**, **EE10**), (**EE3**, **EE9**), (**EE4**, **EE8**), and (**EE5**, **EE7**) are related by σ_2 operation. The rotamers are thus identified as anti1 (**EE2**, **EE5**, **EE7**, **EE10**), anti2 (**EE1**, **EE6**), and syn (**EE3**, **EE4**, **EE8**, **EE9**) forms. The relative energies for the three forms of DH_{EE} , DM_{EE} , MA_{EE} , and DA_{EE} , is also given in Table 2.3. The O–H bond distances (~ 0.98 Å) of enol groups of both the pyrrole rings are similar. The rotamers of each form are isoenergetic.

The destabilization effect due to formation of enol can be thought of as a result of loss of aromaticity in the pyrrole rings by the removal of amine H-atom. No significant effect of substitution at the methylenic carbon on the relative stabilities of KK, KE, and EE forms was observed in the ground state. The transition state structures t-TS1 and t-TS2 for keto-enol tautomerization processes were also obtained. The keto-enol tautomerization barriers for different substituted dipyrromethanes are also nearly same; 27-29 kcal/mol for KK to KE and 28-33 kcal/mol for KE to EE processes. A direct conversion from KK→EE can also happen by a concerted dual proton transfer path. However, the saddle points for concerted paths could not be obtained. To get an insight about the barrier heights for concerted double proton transfer paths, second order saddle points were obtained by performing relaxed optimization with N-H (1.34 Å) and O-H distances (1.24 Å) fixed at single proton transfer transition state structures. The barriers thus calculated for concerted double proton transfer paths are about 11-14 kcal/mol higher in energy than the step-wise single proton transfer paths.

2.3.1.5 Effects of Basis sets and DFT functionals

The effects of basis sets and DFT functionals were investigated by optimizing anti1 isomers of DA_{KK} , DA_{KE} , and DA_{EE} at B3LYP/6-311++G**, M05-2X/6-31+G*, and M05-2X/6-311++G**

Table 2.4: Relative Energies (kcal/mol) of anti1 forms of DA_{KK}, DA_{KE} and DA_{EE} using B3LYP and M05-2X functionals

Molecule	B3LYP		M05-2X	
	6-31+G*	6-311++G**	6-31+G*	6-311++G**
DA _{KK}	0.00	0.00	0.00	0.00
DA _{KE}	18.35	17.21	18.62	17.27
DA _{EE}	35.89	33.38	35.94	33.27

levels of theory and the results are given in Table 2.4. Changing the functional from B3LYP to M05-2X resulted in a deviation less than 1 kcal/mol for the relative energies of DA_{KE} and DA_{EE} isomers. Increasing the basis set to 6-311++G** results in lowering of relative energies, with the maximum lowering seen in the EE form (~ 2.6 kcal/mol).

2.3.2 Photophysics

To understand the photophysics exhibited by the different substituted dipyrromethanes, excited-state calculations were also performed using TDDFT method at B3LYP/6-31+G* level of theory. The excited-state properties were investigated for both cis-trans isomerization and keto-enol tautomerization processes for the four molecules DH_{KK}, DM_{KK}, MA_{KK}, and DA_{KK}.

2.3.2.1 Cis-Trans Isomerization

To investigate the origin of the observed red shifted peak in the absorption spectra, vertical excitation energies (λ_{abs}) from S₀ to S₁, S₂, and S₃ states were computed for anti1, anti2 and syn forms for CC, CT, and TT isomers and are reported in Table 2.5. For all the compounds, S₁ and S₂ transitions are $n \rightarrow \pi^*$ (C=O) while S₃ is $\pi \rightarrow \pi^*$ (pyrrole ring) in nature. The $n \rightarrow \pi^*$ states (S₁ and S₂) for CC and TT are degenerate while for the CT isomers, these are non-degenerate. A mild red shift of ~ 8 nm is seen due to isomerization from CC \rightarrow TT for $n \rightarrow \pi^*$ transition. However, $\pi \rightarrow \pi^*$ transition remains unaffected due to cis-trans isomerization. In addition, the excitation wavelengths for S₁ and S₂ states ($n \rightarrow \pi^*$) and S₃ state ($\pi \rightarrow \pi^*$) are similar for the

Table 2.5: Vertical excitation wavelengths(nm) and transition type types for S_1 , S_2 , and S_3 states for CC, CT, and TT isomers of DH, DM, MA, and DA.

Molecule	Isomer	State	CC		CT		TT	
			λ_{abs}	transition	λ_{abs}	transition	λ_{abs}	transition
DH	anti1	S_1	316	$n \rightarrow \pi^*$	322	$n \rightarrow \pi^*$	324	$n \rightarrow \pi^*$
		S_2	316	$n \rightarrow \pi^*$	317	$n \rightarrow \pi^*$	323	$n \rightarrow \pi^*$
		S_3	293	$\pi \rightarrow \pi^*$	305	$\pi \rightarrow \pi^*$	294	$\pi \rightarrow \pi^*$
	anti2	S_1	314	$n \rightarrow \pi^*$	321	$n \rightarrow \pi^*$	321	$n \rightarrow \pi^*$
		S_2	314	$n \rightarrow \pi^*$	314	$n \rightarrow \pi^*$	321	$n \rightarrow \pi^*$
		S_3	295	$\pi \rightarrow \pi^*$	296	$\pi \rightarrow \pi^*$	293	$\pi \rightarrow \pi^*$
	syn	S_1	316	$n \rightarrow \pi^*$	322	$n \rightarrow \pi^*$	322	$n \rightarrow \pi^*$
		S_2	315	$n \rightarrow \pi^*$	316	$n \rightarrow \pi^*$	322	$n \rightarrow \pi^*$
		S_3	293	$\pi \rightarrow \pi^*$	305	$\pi \rightarrow \pi^*$	294	$\pi \rightarrow \pi^*$
DM	anti1	S_1	316	$n \rightarrow \pi^*$	322	$n \rightarrow \pi^*$	323	$n \rightarrow \pi^*$
		S_2	316	$n \rightarrow \pi^*$	317	$n \rightarrow \pi^*$	323	$n \rightarrow \pi^*$
		S_3	295	$\pi \rightarrow \pi^*$	307	$\pi \rightarrow \pi^*$	295	$\pi \rightarrow \pi^*$
	anti2	S_1	314	$n \rightarrow \pi^*$	320	$n \rightarrow \pi^*$	321	$n \rightarrow \pi^*$
		S_2	313	$n \rightarrow \pi^*$	314	$n \rightarrow \pi^*$	320	$n \rightarrow \pi^*$
		S_3	298	$\pi \rightarrow \pi^*$	299	$\pi \rightarrow \pi^*$	295	$\pi \rightarrow \pi^*$
	syn	S_1	315	$n \rightarrow \pi^*$	321	$n \rightarrow \pi^*$	322	$n \rightarrow \pi^*$
		S_2	314	$n \rightarrow \pi^*$	316	$n \rightarrow \pi^*$	322	$n \rightarrow \pi^*$
		S_3	294	$\pi \rightarrow \pi^*$	298	$\pi \rightarrow \pi^*$	297	$\pi \rightarrow \pi^*$
MA	anti1	S_1	316	$n \rightarrow \pi^*$	323	$n \rightarrow \pi^*$	324	$n \rightarrow \pi^*$
		S_2	316	$n \rightarrow \pi^*$	316	$n \rightarrow \pi^*$	322	$n \rightarrow \pi^*$
		S_3	303	$\pi \rightarrow \pi^*$	300	$\pi \rightarrow \pi^*$	305	$\pi \rightarrow \pi^*$
	anti2	S_1	316	$n \rightarrow \pi^*$	322	$n \rightarrow \pi^*$	323	$n \rightarrow \pi^*$
		S_2	315	$n \rightarrow \pi^*$	314	$n \rightarrow \pi^*$	320	$n \rightarrow \pi^*$
		S_3	297	$\pi \rightarrow \pi^*$	296	$\pi \rightarrow \pi^*$	299	$\pi \rightarrow \pi^*$
	syn	S_1	316	$n \rightarrow \pi^*$	323	$n \rightarrow \pi^*$	324	$n \rightarrow \pi^*$
		S_2	316	$n \rightarrow \pi^*$	316	$n \rightarrow \pi^*$	323	$n \rightarrow \pi^*$
		S_3	296	$\pi \rightarrow \pi^*$	300	$\pi \rightarrow \pi^*$	300	$\pi \rightarrow \pi^*$
DA	anti1	S_1	318	$n \rightarrow \pi^*$	324	$n \rightarrow \pi^*$	325	$n \rightarrow \pi^*$
		S_2	318	$n \rightarrow \pi^*$	319	$n \rightarrow \pi^*$	325	$n \rightarrow \pi^*$
		S_3	302	$\pi \rightarrow \pi^*$	309	$\pi \rightarrow \pi^*$	301	$\pi \rightarrow \pi^*$
	anti2	S_1	315	$n \rightarrow \pi^*$	321	$n \rightarrow \pi^*$	321	$n \rightarrow \pi^*$
		S_2	315	$n \rightarrow \pi^*$	315	$n \rightarrow \pi^*$	321	$n \rightarrow \pi^*$
		S_3	295	$\pi \rightarrow \pi^*$	297	$\pi \rightarrow \pi^*$	293	$\pi \rightarrow \pi^*$
	syn	S_1	317	$n \rightarrow \pi^*$	321	$n \rightarrow \pi^*$	323	$n \rightarrow \pi^*$
		S_2	316	$n \rightarrow \pi^*$	317	$n \rightarrow \pi^*$	322	$n \rightarrow \pi^*$
		S_3	295	$\pi \rightarrow \pi^*$	301	$\pi \rightarrow \pi^*$	298	$\pi \rightarrow \pi^*$

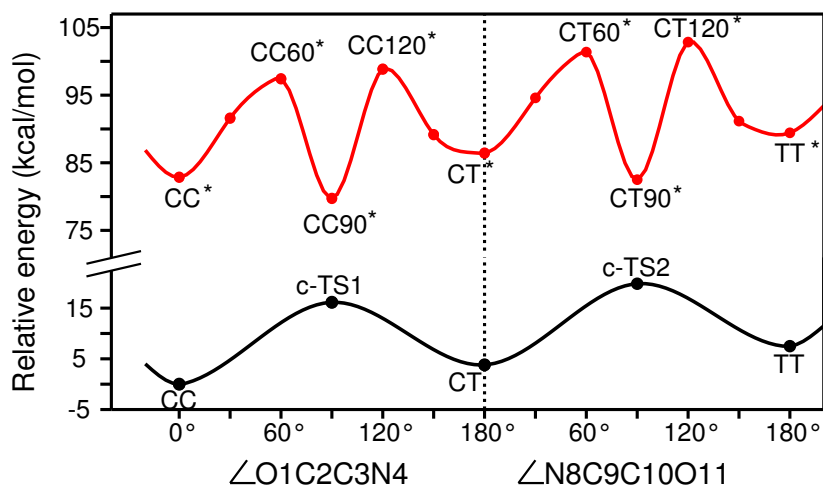


Figure 2.10: Stepwise cis-trans isomerization paths for DH in ground and first excited-state.

CC, CT, and TT isomers, indicating clearly the absence of substitution effects in the absorption properties. From the above results, it is evident that conformational isomerism does not cause any significant red shift in absorption spectra for any of the compounds considered here and no effect of substituents is observed in the absorption spectra.

To gain knowledge about the barriers involved during the CC→TT isomerization processes, a series of relaxed geometry optimizations along cis-trans isomerization path in the first excited-state was carried out by fixing the dihedral angles $\angle\text{O1C2C3N4}$ and $\angle\text{N8C9C10O11}$ at an interval of 30° . The relative energies of stepwise isomerization path obtained from the relaxed PES scan are given in Figure 2.10 for DH. It can be seen from Figure 2.10 that the potential energy profile of cis-trans isomerization path in S_1 state is very different from that in the ground state. The energetics of cis-trans isomerization processes relative to CC^* in S_1 state for the four molecules DH, DM, MA, and DA are reported in Table 2.6. In S_1 state, the maximum of energy was found for the structures, CC60^* with $\angle\text{O1C2C3N4} = 60^\circ$ and CC120^* with $\angle\text{O1C2C3N4} = 120^\circ$. The structures CC90^* with $\angle\text{O1C2C3N4} = 90^\circ$, which were transition states in S_0 , were found to be minima and lower than CC^* by $\sim 2\text{-}4$ kcal/mol in S_1 state. Clearly, CC90^* structures are the most stable conformers in the S_1 state. The transformation from $\text{CT}^* \rightarrow \text{TT}^*$

Table 2.6: Relative energies (kcal/mol) of stationary points along the CC→TT isomerization paths in the first excited-state for the diketo forms of DH, DM, MA, and DA

Molecule	Isomer	Relative Energy ^a				
		CC*	CC90*	CT*	CT90*	TT*
DH	anti1	0.00	-3.13	3.57	0.93	5.03
	anti2	2.16	-2.24	6.43	2.05	8.28
	syn	0.90	-2.68	3.11	1.59	6.72
DM	anti1	0.00	-3.78	1.55	0.41	4.95
	anti2	2.44	-2.95	4.29	1.37	8.37
	syn	0.94	-3.24	3.16	1.44	6.68
MA	anti1	0.00	-3.36	1.63	0.33	5.24
	anti2	0.82	-3.86	1.75	-0.03	5.24
	syn	0.21	-3.16	1.81	0.22	5.45
DA	anti1	0.00	-3.66	1.54	0.18	4.71
	anti2	0.28	-4.20	1.67	-0.66	4.97
	syn	0.27	-3.61	3.60	-0.05	4.91

^aEnergies are relative to anti1 isomer for each molecule.

in S_1 state takes place via minima structures CT90* with $\angle O11C10C9N8 = 90^\circ$. The barriers for CC* →CT* isomerization paths in S_1 state were found to be 14-20 kcal/mol. It is to be noted that the isomerization barriers in excited-state (S_1) are slightly lower than in the ground state. However, no significant effect of substituents R_1 and R_2 on the relative stabilities of CC*, CT*, and TT* isomers and isomerization barriers was observed in excited-state also.

2.3.2.2 Keto-Enol Tautomerization

As seen in the ground state, dipyrromethanes can exhibit keto-enol tautomerization in the excited-state too. To understand the substituent specific red shifted peak observed in the experiments for DA_{KK}, vertical transition energies for the different tautomers (KK, KE, EE) of DH, DM, MA, and DA were computed using TDDFT method and at B3LYP/6-31+G* level of theory and the results are given in Table 2.7. The important orbitals involved in the vertical transitions are shown in Figures 2.11 and 2.12 for DH and DA respectively. In diketo forms, the S_1 and S_2 states are degenerate with λ_{abs} in the range 313-318 nm and correspond to a

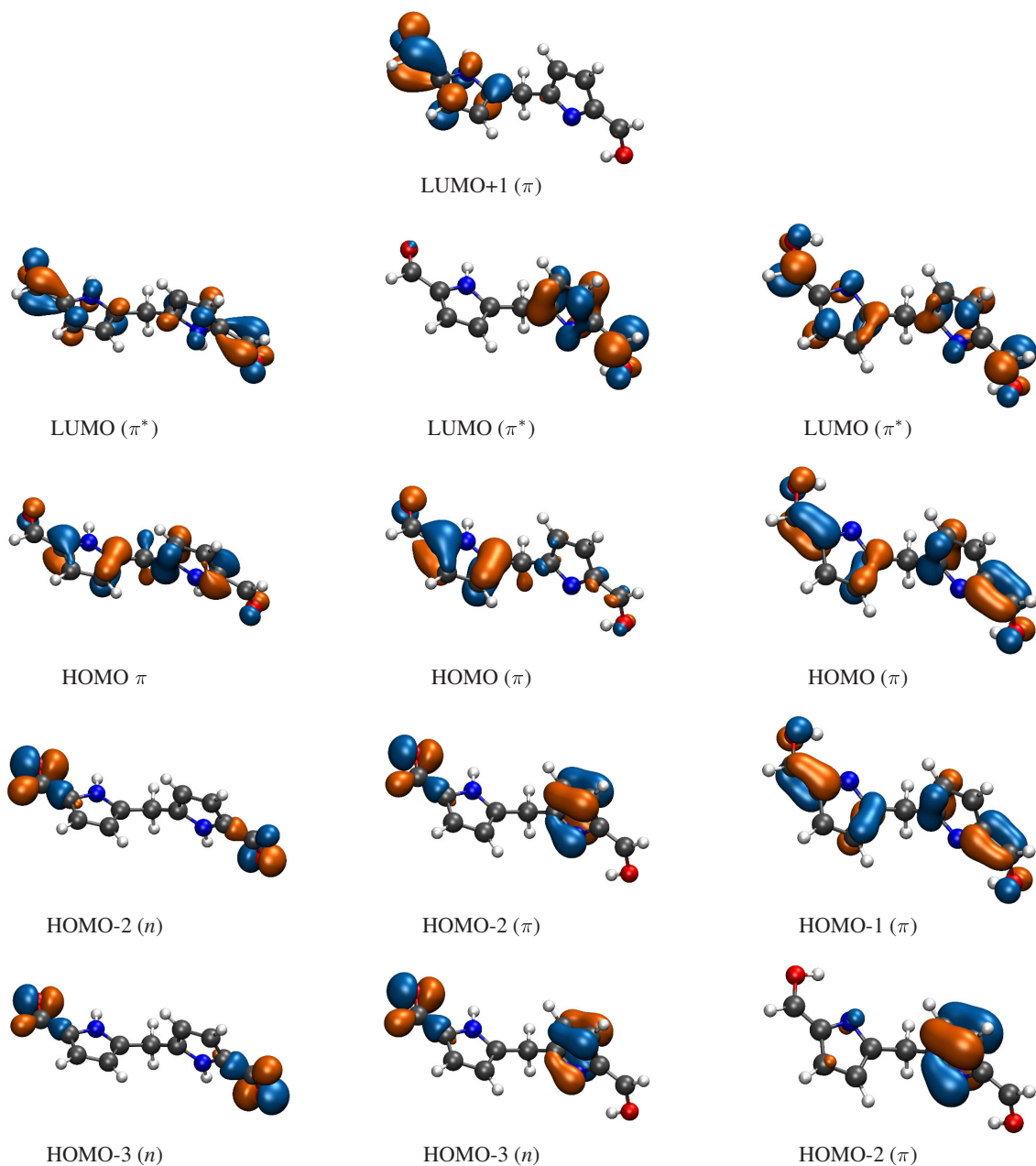


Figure 2.11: Molecular orbital diagram of anti2 isomer of DH_{KK} , DH_{KE} , and DH_{EE} calculated at the B3LYP/6-31+G* level.

$n \rightarrow \pi^*$ transition, while the S_3 states correspond to a $\pi \rightarrow \pi^*$ transition of the pyrrole ring with λ_{abs} in the range 293-303 nm. This is in good agreement with the experimental absorption $\lambda_{\text{max}}^{\text{exp}}$ value of 300 nm for DM, MA, and DA. As seen above, in the excited-state enolization can also follow a stepwise ($\text{KK}^* \rightarrow \text{KE}^* \rightarrow \text{EE}^*$) or a concerted ($\text{KK}^* \rightarrow \text{EE}^*$) path. A stepwise

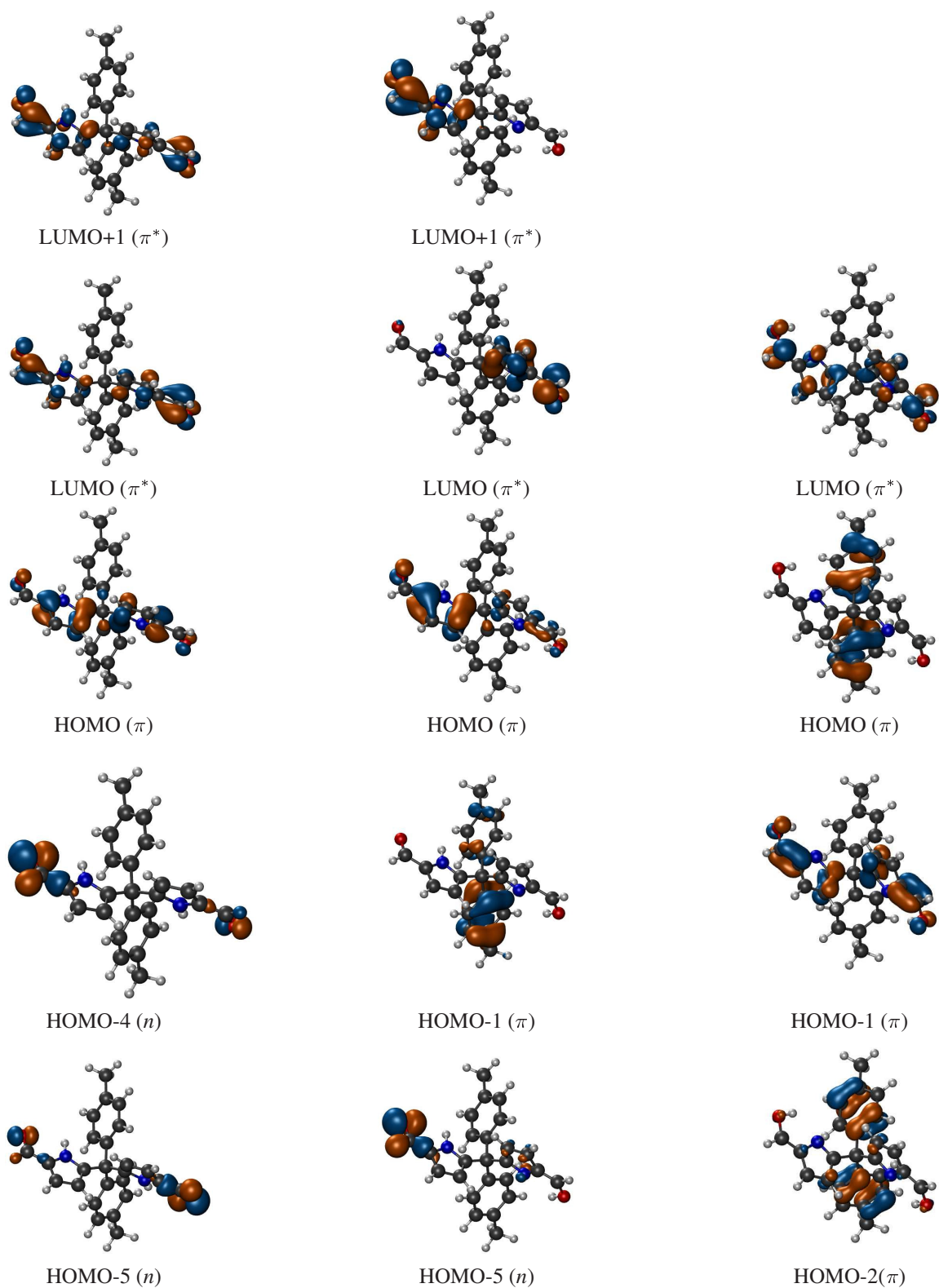


Figure 2.12: Molecular orbital diagram of anti2 isomer of DA_{KK}, DA_{KE}, and DA_{EE} calculated at the B3LYP/6-31+G* level.

Table 2.7: Calculated vertical excitation wavelengths (nm) and transition types of S_1 , S_2 , and S_3 states for different tautomeric forms of DH, DM, MA, and DA

Molecule	Isomer	State	KK		KE		EE		$\lambda_{\text{abs}}^{\text{exp } a}$
			λ_{abs}	Transition	λ_{abs}	Transition	λ_{abs}	Transition	
DH	anti1	S_1	316	$n \rightarrow \pi^*$	375	$\pi \rightarrow \pi^*$	321	$\pi \rightarrow \pi^*$	
		S_2	316	$n \rightarrow \pi^*$	312	$n \rightarrow \pi^*$	303	$\pi \rightarrow \pi^*$	
		S_3	293	$\pi \rightarrow \pi^*$	302	$\pi \rightarrow \pi^*$	301	$\pi \rightarrow \pi^*$	
	anti2	S_1	314	$n \rightarrow \pi^*$	349	$\pi \rightarrow \pi^*$	317	$\pi \rightarrow \pi^*$	
		S_2	314	$n \rightarrow \pi^*$	315	$n \rightarrow \pi^*$	309	$\pi \rightarrow \pi^*$	
		S_3	295	$\pi \rightarrow \pi^*$	299	$\pi \rightarrow \pi^*$	306	$\pi \rightarrow \pi^*$	
	syn	S_1	316	$n \rightarrow \pi^*$	389	$\pi \rightarrow \pi^*$	322	$\pi \rightarrow \pi^*$	
		S_2	315	$n \rightarrow \pi^*$	314	$n \rightarrow \pi^*$	307	$\pi \rightarrow \pi^*$	
		S_3	293	$\pi \rightarrow \pi^*$	306	$\pi \rightarrow \pi^*$	304	$\pi \rightarrow \pi^*$	
DM	anti1	S_1	316	$n \rightarrow \pi^*$	382	$\pi \rightarrow \pi^*$	328	$\pi \rightarrow \pi^*$	300
		S_2	316	$n \rightarrow \pi^*$	313	$n \rightarrow \pi^*$	313	$\pi \rightarrow \pi^*$	
		S_3	295	$\pi \rightarrow \pi^*$	308	$\pi \rightarrow \pi^*$	307	$\pi \rightarrow \pi^*$	
	anti2	S_1	314	$n \rightarrow \pi^*$	351	$\pi \rightarrow \pi^*$	319	$\pi \rightarrow \pi^*$	
		S_2	313	$n \rightarrow \pi^*$	314	$n \rightarrow \pi^*$	310	$\pi \rightarrow \pi^*$	
		S_3	298	$\pi \rightarrow \pi^*$	298	$\pi \rightarrow \pi^*$	306	$\pi \rightarrow \pi^*$	
	syn	S_1	315	$n \rightarrow \pi^*$	352	$\pi \rightarrow \pi^*$	333	$\pi \rightarrow \pi^*$	
		S_2	314	$n \rightarrow \pi^*$	316	$n \rightarrow \pi^*$	303	$\pi \rightarrow \pi^*$	
		S_3	294	$\pi \rightarrow \pi^*$	297	$\pi \rightarrow \pi^*$	300	$\pi \rightarrow \pi^*$	
MA	anti1	S_1	316	$n \rightarrow \pi^*$	375	$\pi \rightarrow \pi^*$	335	$\pi \rightarrow \pi^*$	300
		S_2	316	$n \rightarrow \pi^*$	321	$\pi \rightarrow \pi^*$	314	$\pi \rightarrow \pi^*$	
		S_3	303	$\pi \rightarrow \pi^*$	313	$n \rightarrow \pi^*$	306	$\pi \rightarrow \pi^*$	
	anti2	S_1	316	$n \rightarrow \pi^*$	356	$\pi \rightarrow \pi^*$	347	$\pi \rightarrow \pi^*$	
		S_2	315	$n \rightarrow \pi^*$	315	$n \rightarrow \pi^*$	322	$\pi \rightarrow \pi^*$	
		S_3	297	$\pi \rightarrow \pi^*$	309	$\pi \rightarrow \pi^*$	316	$\pi \rightarrow \pi^*$	
	syn	S_1	316	$n \rightarrow \pi^*$	358	$\pi \rightarrow \pi^*$	339	$\pi \rightarrow \pi^*$	
		S_2	316	$n \rightarrow \pi^*$	319	$\pi \rightarrow \pi^*$	318	$\pi \rightarrow \pi^*$	
		S_3	296	$\pi \rightarrow \pi^*$	315	$n \rightarrow \pi^*$	311	$\pi \rightarrow \pi^*$	
DA	anti1	S_1	318	$n \rightarrow \pi^*$	378	$\pi \rightarrow \pi^*$	345	$\pi \rightarrow \pi^*$	300, 390
		S_2	318	$n \rightarrow \pi^*$	328	$\pi \rightarrow \pi^*$	330	$\pi \rightarrow \pi^*$	
		S_3	302	$\pi \rightarrow \pi^*$	323	$\pi \rightarrow \pi^*$	327	$\pi \rightarrow \pi^*$	
	anti2	S_1	315	$n \rightarrow \pi^*$	352	$\pi \rightarrow \pi^*$	385	$\pi \rightarrow \pi^*$	
		S_2	315	$n \rightarrow \pi^*$	342	$\pi \rightarrow \pi^*$	332	$\pi \rightarrow \pi^*$	
		S_3	295	$\pi \rightarrow \pi^*$	316	$n \rightarrow \pi^*$	331	$\pi \rightarrow \pi^*$	
	syn	S_1	317	$n \rightarrow \pi^*$	350	$\pi \rightarrow \pi^*$	358	$\pi \rightarrow \pi^*$	
		S_2	316	$n \rightarrow \pi^*$	348	$\pi \rightarrow \pi^*$	344	$\pi \rightarrow \pi^*$	
		S_3	295	$\pi \rightarrow \pi^*$	319	$n \rightarrow \pi^*$	333	$\pi \rightarrow \pi^*$	

^a Experimental absorption maximum.⁷⁵

enolization first results in the formation of monoenols (KE^*), an excited-state intramolecular proton transfer (ESIPT) process. In monoenols, the S_1 states are $\pi \rightarrow \pi^*$ in nature. However, λ_{abs} to S_1 state for the different forms of all the molecules (350-390 nm) are similar. For the four molecules considered here, λ_{abs} to S_1 state for anti1, anti2, and syn forms are in the range 375-382 nm, 349-356 nm, and 350-389 nm respectively. The λ_{abs} to the S_1 states are red shifted (~ 50 -95 nm) compared to λ_{abs} ($\pi \rightarrow \pi^*$ transition, S_3) of KK forms for all the molecules considered here. For anti1 and anti2 forms of DH, DM, MA, and DA, the red shifts are similar ca. 74-82 nm and ca. 53-59 nm respectively. While the syn forms of DM, MA, and DA also show similar red shifts ca. 55-62 nm, a larger red shift seen in syn monoenol of DH can be attributed to a formation of hydrogen bonded structure. The above observations suggest the absence of effect of the substituents on the absorption wavelengths for monoenols; the red shifts are similar for all the four molecules.

Enolization of monoenols result in their respective dienols (EE^*) by ESIPT processes. In the dienol forms, S_1 , S_2 , and S_3 states are $\pi \rightarrow \pi^*$ in nature. The λ_{abs} to S_1 state for DH and DM isomers for anti1, anti2, and syn were found to be only ~ 20 -40 nm red shifted with respect to the KK forms. However, by introduction of a aryl group at the methylenic (C6) carbon as in MA_{EE} , the red shift was further increased with a maximum shift of 50 nm seen in anti2 isomer. For two aryl substituted (DA_{EE}) molecule, λ_{abs} to S_1 state for anti1 is 345 nm, anti2 is 385 nm, and for syn it is 358 nm showing a red shift of 43, 90, and 63 nm for anti1, anti2, and syn forms respectively with respect to the $\pi \rightarrow \pi^*$ (S_3) transitions of KK. The observed red shift of ~ 90 nm in λ_{abs} seen in DA (anti2) molecule due to dienol formation clearly demonstrates the effect of substitution (aryl) at the methylenic carbon on the absorption wavelengths. This is consistent with the appearance of a red shifted new peak at 390 nm in the experimental absorption spectrum of DA after irradiation. The new absorption peak seen in the experiment is close to calculated λ_{abs} of 385 nm for anti2 (DA_{EE}) isomer. It is worth pointing out that anti2- DA_{KK} is expected to be more populated in the ground state at equilibrium.

Table 2.8: Relative energies (kcal/mol) of stepwise intramolecular keto-enol tautomerization in S_1 state

Molecule	Isomer	Relative Energy ^a							
		KK [*]	t-TS1 [*]	ΔE_1^* ^b	KE [*]	t-TS2 [*]	ΔE_2^* ^c	EE [*]	$\Delta\Delta E^*$ ^d
DH	anti1	0.00	14.18	14.18	-0.74	36.10	36.84	28.17	22.66
	anti2	2.16	21.54	19.39	5.65	36.03	30.38	27.91	11.00
	syn	0.90	12.64	11.74	-5.87	38.51	44.38	27.67	32.65
DM	anti1	0.00	13.18	13.18	-2.12	35.74	37.87	26.99	24.68
	anti2	2.44	20.05	17.62	5.51	36.90	31.39	27.61	13.77
	syn	0.94	11.71	10.78	-6.90	39.85	46.75	29.13	35.97
MA	anti1	0.00	13.78	13.78	-1.32	34.08	35.40	26.43	21.62
	anti2	0.82	17.96	17.14	3.82	36.52	32.71	25.40	15.56
	syn	0.21	11.75	11.54	1.38	40.27	38.89	26.61	27.35
DA	anti1	0.00	12.60	12.60	-2.28	33.23	35.51	26.55	22.91
	anti2	0.28	20.08	19.80	5.76	32.62	26.86	19.95	07.06
	syn	0.27	18.16	17.89	3.58	33.62	30.03	21.23	12.15

^a Energies are relative to anti1 isomer for each molecule.

^b $\Delta E_1^* = E_{t-TS1^*} - E_{KK^*}$.

^c $\Delta E_2^* = E_{t-TS2^*} - E_{KE^*}$.

^d $\Delta\Delta E^* = \Delta E_2^* - \Delta E_1^*$.

To understand the energetics of the formation of enols in S_1 state, the KE^{*} and EE^{*} structures for syn, anti1, and anti2 isomers of DH, DM, MA, and DA were optimized in the first excited-state using TDDFT (B3LYP/6-31+G^{*}) method. In addition, the transition state (t-TS1^{*} and t-TS2^{*}) structures were also optimized in S_1 state to obtain the barrier heights for KK^{*}→KE^{*} and KE^{*}→EE^{*} proton transfer processes (tautomerization). The relative energies and tautomerization barriers for different isomers obtained are given in Table 2.8. It can be seen that for all the isomers, KE^{*} forms are significantly stabilized in the excited-state compared to that in the ground state. The anti1-KE^{*} forms are lower in energy than the respective anti1-KK^{*} forms and anti2-KE^{*} isomers are higher in energy compared to that of anti2-KK^{*} forms. However, syn-KE^{*} forms are more stable than syn-KK^{*} forms only in DH and DM. In MA and DA, syn-KE^{*} forms are higher than syn-KK^{*} by 1.2 and 3.3 kcal/mol respectively. The barriers for KK^{*} to KE^{*} tautomerization decrease by 9-19 kcal/mol in the excited-state compared to

that in the ground state. Once a KE^* is formed, it can isomerize to an EE^* through a transition state $t-TS2^*$. The relative energies of EE^* forms with respect to KK^* , are lowered by 6-17 kcal/mol in the excited-state compared to that in the ground state. In S_1 state, for DH, DM, and MA, EE^* forms are higher in energy than the respective KK^* by ~ 25 -29 kcal/mol that can be compared to EE energies of 33-35 kcal/mol relative to KK in S_0 state. However, introduction of aryl groups further stabilizes the dienols (EE^*) in S_1 state compared to that in S_0 state. A large lowering of energy was observed for syn and anti2-DA (~ 17 kcal/mol) indicating a significant effect of the aryl substituent on the stability of dienol form in the excited-state.

It is interesting to compare the barriers $KK^* \rightarrow KE^*$ and $KE^* \rightarrow EE^*$ tautomerization processes in S_1 state to that in S_0 state. In S_0 state, the barriers for both $KK \rightarrow KE$ and $KE \rightarrow EE$ processes are similar, ~ 28 kcal/mol for all isomers in all the four molecules. However, in S_1 state, the barriers for $KK^* \rightarrow KE^*$ processes are different from that for $KE^* \rightarrow EE^*$ processes. For $KK^* \rightarrow KE^*$ processes, the barriers for the respective isomers of DH, DM, and MA are similar: ~ 13 , ~ 18 , and ~ 11 kcal/mol for anti1, anti2, and syn respectively. Due to stabilization of KE^* , the barrier heights for $KE^* \rightarrow EE^*$ are higher than that for $KK^* \rightarrow KE^*$ by ~ 22 -25 kcal/mol for anti1 forms in DH, DM and MA. In syn forms of DH, DM, and MA the barriers for $KE^* \rightarrow EE^*$ ESIPT processes are 33, 36, and 27 kcal/mol higher than $KK^* \rightarrow KE^*$ barriers respectively. In anti2 forms, the barriers for $KK^* \rightarrow KE^*$ processes for DH, DM, and MA are higher than those of anti1 and syn forms. However, due to destabilization of the anti2- KE^* forms, the barriers for $KE^* \rightarrow EE^*$ processes are less compared to those of DH, DM, and MA. The energetics of DA in S_1 state is quite different compared to that of DH, DM, and MA. In DA, the barriers for $KK^* \rightarrow KE^*$ processes are 13, 20, and 18 kcal/mol for anti1, anti2, and syn isomers respectively. The barriers for $KE^* \rightarrow EE^*$ conversion are 36, 27 and 30 kcal/mol for anti1, anti2, and syn isomers respectively. In DA, while the $KE^* \rightarrow EE^*$ barrier for anti1 form is similar to that of the anti1 forms of DH, DM, and MA, the barriers for anti2 and syn are lower than their respective forms of DH, DM, and MA. For anti2 form of DA, the $KE^* \rightarrow EE^*$

barrier is ~ 4 -6 kcal/mol lower than that for anti2 forms of DH, DM, and MA. In addition, this barrier for syn form is 14, 17, and 9 kcal/mol lower than the syn forms of DH, DM, and MA respectively. This lowering in the barriers for $\text{KE}^* \rightarrow \text{EE}^*$ in anti2 and syn forms of DA, is in accord with the lowering of anti2 and syn- EE^* energies with respect to that of DH, DM, and MA (by ~ 5 -6 and ~ 5 -7 kcal/mol respectively). Stationary points corresponding to concerted dual proton transfer ($\text{KK}^* \rightarrow \text{EE}^*$) in the excited-state could not be calculated. However, to get insight about the barrier heights, single point vertical excitation energies were calculated using ground state saddle point structures for the concerted paths. These barriers were found to be high and similar for all the four molecules (~ 55 kcal/mol) indicating the infeasibility of concerted proton transfer processes.

To understand the nature of the potential energy surface along the proton-transfer reaction path, single point potential energy surface scan (TDDFT/6-31+G*) was performed by using a set of (r_1, θ_1) and (r_2, θ_2) coordinates obtained from the geometries along the ground state IRC paths for $\text{KK} \rightarrow \text{KE} \rightarrow \text{EE}$ processes. Here, r_1 and r_2 are N4-H12 and N8-H13 distances, θ_1 and θ_2 are the angles $\angle \text{O1N4H12}$ and $\angle \text{O11N8H13}$ respectively. Thus, the set of coordinates faithfully represent both stepwise $\text{KK} \rightarrow \text{KE} \rightarrow \text{EE}$ and concerted $\text{KK} \rightarrow \text{EE}$ processes. The resulting PES for S_0 , S_1 , S_2 , and S_3 states of DH and DA is given in Figure 2.13. The figures depict the possibility of two equivalent paths from $\text{KK} \rightarrow \text{KE} \rightarrow \text{EE}$ where the order of the proton transfer in the rings are reversed. As pointed earlier, enolization can follow a concerted path involving a very high barrier as seen in Figure 2.13.

2.3.2.3 Solvent Effect

To investigate the effect of solvent on photophysical process, DFT calculations were performed using polarizable continuum model (PCM)^{88,89} at B3LYP/6-31+G* level of theory using acetonitrile and cyclohexane as solvents for anti2 isomers of DH and DA. The geometries were optimized in the ground state and vertical excitation energies were computed at the ground state geometries using TDDFT method. The results of the calculations are given in Table 2.9. It

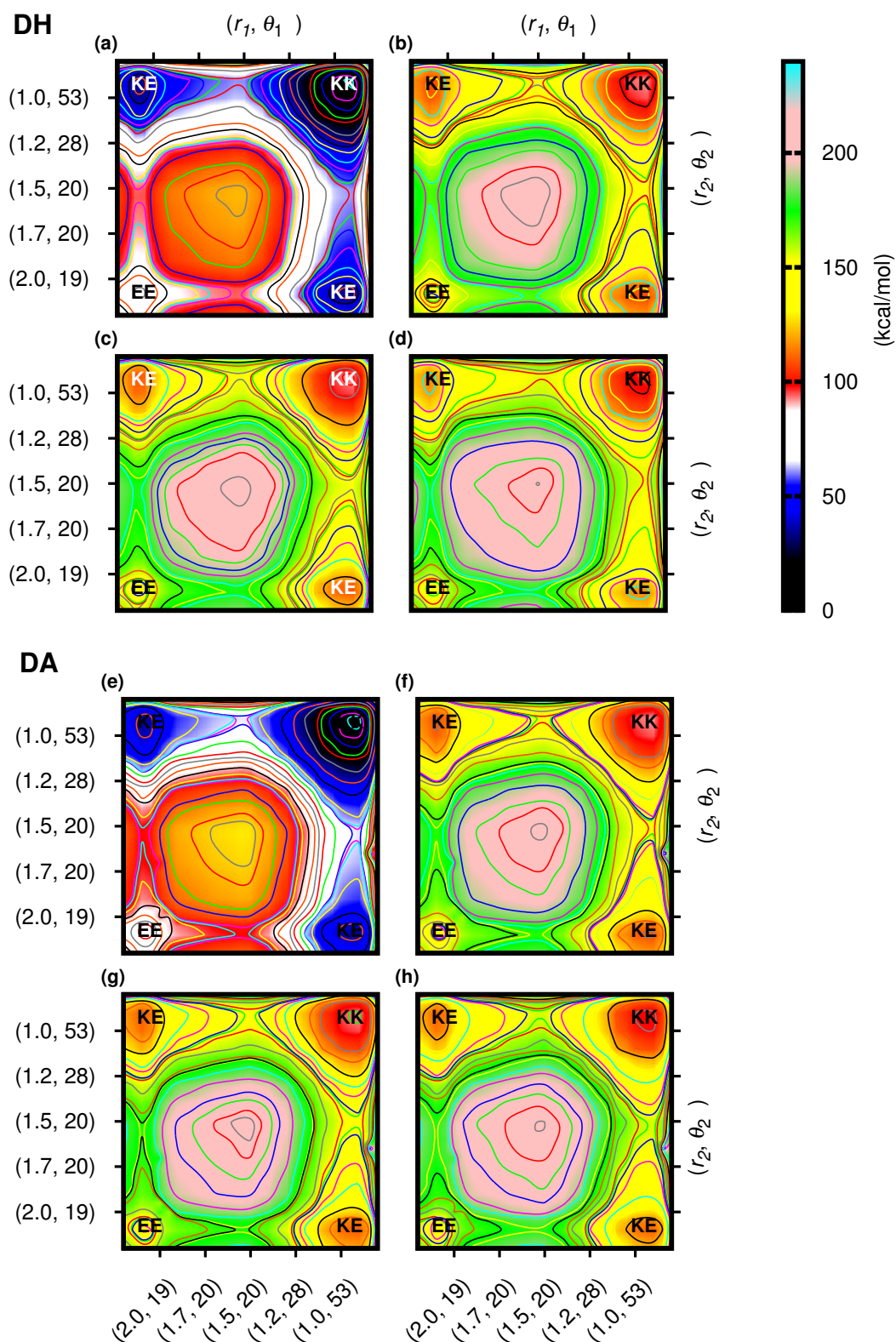


Figure 2.13: Potential energy surface along the reaction paths for proton transfer processes using (r_1, θ_1) and (r_2, θ_2) as sets of coordinates. (a), (b), (c), and (d) represent S_0 , S_1 , S_2 , and S_3 states for DH and (e), (f), (g), and (h) represent S_0 , S_1 , S_2 , and S_3 states for DA. r_1 and r_2 are in Å and θ_1 and θ_2 .

Table 2.9: Vertical excitation wavelengths (nm) for anti2 isomers of DH and DA in acetonitrile and cyclohexane solvents

Molecule	State	Acetonitrile				Cyclohexane			
		KK		EE		KK		EE	
		λ_{abs}	transition	λ_{abs}	transition	λ_{abs}	transition	λ_{abs}	transition
DH	S ₁	309	$n \rightarrow \pi^*$	318	$\pi \rightarrow \pi^*$	311	$n \rightarrow \pi^*$	321	$\pi \rightarrow \pi^*$
	S ₂	307	$n \rightarrow \pi^*$	308	$\pi \rightarrow \pi^*$	310	$n \rightarrow \pi^*$	308	$\pi \rightarrow \pi^*$
	S ₃	305	$\pi \rightarrow \pi^*$	304	$\pi \rightarrow \pi^*$	304	$\pi \rightarrow \pi^*$	306	$\pi \rightarrow \pi^*$
DA	S ₁	311	$n \rightarrow \pi^*$	359	$\pi \rightarrow \pi^*$	312	$n \rightarrow \pi^*$	376	$\pi \rightarrow \pi^*$
	S ₂	310	$n \rightarrow \pi^*$	329	$\pi \rightarrow \pi^*$	311	$n \rightarrow \pi^*$	333	$\pi \rightarrow \pi^*$
	S ₃	302	$\pi \rightarrow \pi^*$	318	$\pi \rightarrow \pi^*$	300	$\pi \rightarrow \pi^*$	327	$\pi \rightarrow \pi^*$

can be seen that λ_{abs} values for KK and EE are slightly blue shifted compared to the gas phase values for both DH and DA. However, the λ_{abs} values (red shifts) follow similar trends for the KK \rightarrow EE process as seen in the gas phase. A red shift of 48 and 64 nm in λ_{abs} for S₀ \rightarrow S₁ transition was seen during KK \rightarrow EE processes in acetonitrile and cyclohexane respectively. Interestingly these red shifts are less compared to the red shift of 70 nm seen in the gas phase.

2.3.2.4 Intermolecular Proton Transfer

The possibility of intermolecular proton transfer via a dimer formation was also investigated using the DFT method for DA and DH. Here only the anti1 isomers are expected to form closed symmetrical dimers. The optimized structures of diketo (KK \cdots KK) and dienol (EE \cdots EE) dimers formed from anti1 monomers for DA are given in Figure 2.14. The dimerization energies and KK \cdots KK \rightarrow EE \cdots EE enolization (intermolecular dual proton transfer processes) energies are listed in Table 2.10. The KK \cdots KK and EE \cdots EE dimers of DH are more stabilized than that of the DA counterparts due to stronger intermolecular hydrogen bonds. The intermolecular NH \cdots OC bond distances are \sim 1.88 and \sim 1.93 Å for DH and DA respectively. However, the enolization energies of the dimers are similar for both DH and DA. The calculated λ_{abs} values for the dimers (Table 2.11) are red shifted compared to their respective monomers for both DH

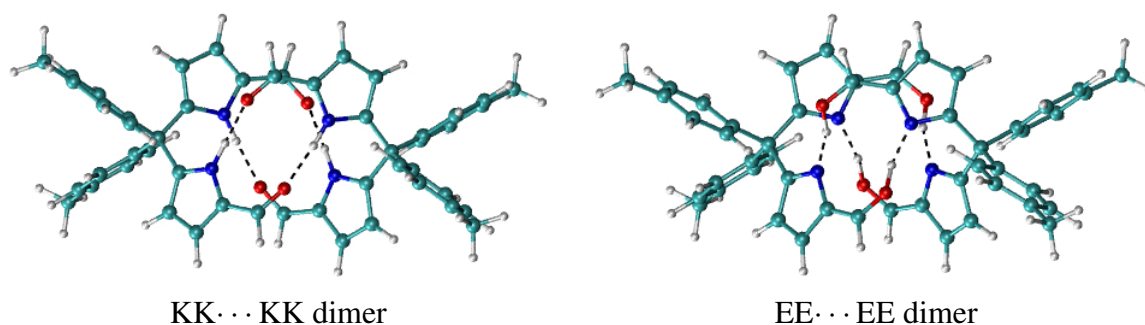


Figure 2.14: Ground state minimum energy structures of KK...KK and EE...EE dimers of DA.

Table 2.10: Relative energies (kcal/mol) for diketo and dienol dimers of DH and DA and their respective enolization energies for diketo-dimer \rightarrow dienol-dimer processes in the ground state

Molecules	Dimerization energy		Enolization energy ^c
	$\Delta_{\text{KK}\dots\text{KK}}^a$	$\Delta_{\text{EE}\dots\text{EE}}^b$	KK...KK \rightarrow EE...EE
DH	-18.71	-25.71	61.00
DA	-13.31	-21.44	63.65

$$^a E_{\text{KK}\dots\text{KK}} - 2 E_{\text{KK}\cdot}$$

$$^b E_{\text{EE}\dots\text{EE}} - 2 E_{\text{EE}\cdot}$$

$$^c E_{\text{EE}\dots\text{EE}} - E_{\text{KK}\dots\text{KK}}$$

and DA. Due to stronger hydrogen bonds, a slightly larger red shift in λ_{abs} is seen for KK...KK dimer of DH. The λ_{abs} values for EE...EE dimers are red shifted compared to the KK...KK dimers and are similar for both DH and DA, in contrast to that seen in the experiment. Hence, intermolecular proton transfer via a dimer formation does not explain the substituent specific red shifts seen in the experiments.

2.3.2.5 Emission Spectra

The vertical emission wavelengths (λ_{em}) were also computed using the minimum energy geometries of the isomers in the excited (S_1) state. The calculated λ_{em} for the different isomers are compared with $\lambda_{\text{em}}^{\text{exp}}$ in Table 2.12. The λ_{em} of KK* are similar \sim 381-386 nm for all the four molecules. However, the λ_{em} of KE* and EE* vary depending on the isomers. The emission wavelengths for anti2 forms of MA_{EE} and DA_{EE} are in reasonable agreement with the

Table 2.11: Vertical excitation wavelengths (nm) for KK and EE dimers of DH and DA

Molecule	State	KK···KK		EE···EE	
		λ_{abs}	transition	λ_{abs}	transition
DH	S ₁	333	$\pi \rightarrow \pi^*$	351	$\pi \rightarrow \pi^*$
	S ₂	325	$\pi \rightarrow \pi^*$	340	$\pi \rightarrow \pi^*$
	S ₃	318	$\pi \rightarrow \pi^*$	337	$\pi \rightarrow \pi^*$
DA	S ₁	320	$\pi \rightarrow \pi^*$	355	$\pi \rightarrow \pi^*$
	S ₂	319	$\pi \rightarrow \pi^*$	346	$\pi \rightarrow \pi^*$
	S ₃	313	$\pi \rightarrow \pi^*$	339	$\pi \rightarrow \pi^*$

experiments.

Table 2.12: Emission wavelengths (nm) obtained from theory and experiments⁷⁵

Molecule	Isomer	λ_{em}			$\lambda_{\text{em}}^{\text{exp}^a}$
		KK*	KE*	EE*	
DH	anti1	386	535	545	–
	anti2	382	470	518	
	syn	385	644	515	
DM	anti1	385	555	628	No emission
	anti2	381	479	522	
	syn	385	642	569	
MA	anti1	386	543	561	442
	anti2	382	483	457	
	syn	385	542	477	
DA	anti1	386	603	495	560
	anti2	383	532	527	
	syn	385	533	524	

^a Experimental emission maximum.

2.4 Discussion

The experimental study⁷⁵ on DM_{KK}, MA_{KK}, and DA_{KK} revealed that irradiation at 310 nm resulted in the appearance of new absorption peak and an increase in the emission intensity only for DA_{KK} and not for DM_{KK} and MA_{KK}. The present computational study on the photophysics

of DH_{KK} , DM_{KK} , MA_{KK} and DA_{KK} explains the experimental observation. The study reveals that substituent specific red shifted peak seen in absorption and emission spectra of DA is due to the formation of dienol by ESIPT processes. The complete processes involved leading to the formation of dienol is as follows. The synthesized dipyrromethanes (DH, DM, MA, and DA) are expected to exist in three rotameric forms anti1, anti2, and syn in the ground state. Due to low energy separation between them and low energy barriers for conversion between them, isomerization between them is possible as observed in the trajectory simulations. The different KK forms of all the four dipyrromethanes exhibit similar absorption maximum as observed in experiments and calculated λ_{abs} values (~ 300 nm). Now, upon irradiation at 310 nm⁷⁵, the KK forms are excited to higher excited-states. Although the λ_{abs} values of the KK forms of the four molecules are similar, the fate of the excited forms (KK*) are quite different depending on the substituent present in the dipyrromethane. This can be inferred from the fact that upon irradiation of DA_{KK} using 310 nm light source, an additional peak in the absorption spectra at 390 nm and increase in the intensity of the emission maximum are seen in DA_{KK} and not in DM_{KK} , and MA_{KK} . This is also clearly supported by the fact that the energetics of keto-enol tautomerization processes in S_0 and S_1 are similar for DH, DM, and MA, and that for DA they are different. Once DA_{KK} is excited, the excited diketo form KK* can relax back to S_0 or undergo isomerization (cis-trans) or proton transfer (keto-enol tautomerization) processes in the excited-state and then relax to S_0 state. DFT investigation of the ground and excited-state energetics of the different processes and absorption properties shed light on the fate of KK* forms. Absence of the effect of substituents on the calculated λ_{abs} values during cis \rightarrow trans isomerization cannot explain the experimental observations. However, proton transfer processes were found to be influenced by the substituents. While proton transfer can follow a stepwise (KK* \rightarrow KE* \rightarrow EE*) or a concerted path (KK* \rightarrow EE*), high barriers involved in the direct dual proton transfer (KK* \rightarrow EE*) rules out the possibility of a concerted mechanism.

The potential energy profiles for keto-enol tautomerization processes in the ground and

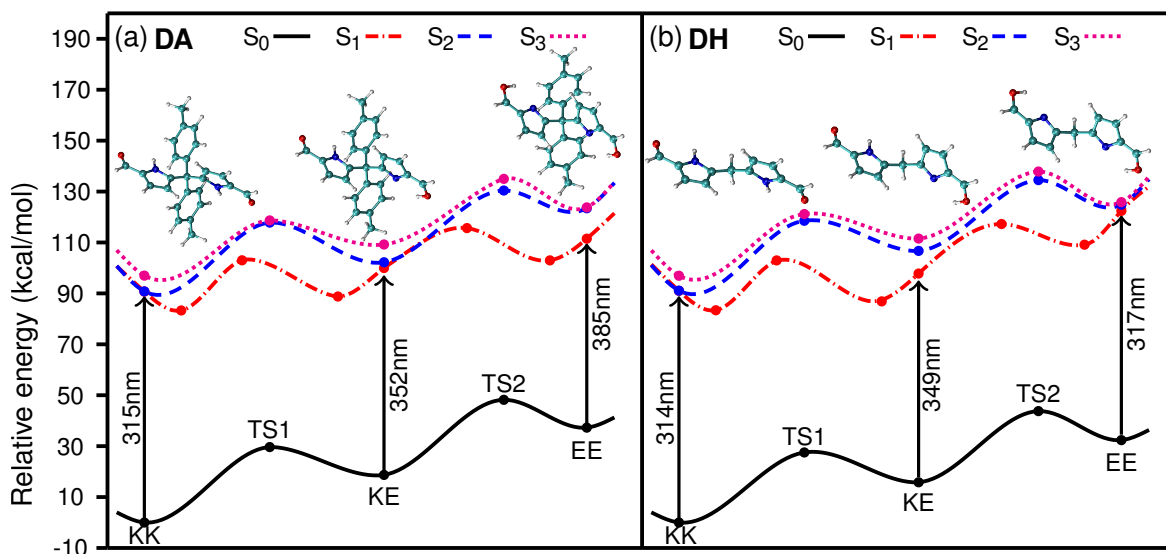


Figure 2.15: Potential energy profile depicting the absorption and keto-enol isomerization processes for anti2 isomers of (a) DA and (b) DH. The dots represent points for which DFT energies were calculated. Dots representing minima/maxima on the potential energy profile of S_0 and S_1 states are stationary points while all other dots represent single point vertical excitation energies from S_0 . The optimized diketo, mono-enol, and dienol structures in S_1 states for DA and DH are shown for clarity.

excited-states for DA and DH are compared in Figure 2.15. ESIPT of KK^* results in KE^* which can undergo another ESIPT process to form EE^* . Now both KE^* and EE^* can relax to S_0 state. Since in the ground state, at equilibrium KK , KE , and EE are expected to coexist, the observed photophysical properties arise due to all the three forms. From the calculated λ_{abs} values, it can be seen that vertical excitation wavelengths of KE and EE forms are red shifted compared to the KK forms. The similar red shifts (78 - 82 nm) seen in λ_{abs} for KE (anti1) forms of all the four molecules, negates the effect of substituents. However, that EE (anti2) forms a large red shift of 90 nm in λ_{abs} seen only for DA in accord with the experiments, explains that the changes seen in the absorption spectrum after irradiation are due to the formation of dienol (DA_{EE}) by ESIPT. The large shift seen in the anti2 form of DA also indicates the importance of the contribution of anti2 form to the absorption spectra of the equilibrium mixture. It should be noted that in the ground state, anti2- KK form is populated more (35%) for DA compared to

DH (4%).

The relevant orbitals involved in the transitions to the excited-states for anti2 forms of DH and DA are shown in Figure 2.11 and 2.12. It can be seen that the $\pi \rightarrow \pi^*$ (S_3) transitions in KK forms of DH and DA involve the pyrrole groups. However, in DH_{EE} and DA_{EE} the nature of the orbitals involved are different. While in DH_{EE} , the $\pi \rightarrow \pi^*$ transition involves orbitals of the pyrrole rings, in DA_{EE} , the $\pi \rightarrow \pi^*$ transition has characteristics of charge transfer nature, involving orbitals of aryl group (π) and pyrrole rings (π^*) illustrating the influence of the aryl groups on the photophysical properties.

2.5 Conclusion

In present study⁷⁶, TDDFT calculated at B3LYP/6-31+G* level of theory were carried out to understand the energy of substituent specific red shift seen in the experimental absorption of 1,9-diformyl-5,5-diaryldipyrromethane (DA_{KK}) upon irradiation. From the simulation results, it was found that DA_{KK} undergoes proton transfer in the excited-state to form dienol (DA_{EE}) that exhibit a large red shifted λ_{abs} compared to DA_{KK} . The red shift in λ_{abs} attributed to charge transfer nature of transitions was seen only for DA_{KK} and not for 1,9-diformyldipyrromethane (DH_{KK}), 1,9-diformyl-5,5-dimethyldipyrromethane (DM_{KK}), and 1,9-diformyl-5-aryldipyrromethane (MA_{KK}) consistent with experimental observations. The calculations also reveal that the proton transfer process follows a step-wise mechanism, i.e. diketo \rightarrow monoenol \rightarrow dienol.

THERMAL DENITROGENATION OF 1-PYRAZOLINE: ENERGETICS

3.1 Introduction

Thermal denitrogenation of 1-pyrazoline gives cyclopropane and olefin.⁹⁰ This reaction has been used in the preparation of cyclopropane derivatives⁹¹ and radical species.^{92,93} It is of fundamental interest to understand the mechanism of the denitrogenation reaction since some substituted pyrazolines give highly stereospecific products while others do not. Several mechanisms have been proposed to explain the stereochemistry of cyclopropane formed from the denitrogenation of 1-pyrazoline. The major single inverted product (cyclopropane) observed in 3,5-dimethyl-1-pyrazoline was explained by conrotatory ring closure of a planar trimethylene diradical.⁹⁰ However, the formation of major single inverted product in the decomposition reaction of exo- and endo-2-methyl-3,4-diazabicyclo[3.3.0]oct-3-enes⁹⁴ and 4-methyl-2,3-diazabicyclo[3.2.0]hept-2-enes⁹⁵ suggested that denitrogenation may not go through a planar intermediate diradical due to the ring strain. It has been proposed that

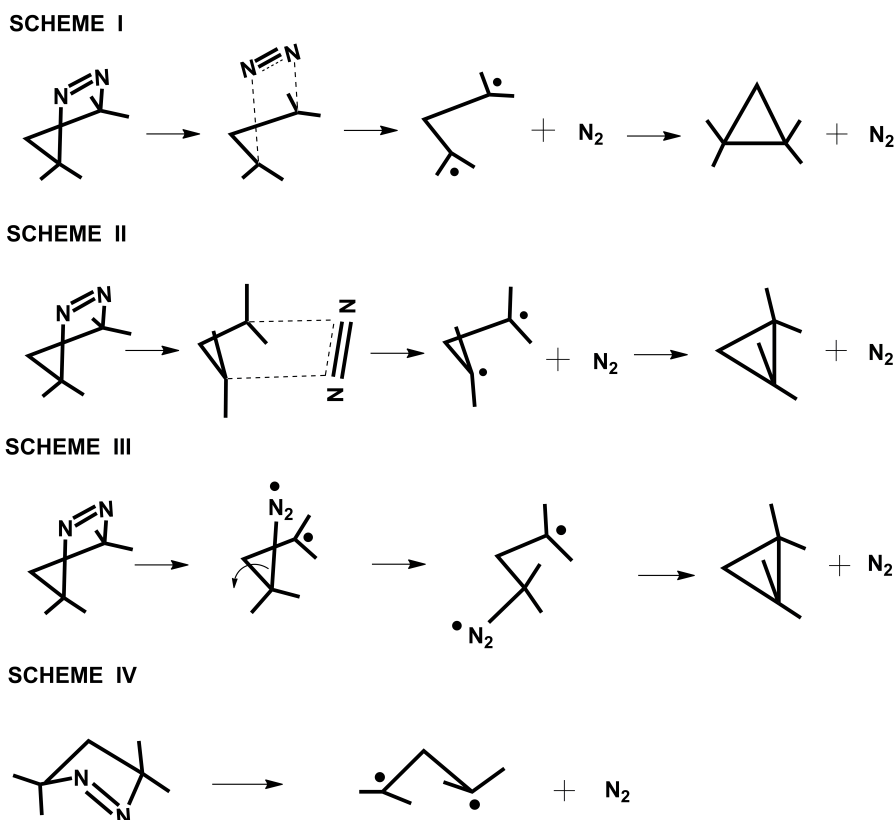


Figure 3.1: Mechanism proposed for the thermal denitrogenation of 1-pyrazoline.⁹⁷

the denitrogenation can happen by a stepwise asynchronous breaking of C–N bonds. Bergman et al⁹⁶ later studied the denitrogenation of *cis* and *trans* forms of 3-ethyl-5-methyl-1-pyrazoline and proposed a non-linear extrusion of N₂ by a pseudo-conrotation of C–C bonds. A detailed *ab initio* study at 3×3 configuration interaction (CI) /STO-3G level of theory was undertaken by Hiberty and Jean⁹⁷. Four paths (Figure 3.1) were investigated: (i) simultaneous breaking of C–N bonds via a planar trimethylene diradical, (ii) simultaneous breaking of C–N bonds via a pyramidal trimethylene diradical, (iii) asynchronous stepwise breaking of C–N bonds via a diazenyl diradical, (iv) non-linear extrusion of N₂ by a pseudo-conrotation of C–C bonds. To explain the experimental observations, they proposed that the low barrier asynchronous path (Scheme III) involving a *trans* or *gauche* diradical would result in a single inverted product.

In contrast, denitrogenation of the bridged bicyclic analogues, 2,3-diazabicyclo[2.2.1]hept-

2-ene(DBH) and 2,3-diazabicyclo[2.2.2]oct-2-ene(DBO) results in major double inverted products.^{98–107} Computational studies at the CASPT2/6-31G* level of theory revealed a synchronous breaking of C–N bonds and the absence of step-wise mechanism in the denitrogenation of DBH.¹⁰³ However, theoretical investigations on a series of substituted DBOs and DBH at UB3LYP/6-31G* and CASPT2 levels of theory suggested the existence of both synchronous and asynchronous mechanisms at high temperature(400-500 K).¹⁰⁴ Denitrogenation of 4-spiro analogous of 1-pyrazoline showed interesting features.^{108–110} Pyrolysis of 4-spirocyclopropane-1-pyrazoline¹⁰⁸ resulted in spiro-pentane while 3-carboalkoxy-substituted 4-spirocyclopropane-1-pyrazoline¹⁰⁹ gave methylenecyclobutane derivatives. However, the percentage of spirocyclopentane product could be increased by adding substituents at C5 in 4-spirocyclopropane-1-pyrazoline.¹¹⁰ DFT calculation at UB3LYP/6-31G* level of theory on 4-spirocyclopropane-1-pyrazoline indicated a concerted cleavage of C–N bonds followed by a conrotatory ring closure as the minimum energy path. However, ab initio classical trajectories showed direct formation of alkylidene cyclobutane in addition to the cyclized product.¹¹⁰ Recently, Izadyar and Harati¹¹¹ reported a DFT study on 1-pyrazoline using B3LYP, MPW1PW91, and PBEPBE functional and 6-311+G(d,p) basis sets and proposed two molecular mechanisms: one that resulted in the cyclopropane formation through a four centered cyclic transition state and another involved a six-centered cyclic TS resulting in propene formation. In addition, a radical mechanism involving trimethylene diradical that resulted in both cyclopropane and propene was proposed.

Thus far ab initio studies to understand the mechanism of predominant single inverted cyclopropane obtained from the thermal denitrogenation of 1-pyrazoline are still inconclusive and need further investigations. Here, we report a detailed investigation on possible mechanisms of denitrogenation of 1-pyrazoline and its substituted analogues using CASSCF method with different active space, CASPT2, DFT, and MP2 methods.¹¹² The role of basis set was examined by computing CASSCF potential energy surface at 6-31+G*, 6-311+G*, cc-pVDZ, aug-cc-

pVDZ, and cc-pVTZ level of theory.¹¹³⁻¹¹⁶

3.2 Methodology

The mechanism for the thermal denitrogenation of 1-pyrazoline was investigated by using Complete Active Space Self-Consistent-Field (CASSCF) method⁴ with 6-31+G* basis set. The CASSCF calculations were performed with (4,4), (6,6), (10,8), (12,10), and (12,12) active spaces. The orbitals used for the different CASSCF calculations are given in Table 3.1 and Figure 3.2. The active space for CASSCF calculations were systematically varied to understand their effect on the calculated reaction pathways. To account for the dynamic electron correlation, single point energy calculations at CASPT2/6-31+G* level of theory¹¹⁷ were performed for the CASSCF(4,4)/6-31+G* geometries. To check the validity of DFT and MP2 methods for this reaction, DFT functionals UB3LYP, UB2PLYP, UM06-2X, and UMP2 method were used to map the potential energy surface for denitrogenation of 1-pyrazoline. All the stationary point structures including transition states(TS) were characterized by computing the harmonic vibrational frequencies. All the transition states and corresponding intermediates they connect were confirmed starting at the TS by following the intrinsic reaction coordinate

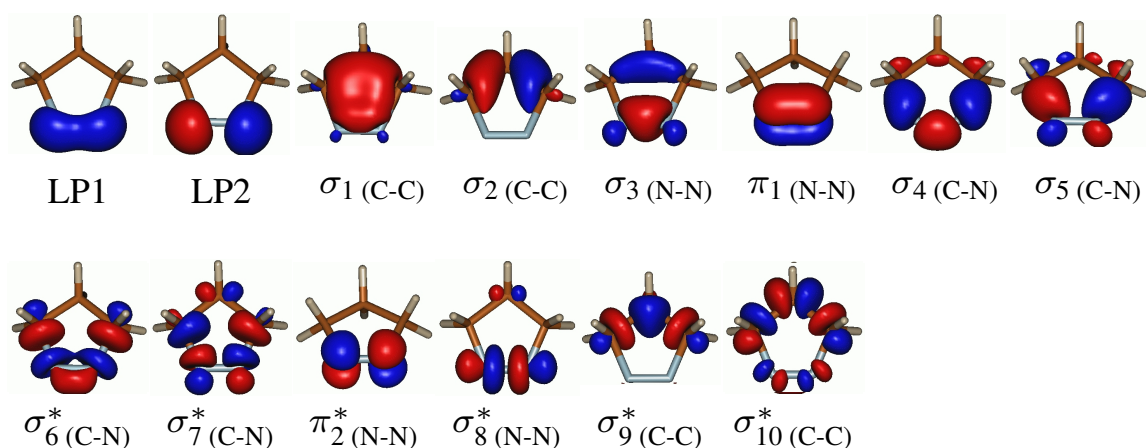


Figure 3.2: Orbitals used in the active space for CASSCF calculations.

Table 3.1: Orbitals used for the different CASSCF calculations

Active space	Orbitals used
CASSCF(4,4)	σ_4 (C-N), σ_5^* (C-N), σ_6 (C-N), σ_7^* (C-N)
CASSCF(6,6)	σ_4 (C-N), σ_5^* (C-N), σ_6 (C-N), σ_7^* (C-N), π_1 (N-N), π_2^* (N-N)
CASSCF(10,8)	σ_4 (C-N), σ_5^* (C-N), σ_6 (C-N), σ_7^* (C-N), π_1 (N-N), π_2^* (N-N), LP1, LP2
CASSCF(12,10)	σ_4 (C-N), σ_5^* (C-N), σ_6 (C-N), σ_7^* (C-N), π_1 (N-N), π_2^* (N-N), σ_3 (N-N), σ_8^* (N-N), LP1, LP2
CASSCF(12,12)	σ_4 (C-N), σ_5^* (C-N), σ_6 (C-N), σ_7^* (C-N), π_1 (N-N), π_2^* (N-N), σ_3 (N-N), σ_8^* (N-N), σ_1 (C-C), σ_2^* (C-C), σ_9 (C-C), σ_{10}^* (C-C)

(IRC). The CASSCF, B3LYP, B2PLYP, and MP2 calculations were performed using Gaussian 09¹¹⁸ and the CASPT2 calculations were done using MOLPRO software¹¹⁹. The numbering scheme for defining geometrical parameters is shown in Figure 3.3. Some of the important geometrical parameters considered are the distances d_1 : C(1)-N(5) and d_2 : C(3)-N(4), angle θ : C(1)-C(2)-C(3), and dihedral angles ϕ_1 : C(1)-C(2)-C(3)-N(4), ϕ_2 : C(2)-C(3)-N(4)-N(5), ϕ_3 : C(3)-C(2)-C(1)-H(6), ϕ_4 : C(3)-C(2)-C(1)-H(10), ϕ_5 : C(1)-C(2)-C(3)-H(7), ϕ_6 : C(1)-C(2)-C(3)-H(8), ϕ_7 : C(2)-C(1)-N(5)-N(4), and ϕ_8 : C(3)-C(2)-C(1)-N(5).

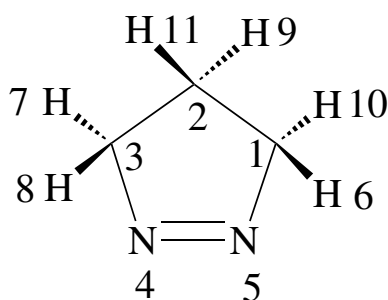


Figure 3.3: Structure of 1-pyrazoline with atom labels and atom numbers used to define geometrical parameters.

3.3 Results and Discussions

The thermal denitrogenation of 1-pyrazoline is expected to follow two types of C–N bond cleavage : (1) synchronous cleavage of the two C–N bonds (2) asynchronous cleavage of the two C–N bonds.

3.3.1 Synchronous Cleavage of the Two C–N Bonds

For the synchronous cleavage of C–N bonds, two reaction pathways as proposed earlier were examined.⁹⁷ The energetics and geometrical parameters of the stationary points along the synchronous denitrogenation path are given in Tables 3.2 and 3.3. The potential energy profiles for the reaction paths are given in Figure 3.4. In the first path, a synchronous cleavage of both C–N bonds results in a planar trimethylene diradical intermediates (**Int1**, propane-1,3-diyl)

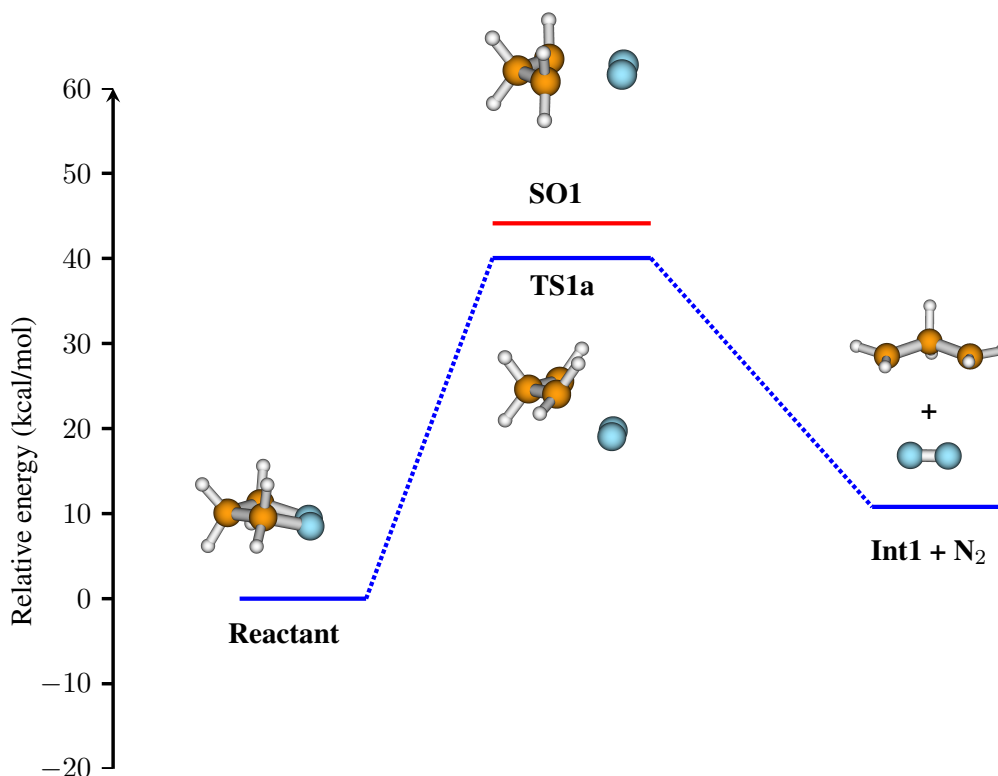


Figure 3.4: Synchronous denitrogenation paths at CASSCF(4,4)/6-31+G* level of theory.

Table 3.2: Relative energies (kcal/mol) for synchronous denitrogenation paths obtained from CASSCF and CASPT2 calculations^a

Structure	CASSCF(4,4)	CASPT2(4,4)// CASSCF(4,4)	CASSCF(6,6)	CASSCF(10,8)	CASSCF(12,10)	CASSCF(12,12)
TS1a	40.04 (34.17)	38.83	34.52 (29.04)	30.72 (25.37)	31.32 (26.01)	36.34 (33.59)
Int1	10.79 (1.0)	35.41	2.21 (-7.41)	0.95 (-8.50)	2.89 (-6.09)	9.55 (1.20)
SO1	44.12 (37.99)	45.22	38.32 (32.56)	34.54 (28.94)	35.29 (29.69)	39.53 (33.99)

^aNumbers in the parentheses are zero point energy corrected values.

through the transition state **TS1a**. In **Int1**, one of the H atoms of the terminal methylene groups are coplanar with the C(1)–C(2)–C(3) plane. **Int1** then closes to cyclopropane via a con or dis rotation of terminal methylene group. The second path is a concerted direct cyclopropane formation involving a simultaneous breaking of the C–N bonds and cyclization of three membered ring. However, this path is feasible only through a second-order saddle point (**SO1**) which is ~ 4 kcal/mol higher in energy than **TS1a**. One imaginary frequency of **SO1** corresponds to symmetric C–N stretching vibration and the other imaginary frequency corresponds to out of plane bending mode. The reactant, **TS1a**, and **Int1** belong to C_s symmetry and **SO1** belongs to C_{2v} point group. The energetics of the paths were found to be quite sensitive to the active space used for the calculations. Increasing the size of active space from (4,4) to (6,6), (10,8), (12,10), and (12,12) caused lowering of the relative energies of **TS1a** and **SO1** by 4-10 kcal/mol. Similarly, the relative energy of **Int1** was lowered by ~ 8 kcal/mol when (6,6), (10,8), and (12,10) active spaces were used. However, **Int1** energy obtained from CASSCF(12,12) is only 1.24 kcal/mol lower than the CASSCF(4,4) energy. The CASPT2(4,4)//CASSCF(4,4) energies for **TS1a** and **SO1** are close to that of CASSCF(4,4) energies. However, CASPT2/6-31+G* level of theory gave a high **Int1** energy of 35.4 kcal/mol, only 3.2 kcal/mol lower than **TS1a**.

It is of interest here to discuss the energetics of the closing of **Int1** to cyclopropane via con or disrotation of the terminal methylene groups^{120–123}. The potential energy profile for closing of **Int1** to cyclopropane via con and disrotation of terminal methylene group obtained at CASSCF(4,4)/6-31+G* level of theory is given in Figure 3.5 and the energetics of stationary

Table 3.3: Geometrical parameters for synchronous denitrogenation path obtained at different CASSCF active space and 6-31+G* basis set

Structure	ϕ_1	ϕ_2	ϕ_3	ϕ_4	ϕ_5	ϕ_6	θ	d_1	d_2
CASSCF(4,4)									
REACTANT	-17.74	12.04	-98.21	136.33	98.21	-136.33	101.59	1.51	1.51
TS1a	-40.78	22.19	-61.98	155.97	61.98	-155.97	113.86	2.08	2.08
TS2	0.00	0.00	-110.11	110.11	110.11	-110.11	118.40	2.10	2.10
Int1	–	–	-27.19	176.04	27.19	-176.04	115.17	–	–
CASSCF(6,6)									
REACTANT	-20.04	13.49	-95.68	138.63	95.68	-138.63	101.68	1.52	1.52
TS1a	-39.81	21.84	-63.72	155.12	63.72	-155.12	113.48	2.05	2.05
TS2	0.00	0.00	-110.11	110.11	110.11	-110.11	117.98	2.07	2.07
Int1	–	–	-27.17	176.09	27.19	-176.04	115.17	–	–
CASSCF(10,8)									
REACTANT	-19.73	13.24	-95.85	138.21	95.85	-138.21	102.04	1.53	1.53
TS1a	-39.71	21.64	-63.66	155.57	63.66	-155.57	114.06	2.05	2.05
TS2	0.00	0.00	-110.10	110.10	110.10	-110.10	118.22	2.08	2.08
Int1	–	–	-27.17	176.09	27.17	-176.09	115.17	–	–
CASSCF(12,10)									
REACTANT	-20.40	13.59	-95.19	138.85	95.19	-138.85	102.38	1.53	1.53
TS1a	-40.16	21.73	-63.11	156.06	63.11	-156.06	114.33	2.06	2.06
TS2	0.00	0.00	-110.08	110.08	110.08	-110.08	118.89	2.09	2.09
Int1	–	–	-27.16	176.09	27.16	-176.09	115.16	–	–
CASSCF(12,12)									
REACTANT	-17.68	12.01	-98.40	136.00	98.40	-136.00	101.24	1.52	1.52
TS1a	-40.71	22.17	-62.12	155.86	62.12	-155.86	113.87	2.08	2.08
TS2	0.00	0.00	-109.82	109.82	109.82	-109.82	118.87	2.11	2.11
Int1	–	–	-25.71	175.53	25.71	-175.53	113.69	–	–

point structures are given in Table 3.4. These calculations were performed by keeping the N atoms at a distance of 10 Å from C(2) atom to maintain consistency of the active space used in other calculations. It can be seen from Figure 3.5 and Table 3.4 that the trimethylene diradical region of potential energy surface is very flat. Several minima corresponding to rotational isomers of **Int1** that differ in the orientation of terminal methylene groups exist on the PES. The relative energies of all the stationary point structures lies within 1.5 kcal/mol. Disrotatory closure of **Int1** via **TS1b** leads to cyclopropane with retention of configuration. Similarly,

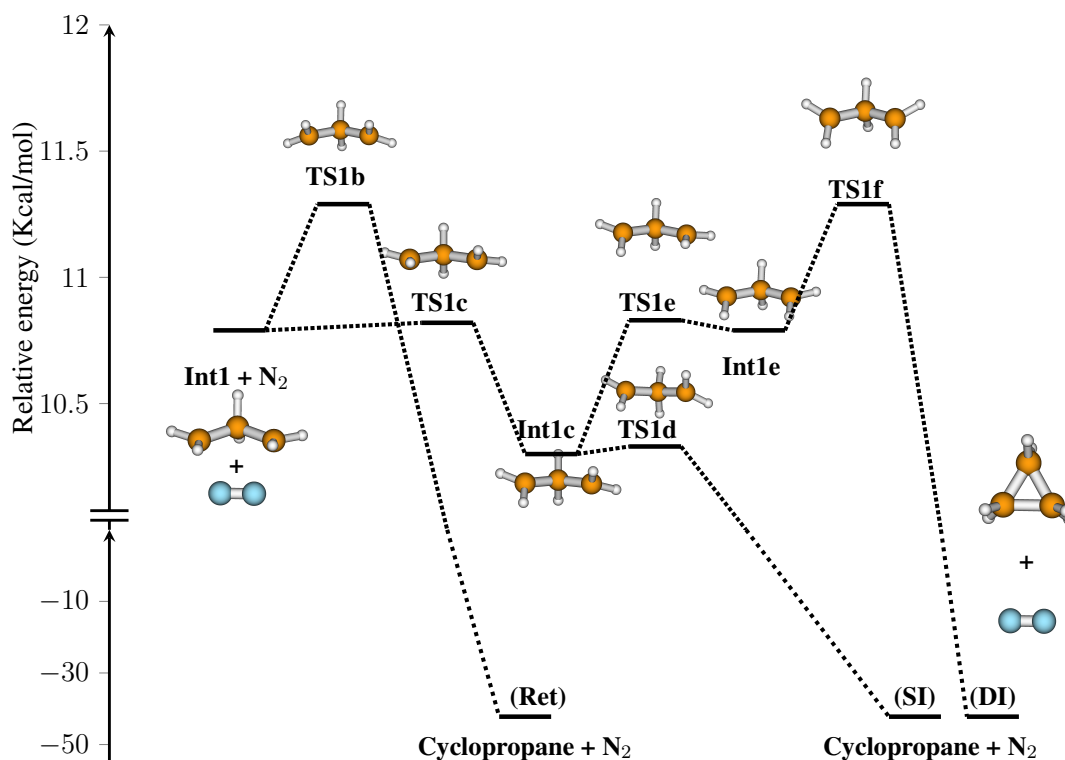


Figure 3.5: Potential energy profile for conrotatory and disrotatory closure of **Int1** to cyclopropane obtained at CASSCF(4,4)/6-31+G* level of theory.

conrotation of terminal methylene groups of **Int1** lead to trimethylene diradical intermediate **Int1c** via the transition state **TS1c**. Further conrotation of terminal methylene group of **Int1c** leads to cyclopropane with single inversion of configuration via the transition state **TS1d**. **Int1c** also leads to trimethylene diradical intermediate **Int1e** via transition state **TS1e**. Now, **Int1e** can close to cyclopropane with double inversion of configuration via disrotation of terminal methylene group. It should be pointed that the cyclopropane thus formed can further

Table 3.4: Relative energies (kcal/mol) of stationary points along conrotatory and disrotatory closure of **Int1** to cyclopropane obtained at CASSCF(4,4)/6-31+G* level of theory

Structure	Int1	TS1b	TS1c	Int1c	TS1d	TS1e	Int1e	TS1f
without ZPE	10.79	11.29	10.82	10.30	10.33	10.83	10.79	11.29
with ZPE	0.99	1.47	0.77	0.70	0.61	0.86	1.08	1.49

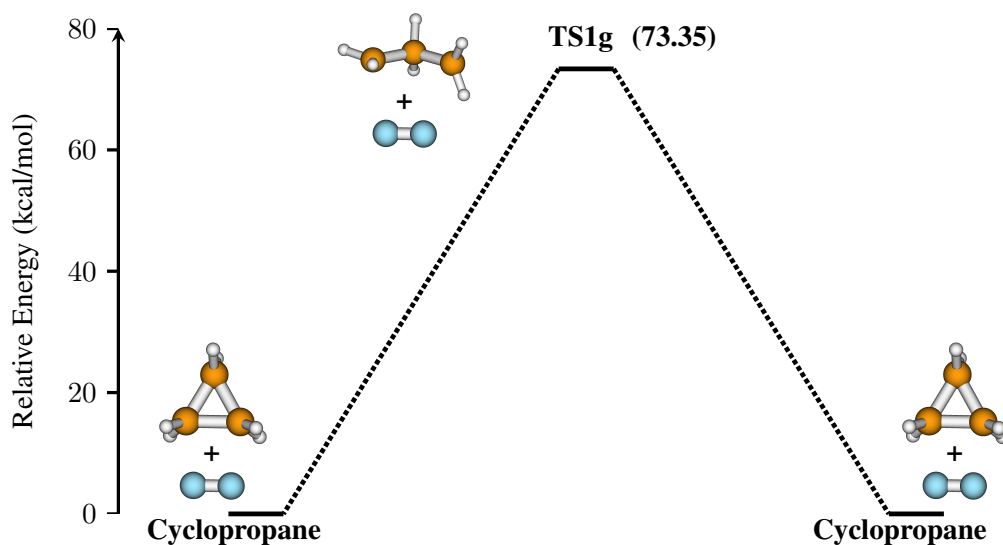


Figure 3.6: Potential energy profile for cis-trans isomerization of cyclopropane via **TS1g**.

undergo ring opening by breaking of one of the C–C bonds and can result in isomerized cyclopropane with single inverted (SI), double inverted (DI), or double retention (Ret) of configurations. The isomerized cyclopropane thus formed is dictated by which of the C–C bonds is/are rotated. Isomerization accompanied by the rotation of C(1)–C(2) or C(2)–C(3) bond involves a transition state (**TS1g**) with a barrier height of 73.35 kcal/mol with respect to cyclopropanes (Figure 3.6). However, this barrier on the complete PES would amount to only 31.14 kcal/mol which is below the energy for **TS1a**.

3.3.2 Asynchronous Cleavage of the C–N bonds

For asynchronous cleavage of the two C–N σ bonds, two different denitrogenation paths were obtained: (1) asynchronous stepwise elimination of N_2 and (2) asynchronous concerted elimination of N_2 .

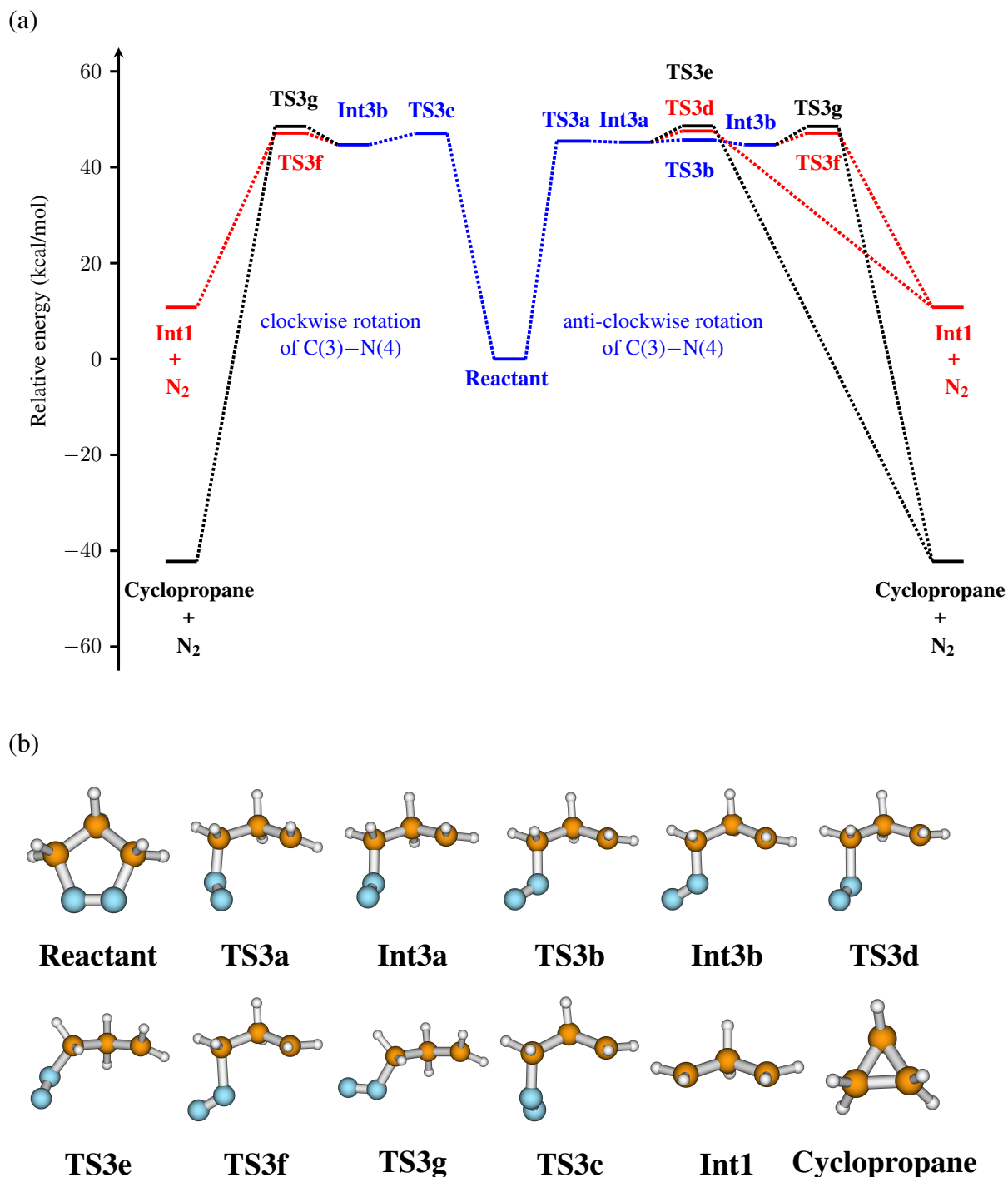


Figure 3.7: (a) Potential energy profile for asynchronous stepwise elimination of N₂ through planar diazenyl intermediates at CASSCF(4,4)/6-31+G* level (b) stationary point structures obtained at CASSCF(4,4)/6-31+G* level.

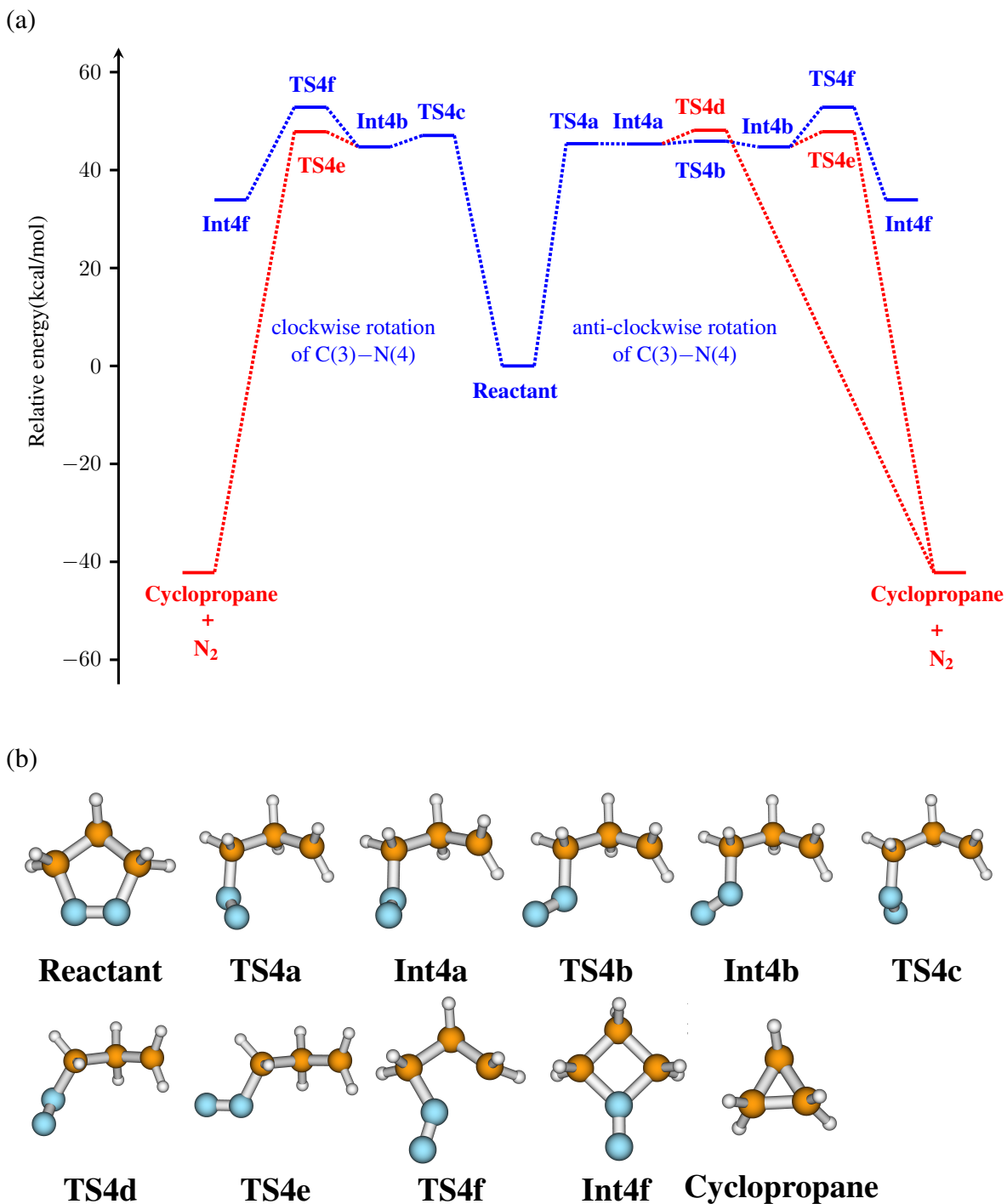


Figure 3.8: (a) Potential energy profile for asynchronous step-wise elimination of N₂ through pyramidal diazenyl intermediates at CASSCF(4,4)/6-31+G* level (b) stationary point structures obtained at CASSCF(4,4)/6-31+G* level.

3.3.2.1 Asynchronous stepwise elimination of N₂

This path involves asynchronous step-wise cleavage of C–N σ bonds leading to diazenyl diradical (**DZ**) intermediates. Here, one of the C–N bonds break first resulting in **DZ**. The asynchronous breaking of a C–N bond can be accomplished by a clockwise or anticlockwise rotation of the one of the C–N bonds contained in dihedral angle ϕ_2 and ϕ_7 . The potential energy surface is symmetrical about the values of ϕ_2 and ϕ_7 . Here the energy profiles (Figures 3.7 and 3.8) obtained at CASSCF(4,4)/6-31+G* level are discussed. Anti-clockwise rotation of C(3)–N(4) bond of the reactant results in **Int3a** through **TS3a**. In **Int3a**, the terminal methylene groups take a nearly planar structure ($\phi_3 \sim -45^\circ$ and $\phi_4 \sim 160^\circ$). For simplicity, this path is noted as path following planar intermediates. Three paths branch out from **Int3a**. In the first path, a direct breaking of the second C–N bond from **Int3a** through **TS3d** gives the diradical **Int1**, that can close by con or dis rotation to give cyclopropane. The second path involves the direct formation of cyclopropane from **Int3a** by a concerted C–N bond cleavage along with ring closure through **TS3e**. In the third path, a further anti-clockwise rotation of C(3)–N(4) bonds converts **Int3a** to a rotational isomer **Int3b** which then can result in a concerted C–N bond cleavage and ring closure (S_H2 type) to form cyclopropane or a simple cleavage of C–N bond giving the diradical **Int1**.

Clockwise rotation of C(3)–N(4) bond can also result in **Int3b** by the breaking of C(1)–N(5) bond. **Int3b** can now result in **Int1** or cyclopropane as discussed above. It should be pointed that a similar S_H2 path was also observed in the photochemical deazetization of DBH.¹²⁴ An anti-clockwise rotation of C(3)–N(4) bond can result in another diazenyl diradical intermediate **Int4a** which is an isomer of **Int3a**. **Int4a** has a pyramidal type methylene group with dihedral angles $\phi_3 \sim -72^\circ$ and $\phi_4 \sim 90^\circ$. Similar to **Int3a**, **Int4a** can directly form cyclopropane via **TS4b**. **Int4a** can also convert to the rotational isomer **Int4b** by **TS4c** which can then give cyclopropane through **TS4d** by S_H2 mechanism. In addition, **Int4b** was also found to isomerize to a four membered cyclic intermediate **Int4f** through a transition state **TS4f**. Cleavage of N₂

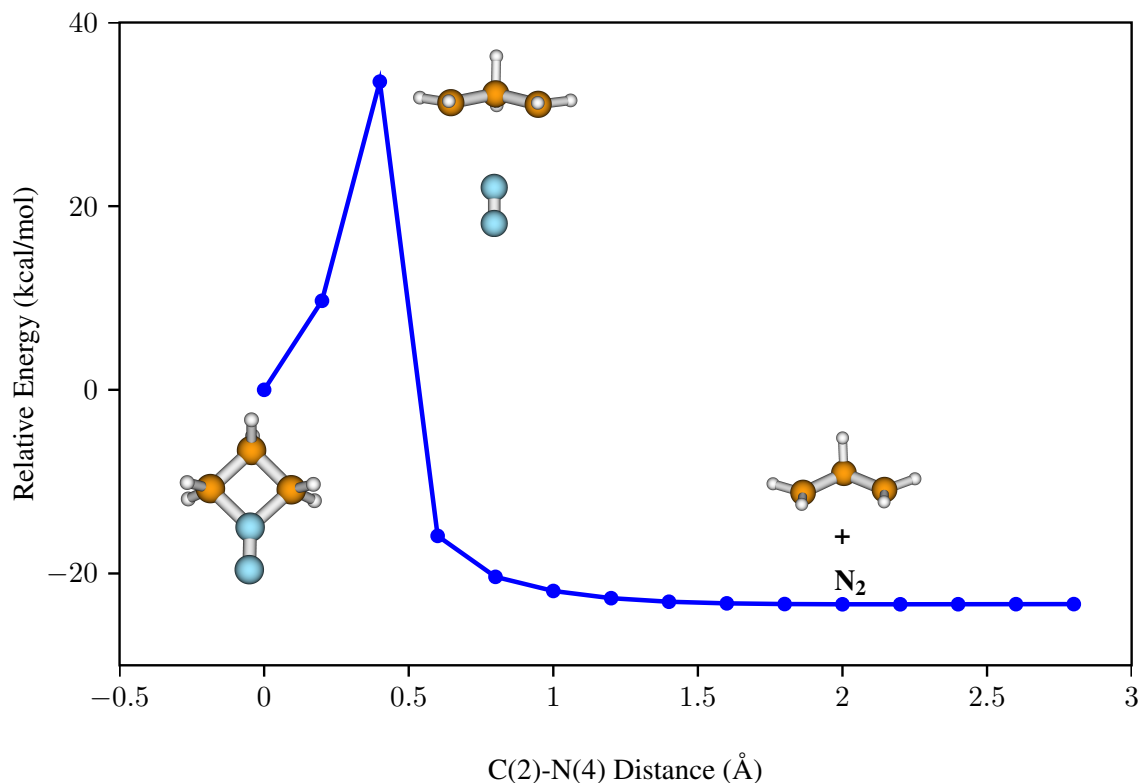


Figure 3.9: Relative energies along constrained geometry optimization path of **Int4f** with fixed C(2)–N(4) distance.

from **Int4f** leads to **Int1**. At CASSCF(4,4)/6-31+G* level, the transition state for this path could not be located. So, to get an insight into the barrier for denitrogenation from **Int4f**, a relaxed PES scan was carried by varying C(2)–N(4) distance (Figure 3.9). The barrier for denitrogenation from **Int4f** was found to be 33.55 kcal/mol.

The energetics and geometrical parameters of stationary points along asynchronous step-wise denitrogenation paths obtained from different CASSCF levels are given in Tables 3.5, 3.6, and 3.7. It can be seen from Table 3.5, that the **DZ** intermediate falls in a very flat region of the potential energy surface. The energies of all the stationary points in this region of PES are within ~ 2 kcal/mol and with the inclusion of zero point energy they further decrease. At CASSCF(4,4)/6-31+G* level, four **DZ** intermediates differing in the orientation of diazenyl (**Int3a**, **Int3b**, **Int4a**, and **Int4b**) are within 1 kcal/mol in energy. The barriers for

their interconversion are also less than 1 kcal/mol. However, at CASPT2(4,4)//CASSCF(4,4) (single point energies), **Int3a** and **Int4a** energies are higher than their respective transition states **TS3a** and **TS4a** and do not appear to be minima.

Unlike synchronous denitrogenation paths, the asynchronous step-wise denitrogenation path is highly dependent on the active space used for the calculations. Some of the stationary points along asynchronous step-wise denitrogenation path obtained at CASSCF(4,4) could not be optimized at higher active space. At CASSCF(6,6), the **DZ** region of PES is described only by the C–N bond breaking coordinate. **DZ** intermediates **Int3a/Int3b** and **Int4a/Int4b** could not be optimized. Optimization of these **DZ** intermediates lead to **Int1**. The transition states **TS3a**, **TS4a**, and **TS4c** were optimized; however, they connect to **Int1** instead of **DZ** intermediates. This is similar to the observation of Carpenter et al¹⁰³ seen in the thermal deazetization of DBH. However, all the four transition states **TS3a**, **TS3c**, **TS4a**, and **TS4c** were obtained at CASSCF(10,8), CASSCF(12,10) and CASSCF(12,12) levels. At these active spaces the flatness **DZ** region of the PES is removed. At CASSCF(10,8) and CASSCF(12,10), **Int3a**, **TS3b**, **Int4a**, **TS4b**, and **Int4b** do not exist. Transition states **TS3a**, **TS3c**, **TS4a**, **TS4c** exist and they connect to **Int3b**. Interestingly, CASSCF(12,12)/6-31+G* level energy profile is comparable with that of CASSCF(4,4)/6-31+G* level. It can be seen that CASSCF(12,12) captures most of the stationary points obtained at the CASSCF(4,4) level except for **Int3a** and **Int4a** and the TSs connected them. **TS3a** is connected to **Int3b** while **TS4a** results in **Int4b**. Similar discrepancies in the nature of the PES for the pyramidalization of alkyl radical center in DBH diazenyl diradical were reported by Olivucci and co-workers¹²⁴ and Khuong and Houk¹⁰⁴ at UB3LYP and CASSCF levels of theory. At UB3LYP level, the alkyl radical center in diazenyl diradical intermediate was planar in nature where as CASSCF method predicted it to be pyramidal. So, Olivucci and co-workers¹²⁴ categorized it to be C_2 -like and C_s -like diazenyl diradicals. However, based on CASPT2 single point energy calculations on CASSCF(4,4) using UB3LYP optimized geometries, Khuong and Houk¹⁰⁴ concluded

Table 3.5: Relative energies (kcal/mol) for asynchronous denitrogenation paths obtained from CASSCF and CASPT2 calculations using 6-31+G* basis set^a

Structure	CASSCF(4,4)	CASPT2	CASSCF(6,6)	CASSCF(10,8)	CASSCF(12,10)	CASSCF(12,12)
Asynchronous step-wise elimination of N₂						
TS3a	45.47 (40.28)	45.25	44.28 (38.62)	39.89 (34.63)	41.11 (35.97)	48.71 (42.48)
Int3a	45.24 (40.24)	45.74				
TS3b	45.72 (40.39)	45.35				
Int3b	44.71 (39.63)	43.72	43.51 (37.68)	38.57 (33.50)	39.81 (34.82)	47.77 (41.34)
TS3c	47.07 (41.85)	46.45		40.65 (35.12)	41.87	49.83 (43.32)
TS3d	47.56 (40.70)	49.75		38.78 (32.70)		
TS3e	48.63 (43.26)	49.47				
TS3f	47.13 (40.32)	48.49				
TS3g	48.51 (43.26)	49.26				39.93 (34.06)
TS4a	45.40 (40.40)	45.06	44.43 (38.75)	40.05 (34.59)	41.30 (35.99)	48.63 (41.92)
Int4a	45.33 (40.33)	45.61				
TS4b	45.90 (40.55)	45.74				
Int4b	44.74 (39.71)	44.00				47.68 (41.47)
TS4c	47.08 (41.90)	46.06	45.73(39.64)	40.80 (35.42)	42.05 (36.77)	49.52 (46.79)
TS4d	48.13 (42.98)	48.30				
TS4e	47.84 (42.72)	48.31			44.41 ^b	50.42 ^b (44.61)
TS4f	52.84 (49.34)	40.57		41.01 (37.51)	42.30 (38.78)	51.86 (48.64)
Int4f	33.92 (32.86)	41.77	38.15	35.70 (34.28)		(32.76)
Asynchronous concerted elimination of N₂						
TS5	48.21 (43.05)	46.37	46.91 ^b (41.76)	41.71 ^b (36.90)	44.55 ^b (40.42)	50.21 ^b (44.36)

^a Numbers in the parentheses are zero point energy corrected values (kcal/mol)^b Structure obtained by constrained geometry optimization by fixing C—N bond length

that C_2 -like and C_s -like geometries of DBH were not different mechanistic entities. In this light, to understand the discrepancies obtained from different CASSCF active spaces on the existence of planar and pyramidal **DZ** intermediates for 1-pyrazoline, CASPT2 single point energy calculations along **Int4b** to **Int3b** conversion pathway were carried out using partially

Table 3.6: Geometrical parameters for asynchronous denitrogenation path (Planar intermediate) obtained at CASSCF(n, m) levels using 6-31+G* basis set

Structure	ϕ_1	ϕ_2	ϕ_3	ϕ_4	ϕ_5	ϕ_6	θ	d_1	d_2
CASSCF(4,4)									
TS3a	-70.28	97.31	-56.83	140.53	173.65	50.38	113.85	3.30	1.54
Int3a	-67.11	125.98	-44.61	157.10	177.43	54.33	113.89	3.63	1.54
TS3b	-61.46	171.17	-46.00	155.03	-179.29	-57.42	113.64	4.02	1.55
Int3b	-59.35	-132.59	-50.74	147.66	179.11	55.60	113.39	4.07	1.53
TS3c	-62.59	-54.36	-46.39	155.20	177.63	55.31	113.99	3.52	1.55
TS3d	-66.14	146.95	-40.09	163.39	-178.83	50.51	114.67	3.90	1.75
TS3e	-123.22	124.94	-51.36	150.77	121.42	-2.51	113.27	4.23	1.54
TS3f	-60.21	-142.12	-42.61	160.63	-177.88	51.03	114.74	4.15	1.75
TS3g	-118.57	-125.68	-52.76	147.29	120.39	-3.61	113.40	4.64	1.54
CASSCF(10,8)									
TS3a	-68.39	113.89	-49.96	151.30	176.13	51.09	114.23	3.41	1.59
Int3b	-54.38	-141.49	-51.01	150.91	-174.73	59.29	112.86	4.03	1.59
TS3c	-63.02	-53.38	-47.86	154.32	178.65	53.76	114.30	3.54	1.61
TS3f	-54.69	-145.66	-46.84	157.32	-173.37	57.31	113.75	4.06	1.68
TS3g	-119.43	-128.96	-52.58	148.04	119.92	-4.15	113.44	4.69	1.55
CASSCF(12,10)									
TS3a	-68.61	103.98	-49.81	151.63	176.13	50.79	114.24	3.43	1.60
Int3b	-57.29	-135.38	-51.58	147.93	-178.41	57.23	112.98	4.08	1.57
TS3c	-63.05	-53.80	-46.93	155.53	178.78	53.44	114.34	3.56	1.63
TS3f	-54.51	-145.12	-47.22	156.90	-173.30	57.56	113.68	4.08	1.68
TS3g	-122.00	-129.22	-54.05	146.79	117.74	-7.06	113.58	4.71	1.54
CASSCF(12,12)									
TS3a	-68.61	103.98	-49.81	151.63	176.13	50.79	114.24	3.43	1.60
Int3b	-57.29	-135.38	-51.58	147.93	-178.41	57.23	112.98	4.08	1.57
TS3c	-63.05	-53.80	-46.93	155.53	178.78	53.44	114.34	3.56	1.63
TS3f	-54.51	-145.12	-47.22	156.90	-173.30	57.56	113.68	4.08	1.68
TS3g	-122.00	-129.22	-54.05	146.79	117.74	-7.06	113.58	4.71	1.54

Table 3.7: Geometrical parameters for asynchronous denitrogenation path (Pyramidal intermediate) obtained at CASSCF(n, m) levels using 6-31+G* basis set

Structure	ϕ_1	ϕ_2	ϕ_3	ϕ_4	ϕ_5	ϕ_6	θ	d_1	d_2
CASSCF(4,4)									
TS4a	-69.65	99.58	-71.50	93.61	174.30	51.06	114.26	3.33	1.53
Int4a	-68.05	119.85	-72.29	90.29	176.47	53.30	114.33	3.58	1.53
TS4b	-63.16	171.47	-67.29	95.85	178.99	55.84	114.11	4.05	1.54
Int4b	-59.95	-131.51	-61.76	103.01	178.41	55.01	113.76	4.09	1.53
TS4c	-63.70	-53.69	-73.05	89.32	176.63	54.29	114.56	3.53	1.54
TS4d	-118.64	124.21	-81.26	78.37	126.03	1.99	113.13	4.18	1.55
TS4e	-113.04	-128.99	-77.59	80.17	125.99	1.83	113.08	4.62	1.55
TS4f	-19.86	162.84	-86.75	127.55	-138.01	91.83	101.36	3.09	1.52
Int4f	0.00	180.00	-113.27	113.28	113.27	-113.28	90.62	2.50	1.52
CASSCF(10,8)									
TS4a	-64.79	152.46	-67.32	96.61	179.29	54.36	114.31	3.95	1.59
Int3b	-54.39	-141.02	-50.82	151.14	-174.75	59.30	112.87	4.03	1.59
TS4c	-64.67	-53.70	-69.77	94.99	176.75	52.48	114.77	3.57	1.59
TS4f	-21.87	162.87	-83.95	131.88	-139.85	88.93	102.80	3.17	1.55
Int4f	0.00	180.00	-112.64	112.61	112.64	-112.61	92.37	2.55	1.57
CASSCF(12,10)									
TS4a	-65.44	150.49	-71.21	91.07	179.11	54.01	114.29	3.95	1.59
Int3b	-55.13	-137.82	-56.97	142.26	-175.36	57.77	113.05	4.05	1.61
TS4c	-64.89	-54.13	-69.60	95.16	176.67	51.97	114.79	3.59	1.60
TS4e	-113.59	-130.89	-79.02	78.91	125.09	2.11	113.28	4.66	1.52
TS4f	-22.19	-162.63	-83.35	132.47	-140.16	88.42	103.09	3.19	1.56
CASSCF(12,12)									
TS4a	-64.61	161.09	-70.91	95.13	179.71	53.96	114.08	4.05	1.61
Int4b	-59.14	-132.70	-63.96	105.63	-179.98	54.37	113.55	4.15	1.59
TS4c	-64.48	-52.66	-73.76	92.93	177.30	51.71	114.48	3.58	1.63
TS4e	-110.34	-127.78	-78.25	82.01	128.52	4.30	112.41	4.65	1.55
TS4f	-17.61	-164.37	-90.39	125.67	-135.52	94.31	100.97	3.14	1.51

optimized geometries obtained at the CASSCF(4,4)/6-31+G* level of for various values of ϕ_4 . The relative energies along **Int4b** to **Int3b** conversion pathway obtained at CASSCF(4,4)/6-31+G* and CASPT2(4,4)//CASSCF(4,4) levels are given in Figure 3.10. It can be seen that at the CASPT2(4,4)//CASSCF(4,4) level, only one minimum whose angle is intermediate

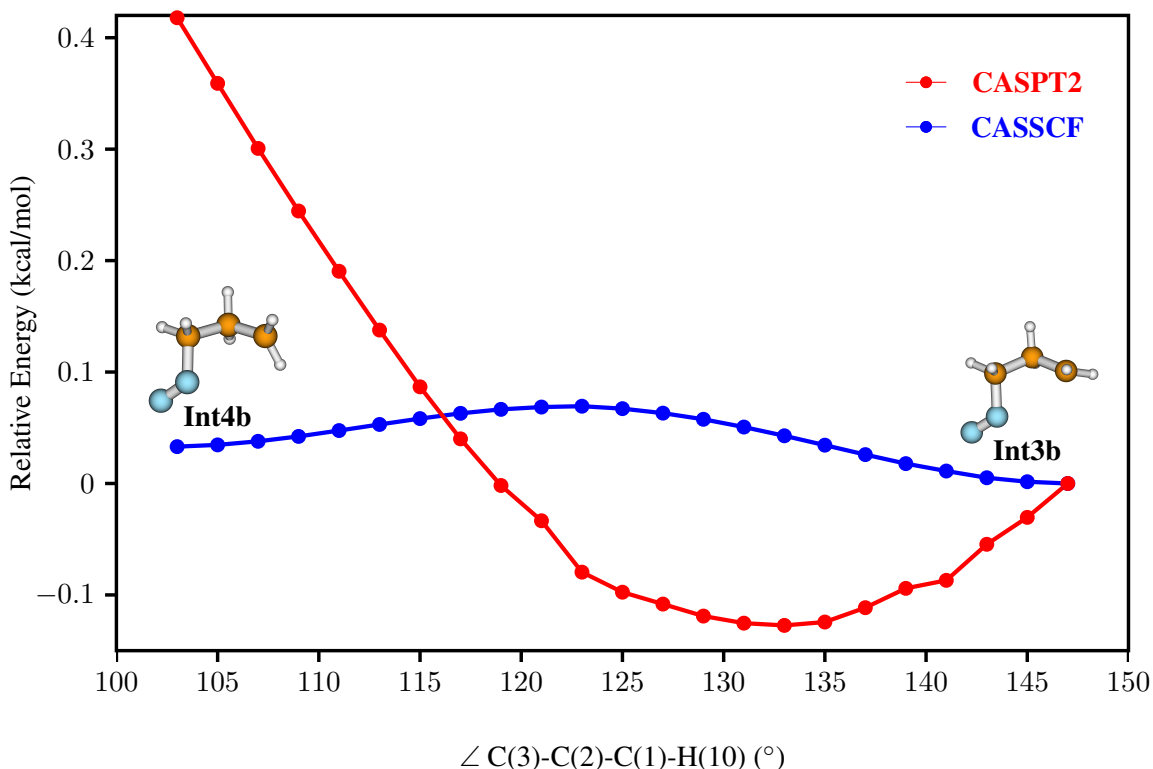


Figure 3.10: Relative energies of diazenyl diradical intermediate along the **Int4b** to **Int3b** path obtained at CASSCF(4,4) and CASPT2(4,4)//CASSCF(4,4) levels using 6-31+G* basis set.

between planar and pyramidal angles ($\phi_3 = -55.94$, $\phi_4 = 131.66$) was found to exist.

3.3.3 Asynchronous concerted elimination of N_2

This path involves a concerted asynchronous cleavage of one of the C–N σ bonds with simultaneous displacement of N_2 through a diazenyl diradical transition state **TS5** by S_H2 like mechanism. It leads to a single inverted cyclopropane formation with the elimination of N_2 . The energy profile for this path obtained at the CASSCF(4,4)/6-31+G* level is shown in Figure 3.11. The transition state (**TS5**) for this path could be optimized only at CASSCF(4,4) level. At higher active spaces (CASSCF(6,6), CASSCF(10,8), CASSCF(12,10), and CASSCF(12,12)) search for the transition state **TS5** resulted in **TS1a**. So at higher active spaces, the transition state for this path was obtained by constrained geometry optimization by fixing C(3)–N(4)

bond length. The relative energy barriers obtained using different CASSCF active spaces for the asynchronous concerted denitrogenation path are given in Table 3.5. The barrier for this path is about 48 kcal/mol at the CASSCF(4,4)/6-31+G* level.

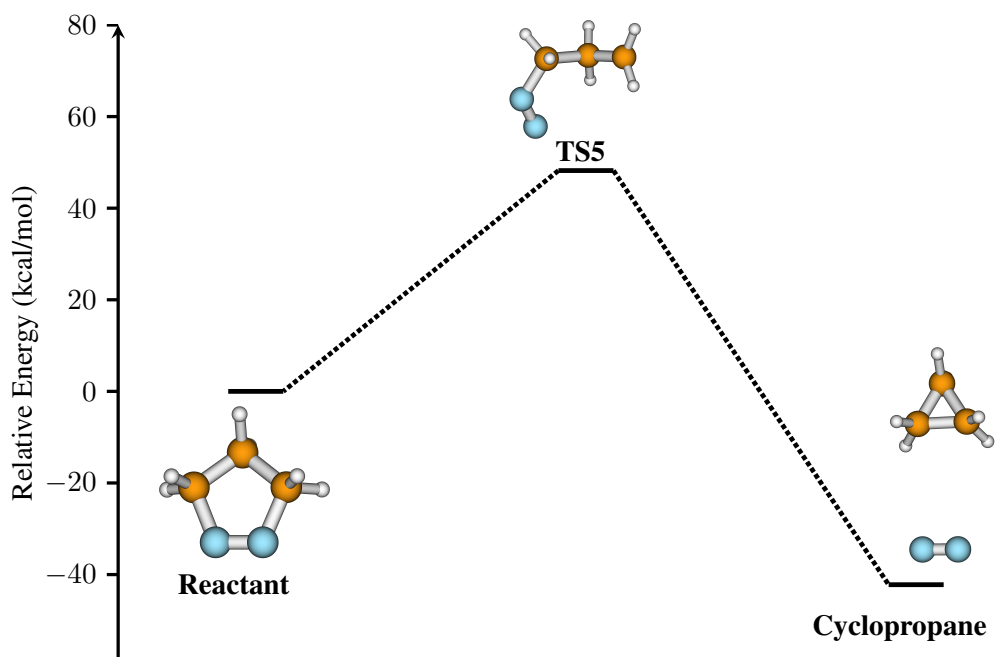


Figure 3.11: Energy profile for the asynchronous concerted denitrogenation path at CASSCF(4,4)/6-31+G* level.

3.3.4 Alkene formation

The thermal denitrogenation of 1-pyrazoline can also result in propene. Alkene formation is possible from **Int1** and cyclopropane and the two pathways for propene formation were obtained at CASSCF(4,4)/6-31+G* level of theory. A schematic representation of the two pathways are given in Figure 3.12. Path 1 is a [1,2] or [2,3]-shift involving a H-transfer from the central carbon atoms of **Int1** to one of the terminal carbon atom leading to the formation of propene. In path 2, ring opening of cyclopropane followed by a [1,3]-shift, involving a H-transfer from one of the terminal carbon atoms to the other terminal carbon atom, results in formation of a carbene. Then a second H-transfer ([1,2] or [2,3] shift) from the central carbon

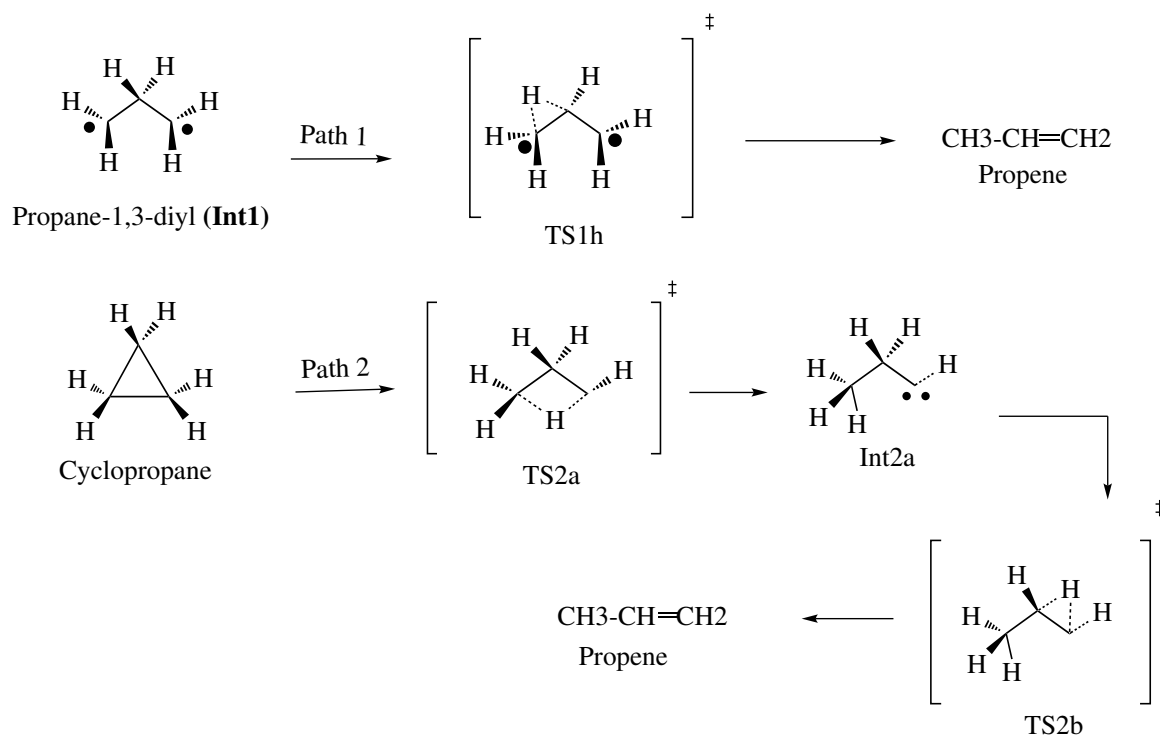


Figure 3.12: A schematic representation of the two different paths that lead to formation of propene.

atom to the carbene carbon atom leads to propene formation. Since both the pathways for propene formation involve H-transfer, the potential energy profiles for propene formation were mapped using two different active spaces: CASSCF(4,4) and CASSCF(6,6) to see the effect of active spaces. Here, the CASSCF(4,4) active space includes two p -type orbitals of methylenic C atoms and π , π^* orbitals of N_2 bond and in CASSCF(6,6), the σ , σ^* orbitals of C–H bond

Table 3.8: Relative energies (kcal/mol) of stationary point structures obtained for the propene formation pathways at CASSCF(4,4)/6-31+G* and CASSCF(6,6)/6-31+G* levels of theory^a

Method	TS1h ^b	TS2a ^c	Int2a ^c	TS2b ^c
CASSCF(4,4)	20.25 (19.49)	76.97 (73.68)	60.31 (57.00)	70.97 (66.49)
CASSCF(6,6)	17.50 (16.48)	77.33 (74.15)	61.96 (58.61)	70.30 (65.88)

^aNumbers in the parentheses are zero point energy corrected values.

^bRelative energy of **TS1h** was calculated with respect to **Int1** energy.

^cRelative energies of **TS2a**, **Int2a**, and **TS2b** were calculated with respect to cyclopropane.

involved in H-transfer were also included in the active space in addition to the orbitals used for CASSCF(4,4) active space. The energetics of stationary point structures obtained for propene formation are given in Table 3.8. At CASSCF(4,4)/6-31+G* level of theory, the barrier for propene formation via path 1 was found to be ~ 20 kcal/mol with respect to **Int1**. This barrier decreases by ~ 3 kcal/mol at CASSCF(6,6)/6-31+G* level of theory. The barrier for propene formation via path 2 was found to be very high. The barrier for [1,3]-hydrogen shift was found to be 76.97 kcal/mol. The resulting carbene lies 60.31 kcal/mol above cyclopropane. The barrier for formation of propene from the carbene intermediate was found to be 10.7 kcal/mol. The energetics of propene formation via path 2 was also found to be stabilized by ~ 3 kcal/mol when CASSCF(6,6) active space was used for the calculations.

3.3.5 Effect of Basis sets

The effect of basis sets was investigated by optimizing all the stationary points along synchronous and asynchronous denitrogenation paths obtained at CASSCF(4,4)/6-31+G* level of theory with 6-31+G*, cc-pVDZ, aug-cc-pVDZ, and cc-pVTZ basis sets and the results are given in Table 3.9. Increasing the basis set from 6-31+G* to 6-311+G* results in lowering of relative energies by ~ 1 kcal/mol. Changing the basis set to correlation consistent basis sets cc-pVDZ, aug-cc-pVDZ, and cc-pVTZ results in a deviation less than 2 kcal/mol. However, at 6-31+G* and 6-311+G* basis sets, the reactant was found to have C_S symmetry but at cc-pVDZ, aug-cc-pVDZ and cc-pVTZ it has C_1 symmetry.

3.3.6 DFT and MP2 methods

To check the validity of DFT and MP2 methods for denitrogenation of 1-pyrazoline, DFT functionals such as B3LYP, B2PLYP, M06-2X, and MP2 methods with 6-31+G* and cc-pVTZ basis sets were used to map the potential energy profile. The results are given in Figures 3.13-3.15. For the synchronous denitrogenation path, the transition states **TS1a** and the second order sad-

dle point **SO1** were obtained with all the DFT functionals (B3LYP, B2PLYP, M06-2X) and MP2 methods. The relative energy barrier for synchronous denitrogenation path (**TS1a**) obtained from these methods are comparable with the CASSCF(4,4) and CASPT2(4,4)//CASSCF(4,4) energies. However, for DFT functionals, IRC calculation from transition state **TS1a** connects to propene instead of **Int1**. In addition, the trimethylene diradical intermediate (**Int1**) could not be optimized with all these DFT functionals. However, **Int1** was obtained with MP2 method, and its energy was found to be very high, 34 kcal/mol above the reactant similar to that obtained at CASPT2(4,4)//CASSCF(4,4) level. Similarly, all the stationary points along asynchronous step-wise denitrogenation path obtained at CASSCF method could not be optimized with DFT and MP2 methods. Using B3LYP and M06-2X functionals, only **TS3c** was obtained. With B2PLYP

Table 3.9: Energetics of denitrogenation of 1-pyrazoline at CASSCF(4,4) with different basis sets

Structure	6-31+G*	6-311+G*	cc-pVDZ	aug-cc-pVDZ	cc-pVTZ
TS1	34.16	33.59	32.30	34.14	33.09
Int1	0.99	-0.61	-0.80	1.10	-1.79
TS3a	40.28	39.90	39.75	40.72	40.21
Int3a	40.23	39.77	39.63	40.61	40.10
TS3b	40.39	39.88	39.83	40.66	40.20
Int3b	39.63	39.16	39.08	39.94	39.46
TS3c	41.84	41.33	41.12	42.09	41.58
TS3d	40.69	39.94	39.78		
TS3e	43.49	43.09	43.07	43.90	43.36
TS3f	40.31	39.51	39.35	40.39	39.60
TS3g	43.33	42.88	42.90	43.64	43.14
TS4a	40.30	39.91	39.79	40.75	40.24
Int4a	40.32	39.26	39.83	40.79	40.29
TS4b	40.55	40.11	40.15	40.87	40.43
Int4b	39.70	39.26	39.25	39.93	39.48
TS4c	41.90	41.44	41.25	42.19	41.70
TS4d	42.98	42.53	42.54	43.39	42.83
TS4e	42.71	42.24	42.29	43.07	42.53
TS4f	49.33	48.65	49.17	50.30	49.13
Int4f	33.91	33.65	34.66	34.58	33.96
TS5	48.21	47.77	47.45	48.44	47.90

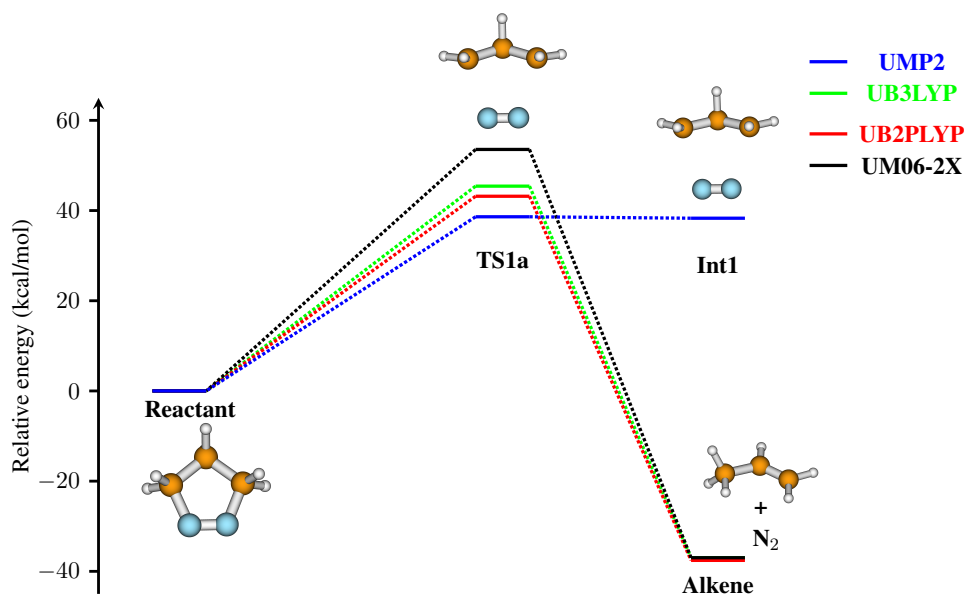


Figure 3.13: Synchronous denitrogenation paths obtained using DFT and MP2 methods.

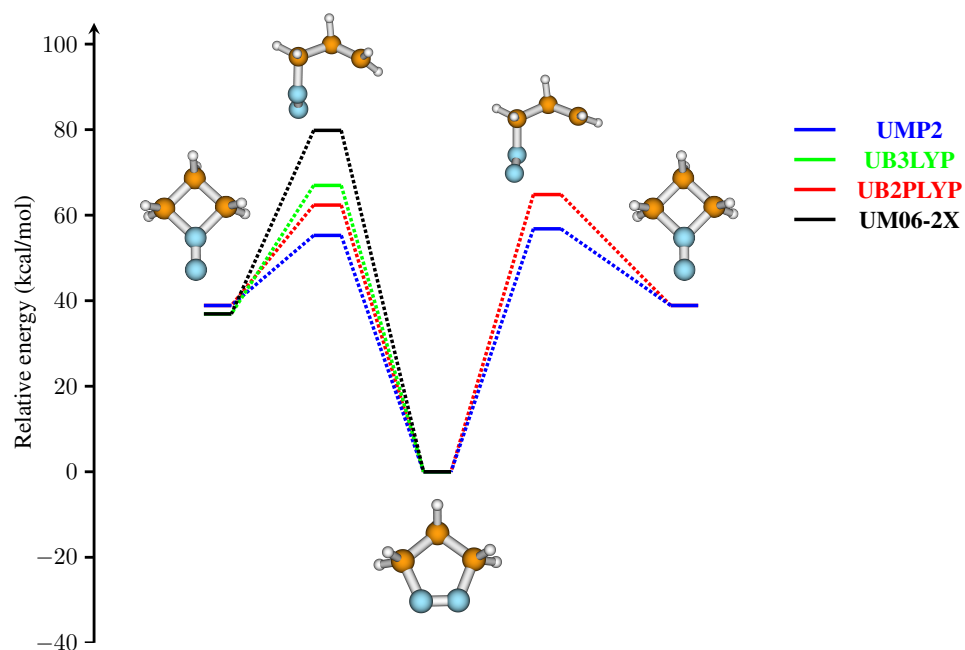


Figure 3.14: Asynchronous step-wise denitrogenation paths obtained using DFT and MP2 methods.

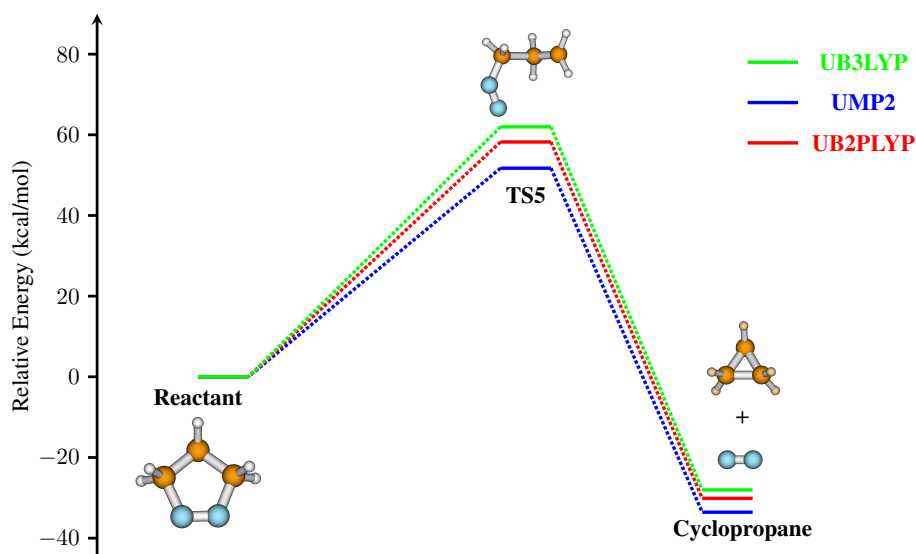


Figure 3.15: Asynchronous concerted denitrogenation paths obtained using DFT and MP2 methods.

method, **TS3a** and **TS4c** were obtained, and at MP2, only **TS4a** and **TS4c** were optimized. IRC calculations from all these transition states lead to **Int4f** instead of **DZ** intermediates (**Int3a/Int3b** or **Int4a/Int4b**). Interestingly, the transition state for asynchronous concerted denitrogenation path which was obtained only at the CASSCF(4,4) level could be optimized with DFT and MP2 methods. The barrier energies obtained for this path were similar to that obtained at CASSCF(4,4) level. The relative energies of stationary points along synchronous and asynchronous denitrogenation paths obtained at DFT and MP2 methods are given in Table 3.10. Thus, it can be seen that for the thermal denitrogenation of 1-pyrazoline, B3LYP and MP2 methods are not reliable as the reaction paths obtained using this methods are very different from that obtained using CASSCF and CASPT2 methods and cannot explain the observed products.

Table 3.10: Relative energies (kcal/mol) of stationary point structures obtained for the denitrogenation pathways obtained at the MP2, B2PLYP, and B3LYP levels of theory

Structure	MP2 6-31+g*	MP2 cc-pVTZ	B2PLYP 6-31+G*	B2PLYP cc-pVTZ	B3LYP 6-31+G*	B3LYP cc-pVTZ
(i) Synchronous elimination of N₂						
TS1a	41.70	38.62	47.80	43.17	50.25	45.40
Int1	41.43	38.30				
SO1	51.75	49.05	57.94	54.05		56.62
(ii) Asynchronous step-wise elimination of N₂						
TS3a			65.62	49.73		
TS3c						
TS4a	57.14	53.55				
TS4c	55.41	51.91	63.26	62.36	68.74	81.20
Int4b		45.43				
TS4d		47.40				
TS4e		49.99				
Int4f	43.03		38.25	38.88	36.57	36.91
(iii) Asynchronous concerted elimination of N₂						
TS5	52.60	51.72	59.78	58.23	64.26	61.97

3.4 Discussion and Conclusion

The potential energy profile for the thermal denitrogenation of 1-pyrazoline was mapped using CASSCF, CASPT2, DFT, and MP2 methods.¹¹² CASSCF calculations were performed with (4,4), (6,6), (10,8), (12,10), and (12,12) active spaces and CASPT2(4,4)//CASSCF(4,4) single point energy calculations were performed for the CASSCF(4,4) optimized geometries. Two possible denitrogenation paths were considered in this study: (1) synchronous denitrogenation path and (2) asynchronous denitrogenation path. For all the different CASSCF and CASPT2 calculations, the synchronous denitrogenation path was 6-10 kcal/mol lower in energy than the asynchronous paths which is in contrast to the previous report⁹⁷ where asynchronous denitrogenation paths were found to be more favourable. It was observed that the energetics of denitrogenation paths were highly sensitive to the active space used for the calculations. The relative energies of the stationary point structures decrease with the increase in active space

from (4,4) to (6,6), (10,8), and (12,10). However, the energetics obtained at CASSCF(12,12) and CASPT2(4,4)//CASSCF(4,4) is closer to that obtained at CASSCF(4,4)/6-31+G* level of theory. For the synchronous denitrogenation path, all the stationary point structures obtained at CASSCF(4,4)/6-31+G* level of theory could be optimized with the higher CASSCF active space used for the calculations. However, for the asynchronous denitrogenation paths, many stationary point structures at the flat diazenyl diradical region of the PES could not be optimized with CASSCF(10,8), CASSCF(6,6), CASSCF(12,10) and CASSCF(12,12) active spaces. The effect of basis set on the energetics of denitrogenation paths were examined by mapping the potential energy profile using CASSCF(4,4) active space and 6-31+G*, 6-311+G*, cc-pVDZ, aug-cc-pVDZ, and cc-pVTZ basis sets. It was observed that, with the increase in basis set from 6-31+G* to 6-311+G* results in lowering of relative energies by ~ 1 kcal/mol. Similarly, changing to correlation consistent basis sets cc-pVDZ, aug-cc-pVDZ, and cc-pVTZ results in a deviation less than 2 kcal/mol. To check the validity of DFT and MP2 method for this reaction, MP2 and DFT functionals such as B3LYP, B2PLYP, and M06-2X were used to map the potential energy profile. However, DFT and MP2 methods failed to provide an accurate description of potential energy profile in the diradical region.

For the different CASSCF calculations, synchronous denitrogenation path was lower in energy than the asynchronous paths. The barrier for synchronous denitrogenation path (40.04 kcal/mol) obtained at CASSCF(4,4)/6-31+G* level of theory agrees well with the experimental activation barrier of 42.4 kcal/mol for thermal denitrogenation of 1-pyrazoline. Synchronous denitrogenation of 1-pyrazoline leads to trimethylene diradical intermediate **Int1** which can close to cyclopropane via con/dis rotation of terminal methylene group or it can lead to propene via proton transfer. Conrotatory closure of terminal methylene group of **Int1** leads to cyclopropane with single inversion of stereochemistry whereas dis rotatory closure leads to cyclopropane with retention or double inversion of stereochemistry. The barrier for con and dis rotation is within ~ 1.5 kcal/mol. If reaction is to follow MEP, than a racemic mixture of

cyclopropane is expected. So, from the potential energy surface alone, the major single inverted cyclopropane obtained from the thermal denitrogenation of 1-pyrazoline could not be explained. Dynamics calculations are necessary to understand the experimental observation for thermal denitrogenation of 1-pyrazolines.

THERMAL DENITROGENATION OF 1-PYRAZOLINE: DYNAMICS

4.1 Introduction

Thermal denitrogenation of cis- and trans-3,5-dimethyl-1-pyrazoline in the gas phase resulted in trans- and cis-1,2-dimethylcyclopropane as the major product respectively.⁹⁰ Similarly a predominant single inversion of configuration was observed for the thermal decomposition of exo- and endo-2-methyl-3,4-diazabicyclo[3.3.0]oct-3-enes.⁹⁴ To understand this stereochemical preference in the product formation during the thermal denitrogenation processes, the potential energy profiles for different paths were mapped for 1-pyrazoline and the results were discussed in Chapter 3. It was observed that at CASSCF and CASPT2 level of theory, the barrier for synchronous denitrogenation path was 6-8 kcal/mol lower in energy than the asynchronous paths. Synchronous denitrogenation of 1-pyrazoline leads to trimethylene diradical intermediate (**Int1**). **Int1** can close to cyclopropane via con or dis rotation of terminal methylene group. Conrotatory closure of terminal methylene group of **Int1** leads to cyclopropane with single inversion of stereochemistry whereas disrotatory

closure of terminal methylene group leads to cyclopropane with retention or double inversion of stereochemistry. The barrier for closing of **Int1** to cyclopropane via con and dis rotation is within 1 kcal/mol. So it is clear that the experimentally observed stereochemical preference in cyclopropane formation can not be explained following the energetics of the reaction alone. There are several reports in literature on the denitrogenation of azoalkanes where potential energy profiles failed to explain the experimentally observed product selectivity.^{103,109,110,124} In such cases, dynamics simulations were necessary to understand the experimental observations.

In the thermal denitrogenation of 4-spirocyclopropane-1-pyrazoline and 3-carboalkoxy-substituted 4-spirocyclopropane-1-pyrazoline, spiro-pentane and methylenecyclobutane derivatives were observed as the major products respectively.^{109,110} However, DFT calculation at UB3LYP/6-31G* level of theory for both the molecules indicated a concerted cleavage of both the C–N bonds to diradical followed by a conrotatory ring closure to spiro-pentane as the lower energy path. So to understand the major formation of methylenecyclobutane derivatives instead of spiro-pentane from the denitrogenation of 3-carboalkoxy-substituted 4-spirocyclopropane-1-pyrazoline, Born-Oppenheimer molecular dynamics (BOMD) simulations were carried out from the synchronous transition state. Although the energy minimum pathway from the synchronous transition state involves generation of 2-spirocyclopropyl-1,3-diyl diradical, chemical dynamics simulation showed direct formation of methylenecyclobutane derivatives from the synchronous transition state along with the diradical intermediate consistent with the experimental observations. Similarly, thermal and photochemical denitrogenation of 2,3-diazabicyclo[2.2.1]hept-2-ene-exo,exo-5,6-*d*₂ (DBH-*d*₂) result in inverted bicyclo[2.1.0]pentane as the major product.^{125,126} Computational studies¹⁰³ at CASSCF and CASPT2 levels of theory with 6-31G* basis set for thermal denitrogenation of DBH revealed synchronous breaking of C–N bond leading to cyclopentane-1,3-diyl diradical to be energy minimum pathway. The formation of inverted bicyclo[2.1.0]pentanes from cyclopentane-1,3-diyl diradical for this system was proposed to involve nonstatistical dynamical effects. However, computational

studies at CASPT2//CASSCF level of theory for photochemical denitrogenation¹²⁴ of DBH indicated asynchronous denitrogenation of DBH to exo-axial diazenyl diradical intermediate. The formation of inverted bicyclo[2.1.0]-pentane from exo-axial diazenyl diradical intermediate was proposed to occur via impulsive population of an axial-to-equatorial pathway. Clearly, these studies indicate the need for dynamical simulations to understand the mechanisms and product distributions in similar system involving diradical intermediates. In the present study, ab initio classical trajectory simulations were carried out to understand the atomic level mechanisms of cyclopropane formation in the denitrogenation of 1-pyrazoline.

4.2 Computational Details

Ab initio classical trajectory simulations were performed by computing the forces on-the-fly at each step of the trajectory at CASSCF(4,4)/6-31+G* level of theory.^{4,113–116} The active space for CASSCF(4,4) calculation includes both the C–N σ , σ^* orbitals. Two sets of trajectory simulations were performed: (1) trajectories initiated from transition states regions and (2) trajectories initiated from reactant the region. The initial coordinates and momenta for the trajectory simulations were selected by using microcanonical normal mode sampling procedure. If one assumes that RRKM theory is valid for a unimolecular reaction, the energy levels at the unimolecular TS will be populated in accord with RRKM theory, which assumes that each energy level has an equal probability of being populated. For the sampling, the vibrational energy levels are chosen randomly and the remaining energy goes into reaction coordinate (RC) translation; i.e. the TS energy above classical potential energy at the TS is

$$E^\ddagger = E_{\text{vib}} + E_{\text{ZPE}} + E_{\text{RT}}$$

for the case there is no rotational energy at the TS. In microcanonical sampling, the total amount of energy available to the system is fixed. The transition state **TS4f** has the highest barrier in the potential energy profile for the thermal denitrogenation of 1-pyrazoline (Chapter 3). Therefore,

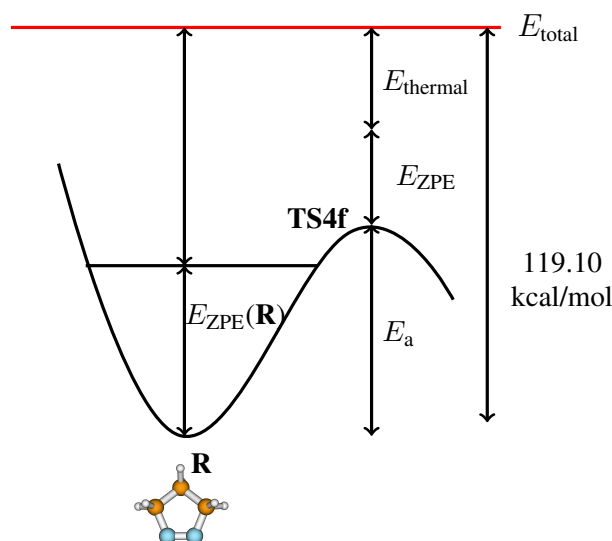


Figure 4.1: Procedure used for calculation of total energy used in microcanonical sampling. ($E_{\text{thermal}} = E_{\text{vib}} + E_{\text{rot}} + RT$)

the total amount of energy available to 1-pyrazoline by assuming Boltzmann distribution at **TS4f** at experimental temperature (510.45 K). The total energy can then be expressed by

$$E_{\text{total}} = E_a(\text{TS4f}) + E_{\text{ZPE}} + E_{\text{vib}} + E_{\text{rot}} + RT$$

where, $E_a(\text{TS4f})$ is the classical barrier at **TS4f**, E_{ZPE} is the ZPE of **TS4f**, E_{vib} and E_{rot} are the average vibrational and rotational energies at 510.45 K, and RT is the excess energy given along the reaction coordinate. The ZPE, average vibrational energy, average rotation energy, and RT energy for **TS4f** at 510.45 K were found to be 59.19, 4.53, 1.52, and 1.01 kcal/mol respectively. The total amount of energy (E_{total}) available to 1-pyrazoline thus calculated was found to be 119.10 kcal/mol. A schematic representation of the energy components used to calculate the total energy in the microcanonical sampling procedure is given in Figure 4.1. When trajectories were integrated from different transition states, an excess energy of $(119 - E_a)$ kcal/mol above classical barrier was given to the TSs, where E_a is energy of the respective TSs. When trajectories were integrated from the reactant, an excess energy of 119.10 kcal/mol was given to the reactant above its classical minimum. The trajectories were integrated using velocity-Verlet algorithm with a stepsize of 0.3 fs. 150 trajectories were integrated from **TS1** and

100 trajectories were integrated from each of the five asynchronous TSs, **TS3a**, **TS3c**, **TS4a**, **TS4c**, and **TS5** and 3000 trajectories were integrated from the reactant region. The transition state trajectories were integrated for 500 fs and trajectories initiated at the reactant region were integrated for 1.5 ps. The trajectory calculations were performed using VENUS/NWCHEM¹²⁷ software package. It should be pointed that although 1-pyrazoline and cyclopropane cannot be differentiated as cis and trans, the mechanism of the product formation were followed with respect to rotation of the terminal methylene groups to compare with the experimental observations for substituted pyrazolines. Three types of products can be expected as discussed earlier (Chapter 3)-SI, DI, and Ret.

4.3 Results and Discussion

4.3.1 Trajectories Initiated from the Transition State Region

4.3.1.1 Trajectories Initiated from TS1 Region

The transition state, **TS1** connects reactant to trimethylene diradical intermediate (**Int1**). **Int1** can close to cyclopropane via con or dis rotation of terminal methylene groups or can form alkene via a proton transfer. The barrier for conrotatory and disrotatory closure of **Int1** to cyclopropane is ~ 1 kcal/mol and the barrier for alkene formation is 6 kcal/mol (Chapter 3). **TS1** can also isomerize to symmetric **TS1'** via a second order saddle point **SO1** as shown in Figure 4.2 from where dissociation of N_2 can happen. To understand the post-transition state dynamics of cyclopropane formation from **TS1**, 150 trajectories were integrated from the **TS1** region. The initial coordinate distribution for the 150 trajectories initiated from **TS1** is given in Figure 4.3. It can be seen from Figure 4.3, the initial (reaction) coordinate distribution is symmetric about the **TS1** coordinate. This shows that the sampling of 150 trajectories are not from a biased region of the reaction coordinate. 54 out of 150 trajectories lead to the reactant and 96 trajectories lead to cyclopropane. 11 out of the 96 trajectories first form the

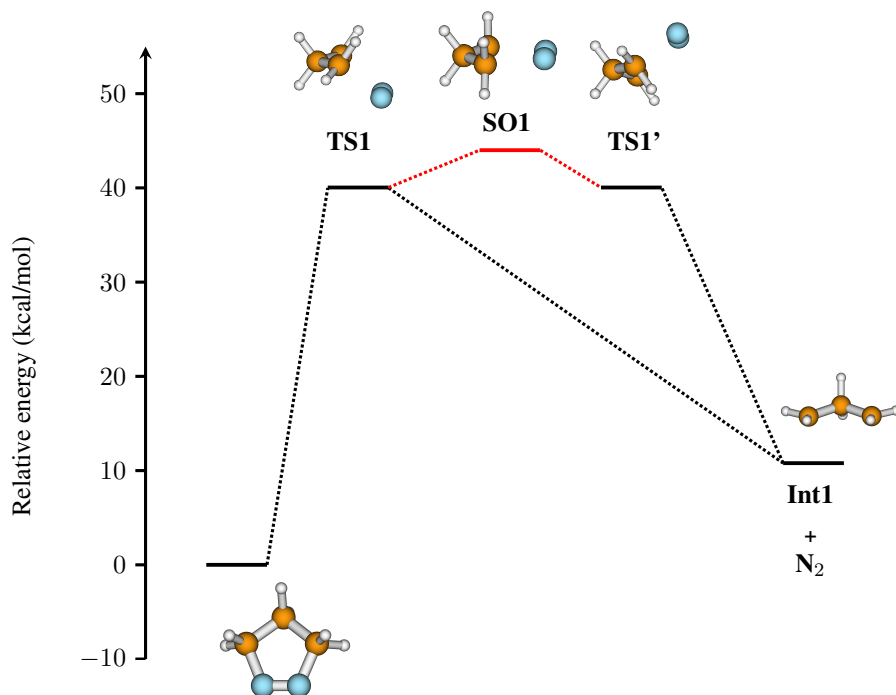


Figure 4.2: Energetics (kcal/mol) of the isomerization of TS1.

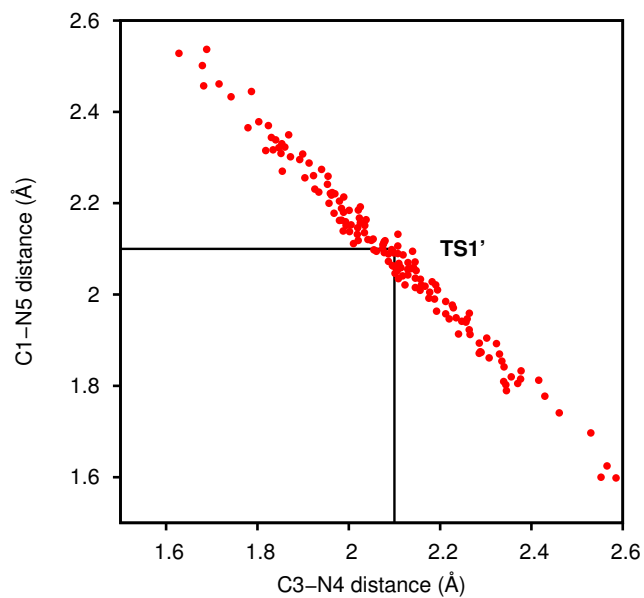


Figure 4.3: Initial coordinate distribution for the trajectories initiated from TS1. The solid lines correspond to the C-N bond distances at the TS1 stationary point.

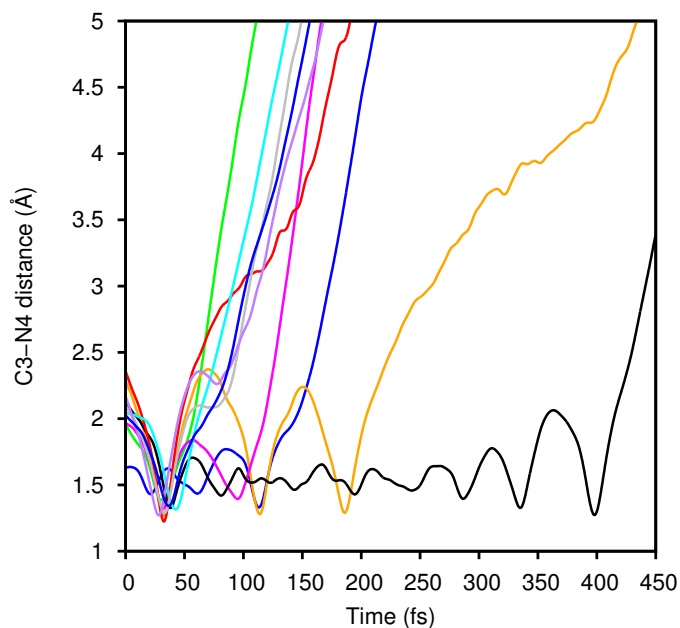


Figure 4.4: Plot of C3–N4 distance (Å) vs time (fs) for trajectories that exhibit recrossing.

reactant and then recross the transition state region to form cyclopropane. A plot of C3–N4 distance vs time for the 11 trajectories that recross the transition state region is given in Figure 4.4. The equilibrium C3–N4 distances for **TS1** and reactant are 2.1 and 1.5 Å respectively. It can be seen from Figure 4.4, that all the trajectories start from the transition state region (C3–N4 distance 1.8–2.2 Å), form reactant and then dissociate to form cyclopropane. Out of 96 trajectories, 56 form single inverted cyclopropane, 30 lead to double inverted cyclopropane, and 10 form cyclopropane with the retention of configuration. So, a preferential formation of single inverted cyclopropane was observed for trajectories integrated from the **TS1** region.

To understand whether the denitrogenation follows a synchronous or an asynchronous path, the C3–N4 and C1–N5 distances for all the trajectories were followed with time and the plot is given in Figure 4.5. It can be seen from Figure 4.5 that, only two trajectories follow asynchronous path and the rest follow synchronous denitrogenation path. Along the minimum energy path (MEP) for synchronous denitrogenation of 1-pyrazoline through **Int1**, there is an increase in the C–N distance, and significant changes in the dihedral angles $\angle C1-C2-C3-N4$,

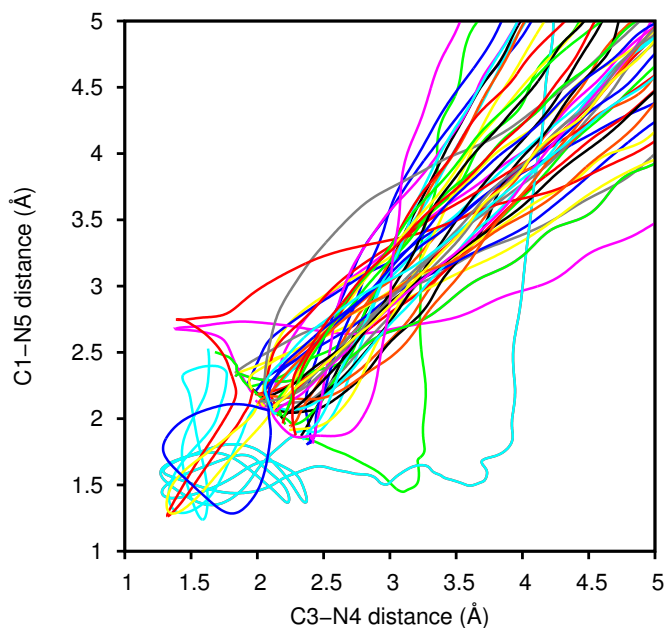


Figure 4.5: Plot of C3–N4 and C1–N5 distance (Å) for trajectories initiated from **TS1**.

$\angle\text{C2-C3-N4-N5}$, $\angle\text{C3-C2-C1-N5}$ and $\angle\text{C2-C1-N5-N4}$. Both the $\angle\text{C1-C2-C3-N4}$ and $\angle\text{C3-C2-C1-N5}$ dihedral angles change from -17.72 to -40.80 and 17.72 to 40.80° respectively and $\angle\text{C2-C3-N4-N5}$ and $\angle\text{C2-C1-N5-N4}$, change from 12.0 to 22.2° . So, any of the four dihedral angles and C–N distances can be followed to understand whether the denitrogenation follows the MEP. Here, the angle $\angle\text{C1-C2-C3-N4}$ vs C3–N4 distance for all the trajectories, transition states **TS1**, **TS1'**, and the MEP obtained at CASSCF(4,4)/6-31+G* level of theory are plotted in Figure 4.6. As seen in Figure 4.6, most of the trajectories follow the IRC path. They dissociate directly from **TS1** and form products. However, in two trajectories, isomerization of **TS1** to **TS1'** was observed, which then dissociates from **TS1'** to form cyclopropane. In addition, three trajectories dissociate through the second order saddle point region.

To understand the atomic level-mechanism of cyclopropane formation and the involvement of trimethylene diradical intermediate in the denitrogenation process, the electron densities of the C–N σ orbitals σ_5 and σ_6 were followed during the dissociation process for all the trajectories. The correlation of the orbitals involved in the reaction along the synchronous

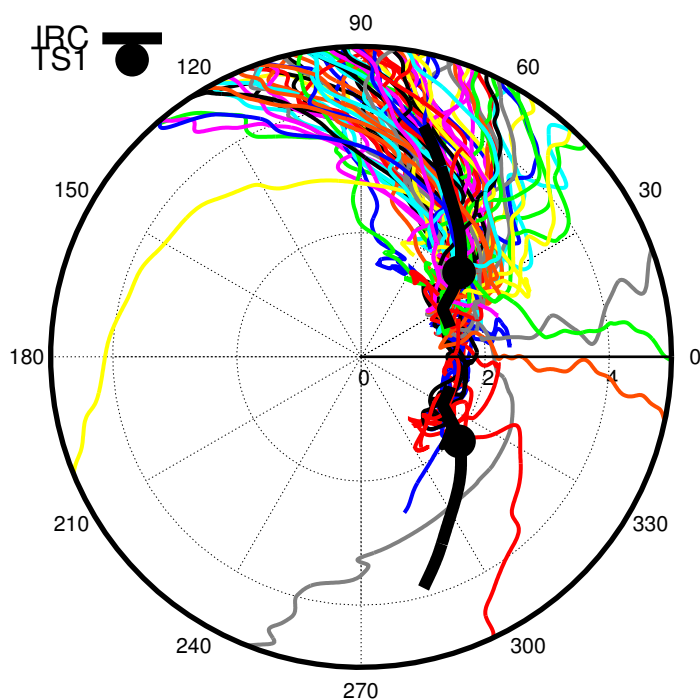


Figure 4.6: Polar plot of $\angle\text{C1-C2-C3-N4}$ vs C3-N4 distance for **TS1**, **TS1'**, IRC, and all the trajectories.

denitrogenation path from 1-pyrazoline to cyclopropane through **TS1** and **Int1** is shown in Figure 4.7. Two types of trajectories were observed: (1) in one type of trajectories (Type 1), the dissociation of C–N bonds and closing of C1–C3 bond happen simultaneously. The plot of C1–C3 bond distance and the electron densities of the σ_{CN} and σ_{CN}^* orbitals vs time are shown in Figure 4.8(a). The initial electron densities (ρ_5 and ρ_6) in the $\sigma_{\text{C-N}}$ and $\sigma_{\text{C-N}}^*$ orbitals are ~ 1.6 and ~ 0.3 . During the course of the reaction, ρ_5 decreases and ρ_6 increases until the diradical is formed when ρ_5 and ρ_6 are ~ 1.0 . During the cyclopropane formation from the diradical, the $\sigma_{\text{C-N}}$ and $\sigma_{\text{C-N}}^*$ orbitals change their character to $\sigma_{\text{C-C}}$ (ρ_5) and $\sigma_{\text{C-C}}^*$ (ρ_6) orbitals. ρ_5 and ρ_6 now become ~ 2.0 and ~ 0 respectively confirming closed shell nature of the wavefunction. Here, in the first type of trajectories, (Figure 4.8a), one can see that the reaction surpasses the diradical region within 100 fs and the products are formed after 100 fs. Thus the lifetime of **Int1** for this type of trajectories is short ~ 30 -100 fs. In the second type of trajectories (Type 2),

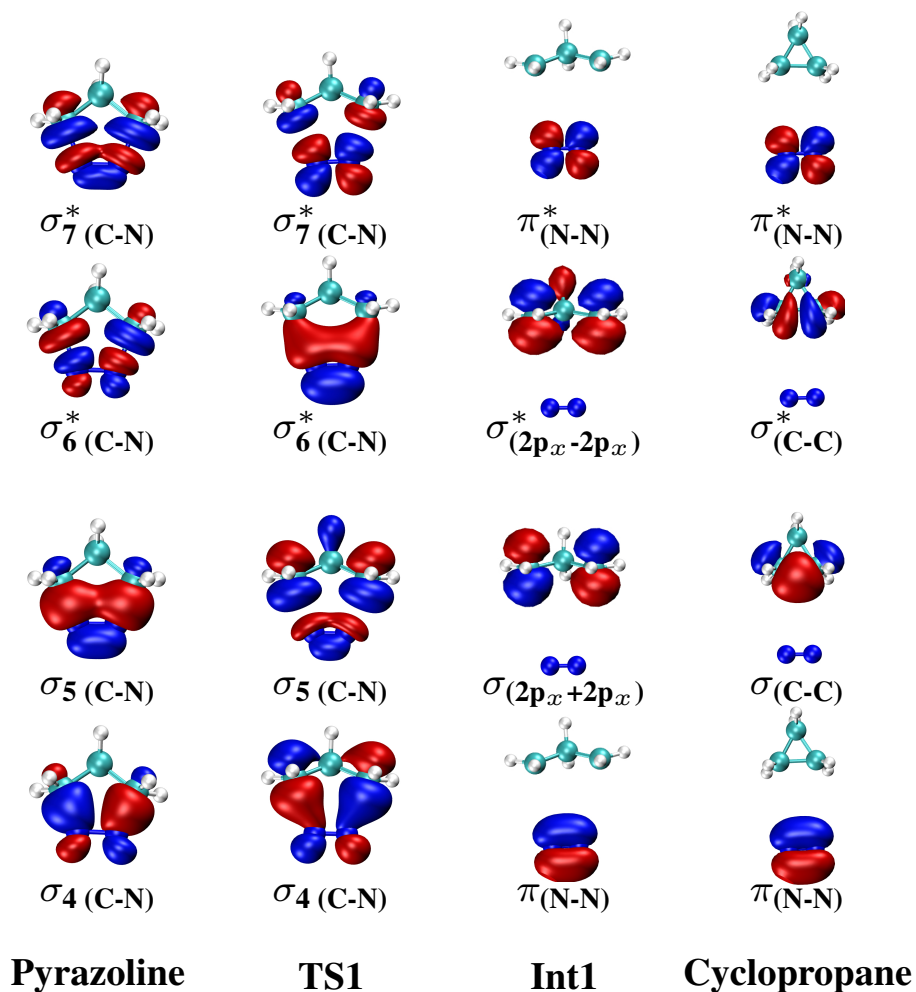


Figure 4.7: Correlation diagram of orbitals along synchronous denitrogenation of 1-pyrazoline to **Int1** and cyclopropane formation.

although the diradicals are formed in about ~ 100 fs, the system stays in the diradical region for longer time before closing to cyclopropane (Figure 4.8(b)). The lifetime of trimethylene diradical obtained for the synchronous trajectories are is given in Figure 4.9. Since, the barrier for rotation of the terminal methylene group of **Int1** is very less, in this set of trajectories, several rotations of terminal methylene group of the diradical **Int1** happen before closing to cyclopropane. These set of trajectories correspond to the formation of **Int1** that have lifetime longer than 100 fs. A plot for the number of C–C bond rotations seen in these trajectories is given in Figure 4.10. It can be seen that Type 2 trajectories exhibit a maximum of 3 C–C bond

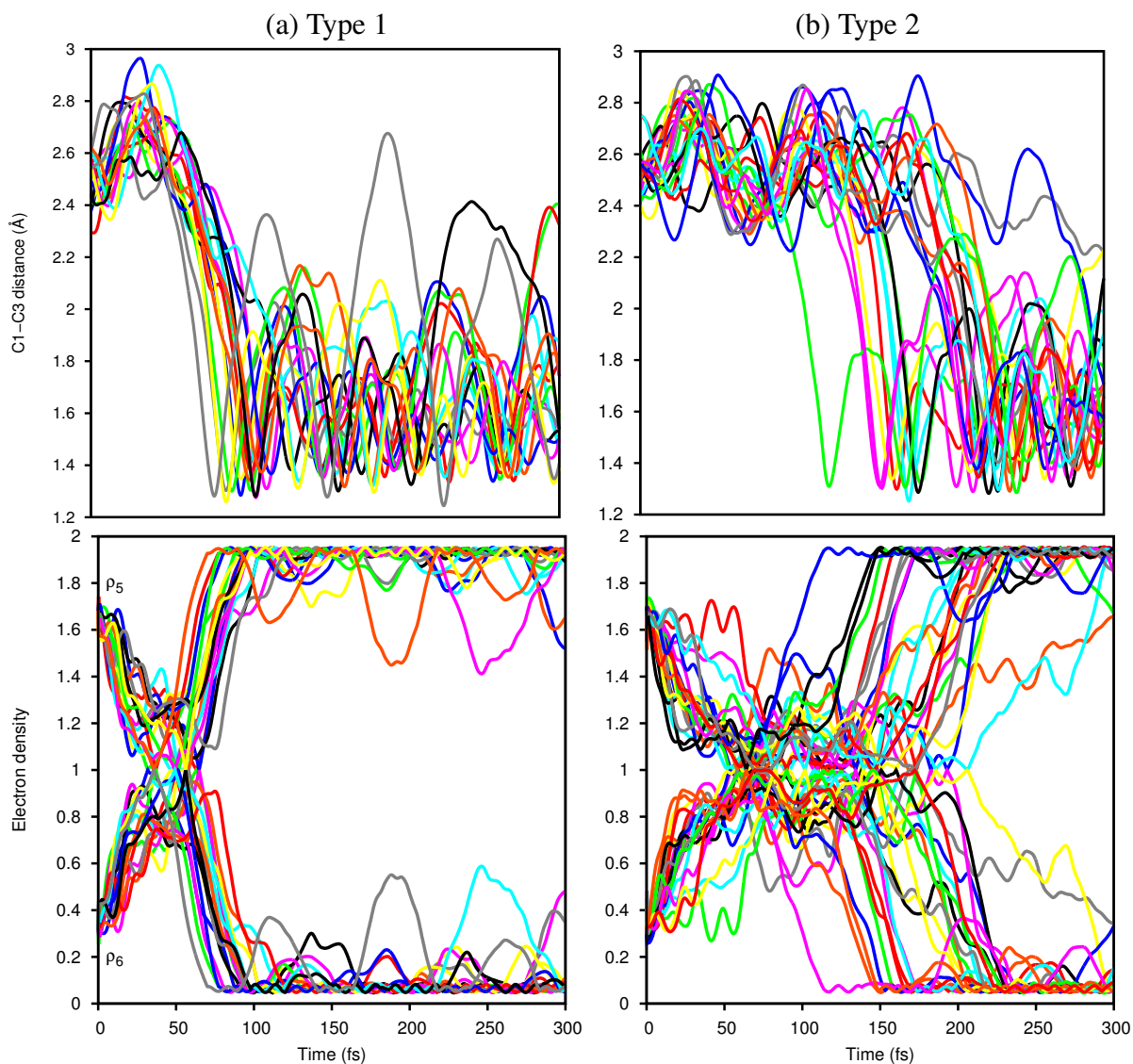


Figure 4.8: Plot of C1–C3 bond distance and electron densities ρ_5 and ρ_6 in σ_5 and σ_6 orbitals vs time for trajectories initiated from **TS1**: (a) Type 1 trajectories having short **Int1** lifetime and (b) Type 2 trajectories having longer **Int1** lifetime.

rotations with most trajectories showing one rotation.

4.3.1.2 Trajectories Integrated from **TS3a**

The asynchronous cleavage of one of the C–N bonds (say C1–N5) from 1-pyrazoline via **TS3a** leads to diazenyl diradical (**DZ**) intermediate **Int3a**. The N_2 group of **Int3a** can undergo

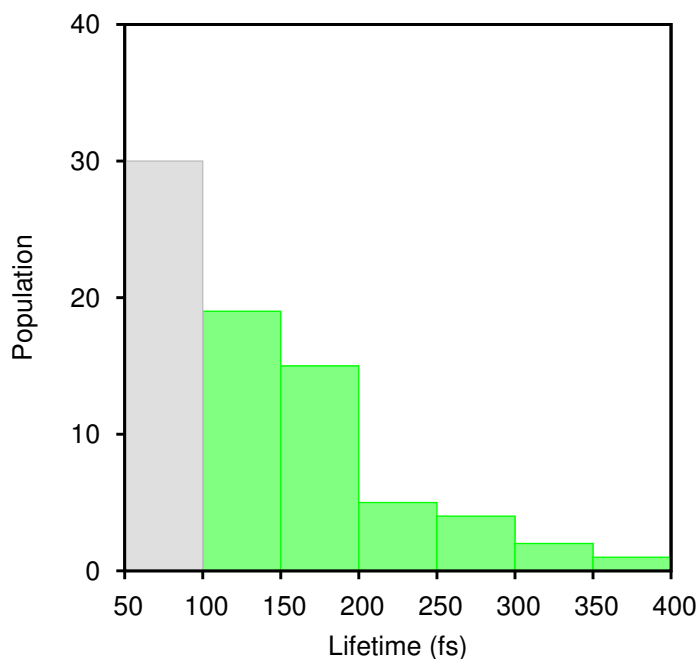


Figure 4.9: Lifetime distribution of trimethylene diradical for Type 1 (light shade) and Type 2 (dark shade) trajectories.

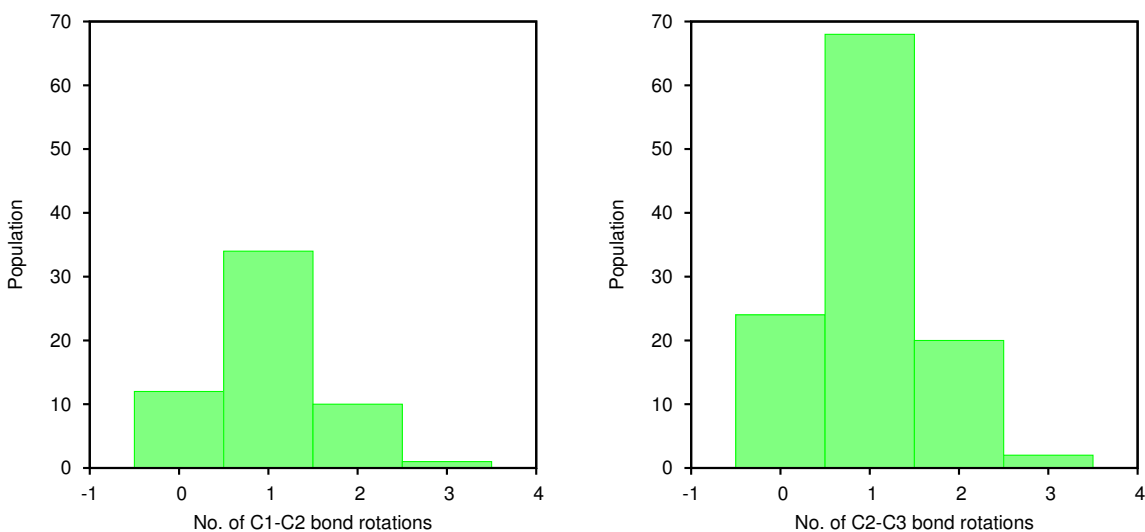


Figure 4.10: Number of C–C bond rotations in the trimethylene diradical intermediate for Type 2 trajectories

a 360° rotation about C(3)–N(4) bond and close back to reactant or it can close to form cyclopropane by the dissociation of C(3)–N(4) bond (Figures 3.8 and 3.9, Chapter 3). The **DZ** region of PES is very flat. Several rotational isomers of **DZ** differ in the orientation of N_2 group

around C(3)–N(4) bond and terminal methylene group exist on the PES. The energetics of all the rotational isomers lie within 1.5 kcal/mol. As pointed earlier the PES is symmetrical about C–N bond cleavage i.e asynchronous cleavage of the C3–N4 bond and C1–N5 bond would result in similar structures. To understand the post-transition state dynamics of cyclopropane formation from **TS3a**, 100 trajectories were integrated from the **TS3a** region. Out of 100 trajectories, 7 trajectories lead to reactant and 93 trajectories gave cyclopropane. 48 out of 93 trajectories result in single inverted cyclopropane, 29 lead to double inverted cyclopropane and 16 gave cyclopropane with the retention of configuration. From the product distribution, it is clear that there is a slight preference for single inverted cyclopropane formation.

In going from reactant to **Int3a** via **TS3a** along the MEP, a clockwise rotation of N₂ group around C3–N4 bond happens with the dissociation of C1–N5 bond. Now, dissociation of the second C–N bond (C3–N4) can happen from **Int3a** or N₂ can further rotate around C3–N4 bond to form **Int3b** from where dissociation of C3–N4 bond is possible or it can close back to reactant. To understand the atomic-level mechanisms of C3–N4 bond dissociation from **TS3a**, the changes in $\angle\text{C2-C3-N4-N5}$ angle as a function of C3–N4 distance was followed for all the trajectories. The plot of change in $\angle\text{C2-C3-N4-N5}$ vs C3–N4 bond distance for MEP, all the stationary points along the MEP, and for all the trajectories are given in Figures 4.11 (a) and (b). The trajectories that do not follow MEP are plotted in Figure 4.11 (a) and the trajectories that follow MEP are plotted in Figure 4.11 (b). As can be seen from the Figure 4.11 (a), most of the trajectories dissociate directly from the transition state **TS3a** without going to the corresponding **DZ** intermediate **Int3a**. Only 35 out of 93 trajectories follow MEP (Figure 4.11 (b)). In the 35 trajectories, the dissociation of C3–N4 bond in 16 trajectories happen from **Int3a**. A complete 180° rotation of N₂ group around C3–N4 was observed in two of the trajectories. One of the two trajectories form reactant and the other trajectory dissociates from **TS3c**. In 12 trajectories, the dissociation of C3–N4 bond happens from **TS3b** and five trajectories dissociates from **Int3b**. In three trajectories, first the reactant is formed from which

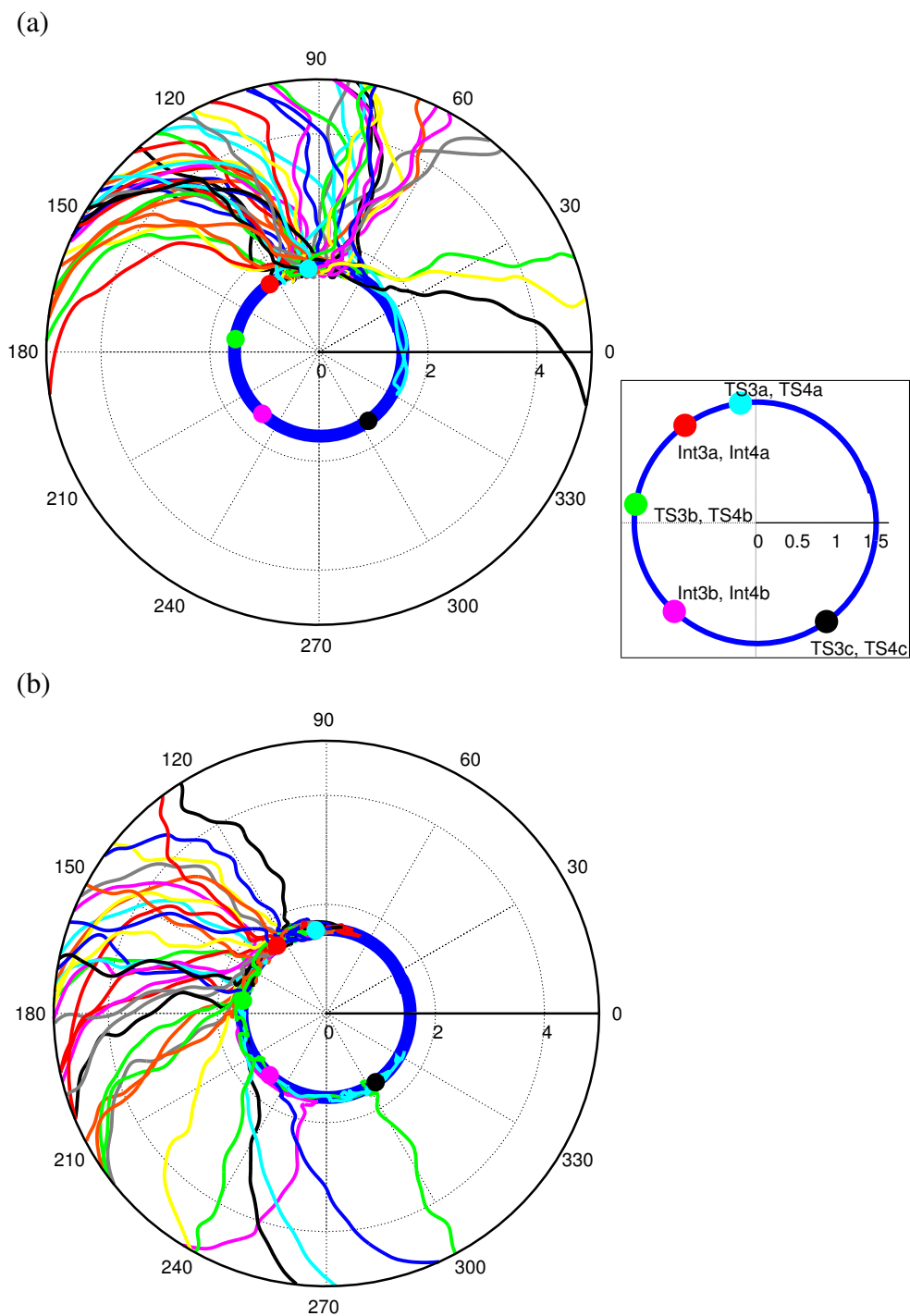


Figure 4.11: Plot of $\angle C2-C3-N4-N5$ (degree) vs $C3-N4$ distance (\AA) for (a) trajectories that do not follow MEP (b) trajectories following MEP. The location of the stationary points along the MEP is given in the box for clarity. The solid thick blue line indicates the MEP.

N₂ dissociates to form cyclopropane without following the minimum energy path.

4.3.1.3 Trajectories Integrated from TS3c

The asynchronous cleavage of C1–N5 bond from 1-pyrazoline by clockwise rotation of C3–N4 bond via **TS3c** leads to diazenyl diradical intermediate **Int3b**. Since, free rotation of N₂ group about C3–N4 bond is possible, the N₂ group of **Int3b** can undergo rotation about C–N bond and close back to reactant or it can form cyclopropane by the dissociation of the second C–N bond (Figures 3.8 and 3.9, Chapter 3). To get an atomic-level understanding of denitrogenation mechanisms from **TS3c**, 100 trajectories were integrated from the **TS3c** region. Out of 100 trajectories, only 6 trajectories lead to reactant and 94 trajectories gave cyclopropane. 53 out of 94 trajectories gave single inverted cyclopropane, 26 gave double inverted cyclopropane and 15 gave cyclopropane with the retention of configuration. From the product stereochemistry, we can clearly see a preference for single inverted cyclopropane formation for trajectories integrated from the **TS3c** region.

In going from reactant to **Int3b** via **TS3c** along the MEP, a clockwise rotation of N₂ group about C3–N4 bond happens with the dissociation of C1–N5 bond. Now, dissociation of the second C–N bond (C3–N4) can happen from **Int3b** which is the most stable **DZ** intermediate or N₂ can further rotate around C3–N4 bond to form the less stable **DZ** intermediate **Int3a** from where dissociation of C(3)–N(4) bond can happen. To understand the atomic-level mechanism of C3–N4 bond dissociation from trajectory simulation, the change in $\angle\text{C2-C3-N4-N5}$ angle as a function of C3–N4 distance was followed for each of the trajectories. The plot of change in $\angle\text{C2-C3-N4-N5}$ vs C3–N4 bond distance for MEP, all the stationary points along the MEP, and for all the trajectories are given in Figures 4.12 (a) and (b). It can be seen from the Figure 4.12 (a) that most of the trajectories do not follow the MEP. They dissociate directly from transition state **TS3c** without going to the intermediate **Int3b** or **Int3a**. Only 15 trajectories follow MEP. The dissociation of C3–N4 bond in 11 trajectories happens from **Int3b**. In two trajectories, the N₂ group rotates 360° around the C3–N4 bond and forms reactant, whereas

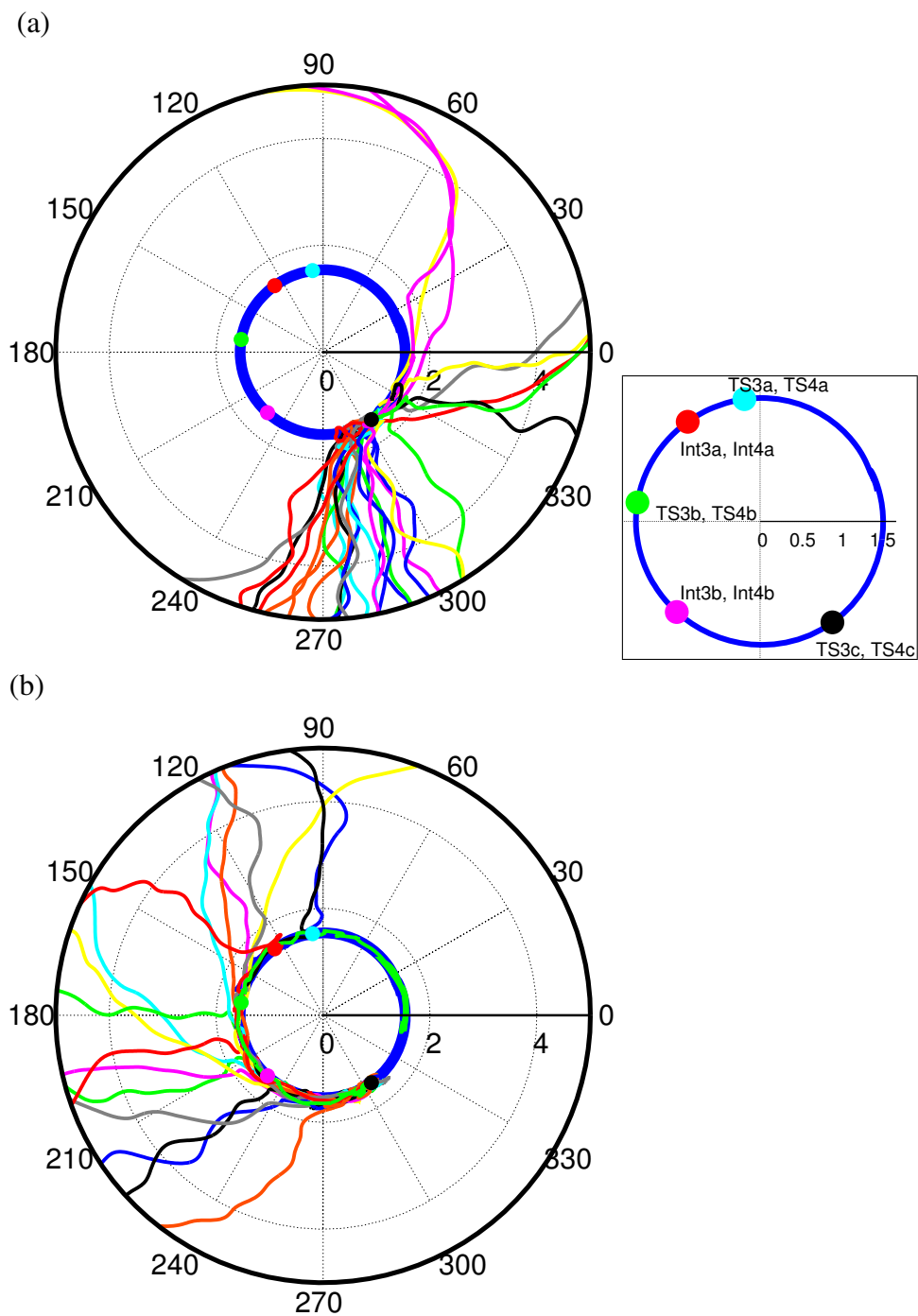


Figure 4.12: Plot of $\angle C2-C3-N4-N5$ (degree) vs $C3-N4$ distance (Å) for (a) trajectories that do not follow MEP (b) trajectories following MEP. The location of the stationary points along the MEP is given in the box for clarity. The solid thick blue line indicate MEP.

in another two of the trajectory, **TS3c** forms reactant and then dissociates via **TS3a** to form cyclopropane.

4.3.1.4 Trajectories Integrated from **TS4a**

In the above mention pathway for asynchronous denitrogenation via **TS3a** and **TS3c**, the terminal methylene group of **DZ** is planar in nature. A similar asynchronous denitrogenation pathway with pyramidal **DZ** also exists on the PES. The barrier for isomerization from planar **DZ** intermediates to corresponding pyramidal intermediates are within 1 kcal/mol. The asynchronous cleavage of C–N bond from 1-pyrazoline via **TS4a** leads to diazenyl diradical intermediate **Int4a**. Similar to **Int3a**, the N₂ group of **Int4a** can undergo rotation around C–N bond and close back to reactant or it can form cyclopropane by the dissociation of C3–N4 bond (Figures 3.8 and 3.9, Chapter 3). To understand the post-transition state dynamics of cyclopropane formation from **TS4a**, 100 trajectories were integrated from **TS4a** region. Out of 100 trajectories, 9 trajectories lead to reactant and 91 trajectories formed cyclopropane. 55 out of 91 trajectories lead to single inverted cyclopropane, 20 lead to double inverted cyclopropane, and 16 gave cyclopropane with the retention of configuration. From the product stereochemistry obtained for the trajectory simulation from **TS4a**, we can clearly see a preference for single inverted cyclopropane formation. To understand the atomic-level mechanisms of denitrogenation from **TS4a**, the \angle C2-C3-N4-N5 and C3–N4 distance for MEP, stationary points along MEP, and all the trajectories were plotted in Figures 4.13(a) and 4.13(b). It can be seen from the Figure 4.13 (a) that, most of the trajectories do not follow the MEP. They dissociate directly from transition state **TS4a** without going to the intermediate **Int4a** or **Int4b**. Only 16 out of 91 trajectories follow MEP. seven out of 16 trajectories dissociate from **Int4a**. Two trajectories dissociate from **DZ** intermediate **Int4b**. In one trajectories, the N₂ group rotates 360° about the C3–N4 bond and form reactant. Four trajectories first form reactant and then dissociate via **TS4c**. Two trajectories dissociate from **Int4b**.

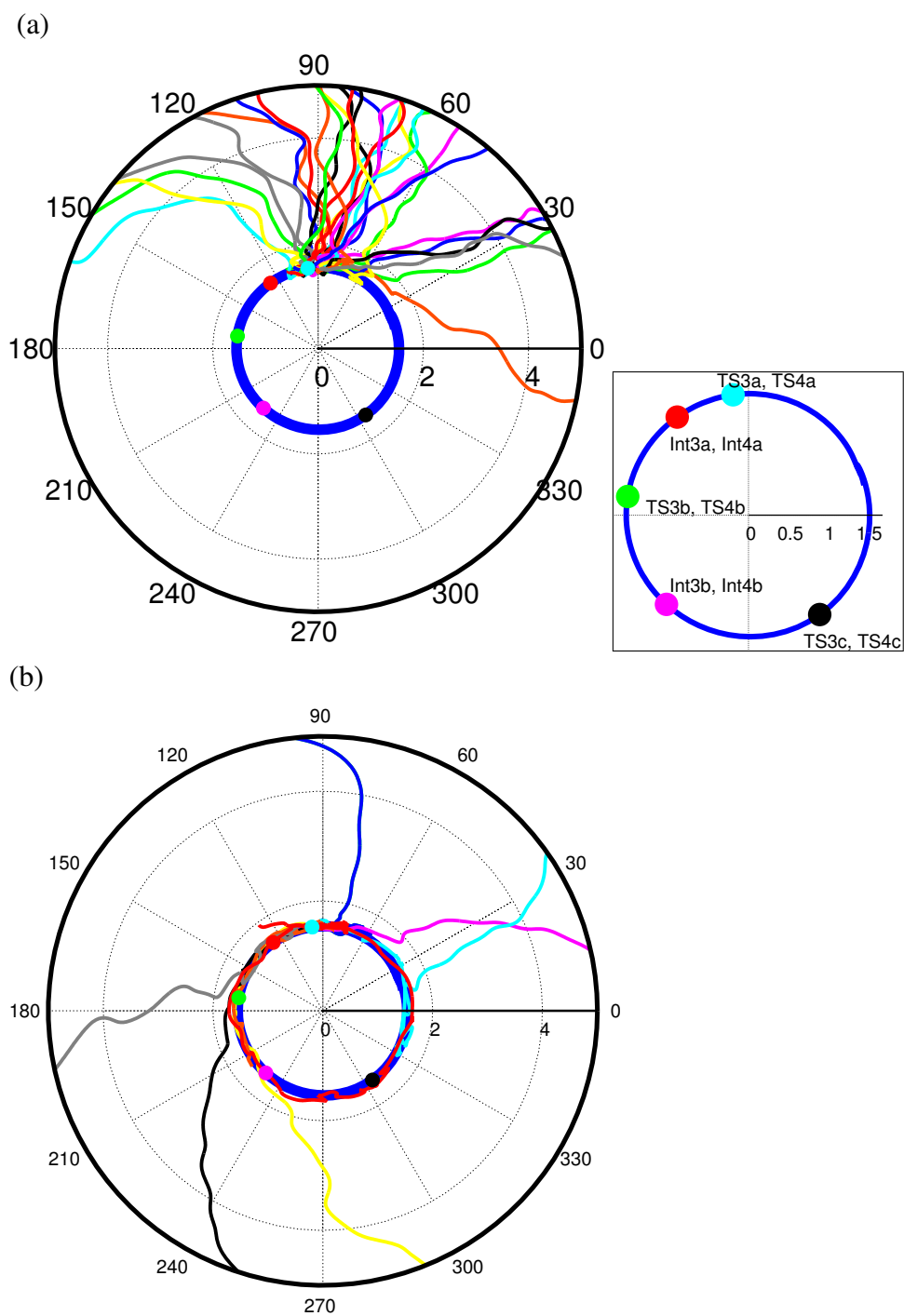


Figure 4.13: Plot of $\angle C2-C3-N4-N5$ (degree) vs $C3-N4$ distance (Å) for (a) trajectories that do not follow MEP (b) trajectories following MEP. The location of the stationary points along the MEP is given in the box for clarity. The solid thick blue line indicate MEP.

4.3.1.5 Trajectories Integrated from TS4c

Asynchronous cleavage of 1-pyrazoline by clockwise rotation of C3–N4 bond via **TS4c** leads to **DZ** intermediate **Int4b**. The dissociation of second C–N bond can happen from **Int4b** or it can isomerizes to **Int4a** from where dissociation of N₂ can happen. 100 trajectories were integrated from **TS4c** region. Out of the 100 trajectories, only 6 trajectories lead to reactant and 94 trajectories gave products. 49 out of 94 trajectories gave single inverted cyclopropane, 30 gave double inverted cyclopropane and 15 gave cyclopropane with the retention of configuration. From the product stereochemistry it can be seen that a slight preference for single inverted cyclopropane formation was observed. To understand the atomic-level mechanism of denitrogenation from **TS4c**, the change in $\angle\text{C2-C3-N4-N5}$ vs C3–N4 distance for MEP, stationary points along MEP, and all the trajectories were plotted (Figures 4.14 (a) and (b)) It can be seen from Figure 4.14 (a), most of the trajectories dissociates directly from transition state **TS4c** without going to the intermediate **Int4b** or **Int4a**. However, 15 trajectories follow MEP. 7 out of 15 trajectories dissociate from **Int4b**. 8 trajectories dissociate from **DZ** intermediate **Int4a**. Two trajectories dissociate from **TS4b**; two trajectories dissociate from **TS4a**, and in one of the trajectories, the N₂ group rotates 360° about the C3–N4 bond forming reactant and then dissociates via **TS3g**.

4.3.1.6 Trajectories Integrated from TS5

Asynchronous concerted cleavage of 1-pyrazoline via **TS5** leads to single inverted cyclopropane. The barrier for this path is 6-8 kcal/mol higher in energy than the synchronous denitrogenation path and 4-5 kcal/mol higher in energy than the asynchronous step-wise denitrogenation paths. To understand the post-transition state dynamics of cyclopropane formation from **TS5**, 100 trajectories were integrated from **TS5** region. Out of 100 trajectories, 4 trajectories lead to reactant and 96 trajectories gave products. 51 out of 96 trajectories gave single inverted cyclopropane, 27 gave double inverted cyclopropane, and 18 gave cyclopropane with the

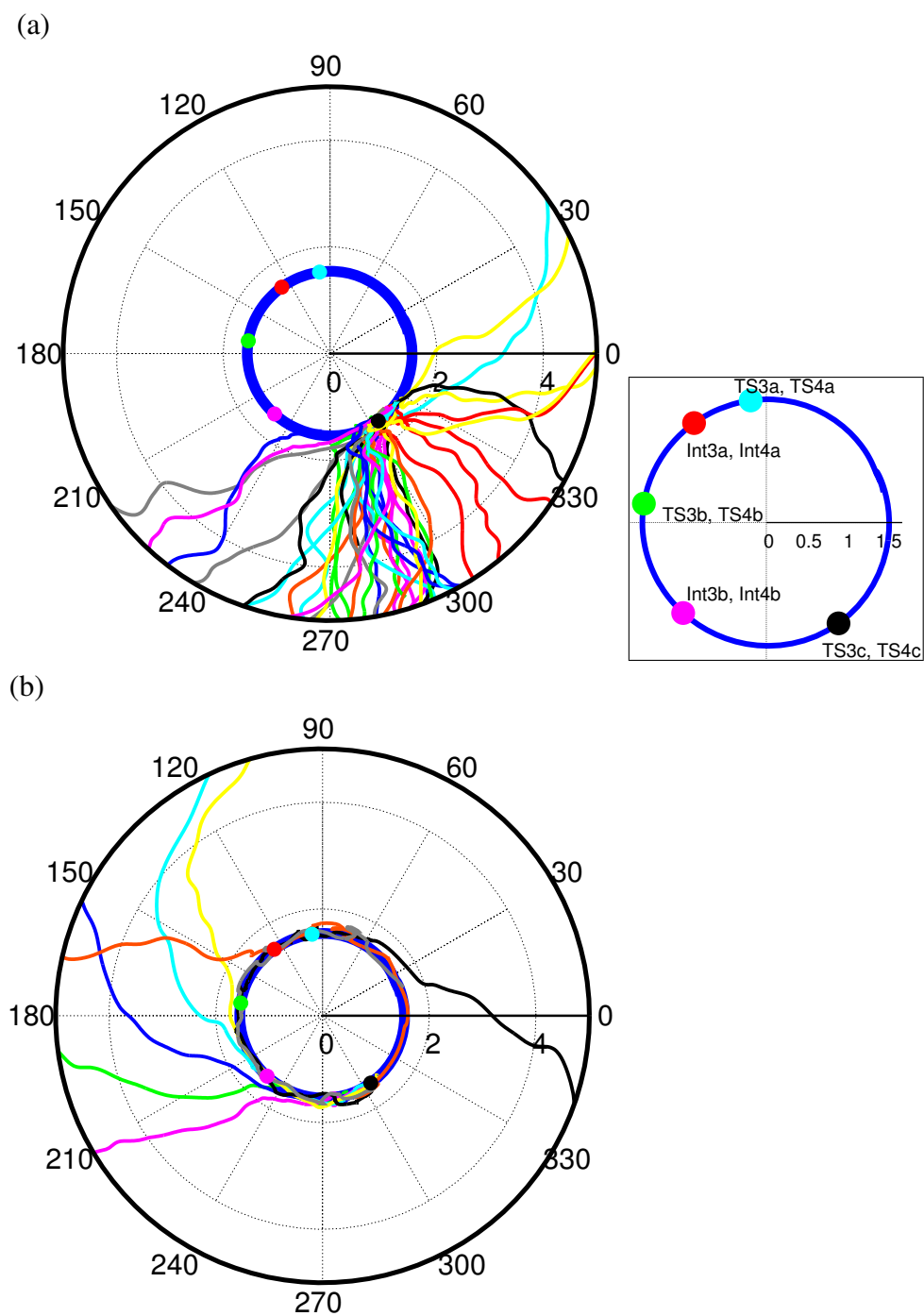


Figure 4.14: Plot of $\angle C2-C3-N4-N5$ (degree) vs $C3-N4$ distance (\AA) for (a) trajectories that do not follow MEP (b) trajectories following MEP. The location of the stationary points along the MEP is given in the box for clarity. The solid thick blue line indicate MEP.

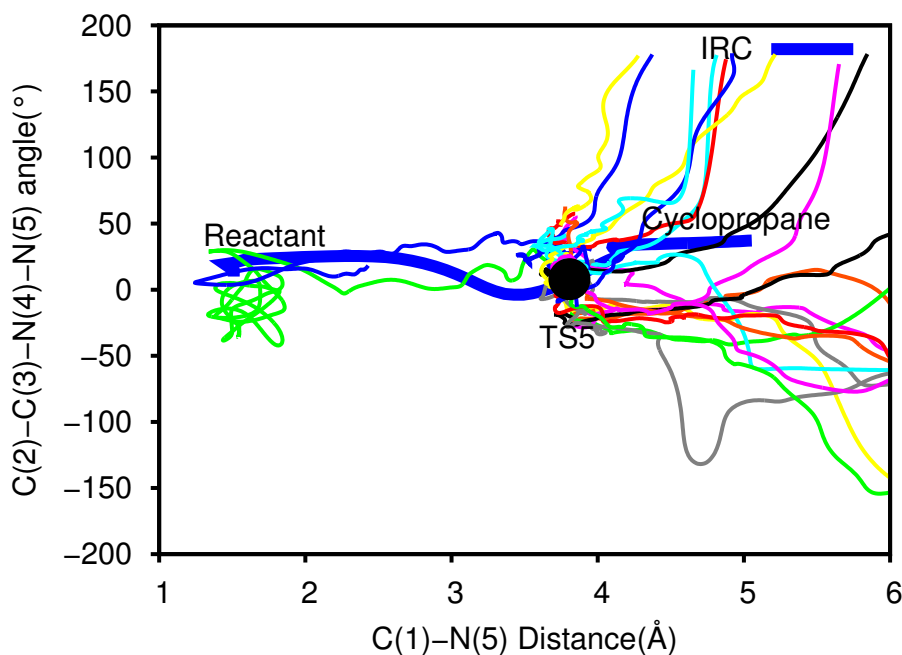


Figure 4.15: Plot of $\angle C2-C3-N4-N5$ and $C1-N5$ distance for MEP and trajectories initiated from **TS5**. Thick filled circle represents **TS5**

retention of configuration. To understand the atomic level mechanism of cyclopropane formation from **TS5**, the $\angle C2-C3-N4-N5$ vs $C1-N5$ distance was plotted for all the trajectories and are given in Figure 4.15. MEP is an asynchronous cleavage of $C1-N5$ σ bond simultaneously accompanied by the displacement of N_2 by a backside attack by $C(1)$ radical center resulting in an inversion at $C(3)$ carbon center. It should be pointed that in the MEP, rotation of terminal methylene group $C(1)$ of **TS5** is not observed. The barrier for this rotation is ~ 1 kcal/mol. Of the 96 trajectories, 7 follow MEP (Figure 4.15). In many of the trajectories, rotation of terminal methyl ($C(1)$) group happens along with the cleavage of second $C-N$ bond, which leads to cyclopropane with double inversion of stereochemistry. Also in many trajectories, retention at both $C(1)$ and $C(3)$ carbon center was observed.

4.3.1.7 Discussion

The product stereochemistry of cyclopropane obtained from trajectory simulations initiated in the six transition state regions are given in Table 4.1. As can be seen from Table 4.1, a preference

in the formation of single inverted cyclopropane (SI) was observed for trajectories initiated from all the six transition state regions. When trajectories were integrated from synchronous transition state **TS1** region, most of the trajectories follow MEP and form **Int1** from **TS1**. Many trajectories stay in the diradical (**Int1**) region for about 100 fs and then close to cyclopropane. Since the barriers for rotation of terminal methylene groups of **Int1** is ~ 1 kcal/mol, several rotation of the terminal methylene groups happen before closing to cyclopropane. However, when trajectories were initiated from the asynchronous transition state regions, most of the trajectories do not follow MEP and dissociate directly from the transition state region without going to the intermediate.

4.3.2 Trajectories Integrated from the Reactant Region

To understand the atomic level mechanism of denitrogenation from 1-pyrazoline, 3000 trajectories were integrated from the reactant region by giving an excess energy of 119.10 kcal/mol to the classical minimum of the reactant. The trajectories were integrated for 1.5 ps. Out of 3000 trajectories, 262 trajectories were reactive within 1.5 ps of which 117 trajectories lead to single inverted cyclopropane, 88 trajectories lead to double inverted cyclopropane, 57 trajectories lead to cyclopropane with retention of configuration. To understand whether denitrogenation follows a synchronous or an asynchronous denitrogenation path, both the C–N bond distances

Table 4.1: Stereochemistry of cyclopropane obtained in the trajectory simulations initiated from different transition states

Transition state	Cyclopropane stereochemistry		
	Single inversion	Double inversion	Retention
TS1	56/96 (58%)	30/96 (31%)	10/96 (10%)
TS3a	48/93 (52%)	29/93 (31%)	16/93 (17%)
TS3c	53/94 (56%)	26/94 (28%)	15/94 (16%)
TS4a	55/91 (60.4%)	20/91 (22%)	16/91 (17.5%)
TS4c	49/94 (52%)	30/94 (32%)	15/94 (16%)
TS5	51/96 (53%)	27/96 (28%)	18/96 (19%)

for all the reactive trajectories are plotted in Figure 4.16. As can be seen from Figure 4.16(a), both the C–N bonds dissociate simultaneously for the trajectories that follow synchronous denitrogenation path whereas for asynchronous trajectories, the dissociation of one of the C–N bonds happen first followed by the other one (Figure 4.16(b)). Out of the 262 reactive trajectories, 149 (57%) trajectories follow synchronous denitrogenation path and 113 (43%) follow asynchronous path. So, although the barrier for asynchronous denitrogenation paths were 6-8 kcal/mol higher in energy than the barrier for synchronous denitrogenation path, from the trajectory simulation it can be observed that both synchronous and asynchronous denitrogenation paths are almost equally probable.

4.3.2.1 Trajectories Following Synchronous Denitrogenation Path

In the potential energy profile for denitrogenation of 1-pyrazoline, only one minimum energy path was seen for synchronous denitrogenation. To understand whether the synchronous trajectories dissociate via the MEP, angles $\angle C1-C2-C3-N4$ and $\angle C3-C2-C1-N5$ along with

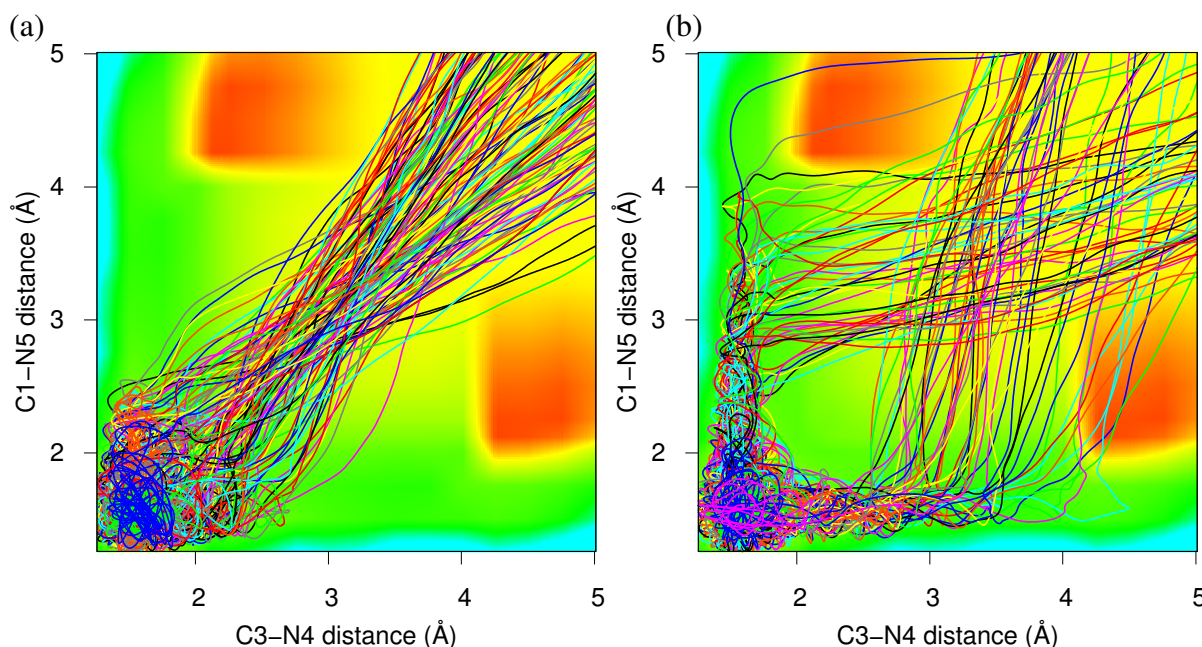


Figure 4.16: (a) Trajectories following synchronous denitrogenation path. (b) Trajectories following asynchronous denitrogenation path.

C3–N4 distance were followed for all the trajectories and are plotted in Figures 4.17 and 4.18. It can be seen in Figure 4.17, that the trajectories which follow MEP dissociate via transition state **TS1**. 114 out of 149 trajectories follow MEP and dissociate via **TS1** to form trimethylene diradicals that subsequently close to cyclopropane. However, the rest 35 trajectories do not follow MEP. 14 out of this 35 trajectories dissociate via a non-linear extrusion pathway where the N₂ group cleaves axially without going through **TS1** region. The plot of $\angle\text{C1-C2-C3-N4}$ and $\angle\text{C3-C2-C1-N5}$ angle and C3–N4 distance for all the trajectories that dissociate via non-linear extrusion pathway are plotted in Figure 4.18. The MEP for the synchronous mechanism

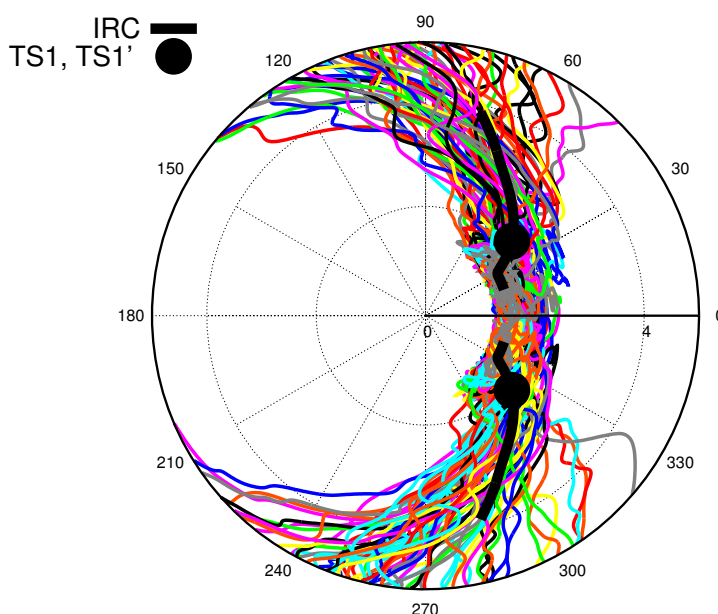


Figure 4.17: Plot of $\angle\text{C1-C2-C3-N4}$ and $\angle\text{C3-C2-C1-N5}$ (degree) vs C3–N4 distance (Å) for trajectories that follow MEP.

involves the stationary point **TS1** and trimethylene diradical **Int1**. It is of importance to understand the lifetime of the diradical **Int1** and its role in the formation of cyclopropane. To calculate the lifetime of **Int1** the electron densities (ρ_5 and ρ_6) of the C–N σ orbitals (σ_5 and σ_6) were monitored during the dissociation process for all the trajectories. Where ρ_5 and ρ_6 of the molecule were found to be between 0.5 and 1.5, the system was considered as the trimethylene diradical. The lifetime of the trimethylene diradical obtained from the synchronous trajectories

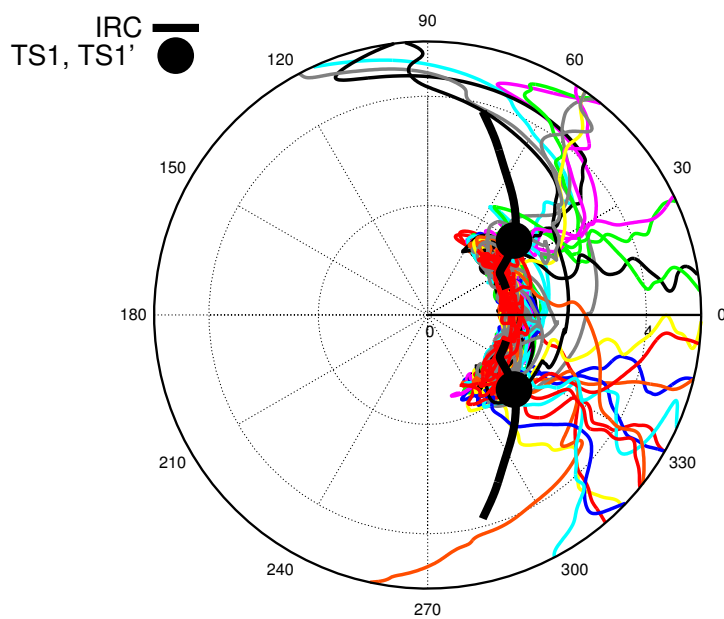


Figure 4.18: Plot of $\angle C1-C2-C3-N4$ and $\angle C3-C2-C1-N5$ vs $C3-N4$ distance for trajectories that do not follow MEP.

are given in Figure 4.19. The lifetime of trimethylene diradical obtained for synchronous

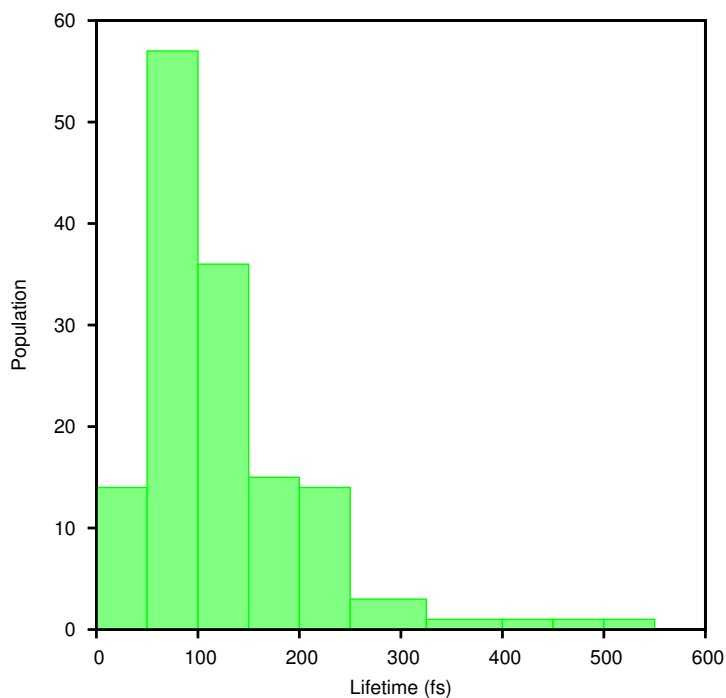


Figure 4.19: Lifetime of trimethylene diradical obtained for the synchronous trajectories

trajectories varies from 35 to 510 fs with an average lifetime of 153 fs.

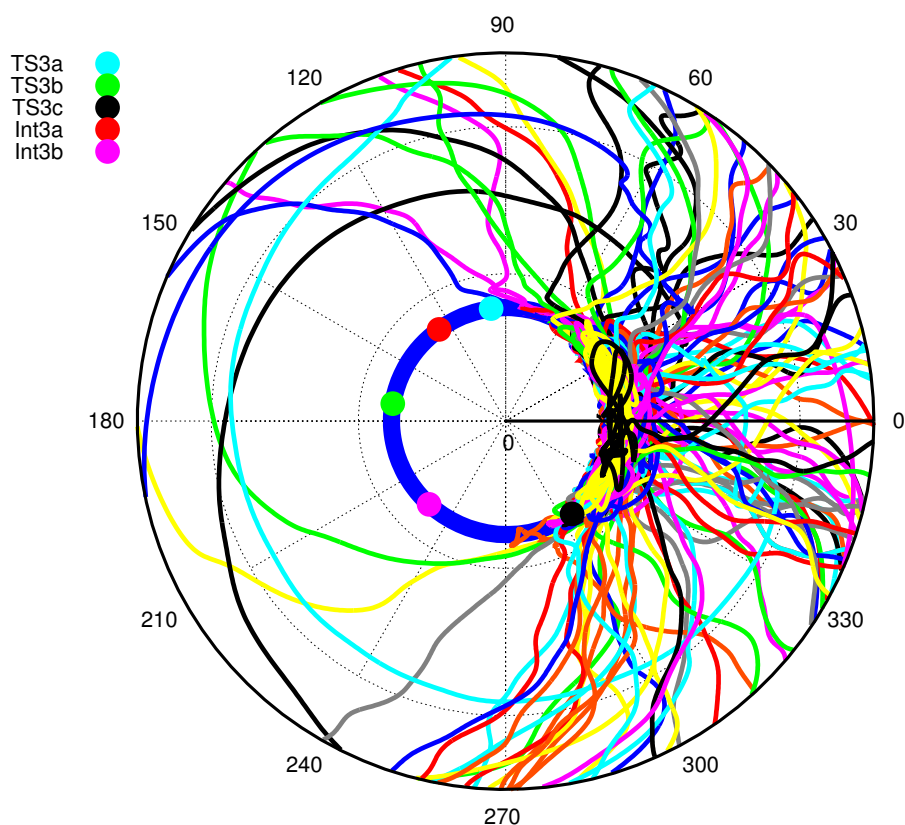


Figure 4.20: $\angle\text{C2-C3-N4-N5}$ vs C3-N4 distance for all the asynchronous trajectories.

4.3.2.2 Trajectories Following Asynchronous Step-wise Denitrogenation Path

From the potential energy profile for thermal denitrogenation of 1-pyrazoline, two different asynchronous paths were observed: (1) asynchronous step-wise denitrogenation path (2) asynchronous concerted denitrogenation path. To understand the atomic-level mechanisms of asynchronous trajectories, $\angle\text{C2-C3-N4-N5}$ vs C3-N4 distance were followed for all the asynchronous trajectories and are plotted along with the MEP for asynchronous path and the stationary points along the MEP in Figure 4.20. 7 out of 113 reactive trajectories follow asynchronous step-wise denitrogenation MEP (Figure 4.21). Several trajectories go through **TS3a**, **TS3c**, **TS4a**, and **TS4c**, however instead of going to the diazenyl diradical intermediates, the second C–N bond dissociates directly from the transition states and closes to cyclopropane.

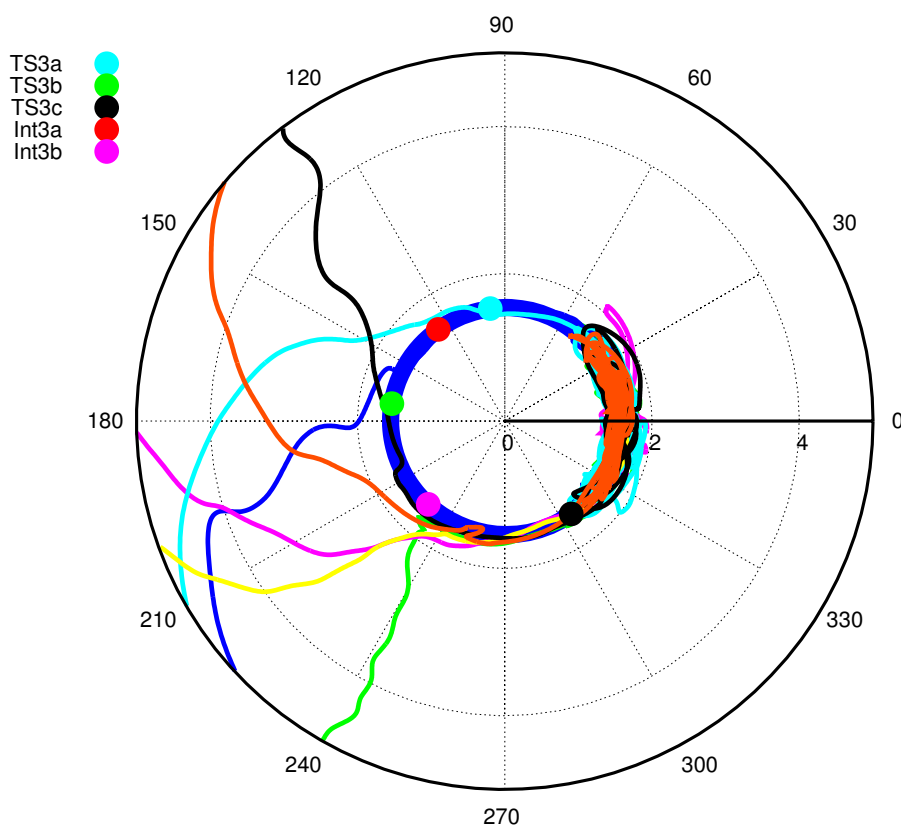


Figure 4.21: $\angle\text{C2-C3-N4-N5}$ vs C3-N4 distance for all the asynchronous trajectories that follow MEP.

4.3.2.3 Trajectories Through Asynchronous Concerted Denitrogenation Path (TS5)

This path involves asynchronous cleavage of one of the $\sigma_{\text{C-N}}$ bonds followed by backside displacement of N_2 by carbon radical center leading to cyclopropane with single inversion of stereochemistry. 6 trajectories go through **TS5**. Of the 6 trajectories, only 3 trajectories close to cyclopropane with single inversion of stereochemistry. Two trajectories close to form double inverted (DI) cyclopropane, and one trajectory form cyclopropane with retention of stereochemistry. In the two DI trajectories, the rotation of the terminal methylene group of the radical center and dissociation of second $\sigma_{\text{C-N}}$ bond from **TS5** happen simultaneously, resulting in an inversion at both C(1) and C(3) carbon centers. However, along the MEP, the rotation of terminal methylene group of **TS5** was not observed. The plot of $\angle\text{C2-C3-N4-N5}$ vs C1-N5 distance during the trajectory is given in Figure 4.22.

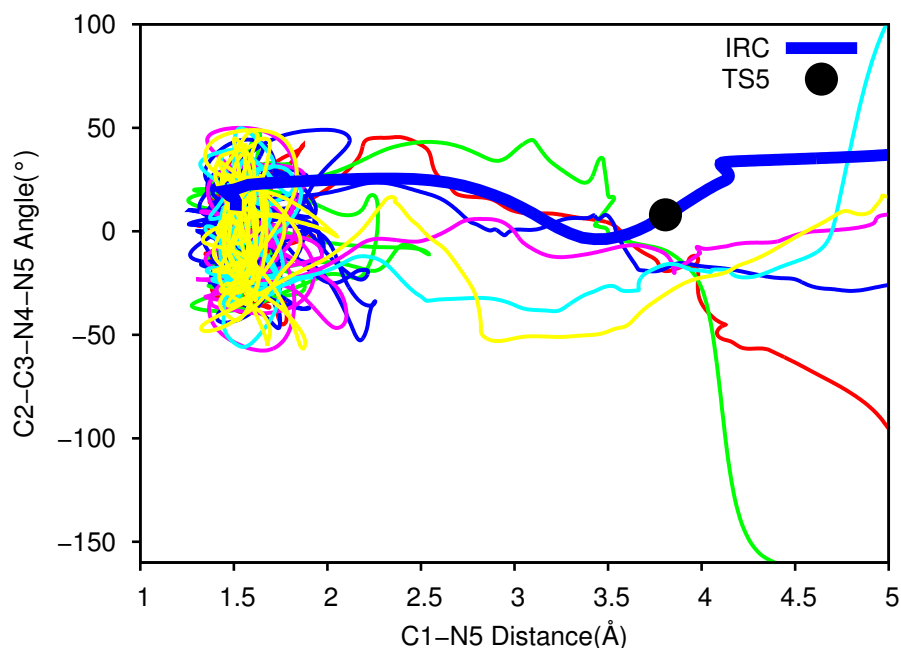


Figure 4.22: Plot of $\angle\text{C2-C3-N4-N5}$ vs C1-N5 distance for trajectories that dissociate via **TS5**.

4.3.2.4 Product Distribution

Distribution of the product cyclopropane along with the stereochemistry of cyclopropane obtained from the trajectory simulations initiated in the reactant region are given in Table 4.2. As can be seen from Table 4.2, the major is SI ($\sim 45\%$), followed by DI ($\sim 33\%$) and retention ($\sim 22\%$). It should be pointed that the distribution of the stereochemistry of cyclopropane formed from trajectories initiated from the reactant region is very similar to the ones initiated from the TS regions. This clearly indicates that the product distribution is independent of the mechanism followed and largely governed by the dynamics of the reaction.

4.3.3 Significance of Second-Order Saddle Point on the Dynamics of Denitrogenation

When trajectories were integrated from the reactant region, it was observed that some of the trajectories that involved synchronous breaking of C–N bonds adopted a structure similar

Table 4.2: Distribution of cyclopropane products obtained from the trajectory simulations initiated from the reactant region

Path ^a	Cyclopropane Stereochemistry		
	SI	DI	Ret
Sync (149)	61 (41 %)	55 (37 %)	33 (22 %)
Async (113)	56 (49.6 %)	33 (29.2 %)	24 (21.2 %)
Total (262)	117 (44.7 %)	88 (33.6 %)	57 (21.7 %)

^aValues in parentheses indicate the number of reactive trajectories.

to that of the second-order saddle point **SO1**. This second-order saddle point, **SO1** lies ~4 kcal/mol higher in energy than **TS1** and has all the five ring atoms lying on the same plane i.e. $\angle\text{C1-C2-C3-N4}$ and $\angle\text{C3-C2-C1-N5}$ are 0° . It is of interest to have a clear picture of the region of the PES involving second order saddle point. 1-Pyrazoline has C_s symmetry with the four atoms belonging two C–N bonds lying on a plane, P . The central CH_2 lie either above (**R**) or below (**R'**) the plane, P . The barrier for flipping of CH_2 group from **R** to **R'** is 0.17 kcal/mol corresponding to a transition state **TS0**. Denitrogenation can happen from both the conformers **R** and **R'** of 1-pyrazoline. Synchronous denitrogenation of **R** leads to **Int1** through the transition state **TS1** and a synchronous denitrogenation of **R'** will also lead to **Int1** through the transition state **TS1'**. The potential energy profile for synchronous denitrogenation of 1-pyrazoline is given in Figure 4.23. Similar to the reactants, the flipping of the central CH_2 group can also happen in **TS1** resulting in **TS1'**. This flipping of CH_2 occurs through **SO1**. **SO1** is a second order saddle point characterized by two imaginary frequencies corresponding to two normal mode vectors. One of the vectors corresponds to a symmetric C–N stretching vibration and the other corresponds to an out-of-plane bending mode. To understand the minimum energy paths that follow from **SO1**, a relaxed potential energy surface was mapped by simultaneously varying the values of the dihedral angles $\angle\text{C3C2C1N5}$ (ϕ_8) and $\angle\text{C1C2C3N4}$ (ϕ_1) at equally fixed values of C–N distances i.e. Both the C–N distances and the two dihedral angles were varied equally during the PES scan. The sets of coordinates

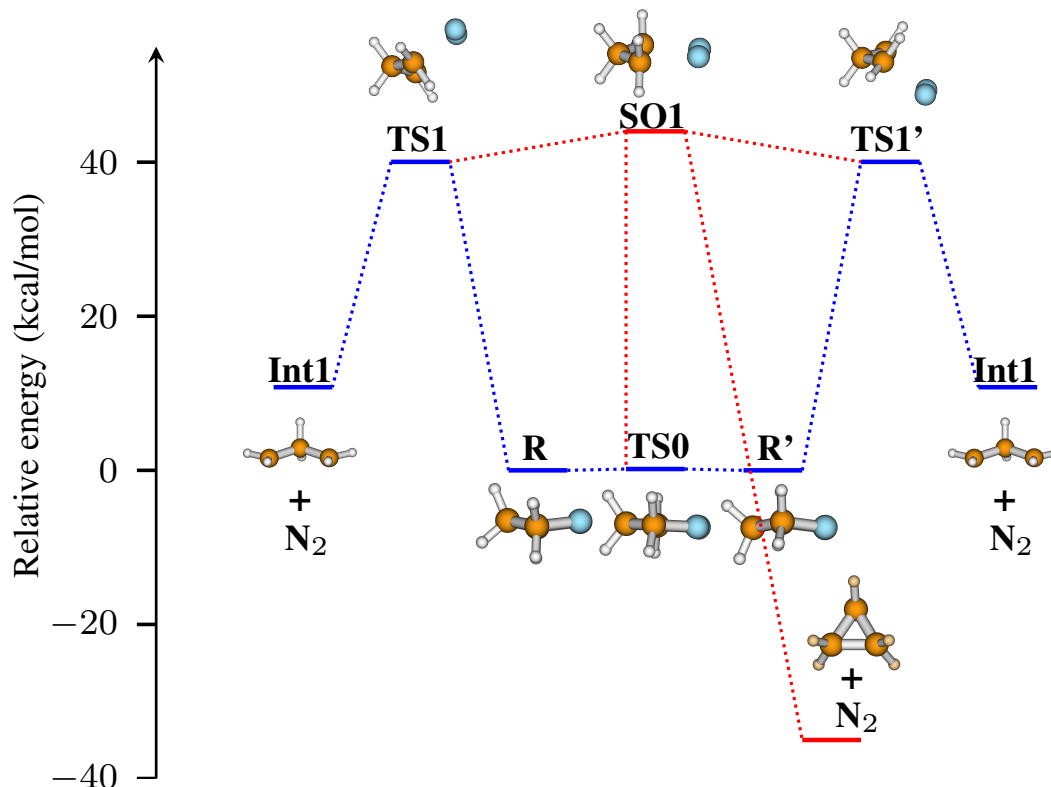


Figure 4.23: Synchronous denitrogenation path for 1-pyrazoline obtained at CASSCF(4,4)/6-31+G* level of theory.

used to generate the PES can be represented using the combined coordinates $\phi_S = (\phi_1 - \phi_8)/2$ and $d_S = (d_1 + d_2)/2$. ϕ_S and d_S also faithfully represent the PES covering the stationary points along the synchronous denitrogenation path. The PES thus obtained along with the MEPs are given in Figure 4.24. It can be seen that **SO1** connects to **TS1** and **TS1'** along the MEP corresponding to the $\angle C3C2C1N5$ angles for C–N distance at 2.1 Å. Along the C–N distance coordinate for $\angle C3C2C1N5 = 0^\circ$, the MEP from **SO1** connects **TS0** in one direction and cyclopropane (Cp) in another direction. Hence, it can be seen that starting from **SO1**, the MEP in one direction along the $\angle C3C2C1N5$ coordinate reaches **TS1** where it bifurcates to **Int1** and **R** and in the other direction the path bifurcates at **TS1'** to **Int1** and **R'**. The MEP along the C–N coordinate from **SO1**, in one direction forms cyclopropane with retention of

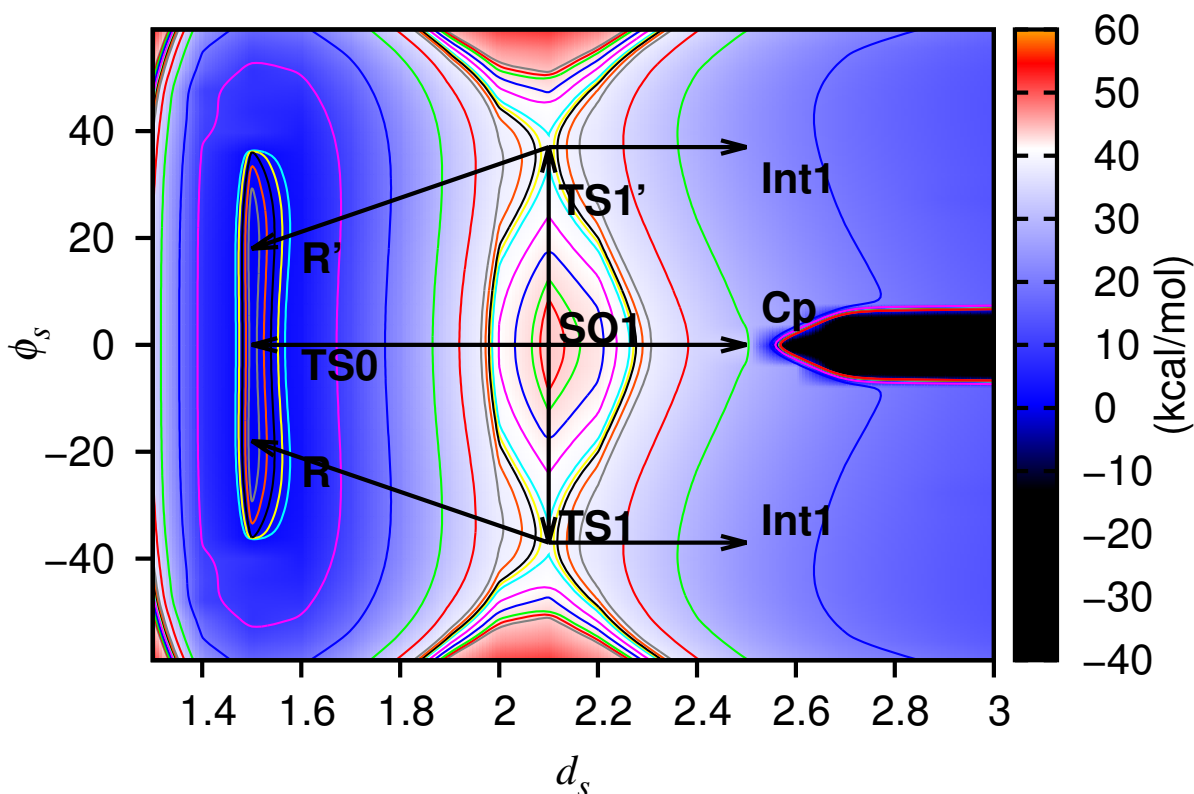


Figure 4.24: Potential energy contours of 1-pyrazoline for different values of ϕ_S (degree) and d_S (Å) and the MEPs connecting the stationary points projected PES for the synchronous path.

configuration and in the other direction reaches **TS0** where it bifurcates to **R'** and **R**. Among the trajectories that followed a synchronous path from the reactant, 21 were found to dissociate via this second order saddle point region. The trajectories are projected on the PES and are shown in Figure 4.25. It can be seen that in all of these trajectories, the molecule initially stays in the reactant region and then passes through the **SO1** region. From the **SO1** region they either directly form cyclopropane or form **Int1** which then converts to cyclopropane.

To understand the dynamics of denitrogenation from the second order saddle point region, 100 trajectories were integrated initialized from the **SO1** region. Out of the 100 trajectories, 27 trajectories lead to reactant and 73 trajectories formed products. Of the 73 trajectories that formed products, 67 formed cyclopropane directly from the **SO1** region. To understand the atomic-level mechanisms for product formation from the second order saddle point region,

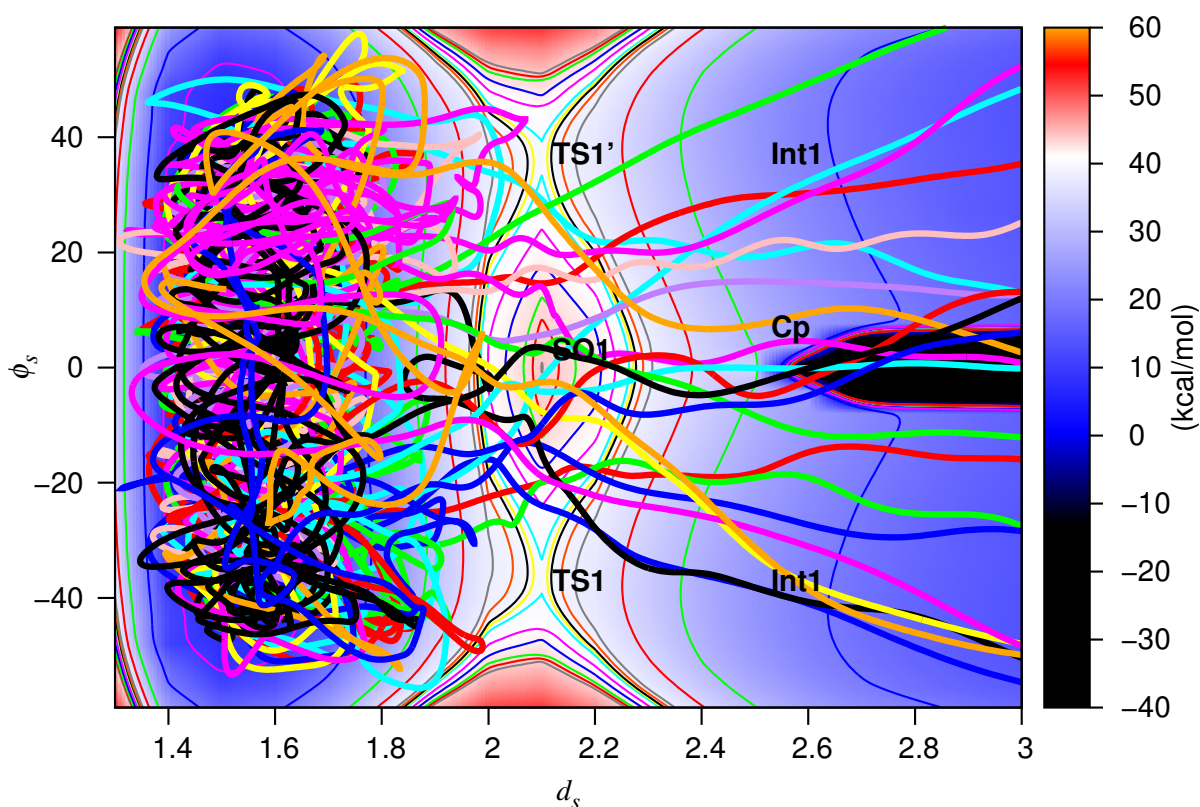


Figure 4.25: Plot of ϕ_S (degree) and d_S (Å) for 15 trajectories projected on the relaxed PES for the synchronous denitrogenation path. The trajectories form cyclopropane from the reactants passing through the **SO1** region.

the ϕ_S and d_S coordinates were followed for all the trajectories that lead to cyclopropane. Figure 4.26 gives the plot of ϕ_S and d_S values for the 67 trajectories projected on the relaxed PES for the synchronous path. It can be seen from Figure 4.26 that most of the trajectories dissociate directly from the second order saddle point region and form products. However, three trajectories dissociate via the **TS1'** region. Of the 73 reactive trajectories, 6 trajectories first form reactant from **SO1** and then N_2 dissociates to form cyclopropane. Interesting dynamics is exhibited by the six trajectories and they are plotted in Figure 4.27. It can be seen that, 5 of the 6 trajectories are bifurcating trajectories. These trajectories start in the **SO1** region and move towards the **TS1** region from where they bifurcate to form the reactant (**R**). After spanning the **R** region for sometime they form **Int1** passing through the **TS1** region. One trajectory directly reaches the **R'** region without following the MEPs from **SO1** and then forms

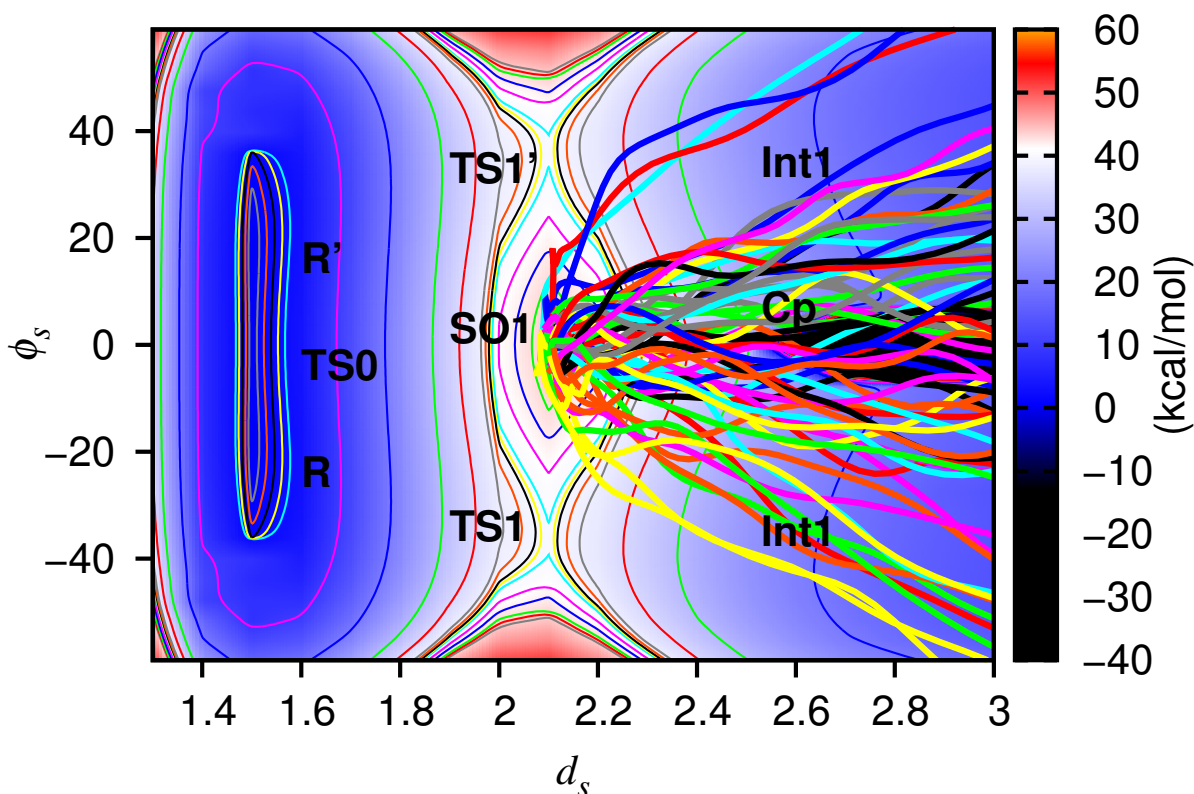


Figure 4.26: Plot of ϕ_S (degree) and d_S (Å) for 73 trajectories projected on relaxed PES for synchronous path. The trajectories directly form cyclopropane from **SO1**.

Int1 through **TS1'**. It should be pointed that these trajectories eventually form cyclopropane. It is interesting to analyze the product distribution of the calculated trajectories. Out of 73 trajectories that form cyclopropane, 18 trajectories lead to SI cyclopropane, 11 trajectories lead to DI cyclopropane, and 44 trajectories lead to cyclopropane with retention of configuration. As seen in Figure 4.26, majority of the trajectories leading to cyclopropane with retention of configuration is expected because most of the trajectories dissociate directly from **SO1** and close to cyclopropane. However, 29 trajectories that lead to SI and DI cyclopropane dissociate via trimethylene diradical intermediate region. These findings indicate the role of **SO1** in the formation of cyclopropane with the retention of configuration. It should be noted that, in several of the trajectories, the N_2 group dissociates axially during its dissociation process. Snapshots of a sample trajectory that dissociates from **SO1** region and leading to single inverted

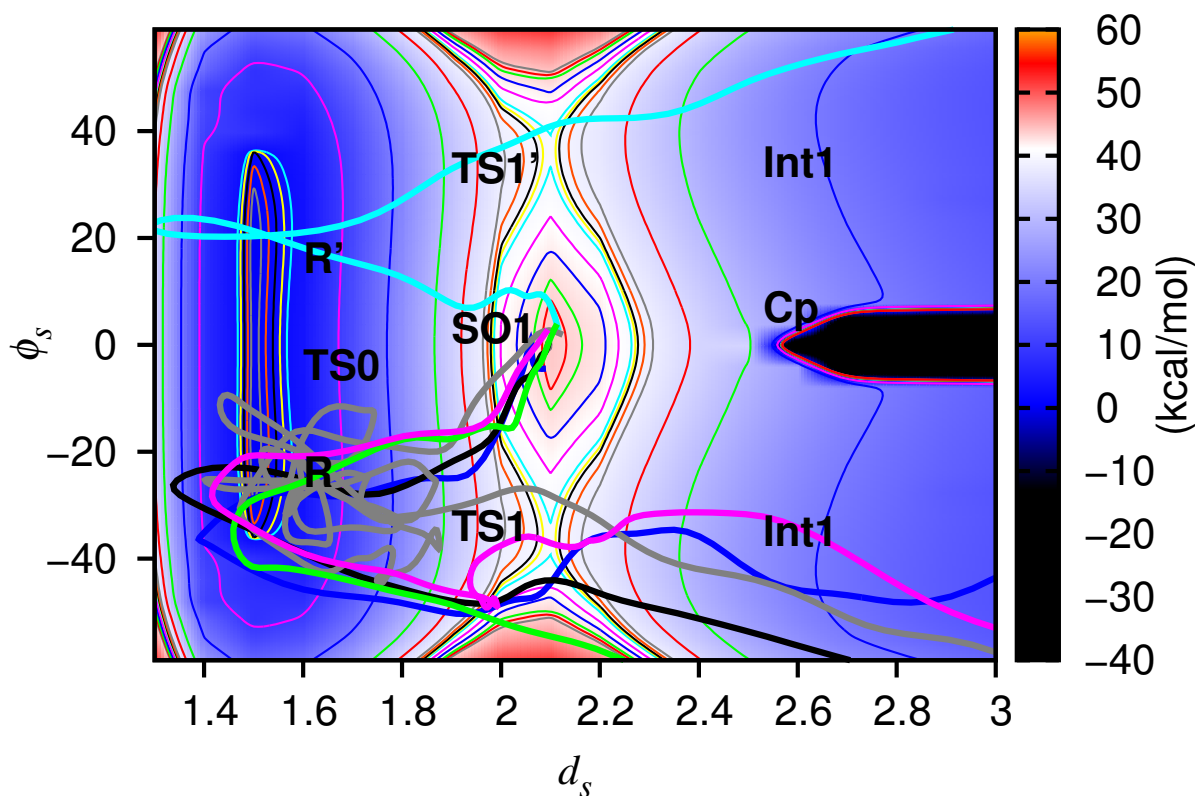


Figure 4.27: Plot of ϕ_S (degree) and d_S (Å) for 6 trajectories projected on relaxed PES for synchronous denitrogenation path. The trajectories labeled and form reactants first before forming cyclopropane.

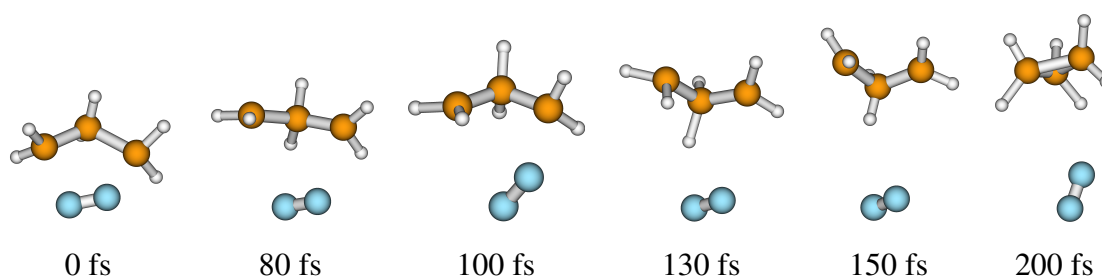


Figure 4.28: Snapshots of a representative trajectory that lead to SI cyclopropane.

cyclopropane is given in Figure 4.28. It can be seen from Figure 4.28 that with the rotation of N_2 group, a rotation of one of the terminal methylene groups happens simultaneously leading to inversion at the carbon center. The trimethylene group then closes to cyclopropane with SI of configuration with the dissociation of N_2 . The $\angle C2C1N5N4$ angle vs $C1-N5$ distance are plotted in Figure 4.29 for 20 representative trajectories that form diradical from **SO1**. It can

be seen from Figure 4.29 that with the increase in the C–N distance, the $\angle\text{C2C1N5N4}$ angle also increases. In many trajectories, a full 360° rotation of the N_2 group is seen. So, although the initial cleavage of C–N bond happens from the **SO1** region, several rotations of terminal methylene groups are observed before it closed to cyclopropane. This set of trajectories lead to formation of racemic mixture of cyclopropane.

4.3.4 Product Energies

During the formation of the products **Cp** and N_2 , the total kinetic energy available to the system is distributed among the translational, rotational, and vibrational degrees of freedom of the products. It is of interest to investigate the internal energies of the products formed. The products were identified by following the two C–N bonds during the course of the trajectory. Products were said to formed when the two C–N bonds reached 15 \AA and C(1)–C(3) bond closed to

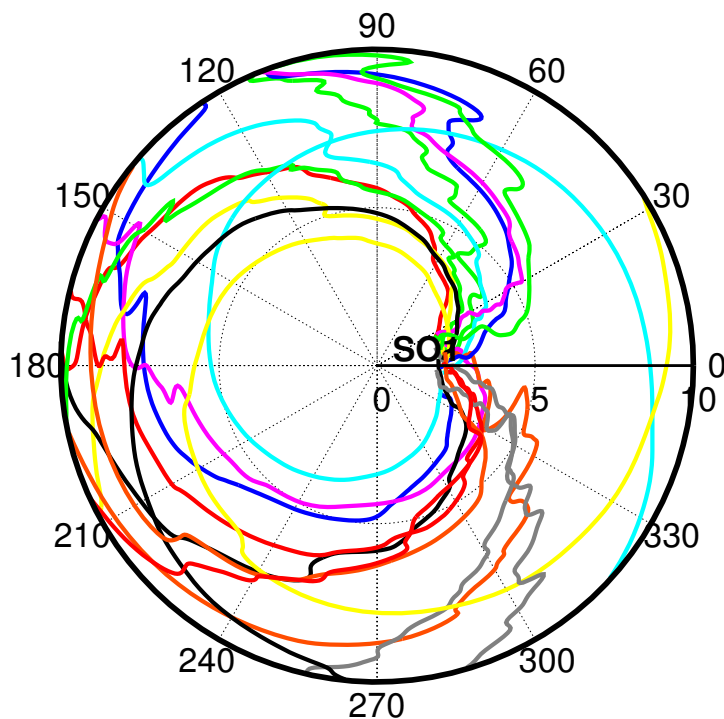


Figure 4.29: Plot of $\angle\text{C2C1N5N4}$ angle (degree) and C1–N5 distance (\AA) for a few representative trajectories.

form the ring. Once, the products are formed, the internal energy of the products, N_2 and Cp were calculated as given elsewhere. The vibrational energy of N_2 was calculated by using the Morse potential model with $D_0 = 79868 \text{ cm}^{-1}$ and $\beta = 2.6898 \text{ \AA}$. Figure 4.30 gives the relative translational energy (E_{rel}), vibrational energy ($E_{\text{v}}(\text{N}_2)$), and rotational energies of N_2 and Cp ($E_{\text{r}}(\text{N}_2)$ and $E_{\text{r}}(\text{Cp})$) for all the reactive trajectories. It can be seen that E_{rel} has a gaussian type distribution with the $\langle E_{\text{rel}} \rangle = 36.6 \text{ kcal/mol}$. The E_{r} and E_{v} for N_2 show exponential type distribution. However, E_{r} for Cp is not an exponential with $\langle E_{\text{r}} \rangle = 7.8 \text{ kcal/mol}$. It is interesting to compare the product energies in the context of asynchronous and synchronous paths followed by the reaction. $\langle E_{\text{rel}} \rangle_{\text{sync}}$ was found to be larger than $\langle E_{\text{rel}} \rangle_{\text{async}}$, 38.3 vs 34.6 kcal/mol, indicating a larger contribution from direct type mechanisms. While the vibrational energies of N_2 are similar for the synchronous and asynchronous paths, the rotational energies are different. $\langle E_{\text{r}}(\text{N}_2) \rangle_{\text{async}} \approx 2 \langle E_{\text{r}}(\text{N}_2) \rangle_{\text{sync}}$ consistent with asynchronous mechanism that involves rotation about C–N bond during the denitrogenation. The internal energy distribution for Cp also shows interesting features. A deconvolution of the rotational energies shows very different distribution for the synchronous and asynchronous trajectories (Figures 4.31 and 4.32). The synchronous trajectories have low rotational energies exhibiting an exponential decay distribution, $\langle E_{\text{r}}(\text{Cp}) \rangle = 4.28 \text{ kcal/mol}$. However, the asynchronous trajectories show a gaussian type distribution with $\langle E_{\text{r}}(\text{Cp}) \rangle = 11.72 \text{ kcal/mol}$ indicating the transfer of angular momentum during the dissociation process. Of particular interest in the present product energy distribution of the trajectories following 2nd order saddle path. These show a larger translational energies, $\langle E_{\text{rel}} \rangle = 39.16 \text{ kcal/mol}$ compared to that of $\langle E_{\text{rel}} \rangle_{\text{sync}}$ and $\langle E_{\text{rel}} \rangle_{\text{async}}$. The N_2 products are found to have low rotational and vibrational energies compared to that seen in the synchronous and asynchronous trajectories.

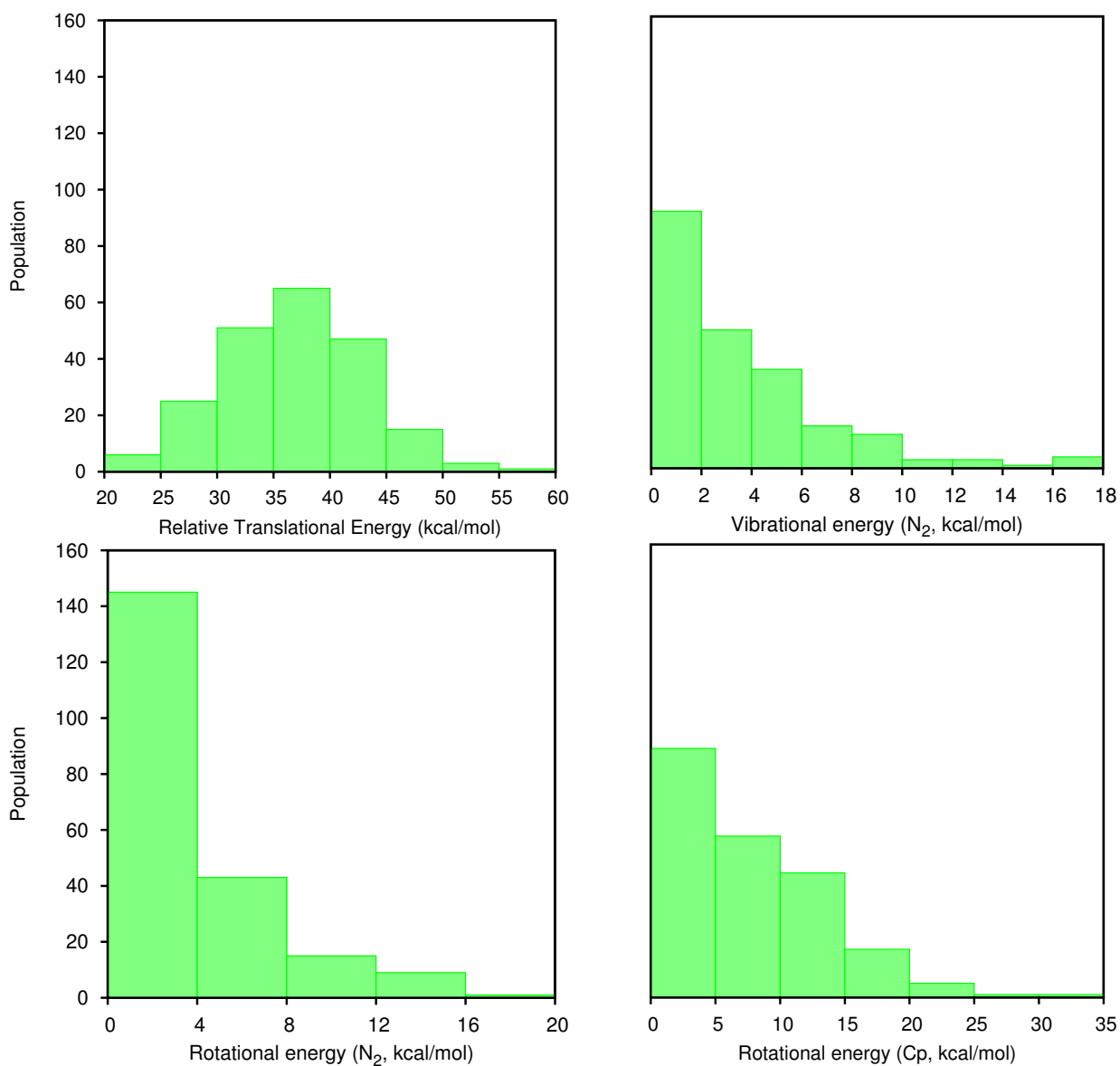


Figure 4.30: Product energies distributions obtained for total reactive trajectories

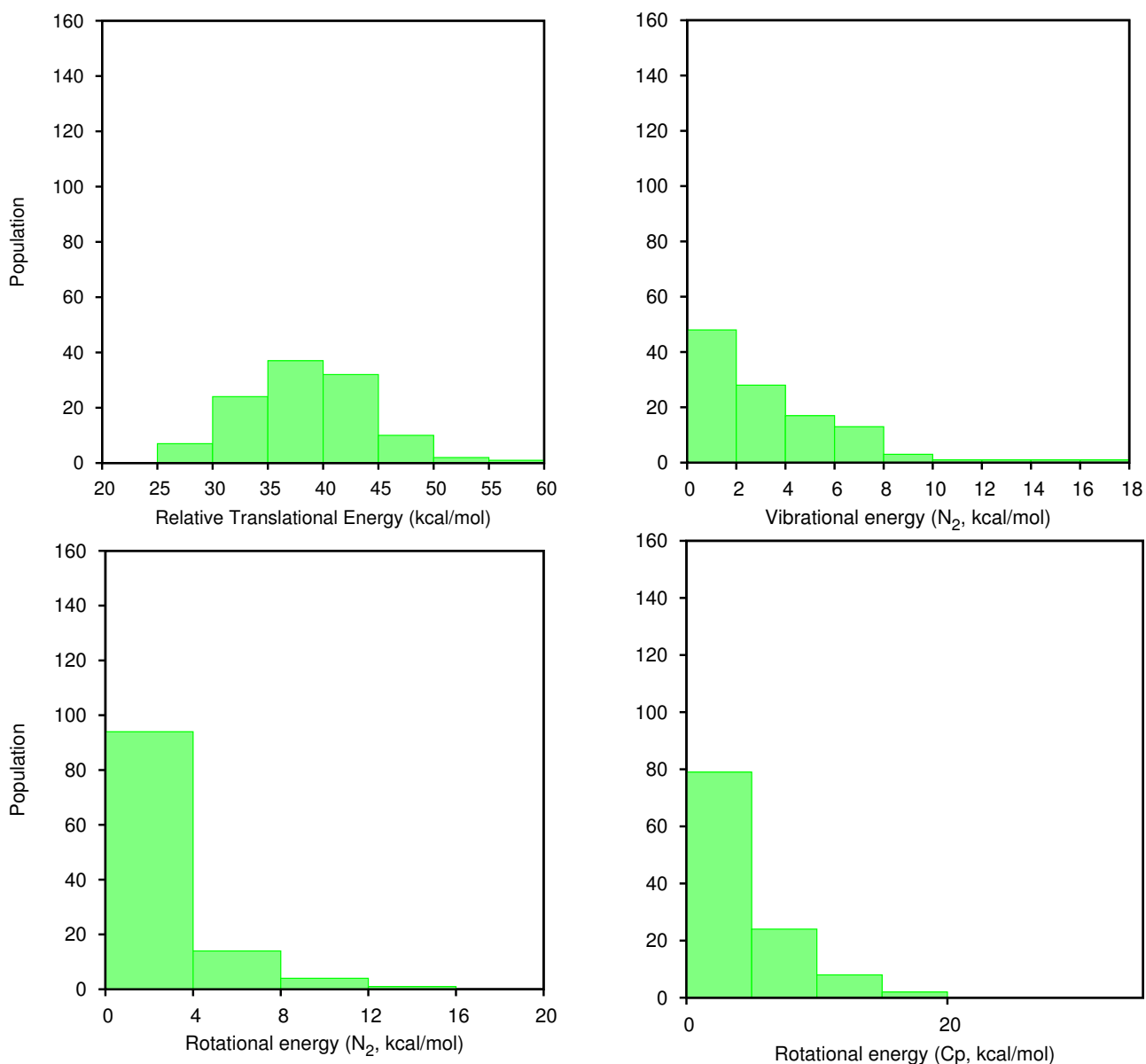


Figure 4.31: Product energies distributions obtained for the synchronous trajectories

4.4 Conclusion

From the experimental studies on thermal denitrogenation of *cis*- and *trans*-3,5-dimethyl-1-pyrazoline, cyclopropane with single inversion of stereochemistry was obtained as the major

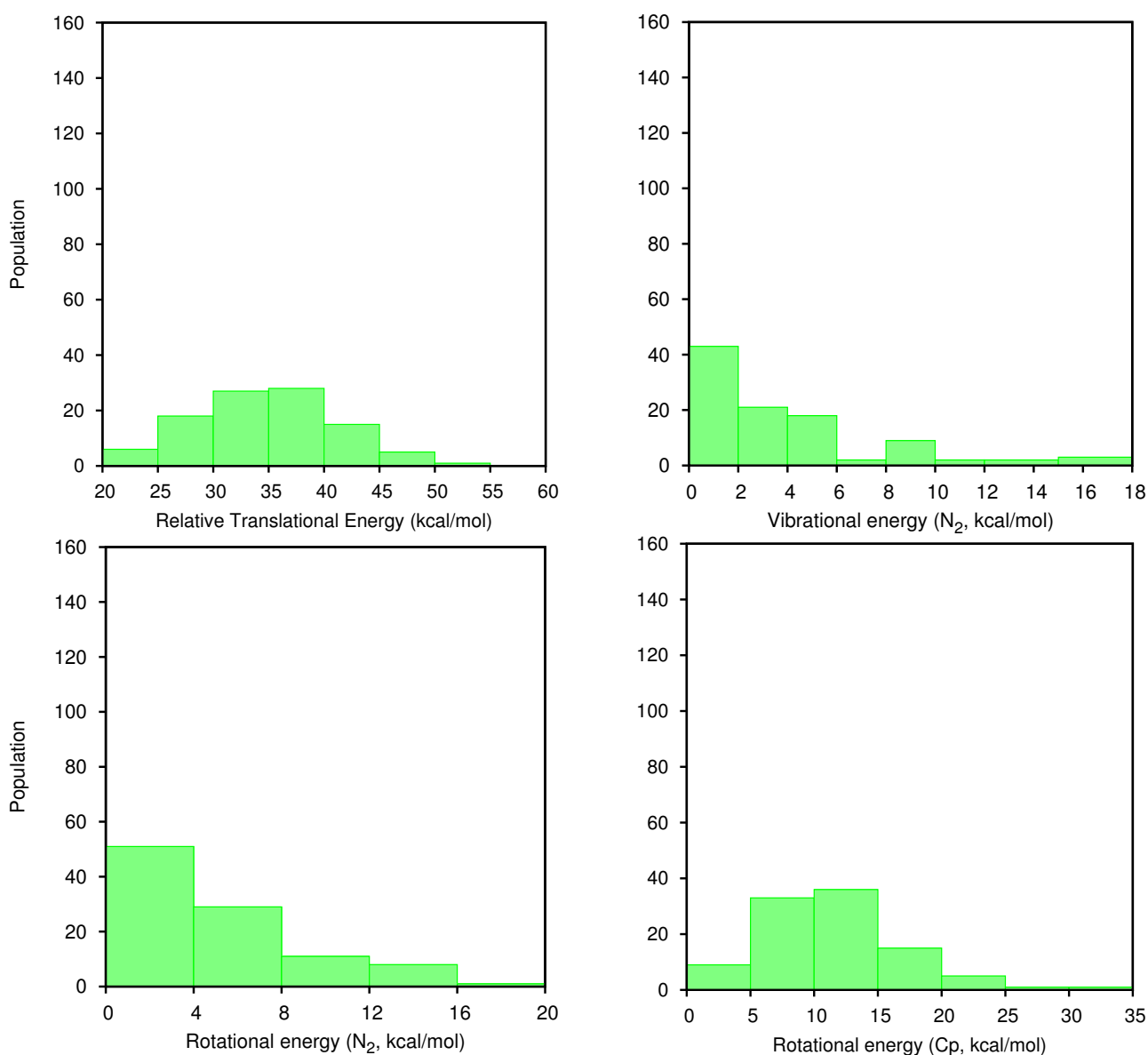


Figure 4.32: Product energies distributions obtained for the asynchronous trajectories

product. To understand the mechanism of thermal denitrogenation, the potential energy profile for 1-pyrazoline was mapped at CASSCF and CASPT2 level of theory and is discussed in Chapter 3. However, the major single inverted cyclopropane obtained from experiments could not be explained from the potential energy profile alone. To understand the post-transition state

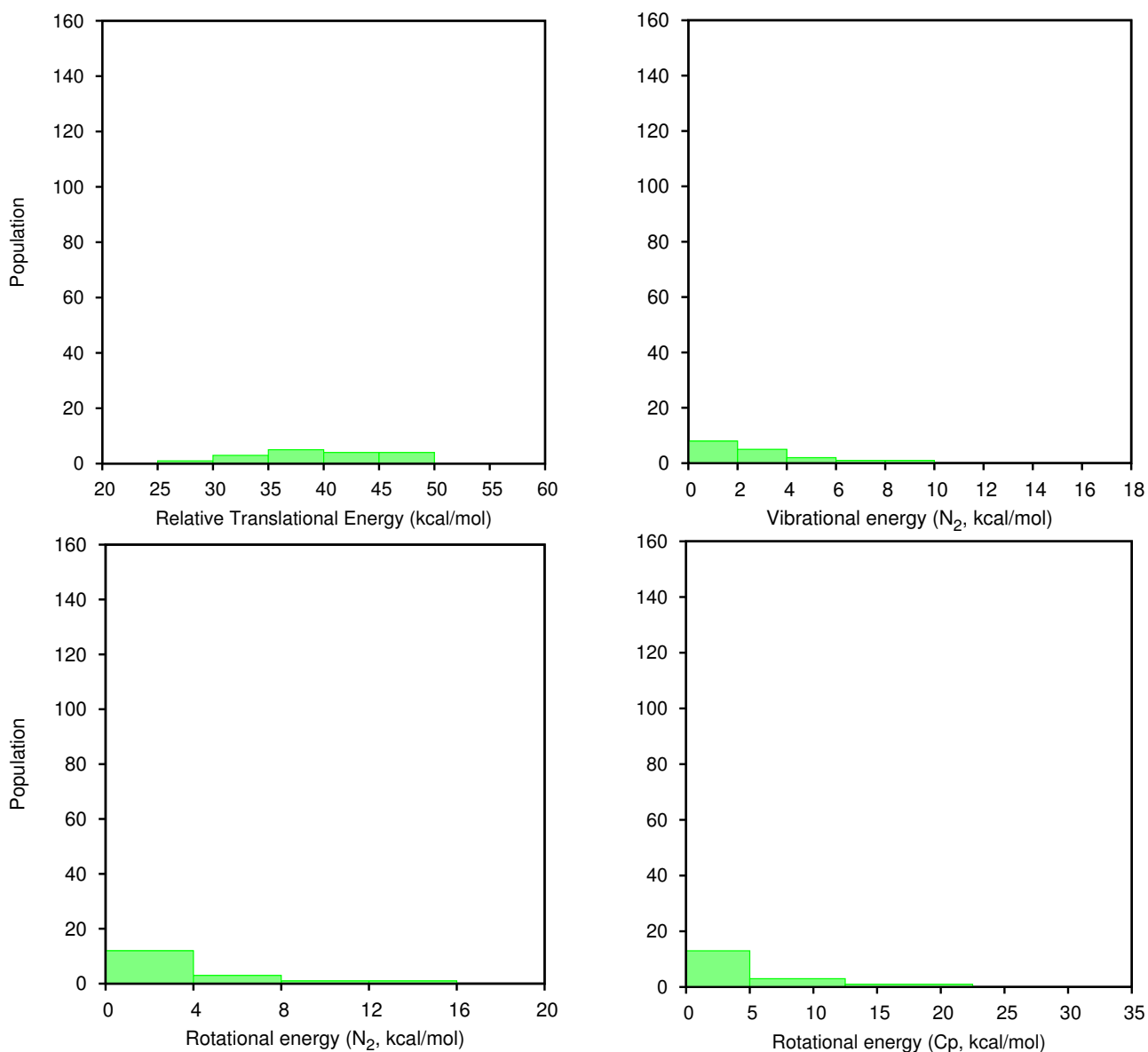


Figure 4.33: Product energies distributions obtained for the trajectories dissociated from second order saddle region

dynamics, ab initio classical trajectory simulations were carried out from six different transition states. It was observed that, most of the trajectories integrated from the synchronous transition state **TS1** region follow MEP whereas most of the trajectories integrated from the asynchronous transition state regions do not follow MEP. A preference for single inverted cyclopropane

formation was observed when trajectories were integrated from all the six transition state regions. To understand the atomic-level mechanism of denitrogenation, trajectory simulations were also performed from the reactant region. From the trajectory simulation results, it was observed that both synchronous and asynchronous denitrogenation paths are almost equally probable. While most of the synchronous trajectories follow MEP, majority of asynchronous trajectories do not follow minimum energy path. Interestingly, some synchronous trajectories dissociate via a second order saddle point. From the simulations it can be observed that a major single inverted cyclopropane is formed followed by double inverted cyclopropane and cyclopropane with the retention of configurations. This is in reasonable agreement with experimentally observed product distribution.⁹⁶ The product distribution was not found to be dictated by the reaction path followed. Both synchronous and asynchronous paths result in similar stereochemical distribution of the products. Rich dynamics is exhibited in these trajectories. Most of the trajectories do not follow MEP. Trajectory calculations performed from the second-order saddle region indicate that this region plays an important role in the formation of the products with retention of configurations.

EFFECT OF SUBSTITUTION ON THE THERMAL DENITROGENATION OF 1-PYRAZOLINE

5.1 Introduction

Thermal denitrogenation of cis- and trans-3,5-dimethyl-1-pyrazoline resulted in trans- and cis-1,2-dimethylcyclopropane as the major product, respectively.⁹⁰ A synchronous denitrogenation of 1-pyrazoline to planar trimethylene diradical intermediate followed by conrotatory closure to cyclopropane was proposed by Mishra et al⁹⁰ to account for the predominant single inversion of stereochemistry obtained from thermal denitrogenation of cis- and trans-3,5-dimethyl-1-pyrazolines. To understand the involvement of planar trimethylene diradical intermediate in the denitrogenation process, Condit and Bergman⁹⁴ studied the denitrogenation of bicyclic azo compounds, exo-2-methyl-3,4-diazabicyclo[3.3.0]oct-3-ene (**1**), endo-2-methyl-3,4-diazabicyclo[3.3.0]oct-3-enes (**2**).⁹⁴, exo-4-methyl-2,3-diazabicyclo[3.2.0]hept-2-ene (**3**), and endo-4-methyl-2,3-diazabicyclo[3.2.0]hept-2-ene (**4**)(Figure 5.1).⁹⁵ Formation of planar trimethylene diradical from these bicyclic azo compounds is expected to be less

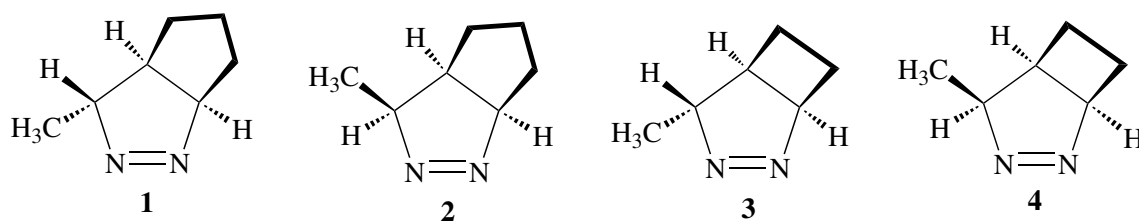


Figure 5.1: exo- and endo-2-methyl-3,4-diazabicyclo[3.3.0]oct-3-enes (**1** and **2**) and exo- and endo-4-methyl-2,3-diazabicyclo[3.2.0]hept-2-enes (**3** and **4**, respectively.)

probable due to ring strain. However, a predominant single inversion of configuration was observed for the products obtained from the thermal denitrogenation of bicyclic azo compounds.⁹⁴ An asynchronous denitrogenation pathway was proposed to account for the major single inverted products obtained from these bicyclic azo compounds. Bergman et al⁹⁶ later studied the denitrogenation of cis- and trans-3-ethyl-5-methyl-1-pyrazoline and proposed a non-linear extrusion of N₂ by a pseudo-conrotation of C-C bonds. A detailed theoretical study for the thermal denitrogenation of 1-pyrazoline and cis- and trans-3,5-dimethyl-1-pyrazolines at 3×3 configuration interaction (CI) /STO-3G level of theory was carried out by Hiberty and Jean⁹⁷. From the ab initio calculations, two asynchronous denitrogenation pathways were found to be energetically more favourable than the synchronous denitrogenation paths.

In Chapter 3, the detailed potential energy profiles for denitrogenation of 1-pyrazoline obtained using CASSCF and CASPT2 methods with various basis sets were discussed. The ab initio dynamics of denitrogenation of 1-pyrazoline was discussed in Chapter 4. From the potential energy profile for denitrogenation of 1-pyrazoline, the synchronous denitrogenation path was found to be 6-8 kcal/mol lower in energy than the asynchronous denitrogenation paths. The barrier obtained for synchronous denitrogenation path at CASSCF(4,4)/6-31+G* (40.04 kcal/mol) for 1-pyrazoline agrees well with the experimental activation energy (42.4 kcal/mol). However, ab initio classical trajectory simulations reveal that both synchronous and asynchronous denitrogenation paths to be equally probable and majority of the trajectories do not follow MEP. The product distribution obtained from the ab initio classical trajectory

simulations indicated a major SI cyclopropane formation. However, the fraction of SI products ($\sim 45\%$) were less compared to that of the experimentally observed SI product distribution of 66 and 72% for *cis* and *trans*-3,5-dimethyl-1-pyrazoline, respectively. The discrepancy in the simulation results can be attributed to (i) substituent effect (ii) inadequacy of the CASSCF method to describe the dynamics of the reaction (iii) non-adiabatic effects resulting from crossing of PESs in certain regions of the PES. In the present study, the effect of substitution on the denitrogenation process is investigated by considering four systems- *cis* and *trans*-3,5-dimethyl-1-pyrazoline and *exo*- and *endo*-2-methyl-3,4-diazabicyclo[3.3.0]oct-3-enes. The energy profiles for denitrogenation paths were mapped using CASSCF methods. To understand the substitution effects on the dynamics of denitrogenation mechanism, *ab initio* classical trajectory simulations were carried out for *trans*-3,5-dimethyl-1-pyrazoline.

5.2 Computational Details

The molecules considered in the study are given in Figure 5.2. The potential energy profiles for the thermal denitrogenation of *cis* and *trans*-3,5-dimethyl-1-pyrazoline and *exo*- and *endo*-2-methyl-3,4-diazabicyclo[3.3.0]oct-3-enes were mapped by using CASSCF methods⁴ with 6-31+G* basis set. The CASSCF calculations were performed with (4,4) active space. The active space for CASSCF calculation included both the σ , σ^* orbitals of C–N bonds. All the stationary point structures were characterized by computing the harmonic vibrational frequen-

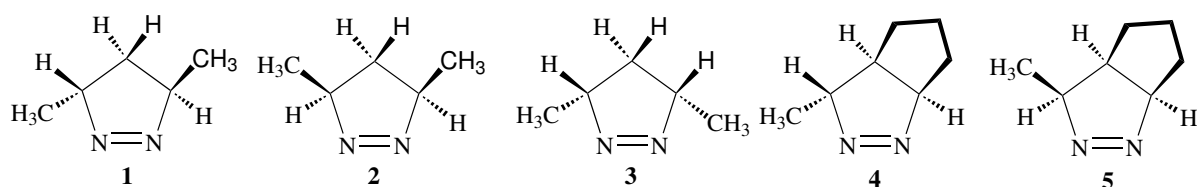


Figure 5.2: Molecules considered in the present study: (3R, 5R) *trans*-3,5-dimethyl-1-pyrazoline (**1**), (3R, 5S) *cis*-3,5-dimethyl-1-pyrazoline (**2**), (3S, 5R) *cis*-3,5-dimethyl-1-pyrazoline (**3**), (3R, 5R) *exo*-2-methyl-3,4-diazabicyclo[3.3.0]oct-3-enes (**4**), and (3S, 5R) *endo*-2-methyl-3,4-diazabicyclo[3.3.0]oct-3-enes (**5**).

cies. TSs and intermediates were connected by following the IRC. To understand the effect of substitution on dynamics of denitrogenation of 1-pyrazoline, ab initio classical trajectory simulations were performed for trans-3,5-dimethyl-1-pyrazoline at CASSCF(4,4)/6-31+G* level of theory.^{4,113–116} The initial coordinates and momenta for the trajectory simulations were selected by using microcanonical sampling procedure. The procedure used for the calculation of total energy is same as that discussed in Chapter 4 for the thermal denitrogenation of 1-pyrazoline. The total amount of energy available to trans-3,5-dimethyl-1-pyrazoline at experimental temperature (493.45 K) was calculated with respect to **TS4f** by adding the ZPE (E_{ZPE}), average vibrational energy (E_{vib}), average rotational energy (E_{rot}), and an excess energy of RT along the reaction coordinate to the classical barrier of **TS4f** (E_{a}). The total energy is then given by

$$E_{\text{total}} = E_{\text{a}} + E_{\text{ZPE}} + E_{\text{vib}} + E_{\text{rot}} + RT \quad (5.1)$$

The ZPE, average vibrational energy, average rotation energy, and RT energy for **TS4f** at 493.45 K are 100.30, 5.05, 1.47, and 0.98 kcal/mol, respectively and the classical barrier for $E_{\text{a}}(\mathbf{TS4f})$ is 52.36 kcal/mol. The total amount of energy (E_{total}) available to trans-3,5-dimethyl-1-pyrazoline at experimental temperature is 160.16 kcal/mol. The trajectories were integrated from the reactant region by using velocity-Verlet algorithm with a stepsize of 0.3 fs for 2 ps. A total of 500 trajectories were integrated from the reactant (trans-3,5-dimethyl-1-pyrazoline) region. The energetics and dynamics simulations were performed using Gaussian 09¹¹⁸ software package.

5.3 Results and Discussion: Energetics

To understand the effect of substitution on the energetics of denitrogenation of 1-pyrazolines, potential energy profile for trans and cis-3,5-dimethyl-1-pyrazoline and exo- and endo-2-methyl-3,4-diazabicyclo[3.3.0]oct-3-enes were mapped at CASSCF(4,4)/6-31+G* level of theory. The

two possible denitrogenation paths were considered in this study: (1) synchronous cleavage of the two C–N bonds, and (2) asynchronous cleavage of the two C–N bonds.

5.3.1 Synchronous Cleavage of the Two C–N Bonds

Trans-3,5-dimethyl-1-pyrazoline. Trans-3,5-dimethyl-1-pyrazoline contains two asymmetric carbon atoms (C(3) and C(5)) and can exist as two different stereoisomers (enantiomers): (3R, 5R) and (3S, 5S) trans-3,5-dimethyl-1-pyrazoline that are isoenergetic. Each of the stereoisomer can have two different envelope conformations (**R** and **R'**) as seen in 1-pyrazoline with a barrier of 0.21 kcal/mol corresponding to **TS0**. A schematic representation of synchronous denitrogenation of (3R, 5R) and (3S, 5S) trans-3,5-dimethyl-1-pyrazoline leading to cyclopropane formation is given in Figure 5.3. As can be seen from Figure 5.3, the synchronous denitrogenation of (3S, 5S)-trans-3,5-dimethyl-1-pyrazoline leads to the diradical trans-pentane-2,4-diyl intermediate. Trans-pentane-2,4-diyl intermediate can close to cyclopropane via con or dis-rotation of terminal methylene group. Conrotatory closure of trans-pentane-2,4-diyl leads to (1R, 2S) cis-1,2-dimethylcyclopropane or (1S, 2R) cis-1,2-dimethylcyclopropane. In (1R, 2S) cis-1,2-dimethylcyclopropane, inversion happens at the C(1) carbon center and in (1S, 2R) cis-1,2-dimethylcyclopropane, inversion happens at the C(1) carbon center and in (1S,

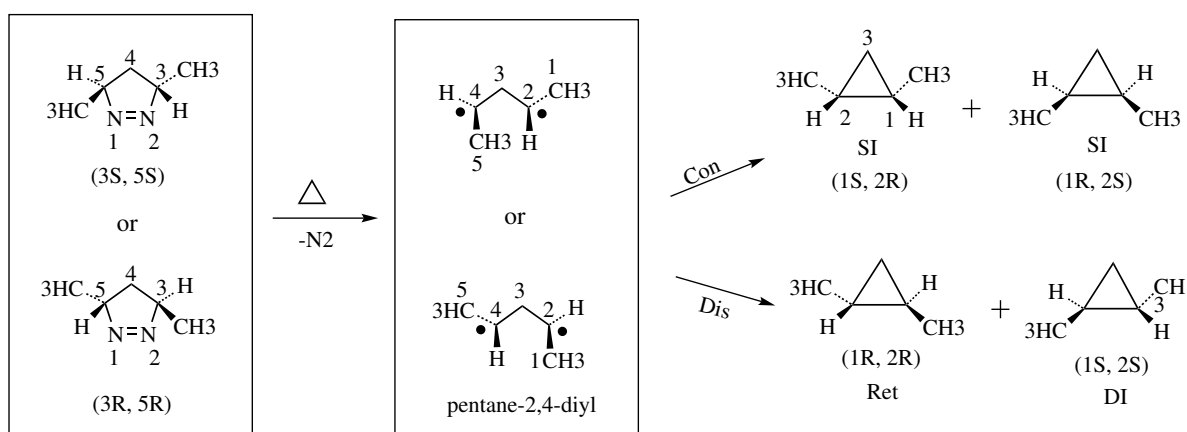


Figure 5.3: A schematic representation of synchronous denitrogenation of the isomers trans-3,5-dimethyl-1-pyrazoline leading to cyclopropane.

2R) cis-1,2-dimethylcyclopropane, inversion happens at the C(2) carbon center. Similarly, two disrotatory pathways for closing of trans-pentane-2,4-diyl to cyclopropane are also possible. One pathway leads to cyclopropane with double retention of configuration ((1S, 2S) trans-1,2-dimethylcyclopropane) and the other pathway leads to cyclopropane with double inversion of configuration ((1R, 2R) trans-1,2-dimethylcyclopropane). Denitrogenation can also happen from (3R, 5R) trans-3,5-dimethyl-1-pyrazoline. Since, the energetics of the denitrogenation paths of both the (3R, 5R) and (3S, 5S) isomers of trans-3,5-dimethyl-1-pyrazoline are expected to be similar, in the present study denitrogenation of only (3R, 5R) trans-3,5-dimethyl-1-pyrazoline was considered. The potential energy profile for the synchronous denitrogenation of

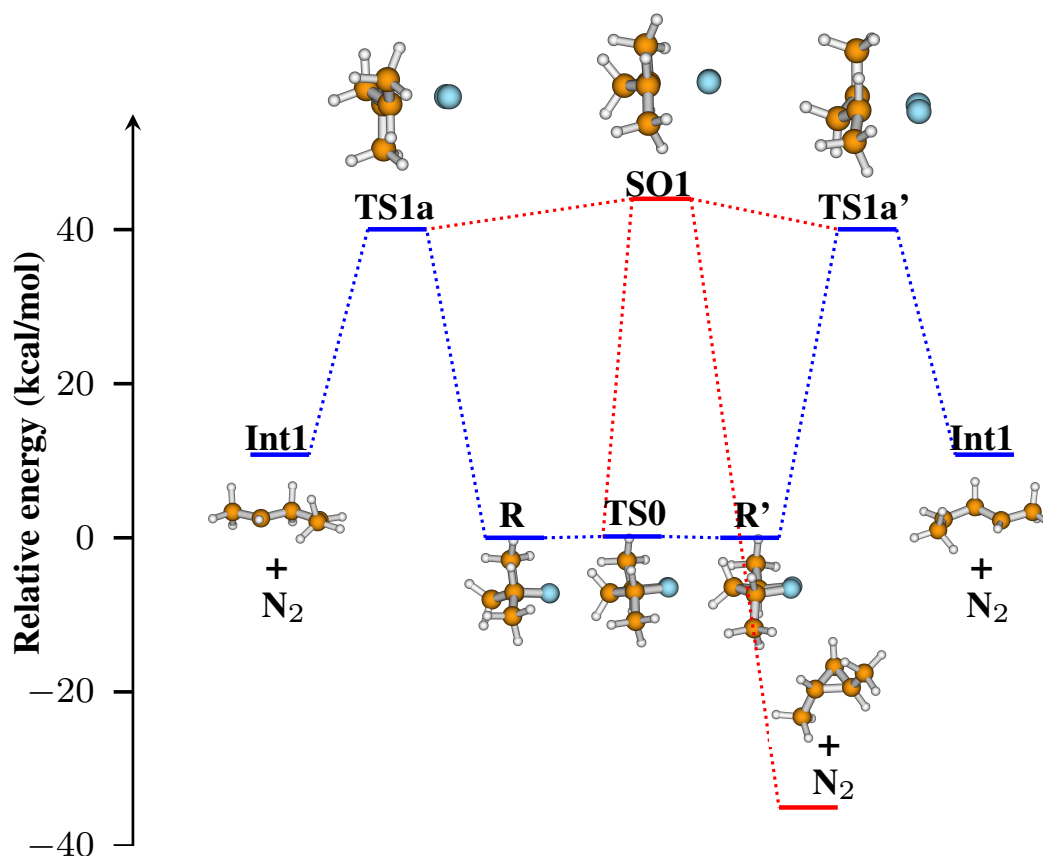


Figure 5.4: Synchronous denitrogenation paths for (3R, 5R) trans-3,5-dimethyl-1-pyrazoline obtained at CASSCF(4,4)/6-31+G* level of theory.

Table 5.1: Relative energies (kcal/mol) of stationary points along synchronous denitrogenation path for substituted 1-pyrazolines (**1** to **5**) obtained at CASSCF(4,4)/6-31+G* level of theory

Structure	1	2	3	4	5
TS0	0.21	0.45	0.27	0.32	0.30
TS1a	39.57	39.51	39.32	37.87	38.82
SO1	43.70	43.33	43.14		
Int1	10.76	11.24	11.25	10.52	10.38
TS1b	12.18	12.29	12.31	13.12	12.88
TS1c	11.25	11.39	11.42	12.76	12.45
Int1c	11.18	11.09	11.17	11.57	11.30
TS1d	11.33	11.42	11.41	12.98	12.69
TS1e	12.03	11.93	11.86	12.63	12.73
Int1e	10.76	11.24	11.25	10.52	10.38
TS1f	12.18	12.29	12.31	13.12	12.88

(3R, 5R) trans-3,5-dimethyl-1-pyrazoline (**1**) mapped at CASSCF(4,4)/6-31+G* level of theory is shown in Figure 5.4 and the energetics are given in Table 5.1. The barrier for synchronous denitrogenation of 1-pyrazoline via **TS1** was found to be 40.04 kcal/mol (Chapter 3). As can be seen from Table 5.1, with the substitution of methyl group at C(3) and C(5) carbon atoms, the barrier for this path decreases by ~ 1 kcal/mol. A similar lowering of activation energies by ~ 2 kcal/mol was also observed in the experimental studies for thermal denitrogenation of (3R, 5R) trans-3,5-dimethyl-1-pyrazoline (40.02 kcal/mol) compared to that for 1-pyrazoline (42.04 kcal/mol).⁹⁰ It is to be pointed that the calculated activation energies obtained for synchronous denitrogenation of trans-3,5-dimethyl-1-pyrazoline agrees well with the experimental energies (39.57 kcal/mol). A second order saddle point **SO1**, which is only 4 kcal/mol above **TS1a** was also found to exist in the potential energy profile for synchronous denitrogenation path. One of the normal mode vectors associated with the imaginary frequencies connects **SO1** to the synchronous transition states **TS1a** and **TS1a'** and the other vector connects **SO1** to **TS0** in one direction and cyclopropane with retention of configuration in the other direction. The synchronous transition state **TS1a** connects reactant to **Int1**. **Int1** can now close to cyclopropane via con or disrotation of terminal methylene groups. The potential energy profile for closing of

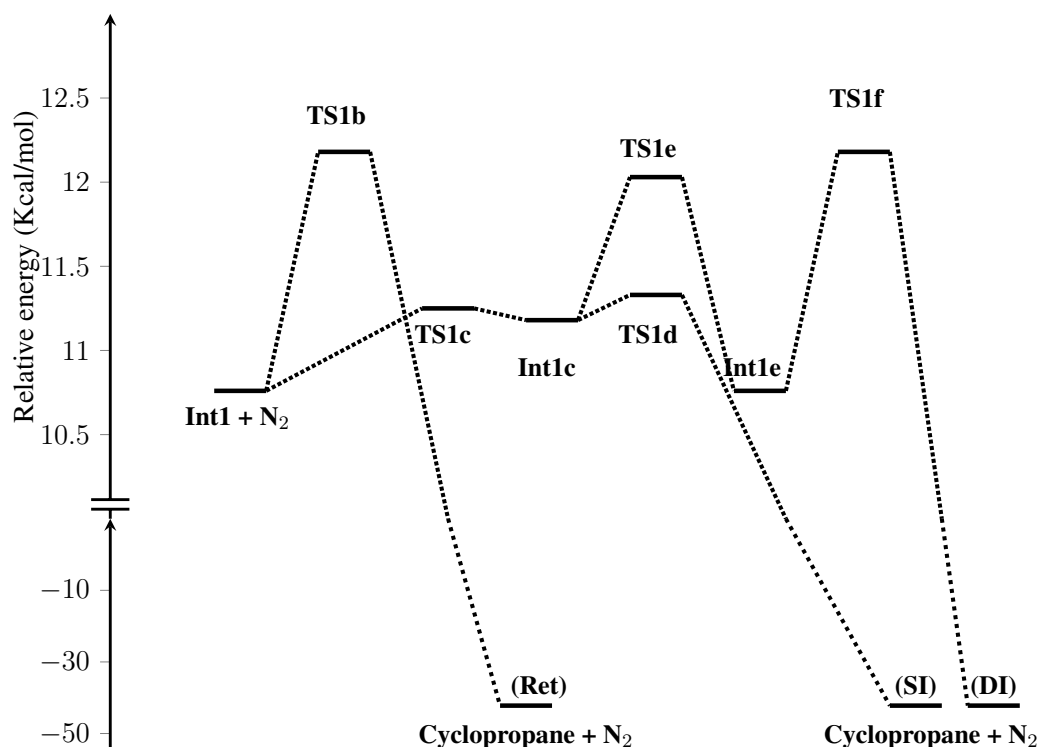


Figure 5.5: Potential energy profile for conversion of **Int1** to cyclopropane obtained for trans-3,5-dimethyl-1-pyrazoline at CASSCF(4,4)/6-31+G* level of theory.

Int1 to cyclopropane obtained for (3R, 5R) trans-3,5-dimethyl-1-pyrazoline is given in Figure 5.5 and the energetics are given in Table 5.1. As can be seen from Figure 5.5 and Table 5.1, the **Int1** region of the potential energy profile is very flat. The relative energies of stationary points along the conrotation and disrotation paths are within 2.5 kcal/mol. Barriers obtained for conrotatory and disrotatory closure of pentane-2,4-diyl to 1,2-dimethylcyclopropane are similar to that obtained for propane-1,3-diyl to cyclopropane (Chapter 3). No significant substitution effects on energetics of synchronous denitrogenation paths were observed.

Cis-3,5-dimethyl-1-pyrazoline. Cis-3,5-dimethyl-1-pyrazoline contains two asymmetric carbons atoms (C(3) and C(5)). Thus, two different stereoisomers of cis-3,5-dimethyl-1-pyrazoline are possible: (3R, 5S) and (3S, 5R) cis-3,5-dimethyl-1-pyrazoline (**2** and **3**). Here again, each isomer can exist in the two envelope forms with a barrier of 0.18 kcal/mol for their interconversion. In the present study, potential energy profile for the denitrogenation of both the isomers

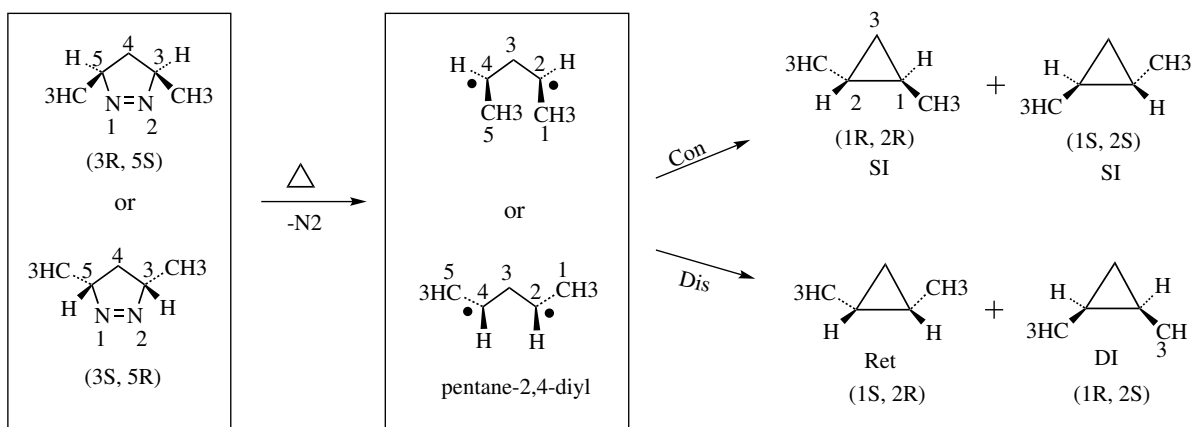


Figure 5.6: A schematic representation of synchronous denitrogenation of the isomers of cis-3,5-dimethyl-1-pyrazoline leading to cyclopropane formation.

were mapped. A schematic representation of the synchronous denitrogenation of the isomers of cis-3,5-dimethyl-1-pyrazoline leading to cyclopropane formation is given in Figure 5.6. Synchronous cleavage of cis-3,5-dimethyl-1-pyrazoline leads to cis-pentane-2,4-diyl intermediate that can close to cyclopropane via con or dis rotation of terminal methylene groups. Conrotatory closure of cis-pentane-2,4-diyl leads to (1S, 2S) and (1R, 2R) 1,2-dimethylcyclopropane. Disrotatory closure of the terminal methylene group of cis-pentane-2,4-diyl intermediate leads to cyclopropane with DI and Ret of configuration. The potential energy profile for the synchronous denitrogenation of the two forms (3R, 5S) and (3S, 5R) of cis-3,5-dimethyl-1-pyrazolines were mapped at CASSCF(4,4) methods. Both the isomers follow similar reaction paths and energetics and stationary point structures are also similar. The energetics of both the isomers (**2** and **3**) of cis-3,5-dimethyl-1-pyrazolines are given in Table 5.1. It can be seen from Table 5.1, that the energies of the stationary point structures are within a difference of 1 kcal/mol. The barrier for synchronous denitrogenation for **2** and **3** were found to be 39.51 kcal/mol and 39.32 kcal/mol, respectively. This barrier energies obtained are close to the experimental activation energy ($E_a^{\text{expt}} = 40.3$ kcal/mol) obtained for cis-3,5-dimethyl-1-pyrazoline.⁹⁰ It should be noted that energetics of cis isomers is also close to that of the trans isomers.

Exo and endo-2-methyl-3,4-diazabicyclo[3.3.0]oct-3-ene. To understand the effect of ring

strain on the energetics of the synchronous denitrogenation path, the potential energy profiles for exo and endo-2-methyl-3,4-diazabicyclo[3.3.0]oct-3-ene were also mapped at CASSCF(4,4)/6-31+G* level of theory. (3R, 5R) exo-2-methyl-3,4-diazabicyclo[3.3.0]oct-3-ene and (3S, 5R) endo-2-methyl-3,4-diazabicyclo[3.3.0]oct-3-ene isomers were only considered in the present study. The energetics of stationary point structures along synchronous denitrogenation paths obtained for exo and endo-2-methyl-3,4-diazabicyclo[3.3.0]oct-3-ene are given in Table 5.1. It can be seen from Table 5.1 that, the barriers for synchronous denitrogenation paths (**TS1a**) further decrease by 1-2 kcal/mol with the substitution of alkyl chain at C(3) and C(4) carbon atom. However, ring strain effect on the relative energies of **Int1** were not observed. The **Int1** energies obtained for both the molecules are comparable to that obtained for cis- and trans-3,5-dimethyl-1-pyrazoline. A slight increase in barriers \sim 1-2 kcal/mol for conrotatory and disrotatory closure of **Int1** to cyclopropane were observed. However, for both the molecules, the relative energies of stationary points along conrotatory and disrotatory closure of **Int1** are within 3 kcal/mol.

5.3.2 Asynchronous Cleavage of the two C–N Bonds

Asynchronous cleavage involves the unsymmetrical breaking of the two C–N σ bonds. The potential energy profiles for two different denitrogenation paths were mapped: (i) asynchronous step-wise elimination of N₂ and (ii) asynchronous concerted elimination of N₂.

5.3.2.1 Asynchronous Step-wise Elimination of N₂

Asynchronous cleavage of one of the C–N σ bonds from the reactant accompanied by a clockwise or anticlockwise rotation of N₂ group around C–N bond leads to diazenyl diradical (**DZ**) intermediate. Two different denitrogenation paths that differ in the orientation of methylene group at C(3) (planar and pyramidal) were obtained for the asynchronous cleavage of C–N bond. In one path, the terminal methylene group at C(3) is planar in nature ($\phi_3 \sim -45^\circ$ and ϕ_4

$\sim 160^\circ$) and in the other path, the terminal methylene group is pyramidal in nature ($\phi_3 \sim -72^\circ$ and $\phi_4 \sim 90^\circ$). Both the paths are discussed below.

The potential energy profiles obtained for *trans*-3,5-dimethyl-1-pyrazoline at CASSCF(4,4)/6-31+G* level of theory involving planar and pyramidal intermediates are given in Figures 5.7 and 5.8, respectively, and their energetics obtained for all the five substituted pyrazolines are given in Table 5.2. The **DZ** region of the potential energy surface is very flat. Several rotational isomers of **DZ** intermediate that differ in the orientation of methylene group at C(3) and azo group about C(5)–N(1) bond exist on the PES. The energetics of all the stationary points along the **DZ** region of PES lie within 3 kcal/mol. Cleavage of the C(5)–N(1) bond can happen from intermediates **Int3a**, **Int3b**, **Int4a**, and **Int4b**. For the **DZ** intermediates **Int3a** and **Int3b**, two different paths were obtained for the cleavage of C(5)–N(1) bond: (1)

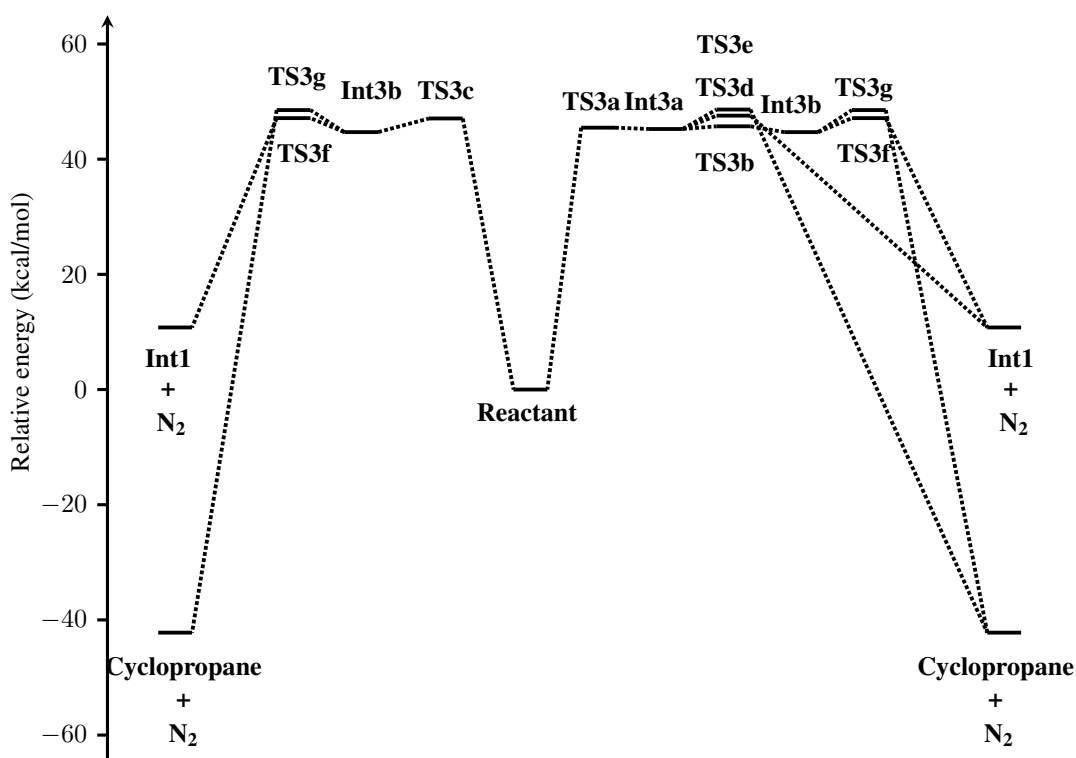


Figure 5.7: Potential energy profile for asynchronous step-wise denitrogenation path (planar intermediate) for *trans*-3,5-dimethyl-1-pyrazoline obtained at CASSCF(4,4)/6-31+G* level of theory.

a simple stretching of C–N bond which leads to **Int1** that can close by con or dis rotation to give cyclopropane or form propene by H-transfer and (2) a $S_{\text{H}2}$ pathway which leads to a SI cyclopropane by displacement of N_2 . Similarly, for the **DZ** intermediates **Int4a** and **Int4b**, two different paths were obtained for the cleavage of C(5)–N(1) bond: (1) isomerization of **Int4b** to a four membered cyclic intermediate **Int4f** through the transition state **TS4f** followed by a cleavage of N_2 from **Int4f** to give **Int1** and (2) a $S_{\text{H}2}$ pathway which leads to a SI cyclopropane. All the stationary points along asynchronous step wise denitrogenation path obtained for 1-pyrazoline could be optimized for all the five different substituted pyrazolines. It can be seen from Table 5.2 that the relative energies of the stationary point structures obtained for the different substituents lie within a difference of ~ 3 kcal/mol. No significant substituent effects on energetics were observed. For all the five substituted pyrazolines, the barriers for

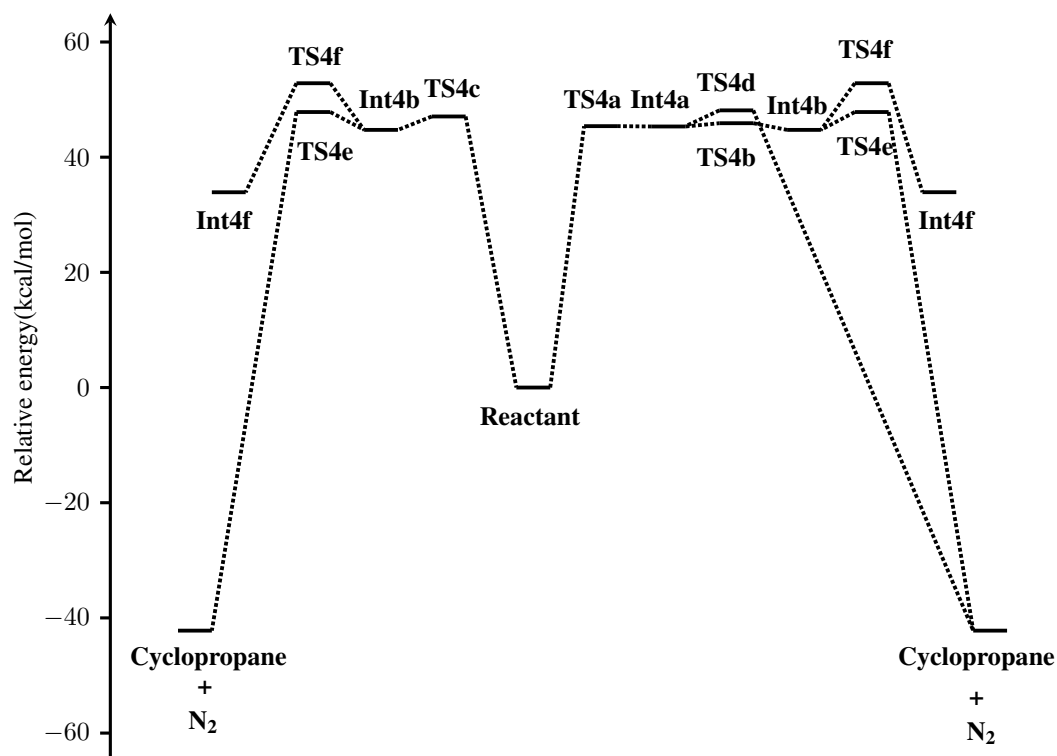


Figure 5.8: Potential energy profile for asynchronous step-wise denitrogenation path (pyramidal intermediate) for trans-3,5-dimethyl-1-pyrazoline obtained at CASSCF(4,4)/6-31+G* level of theory.

Table 5.2: Relative energies (kcal/mol) of stationary point structures along asynchronous denitrogenation paths obtained for substituted pyrazolines at CASSCF(4,4)/6-31+G* level of theory^a

Structure	1	2	4	5
Asynchronous step-wise elimination of N₂				
TS3a	45.65 (40.51)	45.60 (41.13)	44.53 (39.94)	46.85 (42.32)
Int3a	45.10 (40.29)	45.37 (40.99)	44.43 (39.91)	46.21 (42.17)
TS3b	46.65 (41.89)	46.45 (41.80)	45.01 (40.32)	47.21 (42.98)
Int3b	46.13 (41.61)	45.93 (41.56)	44.30 (39.80)	44.51 (40.09)
TS3c	49.21 (44.69)	47.59 (43.05)	47.60 (43.01)	48.50 (43.71)
TS3d	47.54 (41.49)	47.21 (41.19)	46.47 (40.29)	47.76 (42.40)
TS3e	47.95 (43.48)	48.65 (44.31)	48.53 (44.19)	52.92 (48.68)
TS3f	47.52 (41.59)	47.38 (41.45)	45.92 (39.87)	46.47 (40.46)
TS3g	49.85 (45.20)	49.77 (45.38)	49.92 (45.51)	51.72 (47.49)
TS4a	45.41 (40.82)	46.09 (41.39)	47.65 (43.31)	49.63 (45.26)
Int4a	45.15 (40.78)	46.00 (41.58)	46.90 (42.78)	48.12 (44.03)
TS4b	46.41 (41.75)	47.34 (42.43)	47.41 (43.29)	48.79 (44.51)
Int4b	45.82 (41.47)	46.61 (42.07)	45.48 (42.07)	46.29 (41.96)
TS4c	47.25 (42.76)	48.15 (43.70)	49.32 (43.38)	48.89 (45.43)
TS4d	47.95 (43.48)	48.50 (44.97)	49.40 (44.99)	54.39 (49.96)
TS4e	49.06 (44.53)	49.49 (44.97)	50.51 (45.82)	52.78 (48.35)
TS4f	52.36 (48.97)	52.27 (49.00)	51.41 (48.27)	51.98 (48.78)
Int4f	31.46 (30.40)	31.90 (30.94)	33.34 (32.37)	33.38 (32.32)
Asynchronous concerted elimination of N₂				
TS5	50.74(46.22)	49.14 (44.69)		

^aNumber in the parentheses are zero point energy corrected values.

asynchronous step-wise denitrogenation paths were 6-10 kcal/mol higher in energy than that for the synchronous denitrogenation paths.

5.3.2.2 Asynchronous concerted elimination of N₂

This path involves a concerted asynchronous cleavage of C–N bond accompanied by a displacement of N₂ by carbon radical center. It leads to single inverted cyclopropane with the elimination of N₂. The transition state for this path could be optimized only for cis and trans-3,5-dimethyl-1-pyrazoline. The potential energy profiles obtained for cis and trans-3,5-dimethyl-1-pyrazoline at CASSCF(4,4)/6-31+G* level of theory are given in Figure 5.9 and the energetics of the

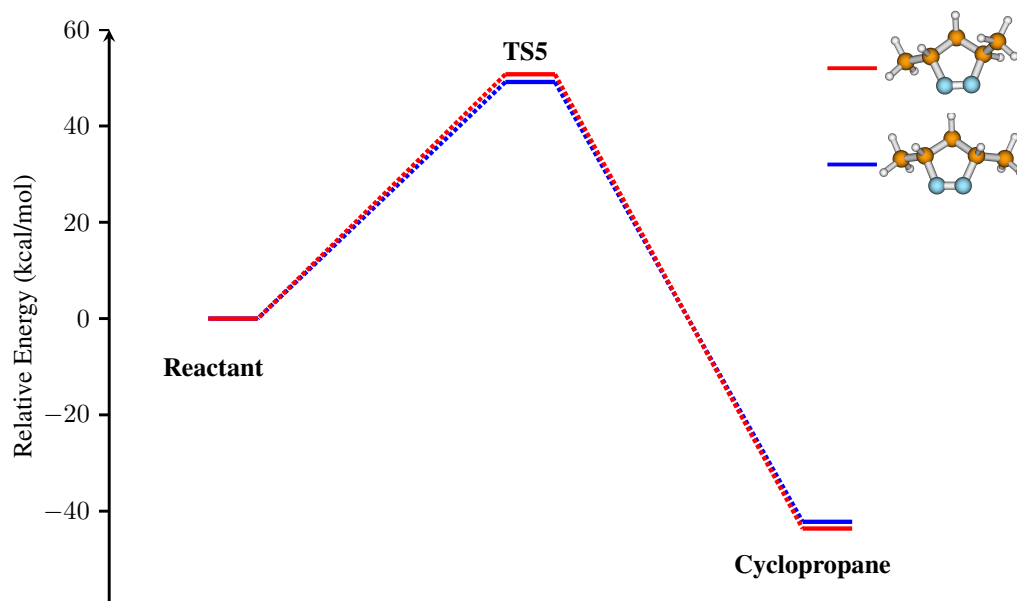


Figure 5.9: Asynchronous concerted denitrogenation path obtained for cis and trans-3,5-dimethyl-1-pyrazoline at CASSCF(4,4)/6-31G* level of theory.

stationary points along asynchronous concerted path are given in Table 5.3. As can be seen from Table 5.2, the barriers (**TS5**) for asynchronous concerted denitrogenation paths are ~ 10 - 11 kcal/mol higher in energy compared to the barriers obtained for synchronous denitrogenation path and ~ 1 - 5 kcal/mol higher in energy than the barriers obtained for asynchronous step-wise denitrogenation paths. No significant substitution effects on the energetics of denitrogenation paths were observed.

5.3.3 Alkene Formation

Thermal denitrogenation of pyrazolines also lead to the formation of alkenes in addition to cyclopropanes. As discussed in Chapter 3, no direct path was obtained for formation of alkene from the pyrazolines. However, alkene can be formed from **Int1** or cyclopropane. A schematic representation of the two possible pathways for alkene formation from pentane-2,4-diyl and cyclopropane are given in Figure 5.10. In path 1, a H-transfer from the central carbon atom to one of the terminal carbon atom of pentane-2,4-diyl leads to formation of pent-2-ene. In path

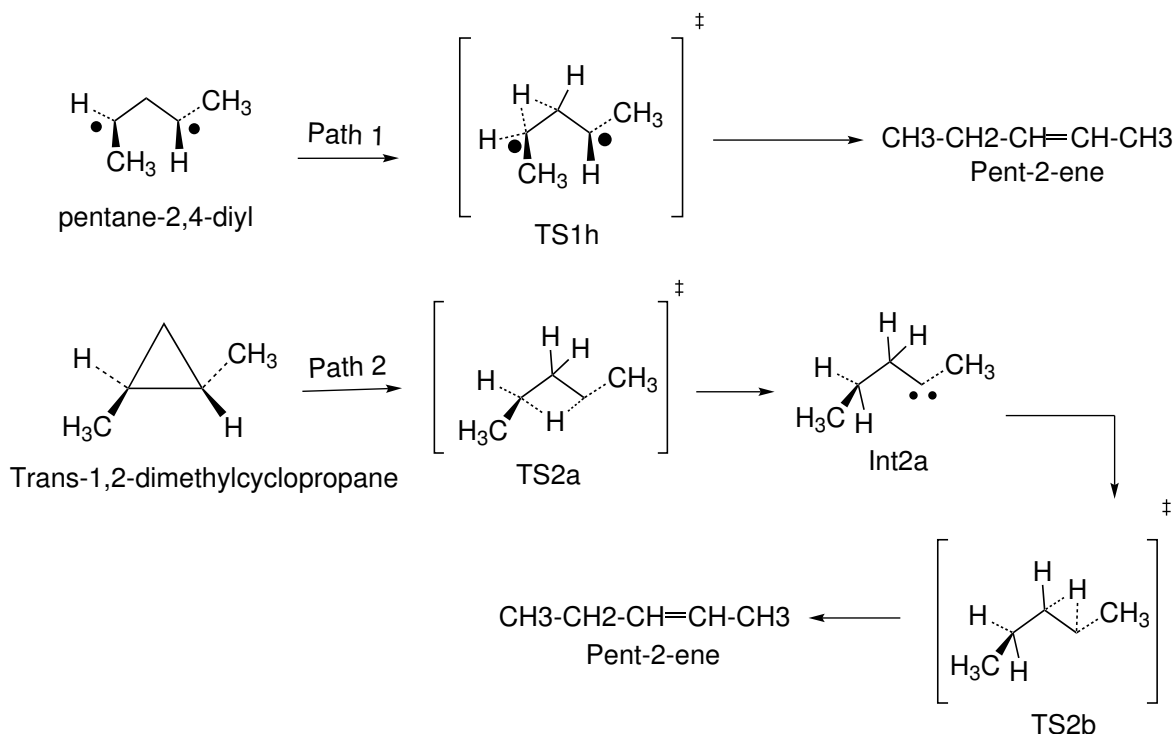


Figure 5.10: A schematic representation of pentane-2,4-diyl to pent-2-ene formation via H-transfer.

2, ring opening of cyclopropane followed by a H-transfer from one of the terminal methylene groups to the other terminal methylene group leads to formation of a carbene. A second H-transfer from the central carbon atom to the carbene carbon atom leads to formation of pent-2-ene. The energetics of stationary point structures obtained for alkene formation are given in Table 5.3. It can be seen that, the barrier for propene formation via path 1 is ~ 23 kcal/mol for cis and trans-3,5-dimethyl-1-pyrazolines. An increase in barriers of ~ 2 kcal/mol for propene formation via path 1 was observed for exo- and endo-2-methyl-3,4-diazabicyclo[3.3.0]oct-3-ene. The barrier obtained for propene formation via path 2 was found to be very high. It can be noted that, the relative energies of stationary point structures of path 2 were calculated with respect to cyclopropane which is ~ 52 kcal/mol lower in energy than **Int1**. The barriers for ring opening of cyclopropane followed by H-transfer from one terminal carbon atom to the other terminal carbon atom was found to be $\sim 77 - 82$ kcal/mol. It leads to formation of carbene

Table 5.3: Relative energies (kcal/mol) of stationary point structures along the alkene formation paths obtained for substituted 1-pyrazolines at CASSCF(4,4)/6-31+G* level of theory^a

Structure	1	2	3	4	5
TS1h ^b	23.19	23.47	23.21	25.01	24.89
TS2a ^c	77.84	77.68	78.10	81.26	81.74
Int2a ^c	61.66	61.27	61.32	64.38	64.81
TS2b ^c	72.09	71.89	71.16	74.18	74.89

^aNumbers in the parentheses are zero point energy corrected values.

^bRelative energy of **TS1h** was calculated with respect to **Int1** energy.

^cRelative energies were calculated with respect to cyclopropane.

which lies 61-65 kcal/mol above cyclopropane. The barriers for formation of propene from the carbene intermediate was found to be ~ 10 kcal/mol.

5.4 Results and Discussion: Dynamics

To understand the effect of substitution on the dynamics of denitrogenation, ab initio classical trajectory simulations were performed for trans-3,5-dimethyl-1-pyrazoline. 500 trajectories were integrated from the reactant region by using velocity Verlet algorithm. The trajectories were integrated for 2 ps. Out of 500 trajectories, 43 trajectories were reactive within 2 ps. The mechanism for the denitrogenation were studied by following various bond distances and dihedral angles in all the reactive trajectories. The product distribution from the trajectories are given in Table 5.4. 24 trajectories formed SI products, while 7 formed DI and 12 formed products with retention of configuration.

Table 5.4: Stereochemistry of cyclopropane obtained for the trajectory simulations from trans-3,5-dimethyl-1-pyrazoline

Cyclopropane stereochemistry		
Single inversion	Double inversion	Retention
24/43 (56%)	7/43 (16%)	12/43 (28%)

5.4.1 Trajectories Following Synchronous Denitrogenation Path

In 25 out of 43 trajectories, it was observed that the C–N bonds dissociated simultaneously. The plot of C–N bond distances for all the trajectories are plotted in Figure 5.11(a). It can be seen that the trajectories after initially spanning the reactant region, both the C–N bonds break in a synchronous fashion. To further understand the atomic-level mechanisms followed in the trajectories that dissociate via synchronous path, the dihedral angles $\angle C(5)-C(4)-C(3)-N(2)$ along with the C(5)–N(1) distances were plotted for all the synchronous trajectories, IRC path (synchronous denitrogenation), and the transition state **TS1a**. The plot of angle $\angle C(3)-C(4)-C(5)-N(1)$ and C(5)–N(1) distance is given in Figure 5.12. As can be seen from Figure 5.12, all the synchronous trajectories dissociate via the transition state **TS1a** region. In nine out of 25 trajectories, the dissociation of C–N bonds and closing of C–C bond happen simultaneously whereas in 16 trajectories the dissociation leads to trimethylene diradical intermediate **Int1**, that close to 1,2-dimethylcyclopropane. Snapshots of a representative trajectory that dissociates via synchronous denitrogenation path is given in Figure 5.13. As can be seen from Figure

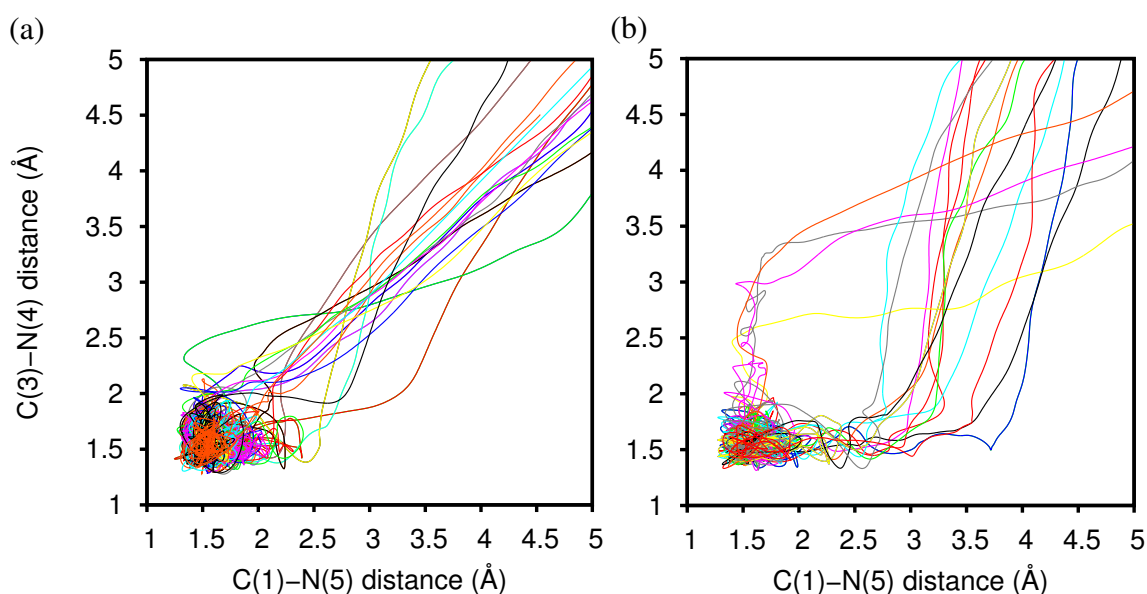


Figure 5.11: (a) Trajectories following synchronous denitrogenation path (b) Trajectories following asynchronous denitrogenation path.

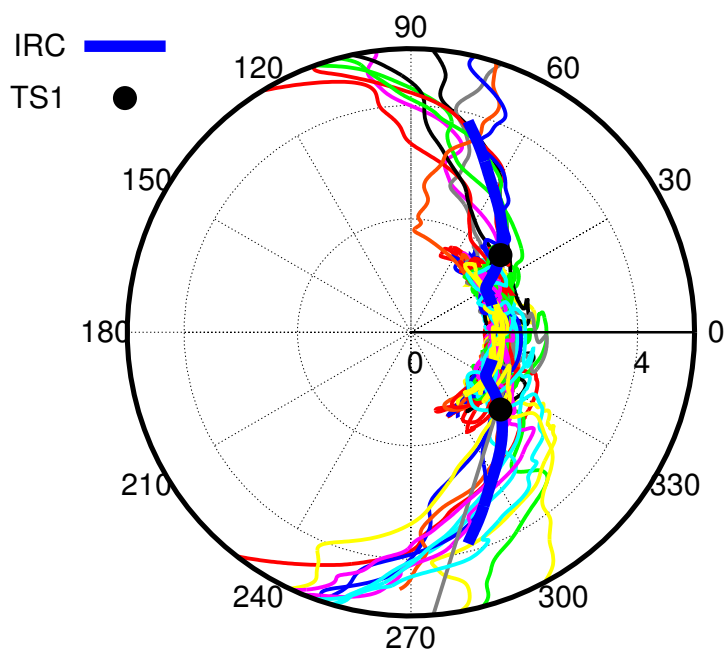


Figure 5.12: Plot of $\angle C(3)-C(4)-C(5)-N(1)$ (degree) vs $C(5)-N(1)$ distance (\AA) for IRC, and **TS1a**, and all the trajectories following synchronous path.

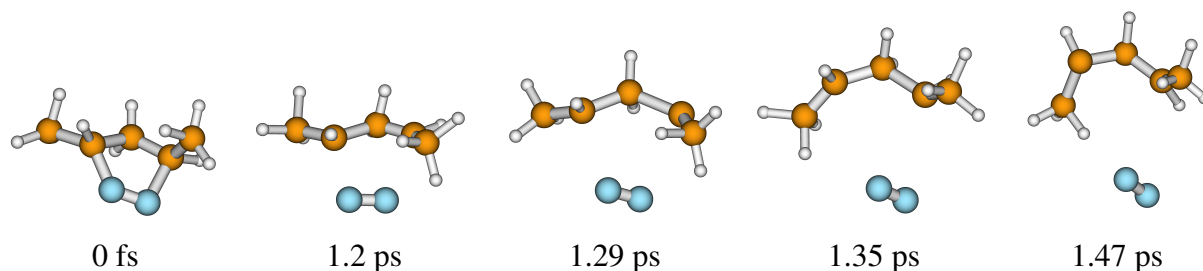


Figure 5.13: Snapshots of a representative trajectory that dissociates via synchronous denitrogenation path.

5.13, the initial dissociation of C–N bonds from pyrazoline is synchronous, but the N_2 group dissociates axially.

5.4.2 Trajectories Following Asynchronous Denitrogenation Path

Among the 43 reactive trajectories, 18 trajectories dissociate via asynchronous denitrogenation path. The plot of C–N distances of denitrogenation process for the 18 trajectories are shown in Figure 5.11 (b). In these trajectories, one of the C–N bonds first breaks followed by the disso-

ciation of the other C–N bond. To understand the atomic-level mechanisms of asynchronous trajectories, the dihedral angle $\angle C(4)-C(5)-N(1)-N(2)$ along with the C(5)–N(1) distances for all the asynchronous trajectories, the MEP for rotation of N₂ group about C(5)–N(1) bond, and stationary points along MEP were plotted in Figure 5.14. It can be seen from Figure 5.14, none of the asynchronous trajectories follow MEP. 16 out of 18 trajectories dissociate directly from the reactant region in an asynchronous fashion. 2 trajectories go through **TS3c**, however instead of going to diazenyl diradical intermediate, the second C–N bond dissociates directly from the transition state and closes to cyclopropane. The N₂ group in all asynchronous trajectories also dissociate axially. Snapshots of a representative asynchronous trajectory that do not follow MEP is given in Figure 5.15.

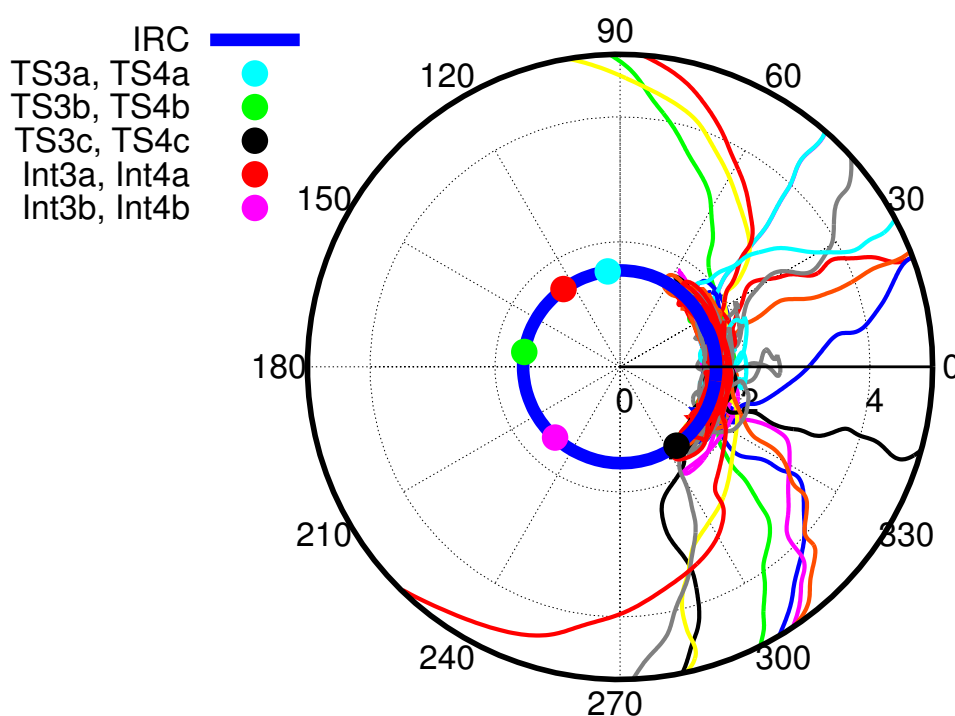


Figure 5.14: Plot of $\angle C(4)-C(5)-N(1)-N(2)$ (degree) vs C(5)–N(1) distance (Å) for all the asynchronous trajectories, IRC for rotation of N₂ group about C(5)–N(1) bond, and stationary points along the IRC.

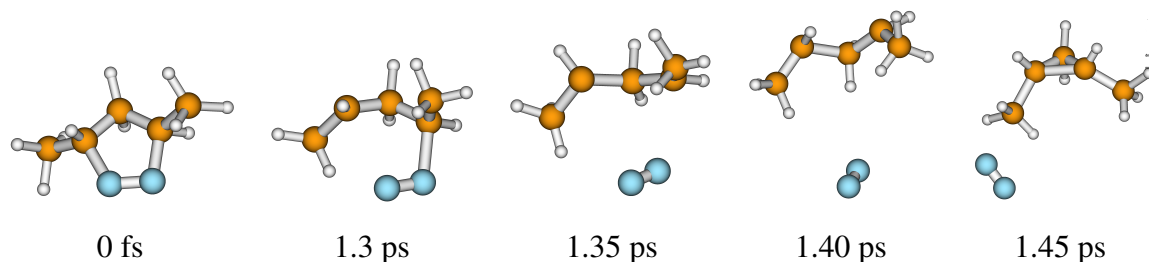


Figure 5.15: Snapshots of a representative trajectory that dissociates via asynchronous path leading to single inverted cyclopropane. This trajectory does not follow the MEP.

5.5 Conclusion

To understand the effect of substitution on the denitrogenation of 1-pyrazoline, the potential energy profiles for five different substituted pyrazolines (cis and trans-3,5-dimethyl-1-pyrazoline and exo- and endo-2-methyl-3,4-diazabicyclo[3.3.0]oct-3-enes) were mapped. For all the five substituted pyrazolines, the synchronous denitrogenation paths were energetically ~ 6 -10 kcal/mol more favourable than the asynchronous step-wise denitrogenation paths and ~ 10 -11 kcal/mol more favourable than the asynchronous concerted denitrogenation path. No significant effect of substitution on energetics of denitrogenation paths were observed. To understand the effect of substitution on dynamics of denitrogenation of 1-pyrazolines, 500 trajectories were integrated from trans-3,5-dimethyl-1-pyrazoline. 43 out of 500 trajectories formed product within 2 ps time. Out of 43 reactive trajectories, 24 trajectories lead to single inverted cyclopropane, 7 trajectories lead to double inverted cyclopropane, 12 trajectories lead to cyclopropane with retention of configuration. From the product distribution, it is clear that there is a preference for single inverted cyclopropane formation consistent with the experiments. From the trajectory simulation results, it was observed that both synchronous and asynchronous denitrogenation paths were equally probable. The synchronous trajectories dissociate via **TS1a** and follow MEP, whereas the asynchronous trajectories do not follow MEP.

DENITROGENATION OF PYRAZOLINES UNDER MECHANICAL STRESS

6.1 Introduction

Mechnochemistry is an emerging field which uses mechanical force to activate chemical reactions.^{128–132} The reaction pathways and products obtained from mechanochemical reactions are often different from that obtained from thermally and photochemically activated reactions.¹³³ To understand the effects of mechanical force on chemical reactions, several experimental and theoretical studies have been carried out.¹³⁴ Benzocyclobutene-based mechanophores have received a lot of attention recently.^{133,135–139} The ring opening of benzocyclobutene is governed by Woodward-Hoffmann rules which is based on conservation of orbital symmetry.^{140,141} According to Woodward-Hoffmann rules,^{140,141} conrotatory ring opening of benzocyclobutene is thermally allowed whereas disrotatory ring opening of benzocyclobutene is photochemically allowed. Thus, the ring opening of cis- and trans-1,2-dimethyl substituted benzocyclobutene in the presence of heat leads to (*E*, *Z*) and

(*E, E*)-*ortho*-quinodimethide (*o*QDM) and in the presence of light, it leads to (*E, E*) and (*E, Z*)-*o*QDM respectively. Moore and co-workers¹³³ recently reported that under sonochemical conditions, the ring opening proceeds along the formally forbidden pathway and both *cis*- and *trans*-substituted benzocyclobutene lead to (*E, E*)-*o*QDM. A similar observation was reported by Lenhardt et al¹⁴² for the ring opening of *gem*-difluorocyclopropane (*g*DFC). The disrotatory ring opening of *g*DFC is thermally allowed and conrotatory ring opening pathway is thermally forbidden. So, ring opening of *cis*-*g*DFC happens through an *s*-*trans*/*s*-*trans* diradical, whereas the *trans*-*g*DFC opens through an *s*-*trans*/*s*-*cis* diradical. However, when this reaction was carried out in the presence of mechanical force generated by ultrasound¹⁴², both *cis*- and *trans*-*g*DFCs opened via the same *s*-*trans*/*s*-*trans* diradical transition state. The mechanochemical cycloreversion of 1,2,3-triazole to azide and alkyne also have gained a lot of attention in the recent years.^{143–146} Several experimental and theoretical calculations have been carried out to understand the possibility of cycloreversion of 1,2,3-triazole under mechanical stress. A theoretical work by Smalø and Uggerud¹⁴³ concluded that mechanical force alone is insufficient to undergo cycloreversion of 1,2,3-triazoles. However, a recent theoretical study predicted the possibility of metal-assisted mechanochemical cycloreversion of 1,5-regioisomers of 1,2,3-triazoles.¹⁴⁵ Based on experimental study using atomic force microscopy (AFM), Khanal et al¹⁴⁶ concluded that mechanical cycloreversion of 1,2,3-triazoles is possible below 860 pN force. A recent experimental study¹⁴⁷ reported stereoselective formation of bicyclo-cyclopropane via ultrasound assisted decomposition of pyrazoline derivatives. A significant increase in rate of the reaction and yield of bicyclo-cyclopropane were observed in the case of ultrasound assisted decomposition of pyrazoline derivatives compared to the decomposition via photolysis method. It is of fundamental interest to understand the mechanism and dynamics of reactions under mechanical stress. In the present study, the effect of mechanical force on 1-pyrazoline and *trans*- and *cis*-3,5-dimethyl-1-pyrazoline was investigated computationally by using CASSCF method and 6-31+G* basis set. The effect of mechanical force on the denitrogenation mechanism of

trans- and cis-3,5-dimethyl-1-pyrazoline was also investigated by mapping the potential energy profiles of denitrogenation paths at different external force.

6.2 Methodology

The effect of mechanical force on 1-pyrazoline and trans- and cis-3,5-dimethyl-1-pyrazolines were investigated by using CASSCF methods with 6-31+G* basis set.^{4,113,116} The CASSCF calculations were performed with (8,8) active space. For 1-pyrazoline, the active space for CASSCF calculations includes $\sigma_{\text{C-N}}$, $\sigma_{\text{C-N}}^*$ orbitals of both the C–N bonds and $\sigma_{\text{C-C}}$ and $\sigma_{\text{C-C}}^*$ orbitals of both the ring C–C bonds. The orbitals used in the CASSCF active space for 1-pyrazoline are given in Figure 6.1(a). The active space for trans- and cis-3,5-dimethyl-1-pyrazoline includes $\sigma_{\text{C-N}}$, $\sigma_{\text{C-N}}^*$ orbitals of both the C–N bonds and $\sigma_{\text{C-C}}$ and $\sigma_{\text{C-C}}^*$ orbitals of the terminal C–CH₃ bonds. The orbitals used for the CASSCF calculations for trans-3,5-dimethyl-1-pyrazolines are given in Figure 6.1(b). Similar orbitals were used for cis-3,5-dimethyl-1-pyrazoline. Constrained geometry simulate external force (COGEF) method¹⁴⁸ was used to understand the effect of external force on 1-pyrazoline, trans- and cis-3,5-dimethyl-1-pyrazoline and their denitrogenation paths. In COGEF method, two atoms of a molecules are considered as pulling points (PPs). Mechanical stress is then simulated by increasing the distance between two PPs gradually in a step-by-step process with a distance constraint between the PPs given by:

$$q(\mathbf{x}) = |\mathbf{x}_i - \mathbf{x}_j| - q_0 \quad (6.1)$$

where $q(\mathbf{x})$ is the distance constraint as a function of nuclear Cartesian coordinates \mathbf{x} , \mathbf{x}_i is the position of atom i , \mathbf{x}_j is position of atom j , and q_0 is the target distance between the pulling points i and j . Due to the constraint imposed on the molecule, the PES of the molecule (COGEF potential) can be obtained by minimizing the function

$$V_{\text{COGEF}}(\mathbf{x}, q) = V_{\text{BO}}(\mathbf{x}) - \lambda q(\mathbf{x}) \quad (6.2)$$

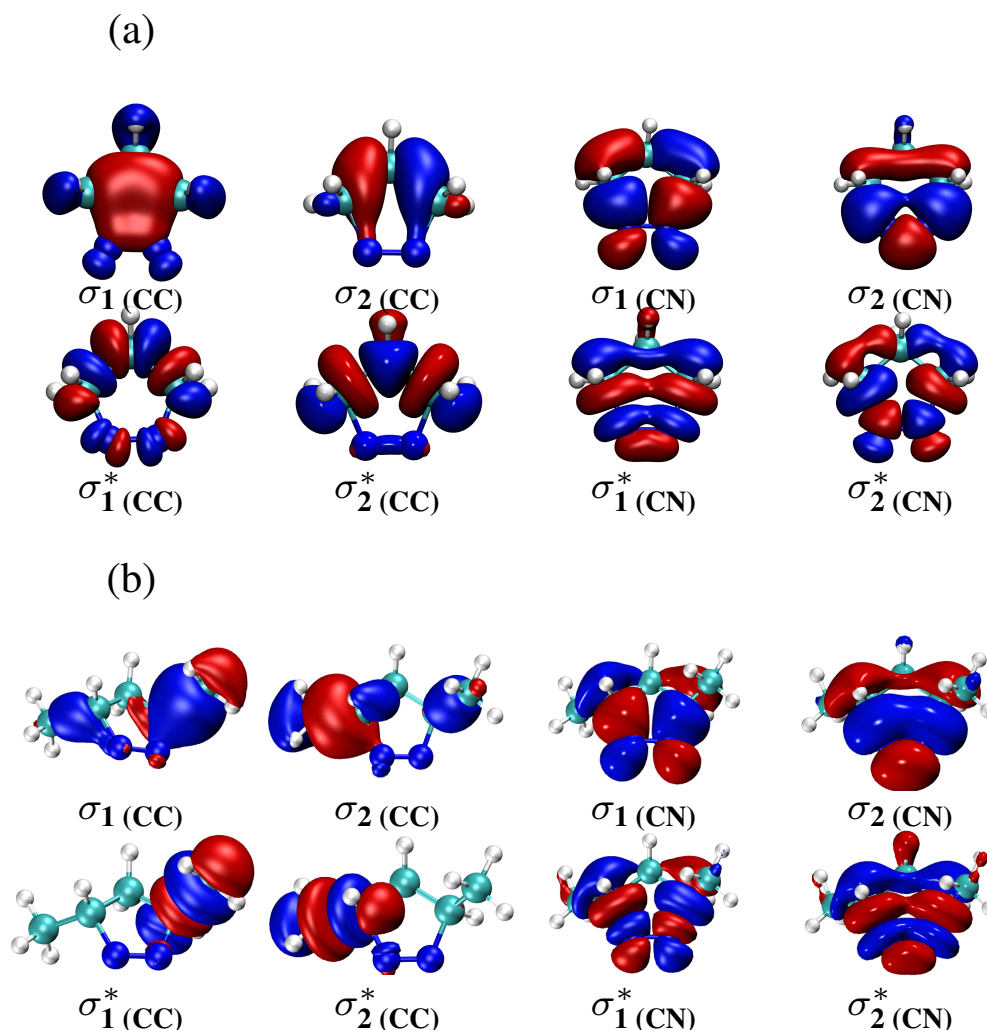


Figure 6.1: Orbitals used in the active space for the CASSCF calculations of (a) 1-pyrazoline and (b) trans-3,5-dimethyl-1-pyrazoline.

with respect to \mathbf{x} and the Lagrange multiplier λ . Here, $V_{\text{COGEF}}(\mathbf{x}, q)$ is the force-modified potential energy and V_{BO} is the Born-Oppenheimer potential energy without any constraints. For stationary points corresponding to each value of PPs distance a restoring force \mathbf{F} of magnitude F acts on the PPs. The molecules considered in the present study along with their atom numbering schemes are given in Figure 6.2. For 1-pyrazoline, the two ring carbon atoms C(1) and C(3), were considered as PPs; for trans-cis-3,5-dimethyl-1-pyrazoline, C(6) and C(9) were considered and for cis-3,5-dimethyl-1-pyrazoline, C(6), C(8) carbon atoms

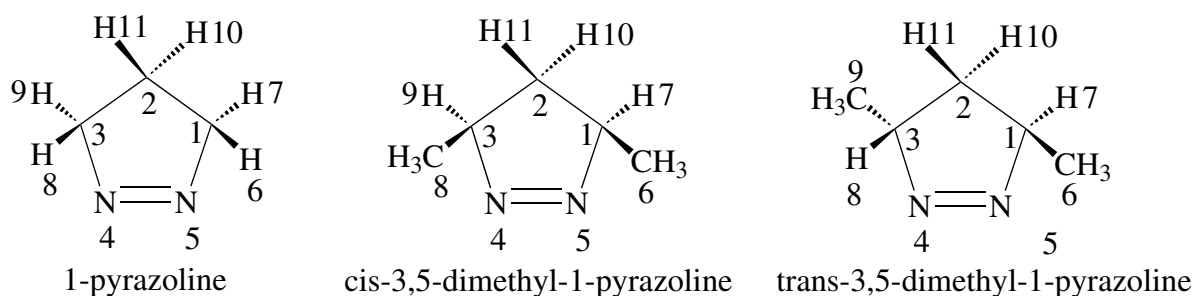


Figure 6.2: Molecules considered in the study and their atom numbering schemes.

were considered as PPs. The stationary point structures were characterized by computing the harmonic vibrational frequencies. All the calculations were performed using Gaussian 09 software packages.¹¹⁸ The important geometrical parameters considered in the study are given in Table 6.1.

Table 6.1: Important geometrical parameters considered in the present study^a

Parameters	1-pyrazoline	trans-3,5-dimethyl-1-pyrazoline	cis-3,5-dimethyl-1-pyrazoline
ϕ_1 : C(1)-C(2)-C(3)-N(4)	✓	✓	✓
ϕ_2 : C(2)-C(3)-N(4)-N(5)	✓	✓	✓
ϕ_3 : C(3)-C(2)-C(1)-H(6)	✓	NA	NA
ϕ_4 : C(3)-C(2)-C(1)-H(7)	✓	✓	✓
ϕ_5 : C(1)-C(2)-C(3)-H(8)	✓	✓	NA
ϕ_6 : C(1)-C(2)-C(3)-H(9)	✓	NA	✓
ϕ_7 : C(3)-C(2)-C(1)-C(6)	NA	✓	✓
ϕ_8 : C(1)-C(2)-C(3)-C(8)	NA	NA	✓
ϕ_9 : C(1)-C(2)-C(3)-C(9)	NA	✓	NA
θ_1 : C(1)-C(2)-C(3)	✓	✓	✓
d_1 : C(1)-N(5)	✓	✓	✓
d_2 : C(3)-N(4)	✓	✓	✓
d_3 : C(1)-C(2)	✓	NA	NA
d_4 : C(2)-C(3)	✓	NA	NA
d_5 : C(1)-C(6)	NA	✓	✓
d_6 : C(3)-C(8)	NA	NA	✓
d_7 : C(3)-C(9)	NA	✓	NA

^aNA: not applicable and ✓ denotes that the parameter is considered.

6.3 Results and Discussion

6.3.1 Effect of External Force on the 1-Pyrazoline

Similar to 1,2,3-triazole, 1-pyrazoline is also formed by the 1,3-dipolar cycloaddition of diazomethane and ethene. So, application of external force along C(1) and C(3) carbon atoms of 1-pyrazoline may lead to breaking of C(2)–C(3) and C(1)–N(5) bonds and form diazomethane and ethene as observed in the case of 1,2,3-triazole or it may lead to breaking of C(1)–N(5) and C(3)–N(4) bonds and form cyclopropane (Figure 6.3). To understand the effect of external force on 1-pyrazoline, COGEF calculations were performed by considering C(1) and C(3) carbon atoms as PPs at CASSCF(8,8)/6-31+G* level of theory. The PPs distance was increased in a step-wise fashion and the geometry of 1-pyrazoline was optimized at each point by fixing the PPs distance. The relative energies of 1-pyrazoline and F values in nano Newton (nN) for different displacement of the PPs from the equilibrium distance (r_0 , $\Delta r = r_{C(1)-C(3)} - r_0$) are given in Figures 6.4 (a) and 6.4 (b), respectively. Here, $r_0 = 2.38 \text{ \AA}$. It can be seen from Figure 6.5 (a) and (b), both the relative energy and force along the C(1)–C(3) carbon atoms increase with the increase in PPs distance. A maximum force of 22.45 nN was observed for the Δr distance of 0.8 \AA corresponding to an energy of 105.99 kcal/mol. The change in geometrical

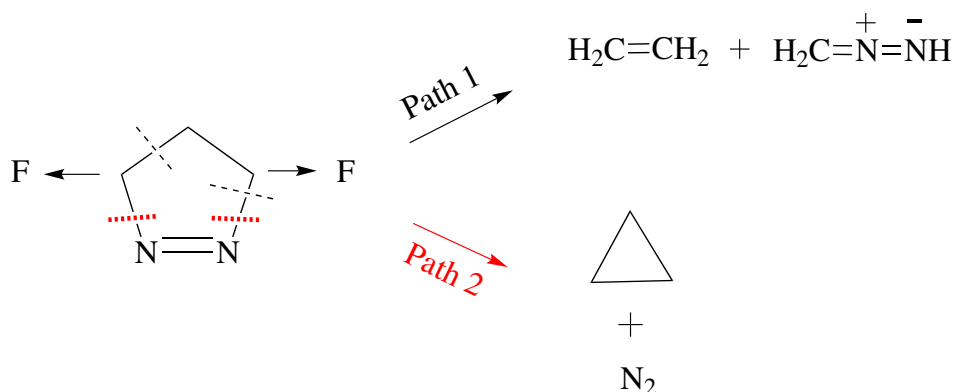


Figure 6.3: The two possible dissociation pathways of 1-pyrazoline in the presence of external force along C(1) and C(3) carbon atoms.

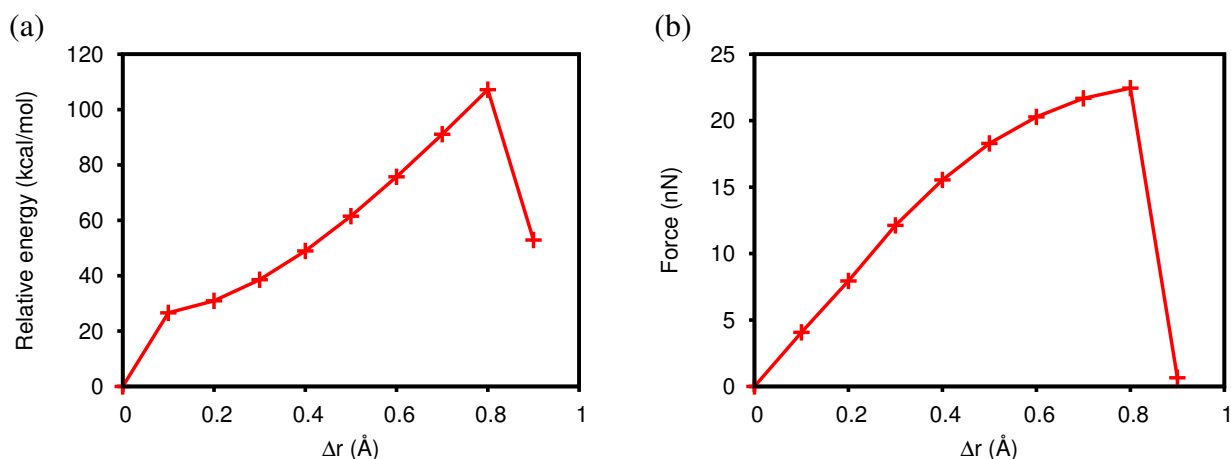


Figure 6.4: (a) Plot of relative energy of 1-pyrazoline vs Δr distance (b) force along terminal C(1)–C(3) carbon atoms in nano Newton (nN) vs Δr distance.

parameters of 1-pyrazoline with the increase in PPs distance is given in Table 2. 1-Pyrazoline has C_s symmetry. C(1), C(3), N(4), and N(5) atoms of 1-pyrazoline lie on the same plane and C(2) methylene group can lie above or below the plane containing C(1)–C(3)–N(4)–N(5) atoms. It can be seen from Table 6.2 that the application of force results in having all the five ring atoms of the molecules on the same plane (ϕ_1 and $\phi_2 = 0^\circ$). It should be pointed that a similar structure was obtained in the potential energy profile of 1-pyrazoline in the

Table 6.2: Geometrical parameters of 1-pyrazoline for different Δr values obtained at CASSCF(8,8)/6-31+G* level of theory^a

Δr (Å)	ϕ_1	ϕ_2	θ_1	d_1	d_2	d_3	d_4
0	-17.68	12.01	101.24	1.52	1.52	1.56	1.56
0.1	-0.03	-0.02	103.36	1.52	1.52	1.58	1.58
0.2	-0.01	0.00	105.92	1.54	1.54	1.62	1.62
0.3	0.00	0.00	108.13	1.56	1.56	1.65	1.65
0.4	0.00	0.00	110.02	1.59	1.59	1.70	1.70
0.5	0.00	0.00	111.65	1.61	1.61	1.74	1.74
0.6	0.00	0.00	113.08	1.64	1.64	1.79	1.79
0.7	-0.01	0.02	114.41	1.67	1.67	1.83	1.83
0.8	0.04	-0.01	115.95	1.72	1.72	1.87	1.87
0.9	-178.74	0.43	51.29	5.48	1.30	3.95	1.36

^a Distances are in Å and angles are in degree.

absence of external force where all the five atoms of the ring are on the same plane. However, it was found to be a transition state which lies ~ 0.5 kcal/mol above reactant that connects two conformational isomers. Thus, the external force stabilizes the **TS** structure to result in a minimum. With the increase in PPs distance, a symmetric increase in both the C–N and C–C distances were observed until $\Delta r = 0.8$ Å. At Δr distance of 0.9 Å, the molecule breaks into diazomethane and ethene.

6.3.2 Effect of External Force on *trans*-3,5-dimethyl-1-pyrazoline

To understand the effects of external mechanical force on *trans*-3,5-dimethyl-1-pyrazoline, COGEF calculations were performed by increasing the distance between C(6) and C(9), the carbon atoms of the substituents at C(1) and C(3). Two different approaches were used to calculate the effect of external force on *trans*-3,5-dimethyl-1-pyrazoline: (1) simultaneous stretching of both the C–CH₃ covalent bonds and (2) stretching of one of the C–CH₃ covalent bonds. A schematic representation of the two paths used to simulate the effect of external force on *trans*-3,5-dimethyl-1-pyrazoline at different PPs is given in Figure 6.5. The distance between the two PPs were increased gradually and the geometries of the stationary point structures were optimized by fixing the PPs distances and relaxing other geometrical parameters. The relative energies of *trans*-3,5-dimethyl-1-pyrazoline and F values for different displacements of PPs from the equilibrium distance (r_0 , $\Delta r = r_{\text{C(6)-C(9)}} - r_0$) for both the pathways are plotted in Figure 6.6. Here, $r_0 = 4.87$ Å. It can be seen from Figure 6.6, with the increase in PPs distance, the energy of *trans*-3,5-dimethyl-1-pyrazoline increases for both the stretching pathways. At lower PPs distances, the relative energies of stationary point structures of the simultaneous stretching pathway are lower in energy than that for one bond stretching pathway. However, at Δr above 1.4 Å, the energies of the stationary point structures along the single C–CH₃ stretching pathway was lower than the simultaneous stretching pathway. At larger PPs distances, the two bond stretching pathway results in the fragmentation of both the terminal

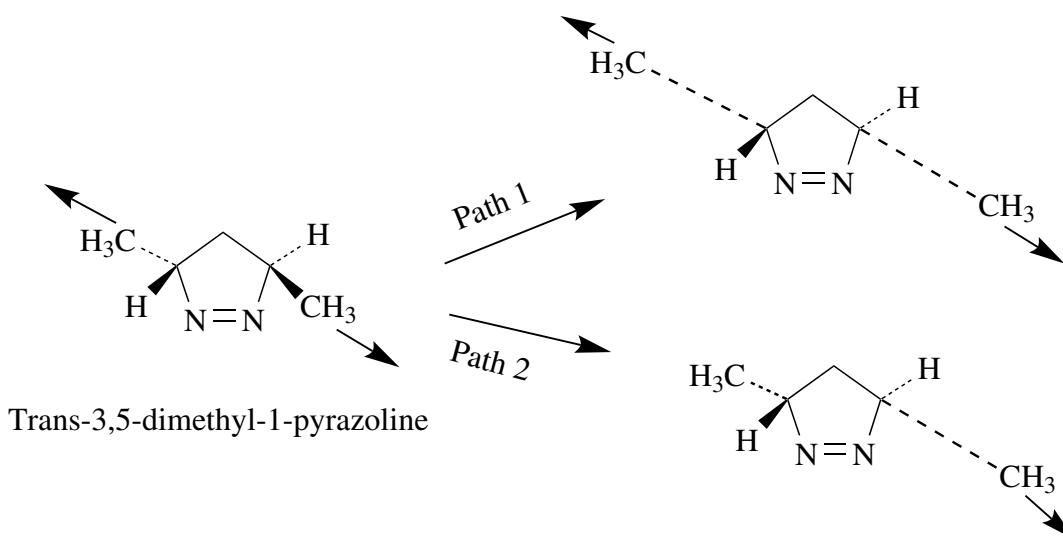


Figure 6.5: Schematic representation of the two approaches used to simulate the effect of external force on trans-3,5-dimethyl-1-pyrazoline.

methyl groups and hence the observed larger energies. However, increasing the PPs distance for single bond stretching would result in the breaking of the stretching bond only. Similarly, the forces for both the pathway initially increases with the increase in PPs distance and then it decreases. The single C–CH₃ stretching pathway attained a maximum force of 10.3 nN at $\Delta r = 0.5 \text{ \AA}$ and simultaneous stretching pathway attained a maximum force of 11.9 nN at $\Delta r = 1.3 \text{ \AA}$. The changes in important geometrical parameters of trans-3,5-dimethyl-1-pyrazoline for

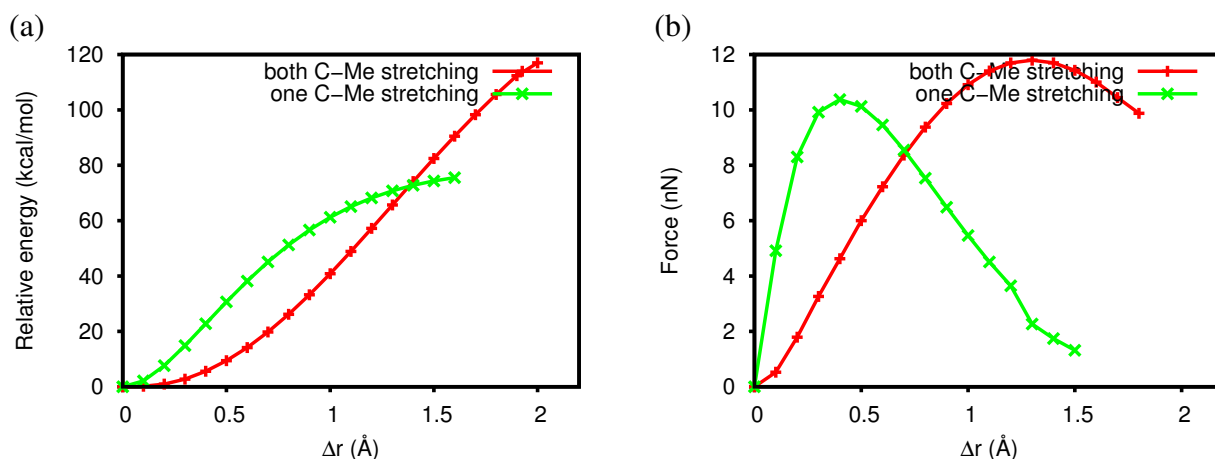


Figure 6.6: (a) Plot of relative energies of trans-3,5-dimethyl-1-pyrazoline vs Δr and (b) F values vs Δr .

different Δr values are given in Table 6.3. It can be seen from Table 6.3, for the synchronous stretching path, with the increase in the PPs distance, the ϕ_1 angle increases and then decreases while ϕ_2 angle decreases and then increases. At Δr between 0.2 and 0.3 Å, trans-3,5-dimethyl-1-pyrazoline attains a planar structure. This planar structure is a transition state in the potential energy profile of trans-3,5-dimethyl-1-pyrazoline in the absence of external force. The ϕ_3 and ϕ_4 angles increase while ϕ_5 and ϕ_6 angles decrease with the increase in PP distance. Similarly, a synchronous increase in d_5 and d_6 distances were observed as expected. However, no significant changes in the C–N distances d_1 and d_2 with the increase in PP distance were observed.

For the single C–CH₃ stretching pathway, no significant changes in ϕ_1 , ϕ_2 , ϕ_3 , ϕ_4 , θ_1 , d_2 , and d_7 parameters with the increase in PP distance were observed. Only changes in d_1 and d_5 distances that are related to pulling direction were observed with the increase in the PP distance. The C–N distance d_1 decreases and the C–C distance d_5 increases with the increase in the PP distance.

Table 6.3: Geometrical parameters of trans-3,5-dimethyl-1-pyrazoline at different Δr values obtained at CASSCF(8,8)/6-31+G* level of theory^a

Δr (Å)	ϕ_1	ϕ_2	ϕ_3	ϕ_4	ϕ_5	ϕ_6	θ_1	d_1	d_2	d_5	d_7
Path 1- Simultaneous stretching of both the C–CH ₃ group											
0	-16.52	10.78	-101.43	131.98	96.82	-136.91	102.71	1.52	1.52	1.55	1.55
0.1	-6.89	4.8	-113.13	120.90	106.60	-127.44	103.47	1.52	1.52	1.56	1.56
0.2	-0.51	1.54	-122.45	112.12	112.02	-122.54	103.93	1.52	1.52	1.57	1.57
0.3	-0.82	2.73	-124.73	110.44	110.43	-124.74	104.28	1.52	1.52	1.59	1.59
0.4	-1.11	3.74	-126.88	108.93	108.93	-126.88	104.61	1.52	1.52	1.61	1.61
0.5	-1.34	4.53	-128.77	107.76	107.76	-128.77	104.93	1.52	1.52	1.63	1.63
1.0	-1.83	6.26	-134.77	105.00	105.94	-134.76	105.94	1.53	1.53	1.75	1.75
Path 2- Stretching of one of the C–CH ₃ group											
0	-16.5	10.78	-101.43	131.98	96.82	-136.91	102.71	1.52	1.52	1.55	1.55
0.1	-17.12	11.24	-99.68	134.69	96.17	-137.52	102.43	1.51	1.52	1.65	1.55
0.2	-17.84	11.75	-97.74	137.49	95.38	-138.26	102.15	1.51	1.52	1.75	1.55
0.3	-18.39	12.18	-96.01	140.16	94.76	-138.85	101.91	1.50	1.52	1.85	1.55
0.4	-18.87	12.58	-94.43	142.75	94.21	-139.37	101.67	1.50	1.52	1.95	1.55
0.5	-19.15	12.87	-93.11	145.14	93.87	-139.70	101.47	1.49	1.52	2.05	1.55
1.0	-19.17	13.30	-89.44	153.73	93.65	-139.88	100.84	1.47	1.52	2.45	1.55

^a Distances are in Å and angles are in degree.

6.3.3 Effect of External Force on Cis-3,5-dimethyl-1-pyrazoline

To understand the effect of external mechanical force on cis-3,5-dimethyl-1-pyrazoline, the energies of cis-3,5-dimethyl-1-pyrazoline at different PPs distances were calculated by using COGEF method. For cis-3,5-dimethyl-1-pyrazoline also, the two methyl carbon atoms C(6) and C(8) were considered as the PPs. The two different approaches were used to calculate the effect of external force on cis-3,5-dimethyl-1-pyrazoline: (1) simultaneous stretching of both the C–CH₃ covalent bonds and (2) stretching of one of the C–CH₃ covalent bonds. A schematic representation of the two paths used to simulate the effect of external force on cis-3,5-dimethyl-1-pyrazoline at different PPs distances are given in Figure 6.7. The relative energies of cis-3,5-dimethyl-1-pyrazoline and F values obtained for displacement of different PPs distances from the equilibrium distance ($r_0 = 4.827$, $\Delta r = r - r_0$) for both the pathways are plotted in Figure 6.8. It can be seen from Figure 6.8, with the increase in the PPs distance, the energy of cis-3,5-dimethyl-1-pyrazoline increases for both the stretching pathways. At lower PPs distances, the relative energies of the stationary point structures for simultaneous stretching pathway are lower in energy. However, for Δr values larger than 1.5 Å, the energies of stationary point structures along the single C–CH₃ stretching pathway was lower than that

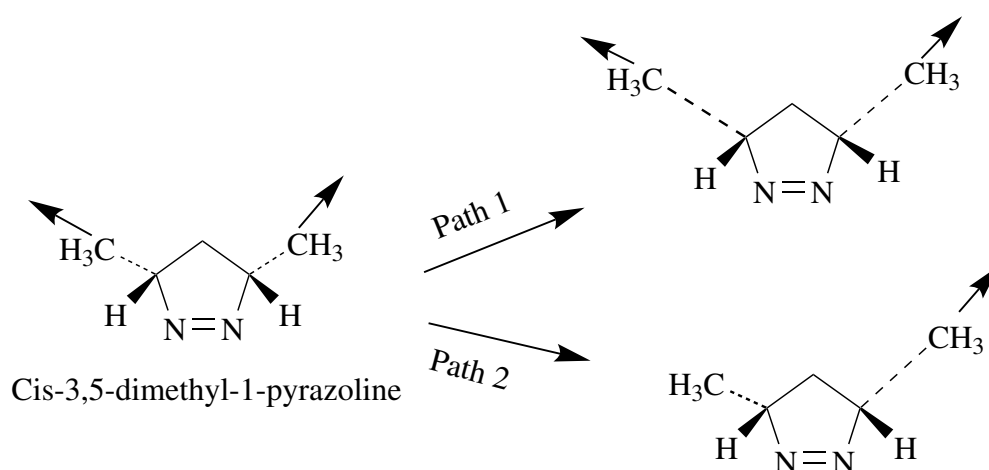


Figure 6.7: Schematic representation of the two approaches used to simulate effect of external force on cis-3,5-dimethyl-1-pyrazoline.

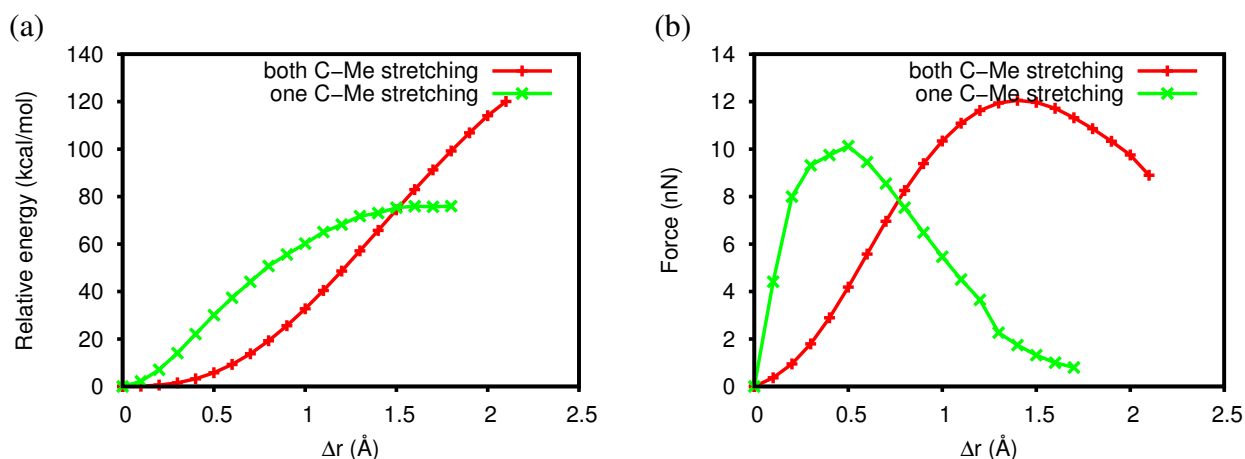


Figure 6.8: (a) Plot of relative energies of cis-3,5-dimethyl-1-pyrazoline vs Δr and (b) F values vs Δr .

for simultaneous stretching pathway. Similarly, the magnitude of forces for both the pathways initially increase with the increase in the PPs distances and then decrease. The maximum force for the symmetrical and asymmetrical stretching occur at Δr values of 1.5 and 0.5 Å, respectively. The important geometrical parameters of cis-3,5-dimethyl-1-pyrazoline at different Δr distances are given in Table 6.4. For the symmetrical stretching path, ϕ_1 angle decreases and ϕ_2 angle increases with the increase in the PP distance which is in contrast to the observation for trans-3,5-dimethyl-1-pyrazoline where these angles become 0° . The dihedral angles ϕ_3 and ϕ_4 increase whereas ϕ_5 and ϕ_6 decrease with the increase in the PPs distance. The distances d_5 and d_6 increase with the increase in PPs distance. No appreciable changes in d_1 and d_2 distances were observed. For single C-CH₃ stretching pathway, no appreciable changes in any of the geometrical parameters were observed except for d_2 and d_6 distances, where d_2 was found to decrease while d_6 increased with increase in PP distance.

6.3.4 Effect of External Force on Energetics of Denitrogenation Paths Obtained for Trans- and Cis-3,5-dimethyl-1-pyrazoline

To understand the effect of external force on the potential energy profile of denitrogenation of trans- and cis-3,5-dimethyl-1-pyrazoline, the denitrogenation paths were mapped at four

Table 6.4: Geometrical parameters of cis-3,5-dimethyl-1-pyrazoline at different Δr distances obtained at CASSCF(8,8)/6-31+G* level of theory^a

Δr (Å)	ϕ_1	ϕ_2	ϕ_3	ϕ_4	ϕ_5	ϕ_6	θ_1	d_1	d_2	d_5	d_6
Path 1- Stretching of one of the C–CH ₃ group											
0	-21.32	14.32	-91.52	141.94	91.52	-141.94	102.17	1.52	1.52	1.55	1.55
0.1	-25.10	16.85	-87.10	146.42	87.10	-146.42	101.63	1.52	1.52	1.55	1.55
0.2	-28.44	19.08	-83.02	150.66	83.02	-150.66	101.06	1.52	1.52	1.55	1.55
0.3	-31.16	20.88	-79.51	154.45	79.51	-154.45	100.55	1.52	1.52	1.56	1.56
0.4	-33.20	22.29	-76.71	153.63	76.71	-153.63	100.20	1.53	1.53	1.57	1.57
0.5	-34.55	23.12	-74.62	160.17	74.62	-160.17	100.04	1.53	1.53	1.59	1.59
1.0	-35.62	23.78	-71.64	166.15	71.64	-166.15	101.08	1.54	1.54	1.74	1.74
Path 2- Simultaneous stretching of both the C–CH ₃ group											
0	-21.32	14.32	-91.52	141.94	91.52	-141.94	102.17	1.52	1.52	1.55	1.55
0.1	-21.50	14.62	-92.43	140.21	92.43	-139.72	102.21	1.52	1.52	1.55	1.56
0.2	-21.74	14.88	-93.28	139.84	93.28	-137.49	102.32	1.52	1.51	1.55	1.57
0.3	-21.83	15.23	-93.83	138.43	93.83	-134.30	102.65	1.52	1.51	1.55	1.59
0.4	-21.98	15.51	-94.42	137.21	94.42	-132.66	103.01	1.52	1.50	1.55	1.61
0.5	-22.17	15.92	-94.78	136.40	94.78	-130.32	103.03	1.52	1.49	1.55	1.64
1.0	-23.01	16.45	-95.89	134.39	95.89	-125.49	104.00	1.52	1.46	1.55	1.71

^a Distances are in Å and angles are in degree.

different magnitude of forces, 0.5, 1.8, 4.6, and 10.2 nN corresponding to the Δr distances 0.2, 0.3, 0.5, and 1.0 Å, respectively. Both synchronous and asynchronous denitrogenation paths were considered in this study.

6.3.4.1 Synchronous Denitrogenation Path

Trans-3,5-dimethyl-1-pyrazoline. Synchronous denitrogenation of trans-3,5-dimethyl-1-pyrazoline leads to trimethylene diradical intermediate **Int1** via the transition state **TS1a**. In the present study, to understand the effect of external force on the synchronous denitrogenation path, **Reactant**, **TS1a**, and **Int1** were optimized at different fixed PPs distance. Here, C(6) and C(9) carbon atoms were considered as PPs. The relative energies of the stationary point structures obtained for the synchronous denitrogenation paths for different F values are given in Figure 6.9 and Table 6.5. It can be seen from Table 6.5, the relative energies of **TS1a** decreases with the increase in F values. However, the **Int1** energies increases by ~ 3 kcal/mol with

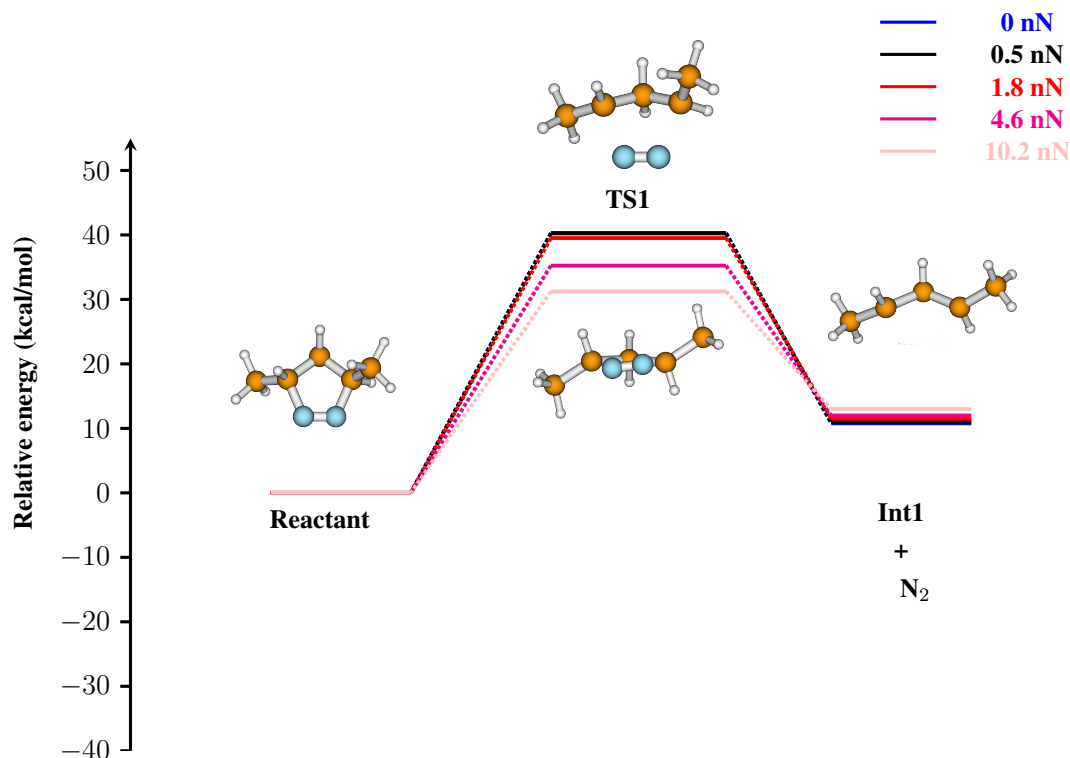


Figure 6.9: Synchronous denitrogenation paths of trans-3,5-dimethyl-1-pyrazoline for different F values.

the increase in F values. The important geometrical parameters of stationary point structures obtained at different F values are given in Table 6.6. It can be seen from Table 6.6, with the increase in the external force, a significant increase in ϕ_1 , ϕ_5 , ϕ_6 , and θ_1 angles and d_5 and d_6 distances and decrease in ϕ_2 , ϕ_3 , and ϕ_4 angles were observed. At a F value of 4.6 nN, the terminal methylene groups of **TS1a** become close to a pyramidal structure ($\phi_3=-103.49^\circ$, $\phi_4=116.76^\circ$, $\phi_5=103.49^\circ$, and $\phi_6=-116.76^\circ$). Similar to **TS1a**, in **Int1** also a significant increase

Table 6.5: Relative energies (kcal/mol) of stationary points along synchronous denitrogenation path of trans-3,5-dimethyl-1-pyrazoline at different F values obtained at CASSCF(8,8)/6-31+G* level of theory

Structure	0 nN	0.5 nN	1.8 nN	4.6 nN	10.2 nN
TS1a	40.30	40.24	39.52	36.24	31.81
Int1	10.83	11.01	11.56	12.20	14.12

Table 6.6: Geometrical parameters for stationary points along the synchronous denitrogenation path for different F values obtained at CASSCF(8,8)/6-31+G* level of theory^a

Structure	F (nN)	ϕ_1	ϕ_2	ϕ_3	ϕ_4	ϕ_5	ϕ_6	θ_1	d_1	d_2	d_5	d_6
TS1a	0	-39.95	19.71	-65.83	151.75	65.83	-151.75	115.69	2.11	2.11	1.53	1.53
	0.5	-34.16	18.34	-76.58	146.98	76.58	-146.98	117.84	2.11	2.11	1.54	1.54
	1.8	-29.23	13.88	-79.27	141.63	79.27	-141.63	118.74	2.12	2.12	1.55	1.55
	4.6	-17.65	14.07	-103.49	116.76	103.49	-116.76	120.01	2.13	2.13	1.56	1.56
	10.2	-2.36	10.62	-131.76	92.95	131.76	-92.95	120.56	2.12	2.13	1.61	1.61
Int1	0	-	-	-109.11	135.67	109.11	-135.67	118.42	-	-	1.53	1.53
	0.5	-	-	-113.51	121.28	113.51	-121.28	119.30	-	-	1.54	1.54
	1.8	-	-	-119.34	114.23	119.34	-114.23	120.89	-	-	1.55	1.55
	4.6	-	-	-126.41	107.18	126.41	-107.18	122.43	-	-	1.57	1.57
	10.2	-	-	-132.32	103.40	132.32	-103.40	125.40	-	-	1.61	1.61

^a Distances are in Å and angles are in degree.

in ϕ_3 , ϕ_5 , and θ_1 angles and d_5 and d_6 distances and a decrease in ϕ_4 , ϕ_6 angles were observed. **Cis-3,5-dimethyl-1-pyrazoline.** The potential energy profiles for the synchronous denitrogenation path of cis-3,5-dimethyl-1-pyrazoline were also mapped at four different magnitude of forces, 0.5, 1.8, 4.6, and 10.2 nN corresponding to Δr distances 0.2, 0.3, 0.5, and 1.0 Å, respectively. For cis-3,5-dimethyl-1-pyrazoline, C(6) and C(8) carbon atoms were considered as PPs. The relative energies of stationary point structures obtained at CASSCF(8,8)/6-31+G* level of theory for different Δr distances are given in Table 6.7 and Figure 6.10. In contrast to trans-3,5-dimethyl-1-pyrazoline, the relative energy of **TS1a** for cis-3,5-dimethyl-1-pyrazoline increases with the increase in the external force up to 4.6 nN and then it decreases at 10.2 nN force. The **Int1** energy increases by ~ 3 kcal/mol with the increase in F up to 10.2 nN. The important geometrical parameters of **TS1a** and **Int1** obtained in the presence of different F values are given in Table 6.8. It can be seen from Table 6.8 that with the increase in external

Table 6.7: Relative energies (kcal/mol) of stationary points along synchronous denitrogenation path of cis-3,5-dimethyl-1-pyrazoline for different F values obtained at CASSCF(8,8)/6-31+G* level of theory

Structure	0 nN	0.5 nN	1.8 nN	4.6 nN	10.2 nN
TS1a	40.15	41.00	42.06	44.84	28.42
Int1	10.79	11.23	11.89	13.18	14.76

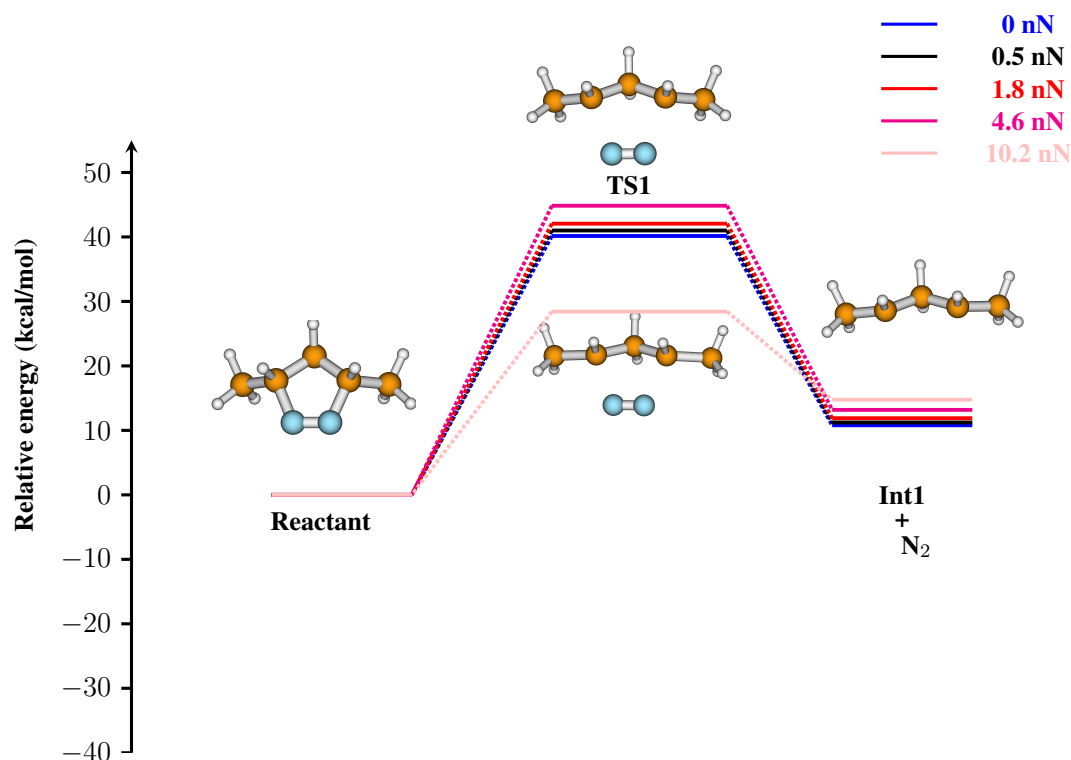


Figure 6.10: Synchronous denitrogenation path of cis-3,5-dimethyl-1-pyrazoline at different external forces.

force, a slight decrease in ϕ_1 angle and a slight increase in ϕ_2 angle of **TS1a** were observed which is in contrast to trans-3,5-dimethyl-1-pyrazoline where a significant increase in ϕ_1 and a decrease in ϕ_2 angle were observed. No significant changes in ϕ_3 , ϕ_4 , ϕ_5 , and ϕ_6 angles were

Table 6.8: Geometrical parameters for stationary points along synchronous denitrogenation path for different F values obtained at CASSCF(8,8)/6-31+G* level of theory

Structure	F (nN)	ϕ_1	ϕ_2	ϕ_3	ϕ_4	ϕ_5	ϕ_6	θ_1	d_1	d_2	d_5	d_6
TS1a	0	-41.17	22.03	-60.08	156.67	60.08	-156.67	113.52	2.11	2.11	1.53	1.53
	0.5	-44.60	24.08	-54.44	163.03	54.44	-163.03	113.21	2.1	2.1	1.55	1.55
	1.8	-45.27	24.52	-52.90	165.04	52.90	-165.04	113.25	2.1	2.1	1.57	1.57
	4.6	-45.33	24.63	-51.62	167.50	51.62	-167.50	113.73	2.08	2.08	1.61	1.61
	10.2	-44.48	24.20	-51.83	168.76	51.83	-168.76	114.94	2.07	2.07	1.67	1.67
Int1	0	-	-	-109.11	133.57	109.11	-133.57	117.47	-	-	1.53	1.53
	0.5	-	-	-118.21	127.18	118.21	-127.18	118.32	-	-	1.55	1.55
	1.8	-	-	-121.32	119.83	121.32	-119.83	121.23	-	-	1.57	1.57
	4.6	-	-	-127.56	111.74	127.56	-111.74	123.54	-	-	1.59	1.59
	10.2	-	-	-131.52	101.10	131.52	-101.10	125.19	-	-	1.62	1.62

^a Distances are in Å and angles are in degree.

observed. ϕ_3 and ϕ_4 angles increases by $\sim 10^\circ$ whereas ϕ_5 and ϕ_6 angle decreases by $\sim 10^\circ$ with increase in the F values. The d_5 and d_6 distances increase symmetrically with the increase in F values. However, no changes in d_1 and d_2 distances were observed.

6.3.4.2 Asynchronous Step-wise Denitrogenation Path

Trans-3,5-dimethyl-1-pyrazoline. The potential energy profiles for asynchronous step-wise denitrogenation paths of trans-3,5-dimethyl-1-pyrazoline were also mapped at four different F values of 0.5, 1.8, 4.6, and 10.2 nN corresponding to the Δr distances 0.2, 0.3, 0.5, and 1.0 Å respectively. The two different asynchronous step-wise denitrogenation paths observed for normal 1-pyrazoline were considered in the present study: (i) asynchronous step-wise denitrogenation path through a planar **DZ** intermediate - where the terminal methylene group of **DZ** is planar in nature (ii) asynchronous step-wise denitrogenation path through a pyramidal **DZ** intermediate - where the terminal methylene group of **DZ** is pyramidal in nature. First, all the four asynchronous step-wise transition states **TS3a**, **TS3c**, **TS4a**, and **TS4c** obtained for the initial cleavage of C–N bond from reactant (Chapter 5) were optimized in the presence of

Table 6.9: Geometrical parameters of **TS3a**, **TS3c**, **TS4a**, **TS4c** at different F values obtained at CASSCF(8,8)/6-31+G* level of theory^a

Structure	F (nN)	ϕ_1	ϕ_2	ϕ_3	ϕ_4	ϕ_5	ϕ_6	θ_1	d_1	d_2	d_5	d_6
TS3a	0.5 nN	-68.13	111.88	-88.79	93.76	49.54	-174.39	114.73	3.46	1.55	1.53	1.55
TS3c	0	-71.20	-11.38	14.70	176.33	45.39	168.54	117.42	3.28	1.56	1.53	1.55
	0.5	-68.53	-4.89	16.11	178.98	47.76	171.16	120.76	3.22	1.56	1.57	1.57
	1.8	-67.38	-1.52	16.49	179.83	48.77	172.23	122.46	3.20	1.56	1.55	1.58
	4.6	-65.26	4.13	16.68	-179.21	50.55	174.08	125.78	3.18	1.56	1.56	1.60
	10.2	-61.74	5.95	15.86	-177.86	52.94	176.41	133.77	3.29	1.56	1.65	1.68
TS4a	0	-69.59	90.34	-74.61	88.24	47.60	172.35	115.18	3.22	1.55	1.53	1.55
	0.5	-64.14	87.48	-90.24	80.70	52.91	177.94	118.98	3.15	1.55	1.53	1.55
	1.8	-65.00	88.74	-116.46	84.43	51.76	176.74	114.34	3.13	1.55	1.53	1.55
	4.6	-54.90	75.23	-130.42	77.52	60.94	-174.07	115.18	2.92	1.55	1.54	1.56
	10.2	-40.30	62.98	-145.53	66.57	72.83	-162.41	118.81	2.85	1.56	1.65	1.67
TS4c	0	-60.29	-60.49	-71.09	87.51	53.50	177.12	115.32	3.53	1.56	1.53	1.55
	0.5	-57.78	-60.39	-91.30	72.74	56.00	-179.96	115.92	3.50	1.56	1.53	1.56
	1.8	-58.80	-71.08	-179.16	15.07	51.49	176.92	115.72	3.67	1.58	1.64	1.67

^a Distances are in Å and angles are in degree.

external forces. The geometrical parameters of **TS3a**, **TS3c**, **TS4a**, and **TS4c** at different F values obtained at CASSCF(8,8)/6-31+G* level of theory are given in Table 6.9. It can be seen from Table 6.9 that ϕ_3 and ϕ_4 angles for **TS3a** at $F=0.5$ nN was found to be -88.79° and 93.76° respectively which are typical values for a pyramidal type **TS**. The transition state **TS3a** could not be optimized for other F values. Optimization of **TS3a** for such external force values leads to the pyramidal transition state **TS4a**. The transition states **TS3c** and **TS4c** could be optimized at all the different external forces. For **TS3a**, a significant increase in ϕ_1 , ϕ_2 , ϕ_4 , ϕ_5 , ϕ_6 , θ_1 angles and **d5** and **d6** distances with the increase in PPs distance were observed. For **TS4a**, ϕ_1 angle increases and ϕ_2 decreases by $\sim 30^\circ$ with the increase in PPs distance. Similarly, the ϕ_3 and ϕ_4 angles decrease by $\sim 70^\circ$ and $\sim 20^\circ$ and ϕ_5 and ϕ_6 angle increases by $\sim 20^\circ$ with the increase in PPs distance. The transition state **TS4c** could be optimized only for the PPs distance of 0.2 \AA . With the further increase in PPs distances, rotation of terminal methylene group of **DZ** transition state happens resulting in a change from a pyramidal to planar form **TS3c**. The relative energies of the transition states **TS3a**, **TS3c**, **TS4a**, and **TS4c** at different F values are given in Table 6.10. It can be seen from Table 6.10, that the relative energies of the asynchronous step-wise transition states decrease with the increase in external force.

Cis-3,5-dimethyl-1-pyrazoline. The potential energy profiles for asynchronous step-wise denitrogenation of cis-3,5-dimethyl-1-pyrazoline were also mapped at four different F values of 0.5, 1.8, 4.6, and 10.2 nN corresponding to the Δr distances of 0.2, 0.3, 0.5, and 1.0 \AA respectively. To understand the energetics of denitrogenation paths, first the four transition states **TS3a**,

Table 6.10: Relative energies (kcal/mol) of **TS3a**, **TS3c**, **TS4a** and **TS4c** for different F values obtained at CASSCF(8,8)/6-31+G* level of theory^a

Structure	0 nN	0.5 nN	1.8 nN	4.6 nN	10.2 nN
TS3a	46.59	46.18	NF	NF	NF
TS3c	50.15	50.27	49.79	47.28	33.23
TS4a	47.21	45.86	43.95	41.63	35.18
TS4c	48.26	47.68	NF	NF	NF

^aNF: not found

Table 6.11: Geometrical parameters of **TS3a**, **TS3c**, **TS4a**, **TS4c** at different F values obtained at CASSCF(8,8)/6-31+G* level of theory^a

Structure	F (nN)	ϕ_1	ϕ_2	ϕ_3	ϕ_4	ϕ_5	ϕ_6	θ_1	d_1	d_2	d_5	d_6
TS3a	0 nN	-69.63	97.18	-53.03	152.65	47.64	172.59	114.27	3.27	1.56	1.53	1.55
	0.5 nN	-71.85	94.12	-45.82	158.95	44.04	169.42	113.97	3.26	1.56	1.55	1.57
	1.8 nN	-71.82	92.63	-43.78	160.36	43.48	169.14	114.21	3.25	1.56	1.57	1.59
	4.6 nN	-71.04	89.65	-40.34	162.84	43.37	169.50	115.22	3.25	1.57	1.59	1.62
	10.2 nN	-70.38	87.03	-38.78	164.00	43.59	169.96	116.16	3.24	1.57	1.65	1.67
TS3c	0 nN	-60.06	-62.23	-42.69	163.91	53.42	177.22	114.41	3.54	1.57	1.53	1.55
	0.5 nN	-61.62	-63.15	-36.70	167.40	50.48	177.67	113.80	3.57	1.57	1.55	1.58
	1.8 nN	-61.46	-65.00	-34.57	168.43	50.02	176.41	113.99	3.60	1.57	1.60	1.60
	4.6 nN	-60.74	-65.40	-30.79	170.25	49.95	174.63	114.91	3.62	1.57	1.61	1.64
	10.2 nN	-60.15	-67.52	-28.75	171.23	50.16	174.93	115.80	3.65	1.57	1.64	1.67

^a Distances are in Å and angles are in degree.

TS3c, **TS4a**, and **TS4c** for the asynchronous cleavage of C–N bond from cis-3,5-dimethyl-1-pyrazolines were optimized at the different external forces. The geometrical parameters of the transition states obtained at CASSCF(8,8)/6-31+G* level of theory are given in Table 6.11. The transition states **TS4a** and **TS4c** of asynchronous step-wise denitrogenation path for cis-3,5-dimethyl-1-pyrazoline do not exist in the presence of external forces. Optimization of these structures in the presence of external forces lead to the corresponding planar transition states **TS3a** and **TS3c**. For transition state **TS3a**, no appreciable change in ϕ_1 , ϕ_6 , and θ_1 angles and d_1 and d_2 distances were observed with the increase in external force. The angle ϕ_2 of **TS3a** decreases by $\sim 10^\circ$ whereas ϕ_3 and ϕ_4 increases by $\sim 10^\circ$ with increase in the force. Both the C-CH₃ distances also increases with the increase in the external force. Similarly, for **TS3c** also, no appreciable change in ϕ_1 , ϕ_2 , ϕ_5 , ϕ_6 , and θ_1 angles and d_1 and d_2 distances were observed with the increase in the force. The ϕ_3 angle decreases by $\sim 14^\circ$ and both the C-CH₃ distances increase with the increase in external force. The relative energies of **TS3a** and **TS3c** at different external forces are given in Table 6.12. It can be seen from Table 6.12 that the relative energies of both the transition states **TS3a** and **TS3c** initially increase with the increase in external force up to 4.6 nN and then decrease by ~ 12 -14 kcal/mol for external force of 10.2 nN.

Table 6.12: Relative energies (kcal/mol) of **TS3a**, **TS3c**, **TS4a**, and **TS4c** at different F values obtained at CASSCF(8,8)/6-31+G* level of theory

Structure	0 nN	0.5 nN	1.8 nN	4.6 nN	10.2 nN
TS3a	46.57	47.80	49.16	50.74	32.80
TS3c	48.55	49.76	51.11	52.90	34.05

6.3.5 Comparison of the Energetics of Denitrogenation

To understand the effects of external force on 1-pyrazoline, trans- and cis-3,5-dimethyl-1-pyrazoline and potential energy profiles for denitrogenation of trans- and cis-3,5-dimethyl-1-pyrazoline, COGEF calculations were performed at CASSCF(8,8)/6-31+G* level of theory. The effects of external force on the potential energy profiles of denitrogenation paths, the transition states of both synchronous and asynchronous denitrogenation paths for trans- and cis-3,5-dimethyl-1-pyrazoline were also mapped at different external forces. The plot of relative energies of the transition states at different F values for trans- and cis-3,5-dimethyl-1-pyrazoline are given in Figure 6.11. It is interesting to compare the barriers for the synchronous and asynchronous paths for different magnitude of the forces. It can be seen from Figure 6.11(a) that for trans-3,5-dimethyl-1-pyrazoline, the synchronous barrier **TS1** decreases by 8 kcal/mol

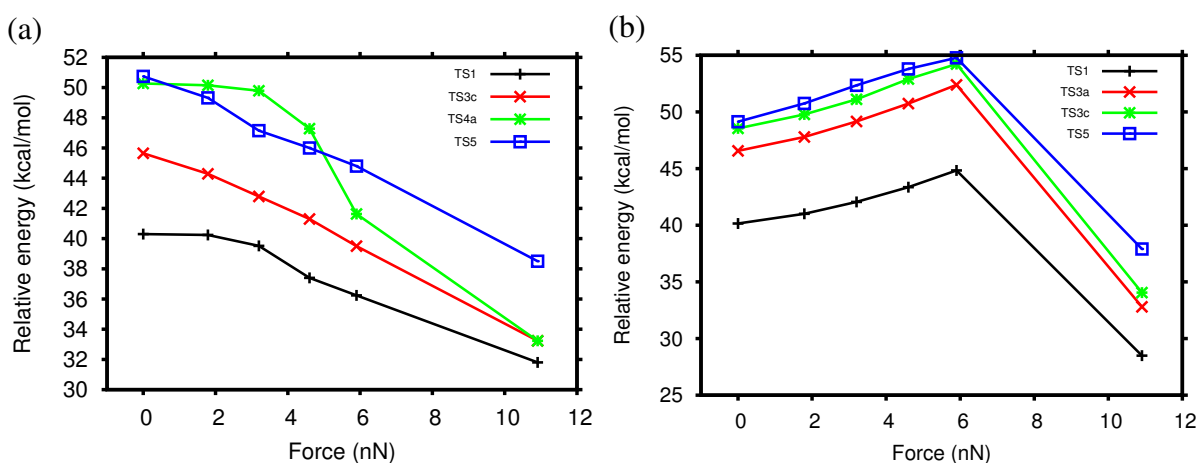


Figure 6.11: Effect of force on the energetics of (a) trans-3,5-dimethyl-1-pyrazoline (b) cis-3,5-dimethyl-1-pyrazoline.

by increasing the force to 10.2 nN. However, asynchronous step-wise path with the large barrier (**TS3c**) ~ 50 kcal/mol decreases the most by ~ 17 kcal/mol. Similar decrease in the barriers are also seen for **TS4a** and **TS5**. For cis-3,5-dimethyl-1-pyrazoline, an increase in the barriers is seen for the four transition states until 4.9 nN and then a sharp decrease is seen. The slopes of the increase are also similar (Figure 6.11(b)). The changes in the barrier heights in particular as seen for **TS3c** is expected to effect the dynamics of denitrogenation reaction in the presence of external force.

6.4 Summary and Conclusion

The effect of external force on the energetics of 1-pyrazoline and the methyl substituted analogues were investigated at CASSCF/6-31+G* level of theory using COGEF method. The presence of external force affected both the geometries and energetics of the systems. For 1-pyrazoline, in the presence of external force, all the five ring atoms formed a planar structure. With the increase in the external force, a synchronous increase in C–N and C–C distances were observed until a Δr distance of 0.8 Å after which molecule dissociates to form diazomethane and ethene.

For trans- and cis-3,5-dimethyl-1-pyrazoline, two types of COGEF calculations were carried out: (1) symmetrical stretching of both the C–CH₃ bonds, and (2) asymmetrical stretching of one of the C–CH₃ bonds. For both trans- and cis-3,5-dimethyl-1-pyrazoline, the relative energies of synchronous stretching pathway was lower in energy than the single C–CH₃ pathway up to a Δr distance of 1.4 Å and 1.5 Å, respectively beyond which the single C–CH₃ stretching pathway was lower in energy. For the single C–CH₃ stretching pathway, no significant changes in geometrical parameters of trans- and cis-3,5-dimethyl-1-pyrazoline were observed except the C–N and C–CH₃ distances associated with the stretching. However, for the synchronous stretching pathway, significant changes in geometrical parameters were observed. Like in 1-pyrazoline, all the ring atoms of trans-3,5-dimethyl-1-pyrazoline were

found to be on the same plane in the presence of the external force. However, for *cis*-3,5-dimethyl-1-pyrazoline, the molecule adapts a non-planar structure for the synchronous C-CH₃ stretching pathway. Interestingly, for both the molecules no significant changes in both the C–N distances with the increase in PPs distances were observed. The F values for both *trans*- and *cis*-3,5-dimethyl-1-pyrazoline initially increases with the increase in PPs distance and then decreases. The effect of force on the energetics of the denitrogenation pathways were investigated by mapping the energy profile for different F values. The barriers for both the synchronous and asynchronous pathways were found to decrease for *trans*-3,5-dimethyl-1-pyrazoline. However, for *cis*-3,5-dimethyl-1-pyrazoline, the barriers increased upto an F value of 6 nN and then they decreases sharply. The changes in the barrier height are expected to affect the dynamics of denitrogenation paths.

BIBLIOGRAPHY

- [1] Szabo, A.; Ostlund, N. S. *Modern Quantum Chemistry: Introduction to Advanced Electronic Structure Theory*; Courier Corporation, 2012.
- [2] Levine, I. N.; Busch, D. H.; Shull, H. *Quantum Chemistry*; Pearson Prentice Hall Upper Saddle River, NJ, 2009; Vol. 6.
- [3] Schmidt, M. W.; Gordon, M. S. *Annu. Rev. Phys. Chem.* **1998**, *49*, 233–266.
- [4] Roos, B. O. *Adv. Chem. Phys.* **1987**, 399–445.
- [5] Hohenberg, P.; Kohn, W. *Phys. rev.* **1964**, *136*, B864.
- [6] Kohn, W.; Sham, L. J. *Phys. rev.* **1965**, *140*, A1133.
- [7] Engel, T.; Reid, P.; Hehre, W.; Rodríguez, A. R.; Román, J. Z.; Pascual, A. B. *Química física*; Pearson Addison Wesley, 2006.
- [8] Eyring, H. *J. Chem. Phys.* **1935**, *3*, 107–115.
- [9] Steinfeld, J. I.; Francisco, J. S.; Hase, W. L. *Chemical Kinetics and Dynamics*; Prentice Hall Englewood Cliffs (New Jersey), 1989; Vol. 3.
- [10] Baer, T.; Hase, W. L. *Unimolecular Reaction Dynamics: theory and experiments*; Oxford University Press on Demand, 1996.
- [11] Sun, L.; Hase, W. L. *Rev. Comp. Ch.* **2003**, *19*, 79–128.
- [12] Fang, C.; Frontiera, R. R.; Tran, R.; Mathies, R. A. *Nature* **2009**, *462*, 200–204.
- [13] Chen, W.-H.; Xing, Y.; Pang, Y. *Org. Lett.* **2011**, *13*, 1362–1365.
- [14] Liu, B.; Wang, J.; Zhang, G.; Bai, R.; Pang, Y. *ACS Appl. Mater. Interfaces* **2014**, *6*, 4402–4407.

- [15] Bucher, D. B.; Schlueter, A.; Carell, T.; Zinth, W. *Angew. Chem. Int. Ed.* **2014**, *53*, 11366–11369.
- [16] Tang, Y.; Lee, D.; Wang, J.; Li, G.; Yu, J.; Lin, W.; Yoon, J. *Chem. Soc. Rev.* **2015**, *44*, 5003–5015.
- [17] Scheiner, S. *J. Phys. Chem. A* **2000**, *104*, 5898–5909.
- [18] Tolbert, L. M.; Solntsev, K. M. *Acc. Chem. Res.* **2002**, *35*, 19–27.
- [19] Hsieh, C.-C.; Jiang, C.-M.; Chou, P.-T. *Acc. Chem. Res.* **2010**, *43*, 1364–1374.
- [20] Wu, J.; Liu, W.; Ge, J.; Zhang, H.; Wang, P. *Chem. Soc. Rev.* **2011**, *40*, 3483–3495.
- [21] Zhao, J.; Ji, S.; Chen, Y.; Guo, H.; Yang, P. *Phys. Chem. Chem. Phys.* **2012**, *14*, 8803–8817.
- [22] Padalkar, V. S.; Seki, S. *Chem. Soc. Rev.* **2016**, *45*, 169–202.
- [23] Tobita, S.; Yamamoto, M.; Kurahayashi, N.; Tsukagoshi, R.; Nakamura, Y.; Shizuka, H. *J. Phys. Chem. A* **1998**, *102*, 5206–5214.
- [24] Agmon, N. *J. Phys. Chem. A* **2005**, *109*, 13–35.
- [25] Zhao, G.-J.; Liu, J.-Y.; Zhou, L.-C.; Han, K.-L. *J. Phys. Chem. B* **2007**, *111*, 8940–8945.
- [26] Zhao, G.-J.; Han, K.-L. *Biophys. J.* **2008**, *94*, 38–46.
- [27] Zhao, J.; Song, P.; Ma, F. *Commun. Comput. Chem.* **2015**, *3*, 44–54.
- [28] Zhao, J.; Li, P. *Commun. Comput. Chem.* **2015**, *3*, 66–74.
- [29] Waluk, J. *Acc. Chem. Res.* **2003**, *36*, 832–838.
- [30] Chai, S.; Zhao, G.-J.; Song, P.; Yang, S.-Q.; Liu, J.-Y.; Han, K.-L. *Phys. Chem. Chem. Phys.* **2009**, *11*, 4385–4390.
- [31] Han, K.-L.; Zhao, G.-J. *Hydrogen Bonding and Transfer in the Excited State*; Wiley-Blackwell, John Wiley & Sons Ltd: Chichester, PO19 8SQ, UK, 2010, 2011; Vol. 2.
- [32] Zhao, G.-J.; Han, K.-L. *Acc. Chem. Res.* **2012**, *45*, 404–413.
- [33] Kungwan, N.; Plasser, F.; Aquino, A. J.; Barbatti, M.; Wolschann, P.; Lischka, H. *Phys. Chem. Chem. Phys.* **2012**, *14*, 9016–9025.

- [34] Catalán, J.; del Valle, J. C.; Palomar, J.; Díaz, C.; de Paz, J. L. G. *J. Phys. Chem. A* **1999**, *103*, 10921–10934.
- [35] Sobolewski, A. L.; Domcke, W. *J. Phys. Chem. A* **1999**, *103*, 4494–4504.
- [36] Sobolewski, A. L.; Domcke, W. *Phys. Chem. Chem. Phys.* **1999**, *1*, 3065–3072.
- [37] Maheshwari, S.; Chowdhury, A.; Sathyamurthy, N.; Mishra, H.; Tripathi, H.; Panda, M.; Chandrasekhar, J. *J. Phys. Chem. A* **1999**, *103*, 6257–6262.
- [38] Mishra, H.; Joshi, H. C.; Tripathi, H. B.; Maheshwary, S.; Sathyamurthy, N.; Panda, M.; Chandrasekhar, J. *J. Photochem. Photobiol.* **2001**, *139*, 23–36.
- [39] Gelabert, R.; Moreno, M.; Lluch, J. M. *ChemPhysChem* **2004**, *5*, 1372–1378.
- [40] Mishra, H.; Maheshwary, S.; Tripathi, H.; Sathyamurthy, N. *J. Phys. Chem. A* **2005**, *109*, 2746–2754.
- [41] Park, S.; Kwon, O.-H.; Kim, S.; Park, S.; Choi, M.-G.; Cha, M.; Park, S. Y.; Jang, D.-J. *J. Am. Chem. Soc.* **2005**, *127*, 10070–10074.
- [42] Paterson, M. J.; Robb, M. A.; Blancafort, L.; DeBellis, A. D. *J. Phys. Chem. A* **2005**, *109*, 7527–7537.
- [43] Maheshwary, S.; Lourderaj, U.; Sathyamurthy, N. *J. Phys. Chem. A* **2006**, *110*, 12662–12669.
- [44] Sobolewski, A. L.; Domcke, W. *J. Phys. Chem. A* **2007**, *111*, 11725–11735.
- [45] Barbatti, M.; Aquino, A. J.; Lischka, H.; Schrieffer, C.; Lochbrunner, S.; Riedle, E. *Phys. Chem. Chem. Phys.* **2009**, *11*, 1406–1415.
- [46] Moreno, M.; Ortiz-Sánchez, J. M.; Gelabert, R.; Lluch, J. M. *Phys. Chem. Chem. Phys.* **2013**, *15*, 20236–20246.
- [47] Zhao, J.; Chen, J.; Liu, J.; Hoffmann, M. R. *Phys. Chem. Chem. Phys.* **2015**, *17*, 11990–11999.
- [48] Amat, A.; Miliiani, C.; Romani, A.; Fantacci, S. *Phys. Chem. Chem. Phys.* **2015**, *17*, 6374–6382.
- [49] Azarias, C.; Budzák, Š.; Laurent, A. D.; Ulrich, G.; Jacquemin, D. *Chem. Sci.* **2016**, *7*, 3763–3774.

- [50] Itoh, M.; Tokumura, K.; Tanimoto, Y.; Okada, Y.; Takeuchi, H.; Obi, K.; Tanaka, I. *J. Am. Chem. Soc.* **1982**, *104*, 4146–4150.
- [51] McMorro, D.; Kasha, M. *J. Am. Chem. Soc.* **1983**, *105*, 5133–5134.
- [52] Itoh, M.; Tanimoto, Y.; Tokumura, K. *J. Am. Chem. Soc.* **1983**, *105*, 3339–3340.
- [53] Bouman, T. D.; Knobloch, M. A.; Bohan, S. *J. Phys. Chem.* **1985**, *89*, 4460–4464.
- [54] Chudoba, C.; Riedle, E.; Pfeiffer, M.; Elsaesser, T. *Chem. Phys. Lett.* **1996**, *263*, 622–628.
- [55] Klymchenko, A. S.; Ozturk, T.; Pivovarenko, V. G.; Demchenko, A. P. *Tetrahedron Lett.* **2001**, *42*, 7967–7970.
- [56] Shynkar, V. V.; Mely, Y.; Duportail, G.; Piémont, E.; Klymchenko, A. S.; Demchenko, A. P. *J. Phys. Chem. A* **2003**, *107*, 9522–9529.
- [57] Shynkar, V. V.; Klymchenko, A. S.; Piemont, E.; Demchenko, A. P.; Mély, Y. *J. Phys. Chem. A* **2004**, *108*, 8151–8159.
- [58] Klymchenko, A. S.; Kenfack, C.; Duportail, G.; Mély, Y. *J. Chem. Sci.* **2007**, *119*, 83–89.
- [59] Kenfack, C. A.; Klymchenko, A. S.; Duportail, G.; Burger, A.; Mély, Y. *Phys. Chem. Chem. Phys.* **2012**, *14*, 8910–8918.
- [60] Chevalier, K.; Grün, A.; Stamm, A.; Schmitt, Y.; Gerhards, M.; Diller, R. *J. Phys. Chem. A* **2013**, *117*, 11233–11245.
- [61] Yu, W.-S.; Cheng, C.-C.; Cheng, Y.-M.; Wu, P.-C.; Song, Y.-H.; Chi, Y.; Chou, P.-T. *J. Am. Chem. Soc.* **2003**, *125*, 10800–10801.
- [62] Lin, T.-Y.; Tang, K.-C.; Yang, S.-H.; Shen, J.-Y.; Cheng, Y.-M.; Pan, H.-A.; Chi, Y.; Chou, P.-T. *J. Phys. Chem. A* **2012**, *116*, 4438–4444.
- [63] Chung, M.-W.; Liao, J.-L.; Tang, K.-C.; Hsieh, C.-C.; Lin, T.-Y.; Liu, C.; Lee, G.-H.; Chi, Y.; Chou, P.-T. *Phys. Chem. Chem. Phys.* **2012**, *14*, 9006–9015.
- [64] Kumar, N.; Chakravorti, S.; Chowdhury, P. *J. Mol. Struct.* **2008**, *891*, 351–356.
- [65] Singla, N.; Kumar, R.; Pathak, A.; Chowdhury, P. *Spectrochim. Acta, Part A* **2013**, *112*, 125–131.

- [66] Singla, N.; Chowdhury, P. *Chem. Phys. Lett.* **2014**, *612*, 25–32.
- [67] Lim, S.-J.; Seo, J.; Park, S. Y. *J. Am. Chem. Soc.* **2006**, *128*, 14542–14547.
- [68] Shono, H.; Ohkawa, T.; Tomoda, H.; Mutai, T.; Araki, K. *ACS Appl. Mater. Interfaces* **2011**, *3*, 654–657.
- [69] Yang, Y.; Zhao, Q.; Feng, W.; Li, F. *Chem. Rev.* **2012**, *113*, 192–270.
- [70] Yuan, L.; Lin, W.; Zheng, K.; He, L.; Huang, W. *Chem. Soc. Rev.* **2013**, *42*, 622–661.
- [71] Lee, M. H.; Kim, J. S.; Sessler, J. L. *Chem. Soc. Rev.* **2015**, *44*, 4185–4191.
- [72] Demchenko, A. P. *FEBS Lett.* **2006**, *580*, 2951–2957.
- [73] Tang, K.-C.; Chang, M.-J.; Lin, T.-Y.; Pan, H.-A.; Fang, T.-C.; Chen, K.-Y.; Hung, W.-Y.; Hsu, Y.-H.; Chou, P.-T. *J. Am. Chem. Soc.* **2011**, *133*, 17738–17745.
- [74] Kim, S. H.; Park, S.; Kwon, J. E.; Park, S. Y. *Adv. Funct. Mater.* **2011**, *21*, 644–651.
- [75] Sreedevi, K. G.; Thomas, A. P.; Aparna, K.; Pradhan, R.; Reddy, M.; Lourderaj, U.; Srinivasan, A. *Chem. Commun.* **2014**, *50*, 8667–8669.
- [76] Pradhan, R.; Harshan, A. K.; Krishnavilasam Chandrika, G. S.; Srinivasan, A.; Lourderaj, U. *J. Phys. Chem. A* **2016**, *120*, 9894–9906.
- [77] Becke, A. D. *J. Chem. Phys.* **1993**, *98*, 5648–5652.
- [78] Lee, C.; Yang, W.; Parr, R. G. *Phys. Rev. B* **1988**, *37*, 785–789.
- [79] Miehlich, B.; Savin, A.; Stoll, H.; Preuss, H. *Chem. Phys. Lett.* **1989**, *157*, 200–206.
- [80] Becke, A. D. *Phys. Rev. A* **1988**, *38*, 3098–3100.
- [81] Stephens, P.; Devlin, F.; Chabalowski, C.; Frisch, M. J. *J. Phys. Chem.* **1994**, *98*, 11623–11627.
- [82] Hertwig, R. H.; Koch, W. *Chem. Phys. Lett.* **1997**, *268*, 345–351.
- [83] Hariharan, P.; Pople, J. *Theor. Chem. Acc.* **1973**, *28*, 213–222.
- [84] Clark, T.; Chandrasekhar, J.; Spitznagel, G. W.; Schleyer, P. V. R. *J. Comp. Chem.* **1983**, *4*, 294–301.

- [85] Marques, M. A.; Gross, E. *Annu. Rev. Phys. Chem.* **2004**, *55*, 427–455.
- [86] Adamo, C.; Jacquemin, D. *Chem. Soc. Rev.* **2013**, *42*, 845–856.
- [87] Zhao, Y.; Schultz, N. E.; Truhlar, D. G. *J. Chem. Theory Comput.* **2006**, *2*, 364–382.
- [88] Schmidt, M. W.; Baldridge, K. K.; Boatz, J. A.; Elbert, S. T.; Gordon, M. S.; Jensen, J. H.; Koseki, S.; Matsunaga, N.; Nguyen, K. A.; Su, S.; Windus, T. L.; Dupuis, M.; Montgomery Jr, J. A. *J. Comput. Chem.* **1993**, *14*, 1347–1363.
- [89] Marenich, A. V.; Cramer, C. J.; Truhlar, D. G. *J. Phys. Chem. B* **2009**, *113*, 6378–6396.
- [90] Crawford, R. J.; Mishra, A. *J. Am. Chem. Soc.* **1966**, *88*, 3963–3969.
- [91] Garratt, P. J.; White, J. F. *J. Org. Chem.* **1977**, *42*, 1733–1736.
- [92] Berson, J. A. *Acc. Chem. Res.* **1978**, *11*, 446–453.
- [93] Little, R. D. *Chem. Rev.* **1996**, *96*, 93–114.
- [94] Condit, P. B.; Bergman, R. G. *J. Chem. Soc. Chem. Comm.* **1971**, 4b–6.
- [95] White, D. H.; Condit, P. B.; Bergman, R. G. *J. Am. Chem. Soc.* **1972**, *94*, 7931–7933.
- [96] Clarke, T. C.; Wendling, L. A.; Bergman, R. G. *J. Am. Chem. Soc.* **1977**, *99*, 2740–2750.
- [97] Hiberty, P. C.; Jean, Y. *J. Am. Chem. Soc.* **1979**, *101*, 2538–2543.
- [98] Simpson, C.; Wilson, G.; Adam, W. *J. Am. Chem. Soc.* **1991**, *113*, 4728–4732.
- [99] Lyons, B. A.; Pfeifer, J.; Peterson, T. H.; Carpenter, B. K. *J. Am. Chem. Soc.* **1993**, *115*, 2427–2437.
- [100] Sorescu, D. C.; Thompson, D. L.; Raff, L. M. *J. Chem. Phys.* **1995**, *102*, 7910–7924.
- [101] Carpenter, B. K. *J. Am. Chem. Soc.* **1995**, *117*, 6336–6344.
- [102] Reyes, M. B.; Carpenter, B. K. *J. Am. Chem. Soc.* **1998**, *120*, 1641–1642.
- [103] Reyes, M. B.; Carpenter, B. K. *J. Am. Chem. Soc.* **2000**, *122*, 10163–10176.
- [104] Khuong, K. S.; Houk, K. *J. Am. Chem. Soc.* **2003**, *125*, 14867–14883.
- [105] Abe, M.; Ishihara, C.; Kawanami, S.; Masuyama, A. *J. Am. Chem. Soc.* **2005**, *127*, 10–11.

- [106] Carpenter, B. K. *Chem. rev.* **2013**, *113*, 7265–7286.
- [107] Safont, V. S.; González-Navarrete, P.; Oliva, M.; Andrés, J. *Phys. Chem. Chem. Phys.* **2015**, *17*, 32358–32374.
- [108] Shen, K. K.-W.; Bergman, R. G. *J. Am. Chem. Soc.* **1977**, *99*, 1655–1657.
- [109] Chowdhury, M. A.; Senboku, H.; Tokuda, M. *Tetrahedron Lett.* **2003**, *44*, 3329–3332.
- [110] Hamaguchi, M.; Nakaishi, M.; Nagai, T.; Nakamura, T.; Abe, M. *J. Am. Chem. Soc.* **2007**, *129*, 12981–12988.
- [111] Izadyar, M.; Harati, M. *Prog. React. Kinet. Mec.* **2012**, *37*, 423–435.
- [112] Pradhan, R.; Lourderaj, U. *Phys. Chem. Chem. Phys.* **2017**, *19*, 27468–27477.
- [113] Hehre, W.; Radom, L.; Schleyer, P. v. R.; Pople, J.; Initio, A. *J. Wiley and Sons, New York* **1986**,
- [114] Dunning Jr, T. H. *J. Chem. Phys.* **1989**, *90*, 1007–1023.
- [115] Kendall, R. A.; Dunning Jr, T. H.; Harrison, R. J. *J. Chem. Phys.* **1992**, *96*, 6796–6806.
- [116] Ren, P.; Wu, C.; Ponder, J. W. *J. Chem. Theory Comput.* **2011**, *7*, 3143–3161.
- [117] Andersson, K.; Malmqvist, P.-Å.; Roos, B. O. *J. Chem. Phys.* **1992**, *96*, 1218–1226.
- [118] Frisch, M. J. et al. Gaussian09 Revision D.01. Gaussian Inc. Wallingford CT 2009.
- [119] Werner, H.-J.; Knowles, P. J.; Knizia, G.; Manby, F. R.; Schütz, M. *WIREs Comput Mol Sci* **2012**, *2*, 242–253.
- [120] Doubleday, C. *J. Phys. Chem.* **1996**, *100*, 3520–3526.
- [121] Doubleday, C.; Bolton, K.; Peslherbe, G. H.; Hase, W. L. *J. Am. Chem. Soc.* **1996**, *118*, 9922–9931.
- [122] Dubnikova, F.; Lifshitz, A. *J. Phys. Chem. A* **1998**, *102*, 3299–3306.
- [123] Doubleday, C.; Bolton, K.; Hase, W. L. *J. Phys. Chem. A* **1998**, *102*, 3648–3658.
- [124] Sinicropi, A.; Page, C. S.; Adam, W.; Olivucci, M. *J. Am. Chem. Soc.* **2003**, *125*, 10947–10959.

- [125] Roth, W.; Martin, M. *Tetrahedron Letters* **1967**, *8*, 4695–4698.
- [126] Roth, W. R.; Martin, M. *European Journal of Organic Chemistry* **1967**, *702*, 1–7.
- [127] Lourderaj, U.; Sun, R.; Kohale, S. C.; Barnes, G. L.; de Jong, W. A.; Windus, T. L.; Hase, W. L. *Computer Physics Communications* **2014**, *185*, 1074–1080.
- [128] James, S. L. et al. *Chem. Soc. Rev.* **2012**, *41*, 413–447.
- [129] Ribas-Arino, J.; Marx, D. *Chem. rev.* **2012**, *112*, 5412–5487.
- [130] Li, J.; Nagamani, C.; Moore, J. S. *Acc. chem. res.* **2015**, *48*, 2181–2190.
- [131] Huang, Z.; Boulatov, R. *Chem. Soc. Rev.* **2011**, *40*, 2359–2384.
- [132] Stauch, T.; Dreuw, A. *Chem. Rev.* **2016**, *116*, 14137–14180.
- [133] Hickenboth, C. R.; Moore, J. S.; White, S. R.; Sottos, N. R.; Baudry, J.; Wilson, S. R. *Nature* **2007**, *446*, 423–427.
- [134] Caruso, M. M.; Davis, D. A.; Shen, Q.; Odom, S. A.; Sottos, N. R.; White, S. R.; Moore, J. S. *Chem. Rev.* **2009**, *109*, 5755–5798.
- [135] Ong, M. T.; Leiding, J.; Tao, H.; Virshup, A. M.; Martínez, T. J. *J. Am. Chem. Soc.* **2009**, *131*, 6377–6379.
- [136] Nava, P.; Carissan, Y. *Phys. Chem. Chem. Phys.* **2014**, *16*, 16196–16203.
- [137] Wang, J.; Kouznetsova, T. B.; Niu, Z.; Ong, M. T.; Klukovich, H. M.; Rheingold, A. L.; Martinez, T. J.; Craig, S. L. *Nat. chem.* **2015**, *7*, 323–327.
- [138] Wang, J.; Kouznetsova, T. B.; Niu, Z.; Rheingold, A. L.; Craig, S. L. *J. Org. Chem.* **2015**, *80*, 11895–11898.
- [139] Wollenhaupt, M.; Krupička, M.; Marx, D. *ChemPhysChem* **2015**, *16*, 1593–1597.
- [140] Woodward, R. B.; Hoffmann, R. *J. Am. Chem. Soc.* **1965**, *87*, 395–397.
- [141] Woodward, R. B.; Hoffmann, R. *Angew. Chem. Int. Ed. Engl.* **1969**, *8*, 781–853.
- [142] Lenhardt, J. M.; Ong, M. T.; Choe, R.; Evenhuis, C. R.; Martinez, T. J.; Craig, S. L. *Science* **2010**, *329*, 1057–1060.
- [143] Smalø, H. S.; Uggerud, E. *Chemical Communications* **2012**, *48*, 10443–10445.

- [144] Jacobs, M. J.; Schneider, G.; Blank, K. G. *Angew. Chem. Int. Ed.* **2016**, *55*, 2899–2902.
- [145] Krupička, M.; Dopieralski, P.; Marx, D. *Angew. Chem.* **2017**,
- [146] Khanal, A.; Long, F.; Cao, B.; Shahbazian-Yassar, R.; Fang, S. *Chem. Eur. J* **2016**, *22*, 9760–9767.
- [147] Msaddek, M.; Ben hamadi, N. *C. R. Chim.* **2012**, *15*, 409–413.
- [148] Beyer, M. K. *J. Chem. Phys.* **2000**, *112*, 7307–7312.

